

# **Real Time Nanogravimetric Monitoring of Corrosion in Radioactive Environments**

By

Tzagkaroulakis Ioannis

*Being a thesis submitted to Lancaster University in partial fulfilment of the  
requirements for the degree of*

**DOCTOR OF PHILOSOPHY**

December 2017



## Declaration

The work presented in this thesis was conducted at Lancaster University between May 2013 and December 2017. Unless stated otherwise, it is the work of the author and has not been submitted in support of any other degree.

Signature: \_\_\_\_\_

Tzagkaroulakis Ioannis

6 December 2017

## Abstract

Monitoring and understanding the mechanism of metal corrosion throughout the nuclear fuel cycle play a key role in the safe asset management of facilities. They also provide information essential for making an informed choice regarding the selection of decontamination methods for steel plant and equipment scheduled for decommissioning. Recent advances in Quartz Crystal Nanobalance (QCN) technology offer the means of monitoring corrosion in-situ, in radiologically harsh environments, in real time and with high sensitivity. Oxalic acid has been widely used in nuclear plants and installations as a corrosion inhibitor for carbon steels and as a decontamination cleaning agent due to its ability to remove rust from the surface of ferritic metals and alloys. As an exemplar system for decontamination, the corrosion behaviour of mild carbon steel and pure iron samples in 1 wt% to 8wt% oxalic acid solutions have been measured and compared in real time and in situ using QCN. Corrosion rates measured using QCN are found to agree with those obtained using corrosion current ( $i_{\text{CORR}}$ ) measurements, with the added advantages of: (i) real time measurements of higher sensitivity with the potential for making them in situ; (ii) reduced uncertainty in the conversion of the QCN measured frequency change to a mass change-based corrosion rate compared to the conversion of the  $i_{\text{CORR}}$  measured by LSV with Tafel extrapolation to mass change; (iii) the provision of mechanistic insights into the action of oxalic acid on Fe-rich steels. QCN has been used as a corrosion monitoring technique to study the impact of radiolytically generated peroxide on the corrosion protection afforded by oxalate to Fe surfaces. Results reveal that QCN can be the ideal means of measuring corrosion rates in situ, in real time, when two chemical reactions are taking place such as the ferrous oxalate layer production and the breakdown of the layer due to Fenton reactions. QCN has been studied as a corrosion monitoring technique for other decontamination solutions such as basic and acid permanganate and oxalic acid / nitric acid mixtures. Results reveal that QCN is a very promising tool for studying the efficacy of these new

decontamination agent formulations with the sensor providing useful mechanistic information of the mode-of-action of the decontaminating agent from the mass change (gain or loss) in real time.

## Acknowledgements

I would like to thank my director of studies, Professor Colin Boxall, for his advice, patience and positivity throughout the course of this research. I would like to thank my industrial supervisor Dr. Divyesh Trivedi of the National Nuclear Laboratory for the keen interest in the work.

I wish to thank the Nuclear Decommissioning Authority for funding this project, the Lloyd's Register Foundation and the UTGARD laboratory for providing the research facilities.

I would like to thank the UTGARD and the Lloyd's Register Foundation research groups (staff and students) for providing a friendly working environment.

Finally, my utmost thanks go to my parents, my brother and my sister for their constant support and for always being there in good and not so good times.

## Contents

Declaration.....	ii
Abstract.....	iii
Acknowledgements.....	v
Contents.....	vi
List of Figures .....	ix
List of Tables .....	xv
Objectives of the work.....	1
Chapter 1.....	4
1. Introduction .....	5
1.1. The nuclear fuel cycle .....	6
1.1.1. Nuclear reactors.....	7
1.1.2. Nuclear spent fuel reprocessing plant .....	8
1.1.3. Evaporators for volumetric reduction of nuclear waste.....	10
1.1.4. Nuclear waste tanks.....	11
1.1.4.1. Waste tanks on the Savannah River Site.....	11
1.1.4.2. Waste tanks on the Hanford Site .....	15
1.1.4.3. Waste tanks in the UK.....	16
1.2. Common applications for corrosion monitoring on nuclear sites .....	17
1.2.1. Water cooling circuits exposed to oxidising coolant .....	17
1.2.2. Integrity of pipework exposed to nitric acid during the reprocessing of spent fuel ....	18
1.2.3. Decontamination of evaporators.....	19
1.2.4. Decontamination of waste tanks on the Savannah River Site, case study of a model system .....	22
1.2.5. Decontamination of waste tanks on the Hanford Site, case study of a model system	25
1.3. Methods of measuring corrosion rates .....	26
1.3.1. Commonly used methods of measuring corrosion rates.....	26
1.3.1.1. Linear polarization resistance .....	27
1.3.1.2. Coupon weight loss.....	29
1.3.1.3. Electrical resistance probe .....	30
1.3.1.4. Galvanic monitoring technique.....	31
1.3.1.5. Summary .....	32
1.3.2. Quartz crystal nanobalance .....	32
1.3.3. Conclusions .....	38

Chapter 2.....	39
2. Experimental.....	40
2.1. Materials and reagents.....	40
2.2. Fabrication of mild carbon steel and iron disc electrodes.....	40
2.3. Electrochemical measurements.....	41
2.4. Electrochemical quartz crystal nanobalance experiments.....	42
2.5. Preparation of iron crystals for electrochemical QCN corrosion experiments.....	46
Chapter 3.....	48
3. Comparison of iron and mild carbon steel corrosion behaviour in oxalic acid environments.....	49
3.1. Behaviour of mild carbon steel and iron electrodes in the presence of oxalic acid.....	50
3.2. Behaviour of mild carbon steel and iron electrodes in the presence of oxalic acid and hydrogen peroxide as a simulant for the products of the radiolysis of water.....	60
3.3. Behaviour of mild carbon steel and iron electrodes in the presence of oxalic acid at high temperature.....	73
3.4. Exploration of the electrochemical activity of oxalic acid and oxalic acid / hydrogen peroxide mixtures at high temperatures.....	77
3.5 Summary.....	79
Chapter 4.....	81
4. Optical Microscope (OM) imaging and Raman studies.....	82
4.1. Optical Microscope (OM) imaging and Raman studies of the iron rod surface immersed in 8wt% oxalic acid.....	84
4.2. Summary.....	93
Chapter 5.....	95
5. Nanogravimetric and electrochemical analysis of iron crystals in oxalic acid environments.....	96
5.1 Non-radioactive environments.....	96
5.2 Simulated radioactive environments.....	103
5.3 Summary.....	123
Chapter 6.....	124
6. Monitoring corrosion rates using corrosion current ( $i_{CORR}$ ) measurements.....	125
6.1 Non-radioactive and simulated radioactive environments.....	125
6.2 Summary.....	129
Chapter 7.....	130
7 Real time nanogravimetric monitoring of corrosion using QCN.....	131
7.1. Non-radioactive environments.....	131
7.2. Simulated radioactive environments.....	135

7.3 Summary .....	140
Chapter 8.....	142
8 The use of QCN technology for the electrochemical / nanogravimetric analysis of steel, and real time monitoring of corrosion, for nuclear clean-out applications. ....	143
8.1 Nanogravimetric and electrochemical analysis of iron and mild steel samples in $\text{H}_2\text{C}_2\text{O}_4 + \text{HNO}_3$ at ambient temperature and at $50^\circ\text{C}$ .....	145
8.2 Nanogravimetric and electrochemical analysis of iron and mild steel samples in $\text{KMnO}_4 + \text{NaOH}$ environments.....	154
8.3 Nanogravimetric and electrochemical analysis of iron and mild steel samples in $\text{KMnO}_4 + \text{HNO}_3$ .....	160
8.4 Summary .....	163
Chapter 9.....	165
9. Conclusions and summary .....	166
9.1 Conclusions .....	166
9.2 Summary .....	169
References .....	172

## List of Figures

<u>Chapters</u>	<u>Pages</u>
<u>Chapter 1</u>	
<b>Figure 1.1.1.:</b> Flow diagram of the nuclear fuel cycle adapted from the website of the United States Nuclear Regulatory Commission [2].....	6
<b>Figure 1.1.1.1.:</b> Schematic diagram of a pressurised water reactor [3].....	8
<b>Figure 1.1.2.1.:</b> Flow of Light Water reactors (LWR) Spent Fuel Reprocessing adapted from the website of the Japan Atomic Energy Agency [10].....	9
<b>Figure 1.1.3.1.:</b> Simplified diagram of the process for volumetric reduction of waste at SRS adapted from the work of Wilusz et. al.[12].....	10
<b>Figure 1.1.4.1.1.:</b> Type I High level waste tank adapted from the work of J Pavletich [18].....	12
<b>Figure 1.1.4.1.2.:</b> F-Tank Farm waste tank composite of 22 waste tanks adapted from the work of DOE/SRS-WD-2012-001[13].....	15
<b>Figure 1.1.4.3.1.:</b> High Level Liquid Waste storage tank in UK adapted from the work of Dobson et. al. [27].....	16
<b>Figure 1.2.3.1.:</b> SRS 2H Evaporator before and after the chemical cleaning process (Nitric acid 1.5M at 90°C ) adapted from the work of Calloway, et. al. [36].....	21
<b>Figure 1.2.4.1.:</b> ECC Process in SRS adapted from the work of Matino et. al.[44], Ketusky et.al.[47] and from the report DOE/SRS-WD-2012-001[13].....	25
<b>Figure 1.3.1.1.1.:</b> Forward going sweeps in the first scan cyclic voltammograms, and associated LSVs, of iron piezoelectrodes in 1 wt% oxalic acid.....	28
<b>Figure 1.3.1.3.1.:</b> Types and shapes of several electrical resistance probes adapted from the work of Roberge [51].....	31
<b>Figure 1.3.2.1.:</b> A) RLC circuit in series and B) Butterworth van Dyke model adapted from document about the basics of a quartz crystal microbalance published by Gamry instruments [55].....	33
<b>Figure 1.3.2.2.:</b> Quartz crystal adapted with iron surface adapted from the work of P. Marcus et. al. [54].....	35
<b>Figure 1.3.2.3.:</b> The mass and current density change of an Fe-25Cr coated crystal in 0.1M H <sub>2</sub> SO <sub>4</sub> + 0.4M Na <sub>2</sub> SO <sub>4</sub> scanned from -0.5V to 1.5V vs standard hydrogen electrode with scan rate equal to 20mV/s adapted from the work of Schmutz et. al. [62].....	36
<b>Figure 1.3.2.4.:</b> A) and B) The mass (b)) and current density (a)) change of iron and Fe-25Cr coated crystals in 0.1 H <sub>2</sub> SO <sub>4</sub> + 0.4M Na <sub>2</sub> SO <sub>4</sub> at fixed potentials vs standard hydrogen electrode respectively (adapted from the work of Schmutz et. al. [62]).....	37

## Chapter 2

<b>Figure 2.2.1.:</b> A) Photographs and B) Schematics of rod samples during fabrication.....	41
<b>Figure 2.4.1.:</b> Schematic of the experimental set up for QCN experiments A) using two electrode cell, B) and three electrode cell.....	43
<b>Figure 2.4.2.:</b> Photograph of the QCN experimental arrangement using three electrode cell.....	43
<b>Figure 2.4.3.:</b> Cyclic voltammogram and voltamassogram of iron crystal immersed in solution of 10 mmol L <sup>-1</sup> CuSO <sub>4</sub> in 100mmol L <sup>-1</sup> H <sub>2</sub> SO <sub>4</sub> (scan rate 0.05Vs <sup>-1</sup> ). A) Plot of potential against current and frequency change and B) plot of charge against frequency change obtained from forward (cathodic) going sweep.....	46

## Chapter 3

<b>Figure 3.1.1.:</b> Comparing cyclic voltammograms of mild carbon steel, (A) and (C), and iron electrodes, (B) and (D), in 1wt % oxalic acid, pH=1.3 (A) and (B) and 8wt% oxalic acid, pH=0.85 (C) and (D). Scan rate = 0.01V/s.....	51
<b>Figure 3.1.2.:</b> Simplified E <sub>h</sub> -pH (Pourbaix) diagrams for the (A) Fe-oxalate-H <sub>2</sub> O and (B) Fe-H <sub>2</sub> O systems, adapted from the work of Saltykov <i>et al.</i> [82] and Pourbaix [81].....	53
<b>Figure 3.1.3.:</b> Cyclic voltammogram of an iron crystal in 1wt% KNO <sub>3</sub> . pH=3.3. Scan rate =0.01V/s.....	53
<b>Figure 3.1.4.:</b> Modification of the mild carbon steel surface during potentiodynamic polarization in 0.3M (=2.7 wt%) aqueous oxalic acid solution adapted from the work of Camalet <i>et. al</i> [74] .....	54
<b>Figure 3.1.5.:</b> A) Current – Potential, B) Capacity – Potential curves recorded at an iron electrode immersed in 0.11M oxalic acid solution adapted from the work of Mengoli <i>et al</i> [76]. Scan rate 20mVs <sup>-1</sup> .....	57
<b>Figure 3.1.7.:</b> E <sub>oc</sub> measurements for iron and mild carbon steel electrodes as a function of oxalic acid concentration in the range 1 to 8 wt%.....	58
<b>Figure 3.1.6.:</b> Forward going sweeps in the first scan cyclic voltammograms, and associated LSVs, of iron rod electrodes in (A) 1 and (B) 8 wt% oxalic acid and of iron piezoelectrodes in (C) 1 and (D) 8 wt% oxalic acid. Scan rate = 0.01V/s.....	59
<b>Figure 3.2.1.:</b> A) The calibration curve for hydrogen peroxide generated by irradiation. The squares and triangles stand for hydrogen peroxide concentration generated by thallium-201 and technetium-99m respectively adapted from the work of Shourian <i>et.al</i> [84]. B) Accumulation of H <sub>2</sub> O <sub>2</sub> during the irradiation of water saturated with oxygen adapted from the work of T. Song <i>et. all</i> [85] .....	62

<b>Figure 3.2.2.:</b> Comparing cyclic voltammograms of mild carbon steel, (A), (C), (E), (G), (I), (K), (M), (O), (Q), (S) and iron electrodes (B), (D), (F), (H), (J), (L), (N), (P), (R), (T) in 1 and 8 wt % oxalic acid as a function of [H <sub>2</sub> O <sub>2</sub> ] from 20 to 100 mM. Scan rate = 0.01V/s.....	67
<b>Figure 3.2.3.:</b> E <sub>OC</sub> measurements for iron and mild carbon steel rod electrodes in 1 and 8 wt% oxalic acid as a function of hydrogen peroxide concentration in the range 0 to 240 mM for titrating 60 mM of hydrogen peroxide periodically after 1800, 2700, 3600 and 4500sec in 1 and 8 wt% oxalic. (A) The relationship between E <sub>OC</sub> and the time (B) The relationship between E <sub>OC</sub> and [H <sub>2</sub> O <sub>2</sub> ].....	72
<b>Figure 3.3.1.:</b> Forward going sweeps in the first scan cyclic voltammograms, of iron and mild carbon steel rod electrodes at 75°C in (A) 1 and (B) 8 wt% oxalic acid and associated LSVs in (C) 1 and (D) 8 wt% oxalic acid. Scan rate = 0.01V/s.....	75
<b>Figure 3.3.2.:</b> Simplified E <sub>h</sub> -pH (Pourbaix) diagrams for iron at 10 <sup>-6</sup> M at 100°C adapted from the work of Beverskog [94].....	76
<b>Figure 3.3.3.:</b> E <sub>OC</sub> measurements for iron and mild carbon steel electrodes as a function of oxalic acid concentration in the range 1 to 8 wt% at 75°C.....	77
<b>Figure 3.4.1.:</b> Cyclic voltammograms of carbon electrode in (A) 1wt % oxalic acid, pH=1.3 and (B) in 8wt% oxalic acid, pH=0.85. Scan rate = 0.01V/s.....	79
 <b>Chapter 4</b>	
<b>Figure 4.1.:</b> Raman spectra of A) iron(II)oxalate and B) iron(III) oxalate adapted from the work of Edwards et al.[95].....	82
<b>Figure 4.2.:</b> Raman spectra of iron particles.....	83
<b>Figure 4.1.1.:</b> Voltamassogram / voltammogram for an iron piezoelectrode in 8 wt% oxalic acid cycled from -1 to 1V.....	84
<b>Figure 4.1.2.:</b> Cyclic Voltammograms of iron crystal in 8 wt% oxalic acid scanned from -1 to 1V.....	86
<b>Figure 4.1.3.:</b> Comparison of the Raman spectra of iron species at different laser powers: A) Raman spectrum of Fe <sub>3</sub> O <sub>4</sub> powder duration time 400sec, 30% of the full laser power of 30mW B) Raman spectrum of Fe <sub>3</sub> O <sub>4</sub> powder duration time 600sec, 30% of the laser power of 30mW, C) Raman spectrum of Fe <sub>3</sub> O <sub>4</sub> powder duration time 600sec, 100% of the laser power of 30mW.....	89
<b>Figure 4.1.4.:</b> FT-Raman spectra of iron samples at 4 points during a cyclic voltammogram of an iron rod in 8wt% oxalic acid.....	91

## Chapter 5

<b>Figure 5.1.1.:</b> Cyclic voltammogram of an iron crystal in A) 1 and B) 8 wt% oxalic acid solution respectively (scan rate = 0.01V/sec).....	97
<b>Figure 5.1.2.:</b> Cyclic voltammograms of iron crystals in 1, 2 and 8wt% of oxalic acid (scan rate = 0.01V/sec).....	99
<b>Figure 5.1.3.:</b> Comparing 3 scan cyclic voltammograms of iron crystals, in 1wt % oxalic acid (A) and in 8wt% oxalic acid (B).....	100
<b>Figure 5.1.4.:</b> The molar mass of the deposited material layer in function of the potential window with starting point of -0.45V when iron quartz crystals immersed in oxalic acid solution.....	102
<b>Figure 5.2.1.:</b> Comparing the voltammetry and mass changes observed on an iron piezoelectrode when the electrode is scanned from -1V to +1V in 1 and 8wt% oxalic acid as a function of [H <sub>2</sub> O <sub>2</sub> ].....	106
<b>Figure 5.2.2.:</b> Cyclic voltammogram of an iron crystal in 60mM H <sub>2</sub> O <sub>2</sub> A) and the corresponding Tafel plot per surface area B).....	107
<b>Figure 5.2.3.:</b> E <sub>OC</sub> and nanogravimetric data as a function of time, recorded from Fe piezoelectrodes using the QCN in 60mM H <sub>2</sub> O <sub>2</sub> .....	110
<b>Figure. 5.2.4.:</b> Forward going sweeps per surface area in the first scan cyclic voltammograms, and associated LSVs, of iron piezoelectrodes in a mixture of 1 and 8 wt% oxalic acid and a variety of H <sub>2</sub> O <sub>2</sub> concentrations.....	113
<b>Figure 5.2.5.:</b> Cyclic voltammogram of an iron crystal in a mixture of 1wt% oxalic acid and 60 mM H <sub>2</sub> O <sub>2</sub> .....	115
<b>Figure 5.2.6.:</b> Comparing the mass change of an iron crystal when the surface is scanned from -1V to +1V in 1 and 8wt% oxalic acid as a function of H <sub>2</sub> O <sub>2</sub> concentration.....	119
<b>Figure 5.2.7.:</b> The molar mass of the deposited material layer in function of the potential window with starting point of -0.45V when iron quartz crystals immersed in, 1wt% oxalic acid / hydrogen peroxide mixtures A) and in 8wt% oxalic acid / hydrogen peroxide mixtures B).....	121

## Chapter 6

<b>Figure. 6.1.1.:</b> Forward going sweeps per surface area in the first scan cyclic voltammograms, and associated LSVs, of iron piezoelectrodes in a mixture of 1 and 8 wt% oxalic acid in presence and absence of H <sub>2</sub> O <sub>2</sub> concentrations.....	127
<b>Figure 6.1.2.:</b> Tafel plots for data in the vicinity of the E <sub>CORR</sub> , extracted from Figures 6.1.1.A, B, C and D respectively. Extrapolated E <sub>CORR</sub> and i <sub>CORR</sub> values are given in Table 6.1.1.....	128

## Chapter 7

**Figure 7.1.1.:** (A) & (B):  $E_{OC}$  and nanogravimetric data as a function of time, recorded from Fe piezoelectrodes using the QCN in 1 and 8 wt% oxalic acid respectively. Time  $t = 0$  corresponds to the point at which the QCN mounted Fe piezoelectrode is first immersed in the relevant oxalic acid solution. (C) & (D): Derivatives with respect to time of the nanogravimetric data of Figures 7.1.1A & 7.1.1B respectively. For convenience, source nanogravimetric data are also reproduced from Figures 7.1.1A and 7.1.1B..... 132

**Figure 7.2.1.:**  $E_{OC}$  and nanogravimetric data as a function of time, recorded from Fe piezoelectrodes in 60 mM  $H_2O_2$  and a mixture of 1wt% oxalic acid and 60 mM  $H_2O_2$ ..... 137

**Figure 7.2.2.:** Derivative with respect to time of the nanogravimetric data of Figures 7.2.1. For convenience, source nanogravimetric data is also reproduced from Figures 7.2.1. Data extracted from  $t=4400$  to 4800 in Figure 7.2.1..... 138

## Chapter 8

**Figure 8.1.1.:** Comparing cyclic voltammograms of mild carbon steel in: A) 1wt% oxalic acid pH=1, B) 0.18M nitric acid pH=1, C) 0.18M nitric acid / 1wt% oxalic acid mixture at room temperature pH=1 and D) 0.18M nitric acid / 1wt% oxalic acid mixture at 50°C pH=1..... 147

**Figure 8.1.2.:** Tafel curves of mild steel disc electrodes in: A) 1wt% oxalic acid, B) 0.18M nitric acid C) 0.18M nitric acid / 1wt% oxalic acid mixture at room temperature and D) 0.18M nitric acid / 1wt% oxalic mixture at 50°C..... 149

**Figure 8.1.3.:**  $E_{OC}$  measurements for a mild steel electrode immersed in: A) 1wt% oxalic acid, B) 0.18M nitric acid C) 0.18M nitric acid / 1wt% oxalic acid mixture at room temperature D) 0.18M nitric acid / 1wt% oxalic acid mixture at 50°C..... 150

**Figure 8.1.4.:**  $E_{OC}$  and nanogravimetric data as a function of time, recorded from Fe piezoelectrodes in A) 1wt% oxalic acid, B) 0.18M nitric acid C) 0.18M nitric acid / 1wt% oxalic acid mixture at room temperature and D) 0.18M nitric acid / 1wt% oxalic acid mixture at 50°C..... 151

**Figure 8.2.1.:**  $E_{OC}$  measurements of mild steel electrode immersed in: A) 0.05M  $KMnO_4$ , pH=9 B) 10M NaOH, pH=15 C) 3M NaOH / 0.05M  $KMnO_4$ , 5M NaOH / 0.05M  $KMnO_4$ , 10M NaOH / 0.05M  $KMnO_4$  mixtures, pH=14.4, 14.7 and 15 respectively..... 156

**Figure 8.2.2.:**  $E_{OC}$  and nanogravimetric data as a function of time, recorded from Fe piezoelectrodes in: A) 0.05M  $KMnO_4$ , pH=9 B) 10M NaOH, pH=15 C) 3M NaOH / 0.05M  $KMnO_4$ , 5M NaOH / 0.05M  $KMnO_4$ , 10M NaOH / 0.05M  $KMnO_4$  mixtures, pH=14.4, 14.7 and 15 respectively..... 157

**Figure 8.2.3.:** Simplified Eh-pH (Pourbaix) diagrams for A) Mn- $H_2O$  system, B) Fe- $H_2O$  system, both adapted from the work of Pourbaix [81]. Please note the slightly different scales on the potential axis..... 158

<b>Figure 8.3.1.:</b> $E_{OC}$ measurements of mild steel electrode immersed in $KMnO_4/ HNO_3$ mixture. pH=1.....	161
<b>Figure 8.3.2.:</b> $E_{OC}$ and nanogravimetric data as a function of time, recorded from Fe piezoelectrodes in $KMnO_4 / HNO_3$ mixture. pH=1.....	161
<b>Figure 8.3.3.:</b> A) Cyclic voltammogram and the corresponding forward B) Tafel curve of mild carbon steel in 0.05M $KMnO_4/0.18M HNO_3$ mixture respectively.....	163

## List of Tables

<u>Chapters</u>	<u>Pages</u>
<u>Chapter 1</u>	
<b>Table 1.1.4.1.1.:</b> Nominal capacities and dimensions and other characteristics of FTF waste tanks adapted from the work of DOE/SRS-WD-2012-001[13], [17].....	12
<b>Table 1.1.4.1.2.:</b> Material construction of nuclear waste tank at Savannah River Site adapted from the work of WSRC-MS-93-300 [15].....	13
<b>Table 1.1.4.1.3.:</b> Maximum composition values of mild steel nuclear waste tank wall at Savannah River Site adapted from the work of WSRC-MS-93-300 [15].....	13
<b>Table 1.1.4.1.4.:</b> Chemical composition of 1018 mild steel from the work of Abbasov <i>et. al.</i> [19].....	14
<b>Table 1.3.1.2.1.:</b> Coupons exposed in different corrosive environments adapted from the work of Ketusky <i>et. al.</i> [42].....	30
<u>Chapter 2</u>	
<b>Table 2.4.1.:</b> Photographs of parts of the QCN holder.....	42
<u>Chapter 4</u>	
<b>Table 4.1.1.:</b> Optical microscopy (OM) images taken at a series of key potentials throughout cyclic voltammogram of iron rod in 8wt% oxalic acid.....	87
<u>Chapter 6</u>	
<b>Table 6.1.1.:</b> Calculating the mass change using $i_{CORR}$ values obtained from the data of Figure 6.1.1 via the extrapolation of the Tafel relationships shown in Figure 6.1.2.....	128
<u>Chapter 7</u>	
<b>Table 7.1.1.:</b> Comparing the mass change rates obtained using $i_{CORR}$ and Quartz Crystal Nanobalance measurements as a function of oxalic acid concentration.....	134
<b>Table 7.2.1.:</b> Comparing the mass change rates obtained using $i_{CORR}$ and Quartz Crystal Nanobalance measurements in presence and absence of 60mM $H_2O_2$ .....	139

## Objectives of the work

Metal materials are ubiquitous throughout the nuclear fuel cycle, for example the water cooling circuits of a nuclear reactor, the pipe work in a spent fuel reprocessing plant, the evaporators for volumetric reduction of nuclear waste and the nuclear waste tanks themselves. Understanding metal corrosion behaviour and measuring the rates of corrosion play a key role in safe asset management. They enable plant life to be better predicted, they can be used in assessing the efficacy of corrosion inhibitors for plant lifetime extensions and they can provide information essential for making an informed choice regarding the selection of decontamination methods for steel plant and equipment scheduled for decommissioning.

Several techniques have been developed to measure corrosion rates and to understand the corrosion behaviour of metals under specific radioactive conditions. All these useful techniques have strengths and weaknesses. Commonly used techniques for monitoring corrosion rates include: the measurement of bulk macroscopic mass changes on corrosion coupons; the measurement of a material's electrical resistance; and the measurement of a material's linear polarization resistance during sample immersion in the putatively corrosive environment. However, the former is unsuitable for real time measurements, the medial and latter are not suitable for measuring corrosion rates of pitting corrosion.

This work presents the development of the Quartz Crystal Nanobalance (QCN) technology as a corrosion monitoring technique for selected nuclear applications. Recent advances in QCN technology offer a means of monitoring corrosion in situ, in radiologically harsh environments, in real time and with high sensitivity. The QCN measures minute changes in the frequency of a quartz crystal resonator that accompany either weight gain or loss. Using the Sauerbrey equation, the drop in frequency observed during corrosion monitoring can therefore be converted into an instantaneous corrosion rate with nanogram sensitivity. QCN technology is suitable for measuring

both uniform and pitting corrosion rates. The recent availability of a wide range of metal coated crystal resonators (steel, Al, Fe, Ti etc) makes QCN ideal for real time, instantaneous corrosion monitoring of steels. However, steel coated crystals can be extremely expensive. For instance, mild carbon steel coated crystals are substantially more expensive than iron coated crystals. Moreover, steel coated crystal resonators for corrosion studies generally are used destructively. As a result QCN technology can possibly be a very expensive technique for measuring corrosion rates.

In this work, the Enhanced Chemical Cleaning (ECC) process used for the decontamination of the mild carbon steel nuclear waste tanks at Hanford and the Savannah River Site (SRS) in the US has been used as a model system for the development of QCN based corrosion monitoring. A large volume of nuclear waste has been produced at these sites due to the reprocessing of spent fuel as part of the US's civil defence nuclear programme. These wastes have been stored in large volume waste tanks constructed of low corrosion resistance mild carbon steel again, ideal as a development system for QCN-based corrosion monitoring.

The ECC method used for the decontamination of the waste tanks uses oxalic acid as a cleaning agent due to its dual ability to act as a rust remover and as a corrosion inhibitor. However, the harsh chemical and radiological environments within the tanks may compromise this protection. Thus, in the interests of maintaining tank integrity, the potentially corrosive effect of any oxalic acid-based decontamination process on the mild carbon steel tank body must be understood and carefully monitored during process deployment. Thus, the findings of this work can be significant in preventing the highly undesirable leaking of High Level Waste (HLW) to the environment. As mentioned above, for the simulation of the ECC process, high unit price mild carbon steel coated crystal resonators are needed to be used destructively.

Thus, one of the objectives of this work is to compare iron and mild carbon steel corrosion behaviour and to test the possibility of using cheaper iron coated QCN crystals as a surrogate for the expensive mild carbon steel crystals, thus allowing the use of less resource intensive iron-based QCN

crystals (compared to high unit price steel crystals) for the monitoring of corrosion during the application of oxalic acid.

This work focuses on measuring corrosion rates in oxalic acid environments using QCN technology and  $I_{CORR}$  measurements, and by comparing the results obtained from the two techniques, highlights the strengths and the weaknesses of the QCN technology.

Studies are focussed on the nanogravimetric and electrochemical behaviour of mild carbon steel coated crystals in oxalic acid using QCN technology in simulated radioactive and non-radioactive environments. Results obtained from this technique could be significant in controlling the corrosion behaviour of the mild steel tank wall in the waste / oxalic acid solutions within those tanks.

The major technological challenge of this work is to measure metal corrosion rates of the mild carbon steel / oxalic acid system in situ, in real time using QCN technology in radioactive and non-radioactive environments. This work simulates the ECC process used for the decontamination of waste tanks at Hanford and the SRS in the US. Mild carbon steel surrogate crystals will be immersed in oxalic acid and the mass change and the natural potential difference will be measured in real time in situ, in radioactive and non-radioactive environments.

Studies are further extended to newer decontamination solution formulations including basic and acid permanganate solutions and oxalic acid / nitric acid blends extending and verifying the development of QCN technology as a real time corrosion monitor technique for nuclear applications.

In summary, this work reports on the applicability of using QCN technology as a corrosion monitoring technique for measuring corrosion rates in real time, in situ, for nuclear applications.

# Chapter 1

## 1. Introduction

This thesis relates the development of a new corrosion monitoring technique that is simultaneously capable of in-situ, real time deployment and the provision of fundamental level insight into corrosion phenomenon and corrosion protection operations both used in the nuclear industry.

According to ISO 8044:2015 corrosion rate is the corrosion effect on a metal per time. Note that the unit used to express the corrosion rate depends on the technical system and on the type of corrosion effect. Thus corrosion rate may be expressed as an increase in corrosion depth per time, or the mass of metal turned into corrosion products per area of surface and per time, etc. The corrosion effect may vary with time and may not be the same at all points of the corroding surface. Therefore, reports of corrosion rates should be accompanied by information on the type, time dependency and location of the corrosion effect. [1]

This thesis introduces the development of the QCN technology as a corrosion monitor technique, providing corrosion rates found as the mass of the metal turned into corrosion products per time accompanied by information associated with the type, time dependence and location of the corrosion effect. Such information can be found in the results and discussion chapters.

However, this introductory chapter is divided into three parts. The first part provides the background to those parts of the nuclear industry where corrosion may be of particular concern. The second part describes the specific need for the measurement of corrosion on nuclear sites, highlighting some examples where the work described in this thesis is applicable. The third part presents commonly used methods of measuring corrosion rates, highlighting the strengths and weaknesses of each technique and emphasizing the advantages of the quartz crystal nanobalance (QCN) technology developed here as a real time, in-situ, corrosion monitoring technique.

## 1.1. The nuclear fuel cycle

This section provides a brief summary of the nuclear fuel cycle before moving on to describing those areas of the nuclear industry where corrosion may be of particular concern.

The nuclear fuel cycle starts with the so called 'front end', which includes the mining of uranium and the production of the uranium fuel. Next comes the 'service period', in which uranium containing fuel rods are used in a reactor to generate electricity. Finally, there is the 'back end', which covers fuel reprocessing, uranium and plutonium recovery and waste management. The nuclear fuel cycle is referred to as a 'closed cycle' when the spent fuel is reprocessed and as an 'open cycle' when the used fuel is not reprocessed but is disposed of directly. Figure 1.1.1. shows a schematic of the nuclear fuel cycle.

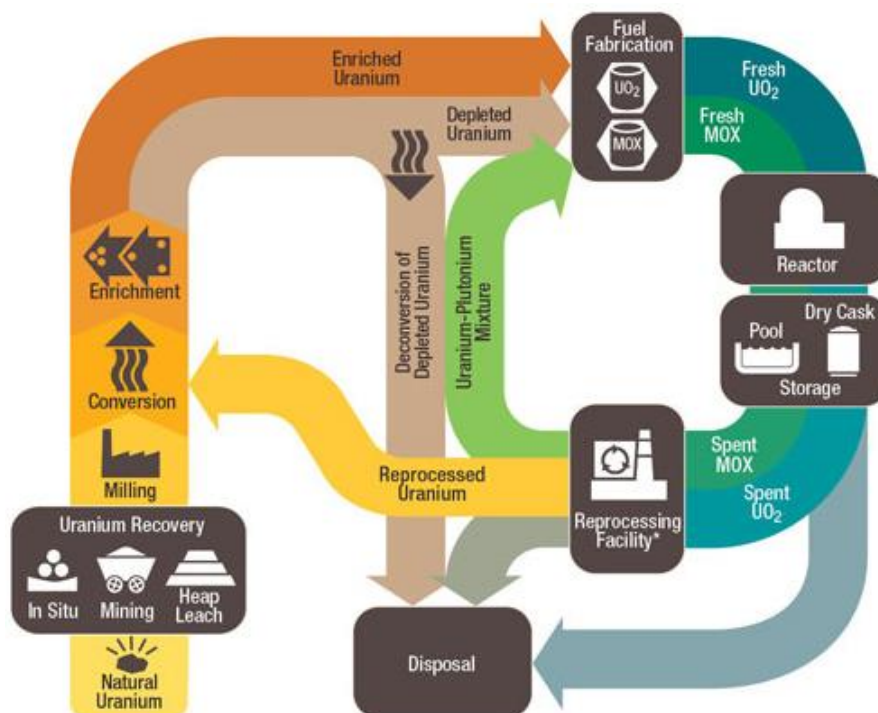


**Figure 1.1.1.:** Flow diagram of the nuclear fuel cycle adapted from the website of the United States Nuclear Regulatory Commission [2].

### 1.1.1. Nuclear reactors

Several types of nuclear reactors are used worldwide including the Pressurized Water Reactor, (PWR), Boiling Water Reactor (BWR), Advanced Gas-cooled Reactor (AGR), among others.

The focus of this section is on the PWR reactor as it is in this type of reactor that aqueous corrosion processes are more relevant. Figure 1.1.1.1 is a schematic diagram of a PWR, [3].

The main purpose of a nuclear reactor is to generate heat, which is then used to turn water into steam to drive a turbine to produce electricity. For reactors that utilize uranium as the fuel source (such as PWRs) the nuclear reaction involves the bombardment of uranium 235 nuclei with neutrons. The uranium atoms split to produce other atoms with mass numbers around both 100 and 140, actinides, neutrons and heat. The neutrons produced will split other uranium atoms producing more neutrons, actinides and heat. The water, at about 600 K, and at a pressure sufficient to prevent boiling, passes to the steam generator. The steam goes to a turbine that runs the generator which produces the electricity. The steam can then be cooled and goes back into the steam generator.

The PWR reactor uses  $\text{UO}_2$  pellets clad in zircalloy, an alloy of zirconium. Water is used as a moderator, converting fast neutrons to the thermal neutrons needed for U 235 fission, and as a coolant in the primary water circuit.

A detailed description of nuclear reactor theory may be found in various texts [4] [5]. Control rods, of boron steel are used to control the power output [6].

Having discussed briefly a PWR reactor as an exemplar system, the next sections will now address the key features of the spent fuel reprocessing plant, the evaporators and the nuclear waste tanks, before moving to the second part of the introduction which focuses on their specific associated corrosion issues.

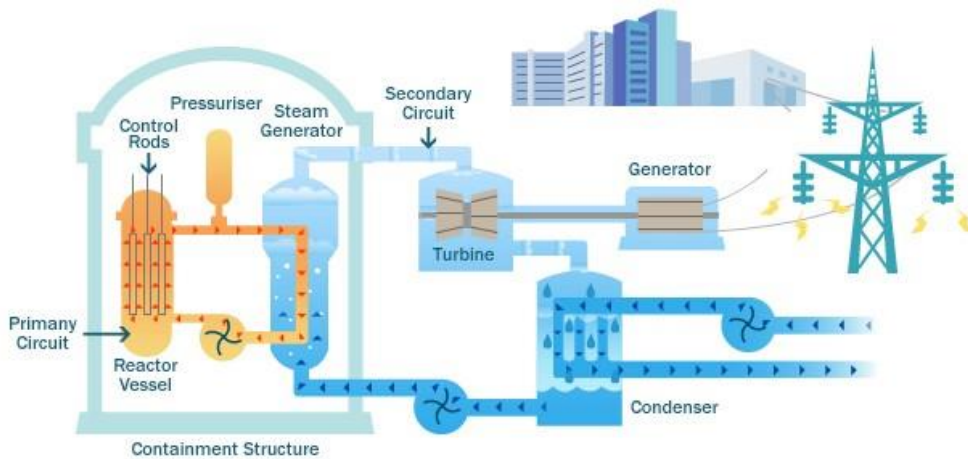


**Figure 1.1.1.1.:** Schematic diagram of a pressurised water reactor [3].

### 1.1.2. Nuclear spent fuel reprocessing plant

In the reprocessing of spent fuel, the uranium and plutonium are separated firstly from the fission products (high-active waste) and then from each other. The recovered uranium can be used in the production of oxide fuel; plutonium can be used in Mixed Oxide (MOX) fuel production or as the fuel in breeder reactors. This section provides a brief description of spent fuel reprocessing before moving on to describing specific associated corrosion problems. The chemical separation stages of a typical reprocessing plant are shown in detail in Figure 1.1.2.1.

At the end of its economic life, the fuel is withdrawn from the reactor. Typically, about one quarter of the core is replaced each year. The spent fuel is transferred to a cooling pond on the reactor site for about a year to allow short lived isotopes to decay away. The fuel is then transported to the reprocessing plant where it is stored under water until it is reprocessed.

AGR fuel has to be first dismantled: The graphite sheath and spacer grids are removed to gain access to the fuel pins. Light water fuel can be reprocessed immediately. For both types of fuel, the fuel pins are chopped into short lengths, about 10cm, which fall into an open mesh basket. This is then lowered into nitric acid and the spent fuel is dissolved up. The hulls, the now empty cladding,

is categorised as Intermediate Level Waste. Any gases evolved must be treated appropriately during the process. [7]

Then follows chemical separation. The solution of spent fuel is fed into a solvent extraction system which uses Tri-Butyl Phosphate (TBP) dissolved in Odourless Kerosene (OK) to selectively extract the uranium and plutonium from the fission products. The uranium and plutonium go into the organic phase (TBP/OK) and the fission product aqueous stream can be run off as high level waste. [7], [8]

The uranium and plutonium are separated from each other by reducing the plutonium to its trivalent state, which has little affinity for TBP. The plutonium is thus in the aqueous layer and the uranium in the organic layer. In order to minimise the level of impurities, uranous nitrate is used as the reducing agent. The uranium and plutonium need further purification to eliminate traces of impurities such as technetium and zirconium. The end products are uranium in the nitrate form and plutonium in the oxalate form. The uranium is denitrated to form  $UO_3$  and the plutonium oxalate is heated to form  $PuO_2$  [8], [9].

Having briefly discussed nuclear fuel reprocessing, the next sections will provide a description of the evaporators and the waste tanks used in the nuclear industry before moving on to their associated corrosion issues.

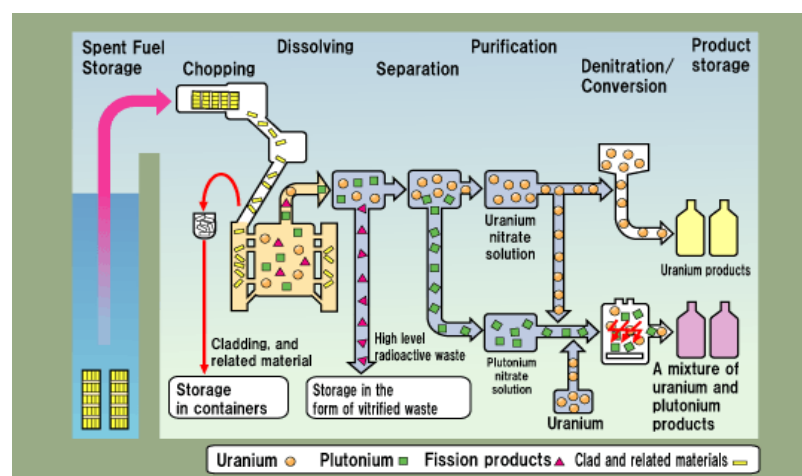


**Figure 1.1.2.1.:** Flow of Light Water reactors (LWR) Spent Fuel Reprocessing adapted from the website of the Japan Atomic Energy Agency [10].

### 1.1.3. Evaporators for volumetric reduction of nuclear waste

Liquids are present throughout the fuel cycle. Of particular concern are the highly active liquid wastes generated from the reprocessing of spent fuel. Typically these wastes are stored in high integrity stainless steel tanks prior to vitrification [11]. However, such storage is expensive and so these wastes are usually reduced in volume by evaporation before being sent to storage. Both the waste tanks and the evaporators used to reduce the volume of liquid waste are made from various grades of steel and so both are vulnerable to corrosion.

As an example, Figure 1.1.3.1 shows a simplified diagram of the process for the volumetric reduction of waste at the SRS adapted from the work of Wilusz et. al.[12]. Low level radioactive waste, wash water used for sludge processing and supernate waste from the waste tank are fed into the evaporator. The temperature can reach boiling point using a steam tube bundle. Vapours containing radioactive caesium and other volatile radionuclides are processed to avoid contaminated emissions. Concentrated waste (from the bottom of the evaporator) is transferred to a receiving tank. [12]

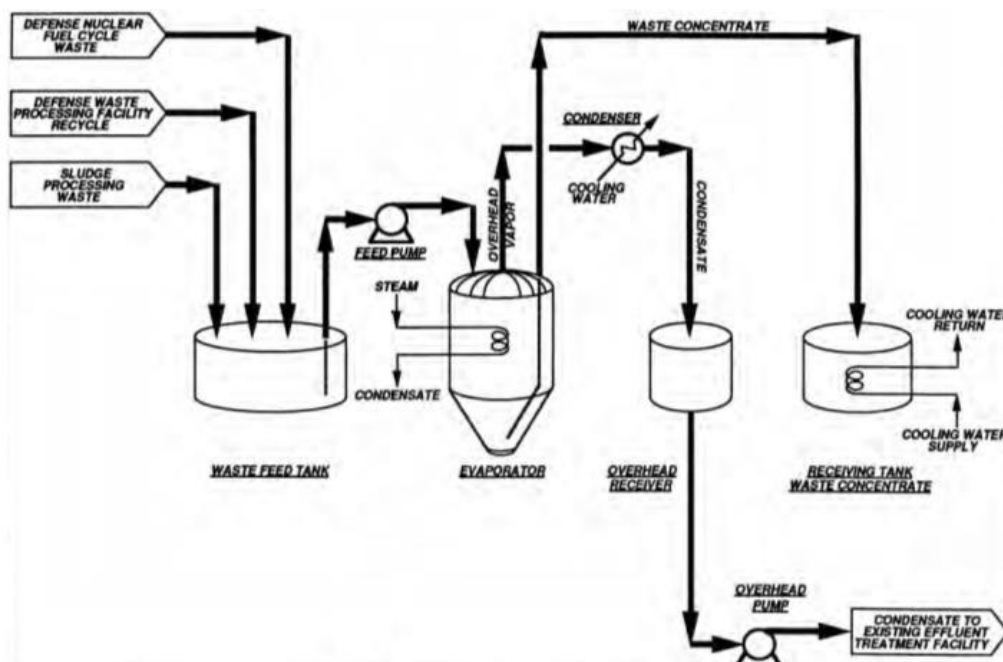


**Figure 1.1.3.1.:** Simplified diagram of the process for volumetric reduction of waste at SRS adapted from the work of Wilusz et. al.[12].

#### 1.1.4. Nuclear waste tanks

This section of the thesis presents some basic information about the waste tanks on the Savannah River Site, on the Hanford Site and in the UK most especially at Sellafield: the dimensions of the tanks, the properties of the waste stored in the waste tanks and the chemical composition of the waste tank walls are detailed.

##### 1.1.4.1. *Waste tanks on the Savannah River Site*

The Savannah River Site (SRS), covering 803 km<sup>2</sup> in South Carolina, is one of the sites of the United States Department of Energy (DOE). It was constructed in the 1950s to produce Pu-239 and tritium for the US Defence programme.

Waste arisings are due to [13]:

- Reprocessing spent fuel
- Producing Pu-239 and tritium for defence applications
- Producing Pu-238 to power satellites [14]

A document issued by the DOE [13] in March 2012 reports that 22 waste tanks at F-Tank Farm (FTF) with different designs (Types I, II, III, IIIA. and IV), were constructed of carbon steel [15], [16], [17]. Table 1.1.4.1.1 illustrates the dimensions and the capacity of the waste tanks at FTF.

**Table 1.1.4.1.1.:** Nominal capacities and dimensions and other characteristics of FTF waste tanks adapted from the work of DOE/SRS-WD-2012-001[13], [17].

Type	Numbers of waste tanks	Diameter (metre)	Height (metre)	Capacity (Litre)	Cooling coils	Secondary containment
I [13]	1, 2, 3, 4, 5, 6, 7, 8	22.86	7.5	3409567	Yes	Yes
II [17]		25.9	8.2	4682473	Yes	Yes
III/IIIA [13]	25, 26, 27, 28, 33, 34, 44, 45, 46, 47	25.9	10.0	5909917	Yes	Yes
IV [13]	17, 18, 19, 20	25.9	10.5	5909917	No	No

Figure 1.1.4.1.1., adapted from the work of J Pavletich, shows a schematic of a Type I waste tank dating from the 1950s[18]. The diameter is about 23 metres and the height is approximately 7.5 metres. The capacity is about 3410 tons. All Type I waste tanks have vertical and horizontal cooling circuits and have secondary mild steel containment. The basemats of the waste tanks were constructed from concrete. [13]

More information and schematics about the different types of waste tanks at the SRS can be found in the work of Pavletich [18].

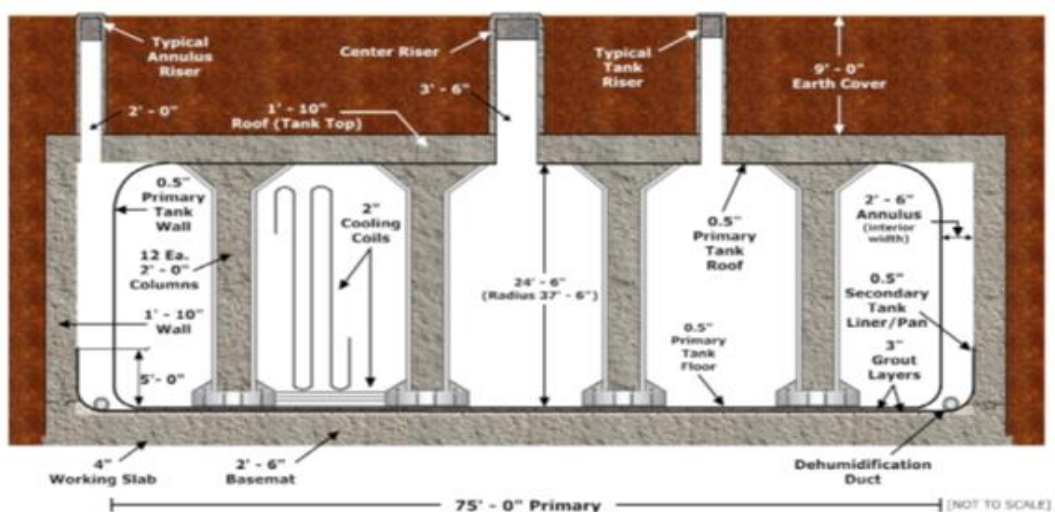


**Figure 1.1.4.1.1.:** Type I High level waste tank adapted from the work of J Pavletich [18].

**Table 1.1.4.1.2.:** Material construction of nuclear waste tank at Savannah River Site adapted from the work of WSRC-MS-93-300 [15].

Type tank	Tank number	Location and construction dates	Material
I	1-12	F and H 1951-1953	A 285-B
II	13-16	H 1955-1956	A 285-B
III	29-32, 33-34	H 1967-1970: F 1969-1972	A 516-70: as rolled
IIIA	35-37, 25-28,	H 1974-1977:F 1975-1978	A 516-70: normalized
IIIA	38-51	H 1976-1891: F1977-1980	A 537-I: normalized
IV		F-1958	A285-B
IV		H-1959-1961	A 212-B

Table 1.1.4.1.2 lists the types of steel used in the construction of the nuclear waste tanks in the F and H areas at the Savannah River Site. The waste tanks are fabricated from A 285-B, A516-70, A 537-I A 212-B steel. Table 1.1.4.1.3 lists the composition of these types of steels and it can be observed that all the types of steel listed in tables 1.1.4.1.2 and 1.1.4.1.3 contain approximately 98% iron. According to Subramanian et. al. [17], they can all be characterized as low (mild) carbon steels.

**Table 1.1.4.1.3.:** Maximum composition values of mild steel nuclear waste tank wall at Savannah River Site adapted from the work of WSRC-MS-93-300 [15].

Material	Carbon	Manganese	Phosphorus	Sulfur	Silicon	Other
A212	0.31	0.90	0.04	0.04	0.15/0.30	Cu-0.25max
A285-B	0.22	0.90	0.035	0.04		
A516-70	0.27	0.85/1.20	0.035	0.04	0.13/0.45	Cu-0.35max
A537-I	0.24	0.70/1.35	0.035	0.04	0.15/0.50	Ni-0.25max Cr-0.25max Mo-0.08

Table 1.1.4.1.4 shows an example of the composition of 1018 mild carbon steel that Abbasov et. al. used as an electrode material for research purposes [19]. In order to simulate the nuclear waste tank wall, common mild steel samples will be used as electrodes for laboratory based work.

Figure 1.1.4.1.2 is a representation of the waste tanks at F-Tank Farm, adapted from DOE/SRS-WD-2012-001 [13]. Approximately  $68.2 \times 10^6$  Litre with  $447.7 \times 10^{16}$  Bq have been stored in 22 nuclear waste tanks across the SRS.

The nuclear waste in these tanks separates into 3 layers:

- i. On the bottom of the tank is the sludge with 6% of the total volume and containing 45% of the radioactivity
- ii. Above is the saltcake with 59% of the total volume and 5% of the total radioactivity
- iii. On the top is the salt supernate with 35% of the volume and containing the 50% of the total radioactivity

Due to the different composition of the waste in each layer, the corrosion behaviour of the mild carbon steel tank wall is expected to be different for each layer. Thus, understanding the corrosion behaviour and measuring the corrosion rates of the mild carbon steel waste tank wall for each layer can be significant in terms of improving the design and the properties of the metal wall.

More information about the waste tanks and waste tank history can be found in various texts issued by the DOE [20], [13], [17], [18], [21], [22], [23].

**Table 1.1.4.1.4.:** Chemical composition of 1018 mild steel from the work of Abbasov et. al. [19].

Element	Si	Ni	Cr	S	C	P	Mn	Fe
Content (wt%)	0.37	0.01	0.07	0.03	0.18	0.03	0.71	Balance

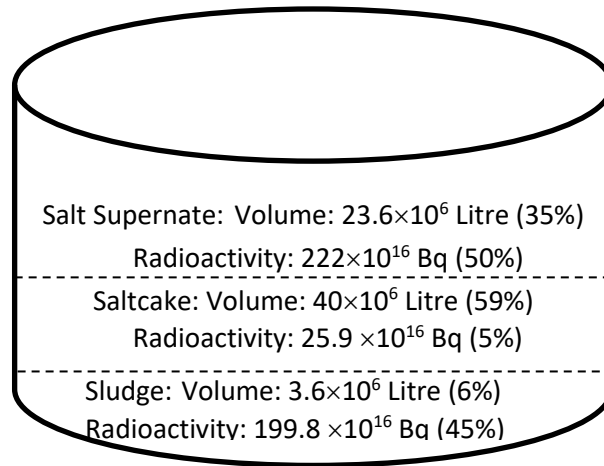


**Figure 1.1.4.1.2.:** F-Tank Farm waste tank composite of 22 waste tanks adapted from the work of DOE/SRS-WD-2012-001[13].

#### 1.1.4.2. Waste tanks on the Hanford Site

The Hanford site in Washington State is one of the sites of the United States Department of Energy (DOE) and was constructed in the 1940s to produce nuclear weapons materials especially Pu for the Manhattan project. Thus, many of the issues related to liquid HLW storage reported at SRS are also seen at Hanford.

It has been reported that after the wastes arising from Pu separation have to be neutralized by the addition of sodium hydroxide, these wastes were stored in reinforced concrete tanks with a mild carbon steel liner again, similar to the situation at SRS. Wastes were stored in 149 mild carbon steel single skin waste tanks with volumes from  $210\text{m}^3$  to  $3,800\text{m}^3$ . In 1980, wastes were transported to 28 double skin tanks with volumes ranging from  $3,800\text{m}^3$  to  $4,300\text{m}^3$  in order to decommission the 149 single skin waste tanks. Again the inside of new waste tank walls was fabricated from mild carbon steel. [24], [25].

More information about the Hanford site can be found in a report by the Pacific Northwest National Laboratory of September 2004 [26].

### 1.1.4.3. Waste tanks in the UK

The properties of the wastes stored in the UK are similar to those stored in the carbon steel tanks at the Hanford and Savannah River sites. The main difference is that in the UK the wastes are stored in acidic forms. Due to the resultant highly corrosive environment, waste tanks in the UK are constructed of stainless steel [27]. Because of this, the waste tanks in the UK have higher corrosion resistance compared to the mild carbon steel that was used in the USA. However, both the UK and US waste tank systems have corrosion issues. The ability to use new technologies for measuring the corrosion rates can be a beneficial tool in effecting decontamination and decommissioning.

Figure 1.1.4.3.1. shows a high level liquid waste storage tank in the UK. It can be seen that the design is similar to those at Hanford and the Savannah River Site. Cooling coils and an agitation system can be seen.

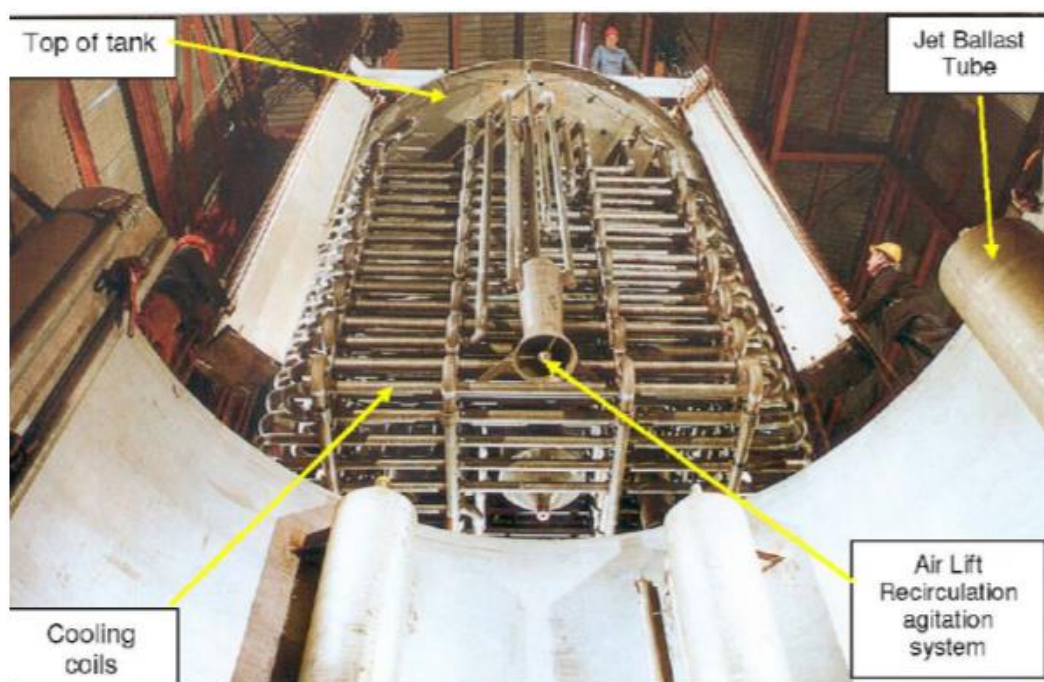


**Figure 1.1.4.3.1.:** High Level Liquid Waste storage tank in UK adapted from the work of Dobson et. al. [27].

## 1.2. Common applications for corrosion monitoring on nuclear sites

This section describes those facets of the nuclear industry, presented in section 1.1., where corrosion may be of particular concern, such as:

1. Water cooling circuits exposed to oxidising coolant
2. Integrity of pipework exposed to nitric acid during the reprocessing of spent fuel
3. Decontamination of evaporators
4. Decontamination of waste tanks on the Savannah River Site
5. Decontamination of waste tanks on the Hanford Site

### 1.2.1. Water cooling circuits exposed to oxidising coolant

Primary coolant circuits in pressurised water reactors are constructed mainly from carbon steel which contains more than 90% Fe [28]. Iron oxides, produced from the corrosion of the pipe steel surface of the primary water coolant can leave the steel surface and enter the coolant flow. From here, they can be transferred to the surface of the fuel and then back to the primary water coolant. During this process, these corrosion products can be bombarded with neutrons emitted by the fissioning fuel, resulting in the generation of radioactive activation products within the corrosion products themselves e.g.  $^{60}\text{Co}$  and  $^{58}\text{Co}$  from the activation of  $^{56}\text{Fe}$  (via multiple neutron captures) and  $^{58}\text{Ni}$  derived from the cooling circuit alloy itself. The loosely-bound activated corrosion products may then detach from the fuel pins and re-enter the coolant, redepositing within the primary coolant surface where the radiation levels will be consequently increased. This phenomenon can be seen in all water cooled nuclear reactors. In terms of safe access for workers periodically checking the system, the radiation doses must be minimized and controlled. This can be managed by either the introduction of corrosion inhibitors into the cooling circuit in order to minimise the corrosion

event in the first place, or by decontamination of the circuit, most usually by use of chemical decontamination techniques. In the case of the latter, the radioactive corrosion products are dissolved and removed by application of a suitable cleaning agent. Due to the complex mixture of oxide corrosion products that can be found on the steel surface of the pipe of the primary water coolant circuit, both the original corrosion process and the means by which the corrosion products are removed during decontamination must be studied and understood, in order to achieve good cleaning results and to minimize secondary waste management issues whilst, at the same time, retaining the structural integrity of the cooling circuit pipework itself. [29] Corrosion monitoring techniques are a key means of providing such information.

### **1.2.2. Integrity of pipework exposed to nitric acid during the reprocessing of spent fuel**

Within the context of a closed nuclear fuel cycle, spent nuclear fuel can be chemically reprocessed and the spent fuel can be reused. During hydrometallurgical reprocessing routes currently employed in the UK, Japan, India and France, the fuel is dissolved and processed in concentrated nitric acid. It is possible corrosion issues may arise due to the corrosive solutions that are used, particularly at the head-end where the fuel is dissolved. At all stages of reprocessing, the harsh chemical environment afforded by the nitric acid can be made additionally corrosive due to the radioactive environments of the process.

The integrity of the reprocessing plant depends on the quality and, especially, the corrosion resistance of the components that are used in the facility. High corrosion resistance metallic components can prevent any possible leakage of radioactivity to the environment, will extend the life time of the process and reduce operator exposure times (a key safety consideration for radiation workers regarding periodic system checks). Austenitic stainless steel such as 18Cr-13Ni-1Nb pre 1980s and 304L post 1980s are commonly used in pipework and vessels due to their abilities to

produce an iron/chromium oxide film that protects against corrosion of the constituent steel surface [30], [31]. However, the use of such high quality materials aside, there is still a need for condition monitoring of the plant whilst in service, including the assessment of corrosion processes occurring therein for the reasons discussed above.

A detailed description of reprocessing and corrosion issues therein may be found in various texts [32], [8], [33], [34].

### **1.2.3. Decontamination of evaporators**

Evaporators are used in nuclear waste treatment plants to reduce the volume of (typically highly active) liquid waste so that it can be stored both safely and cost effectively until further treatment. Both Sellafield in the UK and the Savannah River Site (SRS) in the USA use evaporators for the volumetric reduction of liquid radioactive waste prior to consignment to interim storage tanks. After one to two years, the suspended solids in the liquid waste settle out on to the tank bottom. The top layer of this phase-segregated waste, the so called salt supernate, can be periodically recycled for further volume reduction using the evaporators. [12]

As described by Wilusz et al. [12], a typical evaporator such as those used at the Savannah River Site, is constructed from concrete lined with stainless steel – approximately 5m diameter and 10m high. Monitoring both the extent and rate of corrosion of the stainless steel inner vessel during the operational life time of the evaporator can provide useful information regarding the extension of the vessel lifetime.

At the end of the operational life of the evaporator, chemical decontamination techniques are widely used as a prelude to decommissioning in order to reduce radiation levels during dismantling. However, during such processes, care must be taken to preserve the evaporator vessel

integrity so as to prevent the highly undesirable leaking of liquid HLW to the environment. Thus it is important to measure the corrosion rates of the metallic evaporator body during decontamination campaigns.

Figure 1.2.3.1 shows the effects after one and two acidic strikes of chemical decontamination on the steel evaporators using nitric acid (at 90°C) as a cleaning agent. It is evident, from the photographs, that the method is effective. However, nitric is a harsh cleaning agent and may indiscriminately attack the fabric of the steel structure itself. Currently, the extent of such corrosion is assessed by a combination of post-treatment inspection and theoretical models of the process itself. The former is non-real time and retrospective whilst the latter is highly dependent upon initial conditions and assumptions as to the dominating chemical processes – processes that may change during a maloperations event. There is therefore a need for in situ, real time corrosion monitoring techniques during such exercises. The QCN technology at the heart of this thesis provides just such a technique.

More information about the evaporators can be found in various texts [27], [35].



**Figure 1.2.3.1.:** SRS 2H Evaporator before and after the chemical cleaning process (Nitric acid 1.5M at 90°C ) adapted from the work of Calloway, et. al. [36].

#### 1.2.4. Decontamination of waste tanks on the Savannah River Site, case study of a model system

Waste tanks can be decontaminated after their operational life-time thereby reducing radiation levels and they can then possibly be reused depending on the consistency of the metal body of the waste tanks.

There are three main methods for decontaminating the waste tanks at the SRS as can be seen below (mechanical, vacuum, chemical). A document issued by the DOE [13] reports that the characteristics of the wastes and the condition of the waste tanks play key roles in the choice of the most suitable method, or combination of methods, for decontaminating the tanks. The decontamination of the waste tanks starts with the transportation of the waste from the tanks to be cleaned-up to deposition tanks. This can be achieved using mechanical methods such as agitation, mixer pumps and vacuum extraction. Any solids can be dissolved using chemical methods and transferred to the deposition tank mechanically. The bulk of the waste sludge (see Figure 1.1.4.1.2) is removed by these methods. The residual waste is termed the 'sludge heel' and is not easily removed by slurring. To provide for additional levels of removal, chemically aided techniques are often employed.

The main three categories of methods are summarized below;

- I. Mechanical Heel Removal: The main use of this method is to mix and ensure the transfer of the bulk of the waste to other facilities for further treatment[37]. The main techniques that are used are agitation, spraying lancing, pulse vacuum retrieval etc. [13]
- II. Vacuum Heel Removal: A high pressure water is used to remove the waste to a deposition tank. [13].
- III. Chemical Heel Removal: This method is used to dissolve solids that are insoluble in water and which cannot be removed from the surface of the waste tank wall by mechanical

methods [13]. At SRS, it is recommended that the residual solid in the waste tank be less than 5,000 kg [37]. The main advantage is that using the Chemical Heel Removal technique, the requirements for the waste tank closure can be achieved (less than 5,000 kg solids), due to its ability to remove solids from internal tank surfaces such as walls and cooling coils [13]. The main advantage of the Chemical Heel removal technique is that it can be used to support the stringent requirements for the waste tank closure [37]. The last finding makes Chemical Heel Removal one of the best techniques available as a final decontamination step prior to waste tank closure. This work uses the Chemical Heel Removal method as a model system in order to test the feasibility of using new techniques for metal corrosion monitoring. For Chemical Heel Removal there is a need to choose a suitable decontamination cleaning agent. Several solutions have been proposed as cleaning agents for the decontamination of the waste tanks at the SRS [13]:

- i. oxalic acid
- ii. oxalic acid / citric acid mixture
- iii. oxalic acid / hydrogen peroxide mixture
- iv. nitric acid
- v. formic acid
- vi. other organics agents such as ascorbic acid, EDTA, triethanolamine [38]

Oxalic acid has been recommended as the best choice. Second best choice is nitric acid or formic acid or oxalic acid / hydrogen peroxide mixture. The third choice is oxalic acid / citric acid mixture and the last option are organic agents. The use of oxalic acid as a cleaning agent has been recommended for the following reasons [13]:

- a. It has been used and studied widely as a cleaning agent for US DOE nuclear waste tanks

- b. Waste management issues, such as the production of sodium oxalate in the solids slurry [13], have been studied
- c. It can be used for a variety of sludge types
- d. It is less corrosive compared to the other cleaning agents referred to above
- e. Its ability to produce a passive layer on carbon steel surfaces [37]
- f. It acts as a rust remover and as a corrosion inhibitor [39],[40]

Whilst oxalic acid can be used as a cleaning agent, process engineering and secondary waste management issues have arisen which may be the result of low Na salt solubility ( $37 \text{ g kg}^{-1}$  or  $0.28 \text{ mol kg}^{-1}$  at  $303.15 \text{ }^\circ\text{K}$  in water [41]). The Enhanced Chemical Cleaning (ECC) process using dilute oxalic acid to dissolve solids from the walls of the metal tanks can be used for decontamination. Typically 4-8 wt% of oxalic acid is used as a cleaning agent [40],[42],[43]. However, in order to minimise downstream issues, recent research has been focused on 1wt% and it is proposed that under specific conditions 1wt% can be more effective than the hitherto typical oxalic acid concentrations [42]. Concentrated oxalic acid or oxalic acid crystals produced from waste after the first wash can be regenerated and be reused as a cleaning agent for a second ECC process [43].

Figure 1.2.4.1. illustrates the ECC process adapted from Matino et. al. [44]. Diluted sludge and other solids can be removed to the ECC reactor using oxalic acid. Concentrated gaseous ozone will increase the pH of the liquid and will decompose oxalate ions to form carbon dioxide gas. The chemical decomposition of oxalate ions can be increased in UV light [45], [46].

The volume of the dissolved sludge, comprising a high concentration of metal oxides, can be reduced in the evaporator by extracting the water and reusing it in subsequent campaigns [47].

Ketusky et.al report that, as mentioned above, in the absence of UV light the decomposition rate of oxalate products from the waste tanks due to the clean-up process, was reduced in both F and H waste tanks [37].

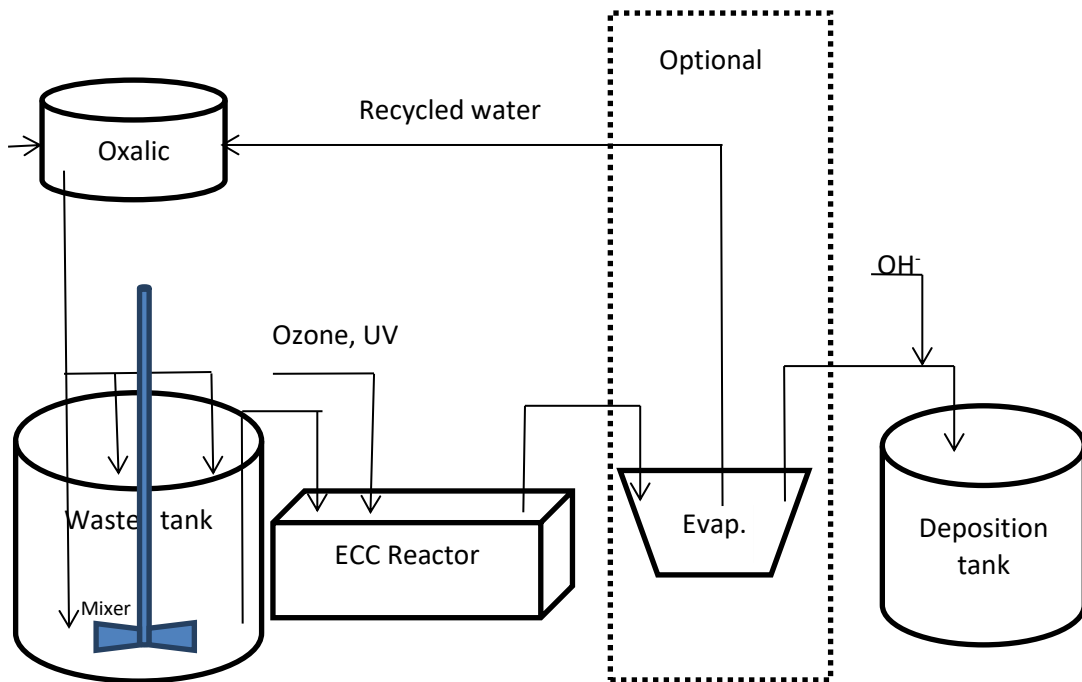


**Figure 1.2.4.1.:** ECC Process in SRS adapted from the work of Matino et. al.[44], Ketusky et.al.[47] and from the report DOE/SRS-WD-2012-001[13].

This work, in terms of developing new methods of measuring corrosion rates, uses the ECC process as an exemplar system and presents experimental results using mild carbon steel samples, representing the mild carbon steel waste tank wall, immersed in oxalic acid solution to represent the oxalic acid cleaning agent during the ECC process (see chapter 3, 4, 5, 6).

### 1.2.5. Decontamination of waste tanks on the Hanford Site, case study of a model system

Like the Savannah River Site, one of the main missions of the Hanford site is to decontaminate the nuclear waste tanks that were fabricated in the 1940s [24]. Oxalic acid has been used as a cleaning agent to decontaminate the surface of the waste tanks fabricated from mild steel [43].

This work examines the feasibility of using new methods to measure corrosion rates and to understand the mild carbon steel surface corrosion behaviour when a cleaning agent such as oxalic

acid is used for surface decontamination. The mild carbon steel – oxalic acid system that is discussed in Chapter 3 simulates the Enhanced Chemical Cleaning (ECC) process of the mild carbon steel waste tanks at the SRS and Hanford site. It provides the interrelationship between the oxalic acid concentration, temperature and level of the exposed radiation doses that effect the mild carbon steel / oxalic acid system. Properties of the mild carbon steel from which the waste tanks are constructed and the status of the variety of the waste tank types at the Hanford site and at the SRS can be found in the report DOE/ER/75784—77, [48]. The main points of relevance to this thesis are the composition of the steel, which may be found in Table 1.1.4.1.3 above.

### **1.3. Methods of measuring corrosion rates**

Several techniques for measuring corrosion rates are reported and available commercially. Such measurement is important for predicting plant longevity and assessing the efficacy of corrosion inhibitors for plant lifetime extensions.

The first part of this section reports four common methods of measuring corrosion rates. The second part presents the QCN technology used as a corrosion monitor technique.

#### **1.3.1 Commonly used methods of measuring corrosion rates**

This section briefly reports some of the main methods that are used to measure corrosion rates, highlighting their main differences as corrosion monitoring techniques.

The techniques discussed are as follows:

- i. Linear polarisation resistance measurement;

- ii. Coupon weight loss measurements;
- iii. Electrical resistance monitoring;
- iv. Galvanic measurement

### 1.3.1.1. Linear polarization resistance

In this technique the metal surface of an electrode is scanned with a small step potential on both sides of the corrosion potential and the mass change can be calculated from the slope of the curve found by plotting the log of the current against the potential [49]. However, this technique can be used only when a defined electrolyte is used [50].

Linear polarization resistance has high sensitivity and so it is possible to achieve good quality results in a short period of time. As a result it is possible to measure the corrosion rates in real time. However, this technique is suitable only for uniform corrosion phenomenon and at unstable corrosion current measurements will produce incorrect corrosion rates [51].

Figure 1.3.1.1.1. shows the forward going sweeps in the first scan of a voltammogram and the anodic and cathodic polarization curves of an iron sample in 1wt% oxalic acid. The open circuit potential is found to be equal to the  $E_{CORR}$ .

The corrosion current and the mass change can then be found using equations 1.3.1.1.1, 1.3.1.1.2 and 1.3.1.1.3 [42], [52].

$$i_{corr} = \frac{\beta_a \beta_c}{2.3 (\beta_a + \beta_c) R_p} \quad \text{Equation 1.3.1.1.1.}$$

$$R_p = R_a - \rho l \quad \text{Equation 1.3.1.1.2.}$$

$$CR = 0.13 \frac{i_{corr} E_w}{\rho} \quad \text{Equation 1.3.1.1.3.}$$

Where:

$\beta_a$  = anodic Tafel slope

$\beta_c$  = cathodic Tafel slope

$R_p$  = the true polarization resistance, ohm  $cm^2$

$R_a$  = the apparent polarization resistance, ohm  $cm^2$

$\rho$  = the electrolyte resistivity, ohm  $cm$

$l$  = the distance between the specimen electrode and the reference electrode,  $cm$

$E_w$  = Equivalent weight of the metal (for iron is 27.9grams/equivalent)

$\rho$  = density of the metal (for iron is  $7.86 \text{ g/cm}^3$ )

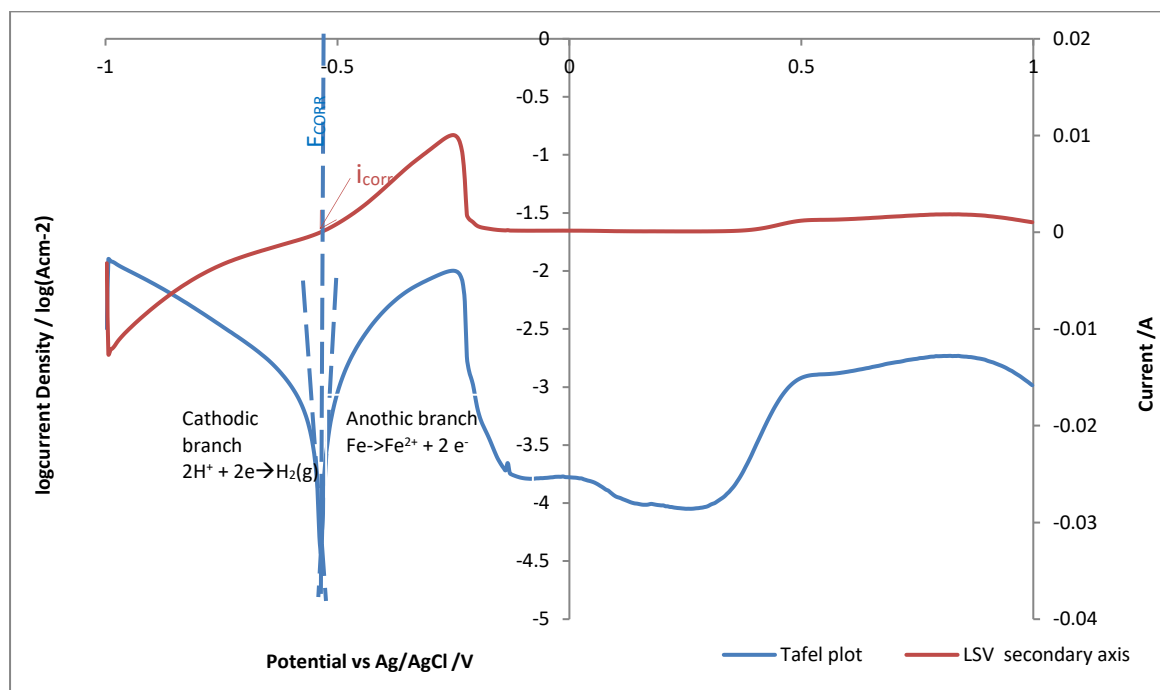


**Figure 1.3.1.1.1.:** Forward going sweeps in the first scan cyclic voltammograms, and associated LSVs, of iron piezoelectrodes in 1 wt% oxalic acid.

### 1.3.1.2. Coupon weight loss

In this technique the mass change of the coupons can be measured gravimetrically before and after their immersion. Strip, flush disks and rod samples can be used as coupon samples. Photographs taken during the exposure can be very useful for understanding the chemical and electrochemical processes that occur on the immersed surfaces of the coupons. This technique is suitable for long term experiments in order to achieve accurate results. It is difficult to measure corrosion rates and identify the chemical and electrochemical behaviour of the coupon over short periods of time. [50], [51]

The main advantage of the technique is that it is low cost and several corrosion processes can be simulated at the same time using coupon samples. Table 1.3.1.2.1 shows photographs of coupons exposed in a mixture of oxalic acid and a spent fuel reprocessing type simulant waste sludge used on the Savannah River Site. The corrosion rates can be measured using equation 1.3.1.2.1. [42]

$$CR = \frac{3.45 \cdot 10^6}{A T \rho} 10^6 W \quad \text{Equation 1.3.1.2.1.}$$

Where;

$W$  = Measured mass change in g

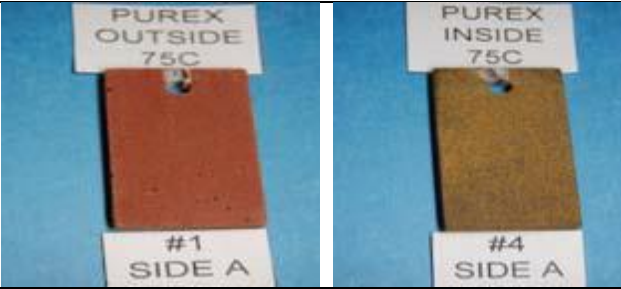
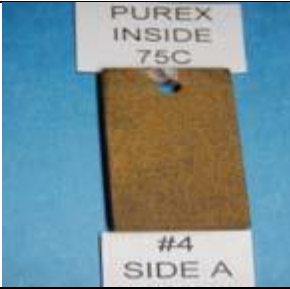
$CR$  = General corrosion rate in mils/yr

$A$  = Area of the exposed coupon in g

$T$  = The exposure time of the coupon in hours

$\rho$  = Density of the exposed coupon in  $\frac{g}{cm^3}$

**Table 1.3.1.2.1.:** Coupons exposed in different corrosive environments adapted from the work of Ketusky *et. al.* [42].

Oxalic acid Concentration	Acid/Sludge, Mixing	Acid/Sludge, Stagnant	Pure Acid, Stagnant
Temperature			
1wt% 75°C			
1wt% 45°C			

### 1.3.1.3. Electrical resistance probe

The electrical resistance probe technique is able to convert the change in electrical resistance of an electrode before and after its immersion into a gaseous or liquid medium into mass change.

The electrical resistance technique operates on the principle that the electrical resistance of a measuring element (wire, strip, or tube of metal Figure 1.3.1.3.1. [51]) increases as its conductive cross sectional area decreases as the result of corrosion. In practice, the electrical resistance ratio between a measuring element exposed to the test solution and a protected reference element is measured in order to compensate for resistance changes due to temperature. Because the resistance of the test element is very small, very sensitive electronics must be used. [53]

In order to convert accurately the resistance change to a mass loss, it is essential that the surface of the electrode has changed uniformly and so it is recommended only for measuring the corrosion rates for uniform corrosion phenomenon.

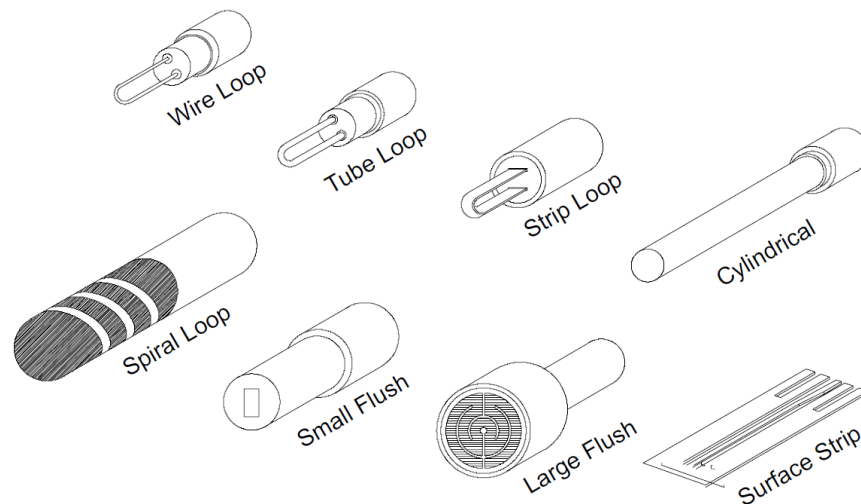


**Figure 1.3.1.3.1.:** Types and shapes of several electrical resistance probes adapted from the work of Roberge [51].

#### **1.3.1.4. Galvanic monitoring technique**

In this technique, the mass change is found by measuring the galvanic current that flows between two electrodes of dissimilar metals or occasionally two electrodes of the same alloy, but in a different metallurgical/electrochemical state e.g. actively corroding steel as the anode and passivated steel as the cathode.

It is a very simple method of measuring corrosion rates and can be used as a standard method to identify the effectiveness of any treatment used to prevent corrosion. However, the measured current is not proportional to the corrosion rate and so an observed increase in the current does not always corresponds to an increase in corrosion rate. [51]

Also, results obtained using galvanic probes in the laboratory do not always correspond to corrosion rates at the plant due to area and geometry differences. [53]

#### **1.3.1.5. Summary**

As described above, there are four commonly used methods to monitor corrosion: Coupon weight loss, electrical resistance probe, linear polarization resistance and galvanic monitoring. However, as also discussed above, each of these methods has significant disadvantages. In summary:

- ✓ Coupon weight loss is unsuitable for real time monitoring [50];
- ✓ Electrical resistance probes exhibit low sensitivity [51]; and
- ✓ Linear polarization resistance and galvanic monitoring, while in situ measurements, do not directly measure the corrosion rate. [51]

An alternative technique is the quartz crystal nanobalance (QCN). Through the piezoelectric effect the QCN measures minute changes in frequency of a quartz crystal which can be converted to mass change (gain/loss) with nanogram sensitivity. Advantageously, this can also be coupled with traditional galvanic and cyclic voltammetric analysis in the QCN to provide both in situ measurements of mass change and electrochemical corrosion behaviour information. A description of the QCN, and its potential application in real time, in situ corrosion monitoring, is given in the next section.

#### **1.3.2. Quartz crystal nanobalance**

The electrochemical quartz crystal nanobalance (QCN) is a well-established method for the measurement of small changes in electrode mass due to reactions occurring at the electrode-

solution interface. The transducing element is made of a single quartz crystal, coated with two electrodes, one on each side providing an AC field and the crystal oscillates. When the thickness of the crystal is twice the acoustic wavelength, a standing wave can be established and the frequency is called the resonant frequency ( $f_0$ ) [54]. A mass change of the electrode surface will change the value of the resonant frequency. One of these electrodes can also be used as the working electrode in an electrochemical cell with the added advantage of being able to run basic electrochemical experiments whilst the mass change of the electrode can be measured.

A typical RLC circuit (resistor-R, inductor-L, capacitor-C) can be used as an equivalent circuit of a QCN. Where R represents the dissipating energy due to oscillation, C the stored energy during oscillation and L the inertial component related to the displaced mass [54]. At a resonant frequency,  $f_s$ , the effective resistance (impedance) of the circuit is minimum and equal in magnitude to  $R_1$  [55]. Electrical contact of the QCN with a metal material surface can be achieved if a quartz crystal is formed by an additional metal (i.e. gold). The gold surface will have an additional capacitor in parallel with the series RLC, commonly known as Butterworth van Dyke (BVD) model [54]. The BVD model has the series and parallel resonant frequency  $f$  series (the minimum) and  $f$  parallel (the maximum) respectively. Many QCN models, including the one used in the work reported here, directly report both frequencies. However, in terms of simplicity it is sufficiently accurate to report only the series resonant frequency in order to measure the mass change manually [55], [54].

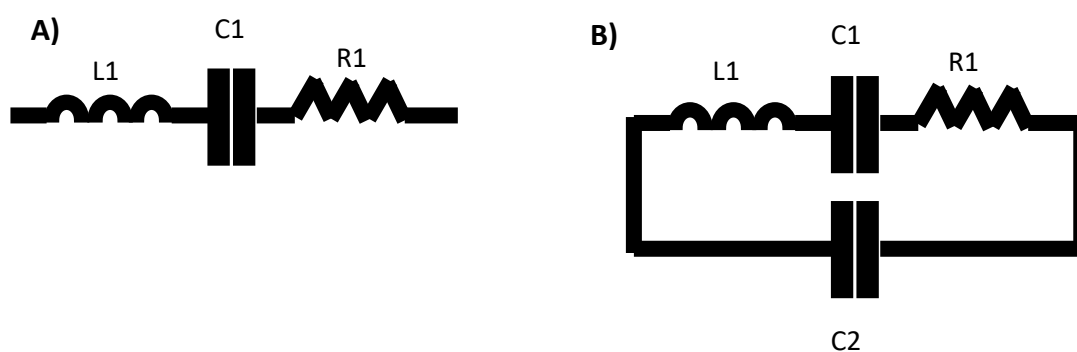


**Figure 1.3.2.1.:** A) RLC circuit in series and B) Butterworth van Dyke model adapted from document about the basics of a quartz crystal microbalance published by Gamry instruments [55].

Figure 1.3.2.1. illustrates an RLC circuit in series and a BVD model adapted from a document about the basics of a quartz crystal microbalance published by Gamry instruments [55].

Assuming mass is rigidly bound; the measured shift in the resonant frequency is converted to a mass change via the full or abbreviated Sauerbrey equations of 1.3.2.1 and 1.3.2.2 respectively.

$$\Delta f = - \left( \frac{2f_0^2}{A\sqrt{\rho_q\mu_q}} \right) \Delta m \quad \text{Equation 1.3.2.1.}$$

Where  $f_0$  and  $\Delta f$  is the resonant frequency and the change in resonant frequency (Hz) of a quartz crystal respectively.  $\Delta m$  is the mass change (g) at the piezoelectric crystal surface.  $A$  is the active area of the quartz crystal ( $\text{cm}^2$ ).  $\rho_q$  and  $\mu_q$  are the density ( $2.648 \text{ g cm}^{-3}$ ) and the shear modulus ( $2.947 \cdot 10^{11} \text{ g cm}^{-1} \text{ s}^{-2}$ ) of the quartz crystal respectively.

$$\Delta f = -C_f \Delta m \quad \text{Equation 1.3.2.2.}$$

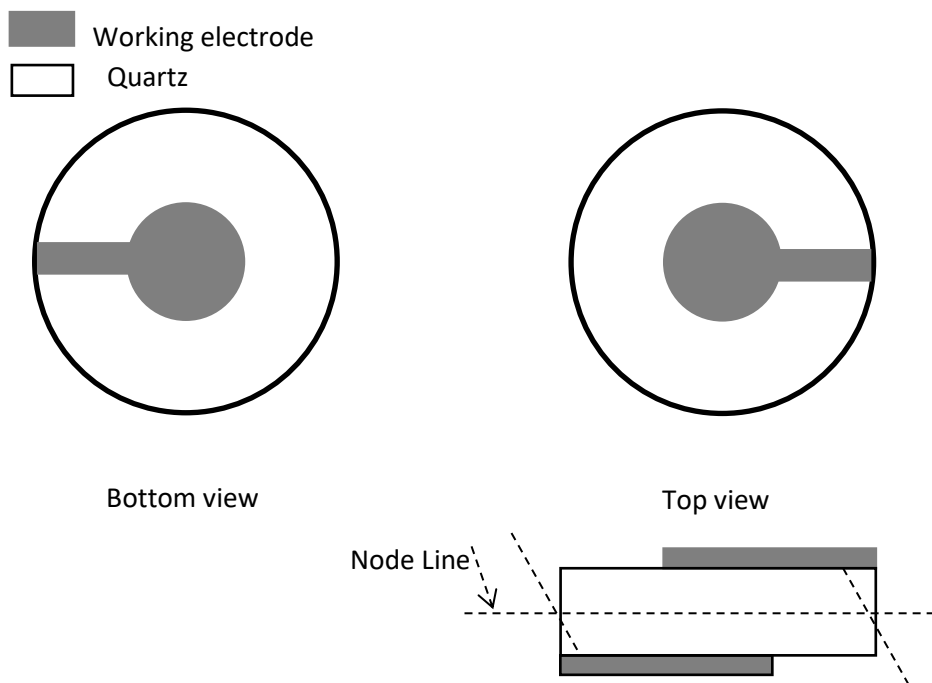
Where  $C_f$  (equivalent at the bracketed terms of equation 1.3.2.1) is the sensitivity constant in  $\text{Hz (ng cm}^{-2}\text{)}^{-1}$ . Using the Sauerbrey equation the value of  $C_f$  can be determined from the resonant frequency and electroactive area of the crystal and the theoretical value is equal to  $0.226 \text{ Hz (ng cm}^{-2}\text{)}^{-1}$  for the 10 MHz crystals employed here (*vide infra*) [56].

Figure 1.3.2.2 is a schematic of a keyhole design quartz crystal adapted from the work of Marcus et. al. [54].

The change of frequency of a piezoelectric crystal that can be observed under mechanical stress can be measured in terms of mass change (gain or loss) using QCN technology. For mass change measurements, a metallic layer is bonded onto the quartz sample. In terms of the work presented in this thesis, this means that the mass change due to metal dissolution or surface solid formation due to corrosion processes can be found by measuring the frequency change. Resonant frequency loss corresponds to mass gain and vice versa. Quartz crystal plates are available in a

variety shapes and metal coated materials. A detailed description of QCN theory may be found in various texts [57], [58], [59], [60], [61].

QCN can be coupled with a potentiostat allowing QCN and potentiostat measurements to be combined. Commonly conducted experiments include measurement of current and mass as applied potential is (linearly) varied with time, or the measurement of current and mass as a function of time when a constant potential is applied to the QCN electrode surface. Examples follow.



**Figure 1.3.2.2.:** Quartz crystal adapted with iron surface adapted from the work of P. Marcus *et. al.* [54].

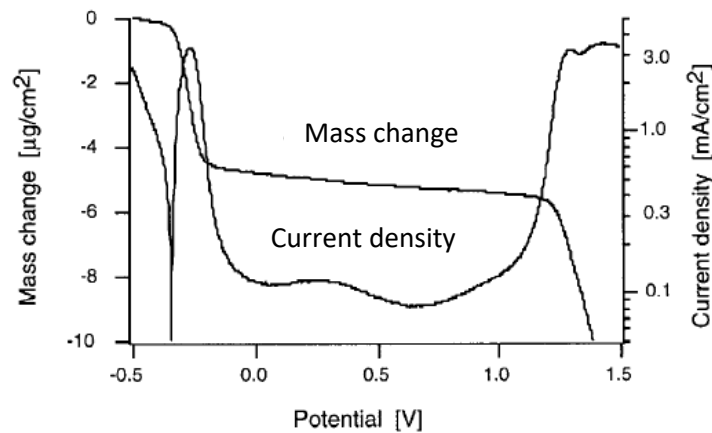


**Figure 1.3.2.3.:** The mass and current density change of an Fe-25Cr coated crystal in 0.1M H<sub>2</sub>SO<sub>4</sub> + 0.4M Na<sub>2</sub>SO<sub>4</sub> scanned from -0.5V to 1.5V vs standard hydrogen electrode with scan rate equal to 20mV/s adapted from the work of Schmutz et. al. [62].

Figure 1.3.2.3, adapted from the work of Schmutz et. al. [62], illustrates the measured current density and the associated mass change when the surface of an Fe-25Cr coated crystal immersed in 0.1M H<sub>2</sub>SO<sub>4</sub> + 0.4M Na<sub>2</sub>SO<sub>4</sub> is scanned from -0.5V to +1.5V (vs standard hydrogen electrode). At the active region there is a mass loss due to dissolution. At the passive region metal dissolution decreases and a slight mass loss can be observed whilst at higher potentials the mass loss increases due to transpassive dissolution. [62]

The mass change can be measured in real time at fixed potentials. For example, Figures 1.3.2.4 A and B, adapted from the work of Schmutz et. al. [62], illustrate the mass change of iron and Fe-25Cr coated crystal at fixed potentials in the region of -0.4V to +0.6V (vs standard hydrogen electrode). For potentials from 0V to +1V, the Fe-25Cr surface of the crystal passivates according to Figure 1.3.2.4.Bb and a rapid mass gain can be seen at the beginning of the experiment (until approximately 500sec). It is possible that, during the first few seconds, the iron surface reacts with the 0.1M H<sub>2</sub>SO<sub>4</sub> + 0.4M Na<sub>2</sub>SO<sub>4</sub> solution producing an insoluble layer on the surface. This additional layer on the surface can be explained by the mass gain. The surface is insulated due to the new layer that is on the surface acting as a corrosion inhibitor and the surface passivates. That is in agreement with the negligible mass change of the crystal that can be seen after 500 sec. Similar results can be seen using iron coated crystals, with the main difference being that the initial mass gain is more pronounced. [62]

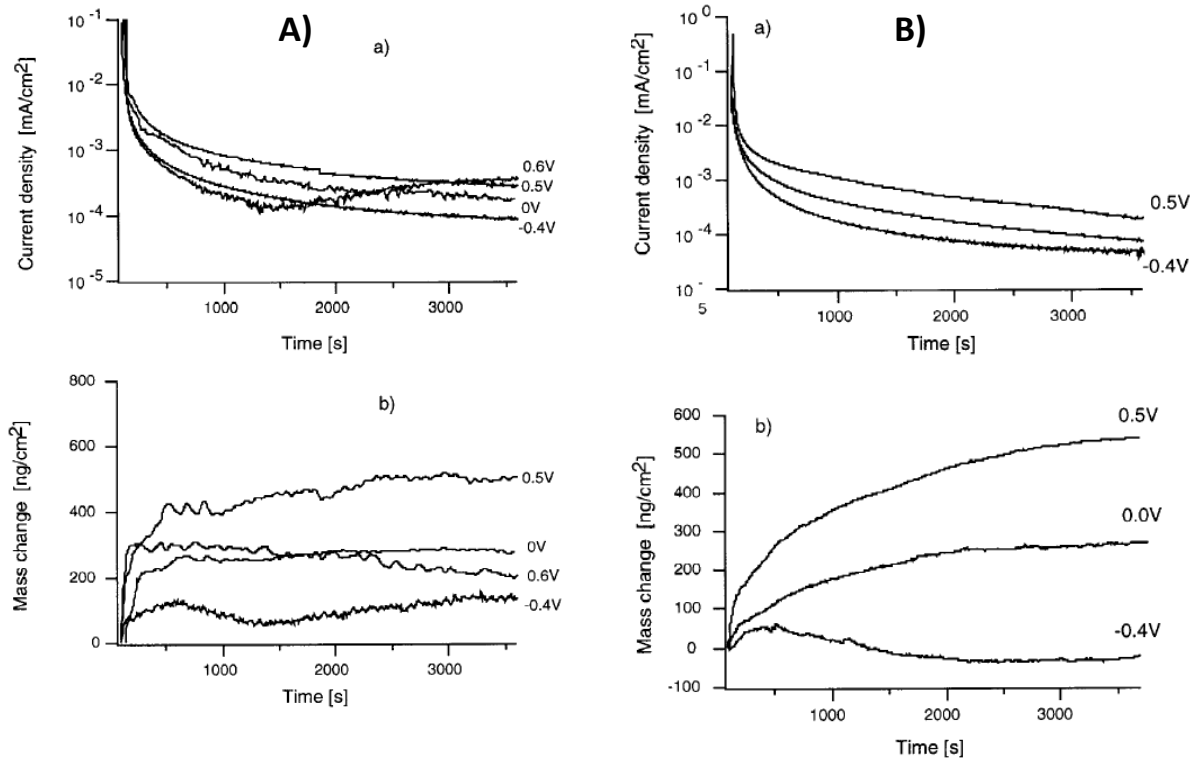


**Figure 1.3.2.4.:** A) and B) The mass (b)) and current density (a)) change of iron and Fe-25Cr coated crystals in 0.1 H<sub>2</sub>SO<sub>4</sub> + 0.4M Na<sub>2</sub>SO<sub>4</sub> at fixed potentials vs standard hydrogen electrode respectively (adapted from the work of Schmutz et. al. [62]).

Let us now consider any limitations of the QCN technology. As described above the resonant frequency can be converted to a mass change. However, the resonant frequency depends on several parameters including the change in mass, temperature, pressure and roughness of the resonator surface, and the density and viscosity change of the surrounding media. [63], [64]

$$\Delta f = \Delta f_m + \Delta f_T + \Delta f_P + \Delta f_r + \Delta f_{pn} \quad \text{Equation 1.3.2.3}$$

Where  $\Delta f$  is the observed frequency change,  $\Delta f_m$ ,  $\Delta f_T$  and  $\Delta f_P$  is the frequency change due to mass, temperature and pressure change of the resonator surface respectively,  $\Delta f_r$  is the frequency change due to roughness change of the resonator surface and  $\Delta f_{pn}$  is the frequency change due to density and viscosity change of the surrounding media.

By keeping the temperature, pressure, density and viscosity constant, the total frequency change depends on mass change and the roughness change of the resonator surface. Assuming that

the frequency change due to roughness change of the resonator surface is negligible compared to the frequency change due to mass change, the observed frequency change is equal to the frequency change due to mass change of the resonator ( $\Delta f = \Delta f_m$ ). In order to use the QCN technology for real time in-situ corrosion measurements, for instance in waste tanks at Savannah River Site, it is essential the above parameters carefully to be studied avoiding inaccurate results.

### 1.3.3. Conclusions

As described in section 1.3.1. there are four main common means of monitoring rates of corrosion, all with limitations: coupon testing (unsuitable for real time monitoring); electrical resistance monitoring (has sensitivity issues); linear polarisation resistance; and galvanic monitoring (both indirectly inferring corrosion rate in mm/year from current measurements).

Recent advances in Quartz Crystal Nanobalance technology [65] offer a means to avoid these issues. The QCN measures minute changes in frequency of a quartz crystal resonator with weight gain/loss. Using the Sauerbrey equation (see Equation 1.3.2.1 and 1.3.2.2), the frequency change observed during corrosion testing can be converted to an instantaneous mass change (gain or loss, depending upon the direction of frequency change); study of the time dependence of these changes allows for the calculation of corrosion rate with nanogram sensitivity. The recent availability of a wide range of metal coated crystal resonators (steel, Al, Fe, Ti etc) makes the QCN ideal for real time, instantaneous corrosion monitoring of steels. Its sensitivity makes it ideal for the measurement of low corrosion rates (e.g. passive corrosion) whilst its capacity for remote deployment allows for use in radiologically harsh environments with reduced operator exposure times, a key safety consideration for radiation workers.

The work in this thesis thus explores the potential of using QCN technology as a corrosion monitoring technique for measuring corrosion rates in real time, in situ, for nuclear applications.

## Chapter 2

## 2. Experimental

This chapter records the materials and reagents used in the experiments. A detailed description is given of the fabrication of the steel and iron electrodes as well as of the experimental set up for the QCN experiments and the iron crystal preparation prior to immersion. The methodology of calibration is also presented.

### 2.1. Materials and reagents

All reagents were ACS reagent grade or higher and purchased from Fisher Scientific (Loughborough, UK) or Sigma Aldrich (Gillingham, Dorset, UK) and used without further purification. All solutions were prepared using doubly deionised water, DDW. DDW was prepared using a Direct-Q 3 UV Millipore water purification system (Millipore, Watford, UK) to a resistivity of 18.2 M $\Omega$ .cm. Unless otherwise noted, all solutions were de-aerated by purging with high purity N<sub>2</sub> (BOC, UK) for 15 mins before and during each electrochemical experiment.

### 2.2. Fabrication of mild carbon steel and iron disc electrodes

Mild carbon steel and iron disc electrodes were fabricated by mounting short lengths of 10 mm diameter mild carbon steel (iron 98.81% – 99.26%, carbon 0.18%, manganese 0.6 – 0.9%, phosphorus 0.04% max, sulphur 0.05% max, Goodfellows, UK) or pure iron rods (99.99+% purity, Goodfellows, UK) onto a brass head using silver loaded epoxy (ABL (STEVENS) Resin & Glass, Cheshire, UK [www.resin-supplies.co.uk](http://www.resin-supplies.co.uk)). This assembly was then placed in a cylindrically shaped mould and sealed in epoxy resin (ABL (STEVENS) Resin & Glass) with 6 days curing at 50°C in order to

produce a suitable working electrode. The resultant 10 mm diameter disc electrodes were polished before each experiment using decreasing grades of SiC abrasive papers (Struers FEPA P#1000, Buehler-Met P#1200, Struers FEPA P#2400), followed by decreasing grades of diamond slurries (6, 3, 1 $\mu$ m) (Marcon) and a final polish on a clean cotton polishing (item No 40-7212 Buehler, lake Bluff, Illinois, USA) pad soaked in distilled water. After polishing the electrodes were washed with deionized water to remove any debris remaining from the polishing stages. Photographs and schematics during the rod electrode fabrication are shown in Figure 2.2.1.

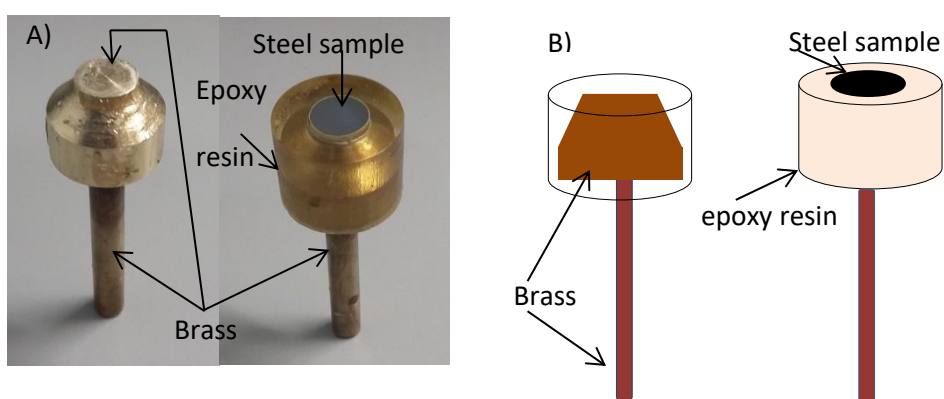


**Figure 2.2.1.:** A) Photographs and B) Schematics of rod samples during fabrication.

### 2.3. Electrochemical measurements

All electrochemical measurements, unless stated otherwise, were carried out on a Gamry Model 600 Potentiostat/Galvanostat/ZRA (SciMed Ltd., Stockport, Cheshire, UK) using a Gamry Resonator and EChem Analyst control, data acquisition and analysis software packages. All Cyclic Voltammetric (CV) and Linear Sweep Voltammetry (LSV) experiments were conducted in a 3 electrode cell with a Pt wire mesh (Goodfellow Cambridge Ltd., Huntingdon, UK) counter electrode and a Ag/AgCl (Alvatek Ltd. Gloucestershire, UK) reference electrode used in a double junction (Alvatek Ltd.) configuration with saturated K<sub>2</sub>SO<sub>4</sub> solution. For both CV and LSV experiments a sweep rate of 0.01V/s was used with a staircase step of 4.42mV. Open circuit potential ( $E_{oc}$ ) measurements

were conducted using a simple 2 electrode cell in conjunction with the same potentiostat and Ag/AgCl reference electrode as above. The Gamry potentiostat was calibrated using a Gamry dummy cell comprised of three resistors in series with values of  $47\Omega$ ,  $200\Omega$ , and  $3k\Omega$  with a  $1\ \mu\text{F}$  capacitance in parallel across the last resistor to provide a Randles equivalent circuit for the working electrode – reference electrode interface [66].

## 2.4. Electrochemical quartz crystal nanobalance experiments

The QCN experiments were conducted using a Gamry Potentiostat model 600, coupled with a Gamry QCN model 10M (SciMed Ltd.), using a Gamry QCN holder.

**Table 2.4.1.:** Photographs of parts of the QCN holder.

<b>Photographs</b>			
<b>Parts of the QCN holder</b>	1) The base	2) O-ring rubbers	3) The base with the O-ring
<b>Photographs</b>			
<b>Parts of the QCN holder</b>	4) The base with the crystal and the O-ring	5) The walls of the holder	6) The walls connected to the base and the crystal
<b>Photographs</b>			
<b>Parts of the QCN holder</b>	7) The lid	8) The QCN holder ready to be connected to the QCN	

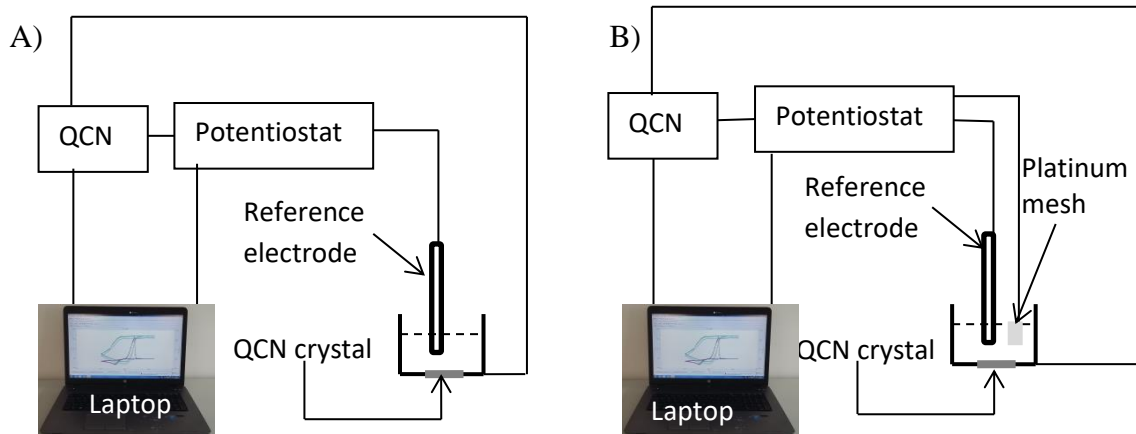


**Figure 2.4.1.:** Schematic of the experimental set up for QCN experiments A) using two electrode cell, B) and three electrode cell.

The Gamry QCN holder, made of Teflon, consists of the base (where the crystal is lying), the walls of the holder and the lid as can be seen in Table 2.4.1. These parts are connected using four screws. In order to avoid liquid leaks between the crystal and the Teflon holder, high corrosion resistance O-rings are located between the crystal and the holder. A schematic and a photograph of the experimental set up for the QCN experiments can be seen in Figure 2.4.1 and 2.4.2 respectively.

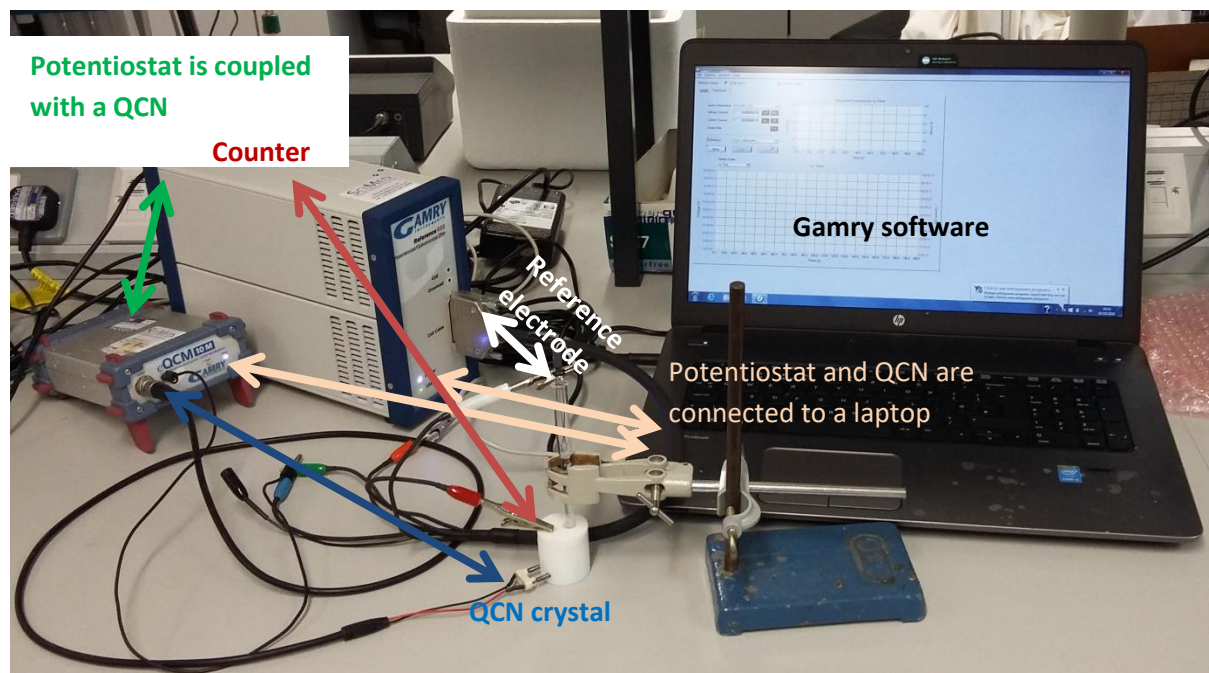


**Figure 2.4.2.:** Photograph of the QCN experimental arrangement using three electrode cell.

Experiments were performed in a ground floor laboratory sited directly on building foundations and isolated from heavy machinery and vibration sources. The Memmert Model US 100 laboratory oven was used to perform experiments at high temperatures.

In order to calibrate the QCN the sensitivity constant  $C_f$  was measured and compared with the theoretical value using a solution of 10mmol L<sup>-1</sup> copper (II) sulphate (CuSO<sub>4</sub>) in 100mmol L<sup>-1</sup> sulphuric acid (H<sub>2</sub>SO<sub>4</sub>). Using the Gamry software, the change of the current and frequency can be found when the surface of an iron crystal is scanned from -0.6 to +0.6V, as can be seen in Figure 2.4.3. Scanning from +0.6V to -0.6V there is a frequency loss (Figure 2.4.3 A) due to a two electron absorption by the copper (II) ion to form metallic copper (mass gain) and a sulphate ion, as represented by equation 2.4.1. The reverse phenomenon can be seen by scanning from -0.6V to +0.6V.



In order to determine the sensitivity constant, it is necessary to calculate the number of moles of copper reduced at the electrode surface. This is done by calculating the charge passed through the electrode during either the mass deposition or dissolution steps. The charge passed  $\Delta Q$ , through electrode during either the mass deposition or dissolution steps is calculated using equation 2.4.2, by integrating the current passed,  $i$ , as a function of time,  $t$ :

$$\Delta Q = \int_0^t i(t) \quad \text{Equation 2.4.2.}$$

Because the potential increment between each recorded data point is small (2.44mV), it is possible to integrate this function numerically in an Excel® spreadsheet, using the trapezium rule given by Equation 2.4.3. [67],[68] :

$$\Delta Q = \sum_j \left( \frac{i_j + i_{j+1}}{2} \right) \cdot \frac{\Delta E}{v} \quad \text{Equation 2.4.3.}$$

Where:  $\Delta Q$ = Total charge passed (C)

$i_j$  = Current for data point j (A)

$\Delta E$  = Potential step (V)

$v$  = Scan rate of the experiment ( $V s^{-1}$ ).

Charge passed may be related to mass deposited using the Faraday equation.

$$\Delta Q = \frac{z \cdot F \cdot \Delta m}{M} \quad \text{Equation 2.4.4.}$$

Where:  $M$ =Molar mass ( $g mol^{-1}$ ) of the substance. ( $M_{Cu}$ =63.545 g/mol)

$\Delta m$ = Mass change (g)

$F$ = Faraday constant ( $96485 C mol^{-1}$ )

$z$ =Number of electrons (For Cu  $z$  is equal to 2)

Dividing the mass change by the total frequency change observed over the potential range considered in equation 2.4.3 after deposition or dissolution and taking into account the piezoelectric active area,  $A_p$  through equation 2.4.5 gives the sensitivity constant of the crystal,  $C_f$ .

$$C_f = - \frac{\Delta F \cdot A_p}{\Delta m} \quad \text{Equation 2.4.5.}$$

Substitution of equation 2.4.4 into 2.4.5 gives equation 2.4.6

$$C_f = -A_p \frac{z \cdot F}{M} \cdot \frac{\Delta F}{\Delta Q} \quad \text{Equation 2.4.6.}$$

Analysis of the current and frequency data was achieved using a simple Excel™ spreadsheet. This also served to import the cyclic voltametric and frequency data from the Gamry software. Simultaneous plots of current versus potential and frequency change versus potential for a copper deposition / stripping experiment are shown in Figure 2.4.3.A.

The separate scans were then analysed in accordance with equation 2.4.2 and 2.4.5 above and sensitivity constant values were calculated for the forward sweep (metal deposition) and return sweep (metal stripping). A plot of frequency change vs charge passed for the forward going sweep of Figure 2.4.3.A is given in Figure 2.4.3.B. From the slope of the curve and equation 2.4.6, a sensitivity constant  $C_f$  of 212 Hz  $\text{cm}^2/\mu\text{g}$  can be calculated, which is in good agreement with the theoretical value of 226 Hz  $\text{cm}^2/\mu\text{g}$ , of 10MHz as presented by Glassford et.al. [56].

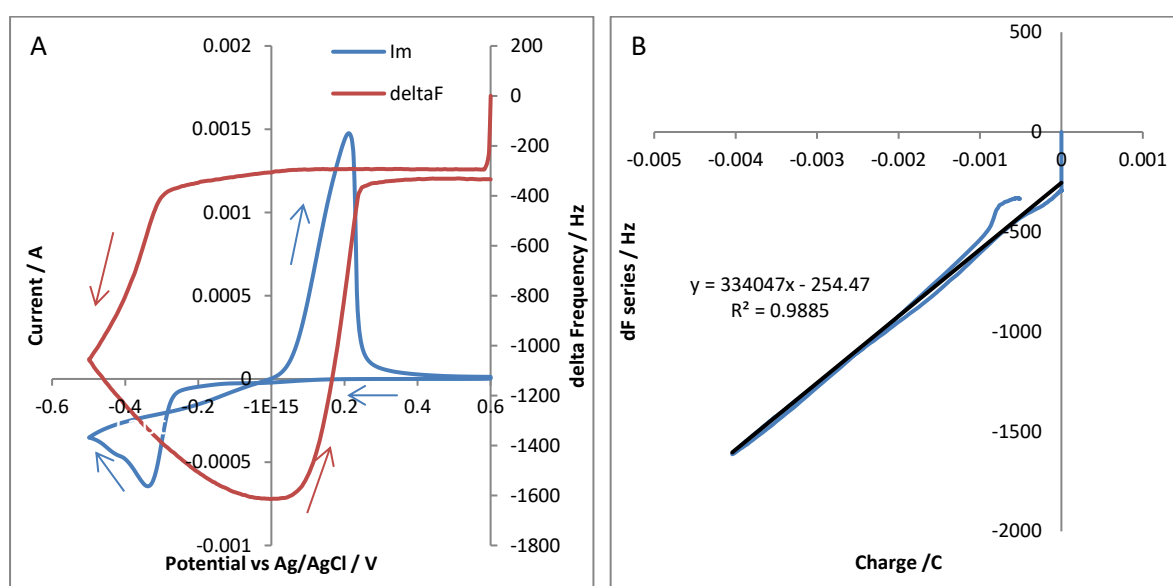


**Figure 2.4.3.:** Cyclic voltammogram and voltamassogram of iron crystal immersed in solution of 10 mmol  $\text{L}^{-1}$   $\text{CuSO}_4$  in 100mmol  $\text{L}^{-1}$   $\text{H}_2\text{SO}_4$  (scan rate  $0.05\text{Vs}^{-1}$ ). A) Plot of potential against current and frequency change and B) plot of charge against frequency change obtained from forward (cathodic) going sweep.

## 2.5. Preparation of iron crystals for electrochemical QCN corrosion experiments

AT cut iron QCN piezoelectrodes with a 10 MHz resonant frequency (International Crystal MFG, USA) were used which consisted of a 1.37 cm diameter Au blank (reverse side) electrode and a 0.51 cm diameter Fe working (forward side) electrode. The Au and Fe electrodes were comprised of 100 nm thick layers Au & Fe respectively, each over a 10 nm Ti binding layer. Both the Fe and Au surfaces of these piezoelectrodes were cleaned prior to each experiment using a procedure given by

Wilbraham et al. [69] and described as follows. Crystals were washed using a polypropylene eye dropper with, successively, chloroform, acetone and ethanol. The crystals were dried after each wash by blowing with white spot N<sub>2</sub> (BOC).

## Chapter 3

### 3. Comparison of iron and mild carbon steel corrosion behaviour in oxalic acid environments

Oxalic acid has been used widely to decontaminate cooling circuit pipework in water cooled reactors, as an oxide deposit remover in power plants [70], [71], and as a decontamination agent during the Post Operational Clear Out (POCO) of nuclear facilities scheduled for decommissioning. Such facilities include not only reactors at the end of their operational lifetime but also reprocessing plant pipework and vessels etc. In particular, it is currently being studied as an Enhanced Chemical Cleaning (ECC) decontamination agent in the decommissioning of high level waste (HLW) storage tanks at the Hanford and Savannah River Sites (SRS) in the US[43].

As discussed in Chapter 1, oxalic acid has been used as a cleaning agent due to its ability to act as a rust remover and as a rust inhibitor. Typically 4-8 wt% of oxalic acid is used for ECC. However, process engineering and secondary waste management issues have arisen which may be due to low Na salt solubility ( $37 \text{ g kg}^{-1}$  or  $0.28 \text{ mol kg}^{-1}$  at  $303.15 \text{ }^{\circ}\text{K}$  in water [72]). In order to decrease downstream issues, recent research has been focused on 1 wt% solutions of oxalic acid and it is proposed that under specific conditions 1 wt% can be more effective than the hitherto typical oxalic acid concentrations [42]. Downstream issues also can be minimized using mechanical methods prior to using ECC. Finally, concentrated oxalic acid or oxalic acid crystals produced from wastes after the first wash can be regenerated and be reused as a cleaning agent for a second ECC process [43].

In order to develop QCN for measuring the corrosion rates in real time, it is essential to choose suitable QCN coated crystals to simulate the chemical cleaning process. As has been discussed in Chapter 1 the walls of nuclear waste tanks used in recent years are fabricated from mild carbon steel. For this work, it is evident that the best scenario is to use mild carbon steel resonator crystals. However, mild carbon steel coated crystal resonators are extremely expensive (price per crystal > £100). Unfortunately, the crystals will be used destructively and for the current work a

considerable number of coated crystals will be required. As discussed in Chapter 2, mild steel contains about 99% iron and iron crystals are not as expensive as mild carbon steel ones (price per crystal < £30). There will thus be an economically significant benefit if iron coated crystals can be used as a surrogate to mild carbon steel coated resonator crystals.

Thus, in this chapter, the corrosion behaviour of mild carbon steel and pure iron electrodes in low ( $\approx 1\text{wt}\%$ ) and high ( $\approx 8\text{wt}\%$ ) concentrated oxalic acid environments titrated and non-titrated with hydrogen peroxide is presented. The objective of the work in this chapter is to compare the electrochemical behaviour of mild carbon steel and iron samples in order to test the feasibility of using iron resonator crystals as a surrogate to mild carbon steel resonator crystals under solution conditions typical of those encountered during HLW tank clean out and thus those employed in the rest of this thesis. Basic electrochemical experiments such as cyclic voltammetry and chronopotentiometry zero current have been performed and compared using mild carbon steel and iron rod samples.

### **3.1. Behaviour of mild carbon steel and iron electrodes in the presence of oxalic acid**

This section compares and explains the corrosion behaviour of iron and mild steel samples in 1 and 8wt% oxalic acid. Several researchers have reported similar experimental work using as a working electrode metals with similar properties to mild carbon steel and iron samples, at a variety of different oxalic acid concentrations [73], [74], [75], [76], [77], [78] [79], [80].

Figure 3.1.1 shows the cyclic voltammetric behaviour recorded in this laboratory of iron and mild carbon steel disc electrodes scanned between -1V and +1V in 1 and 8 wt% oxalic acid solutions. Each voltammogram has the following features in common:

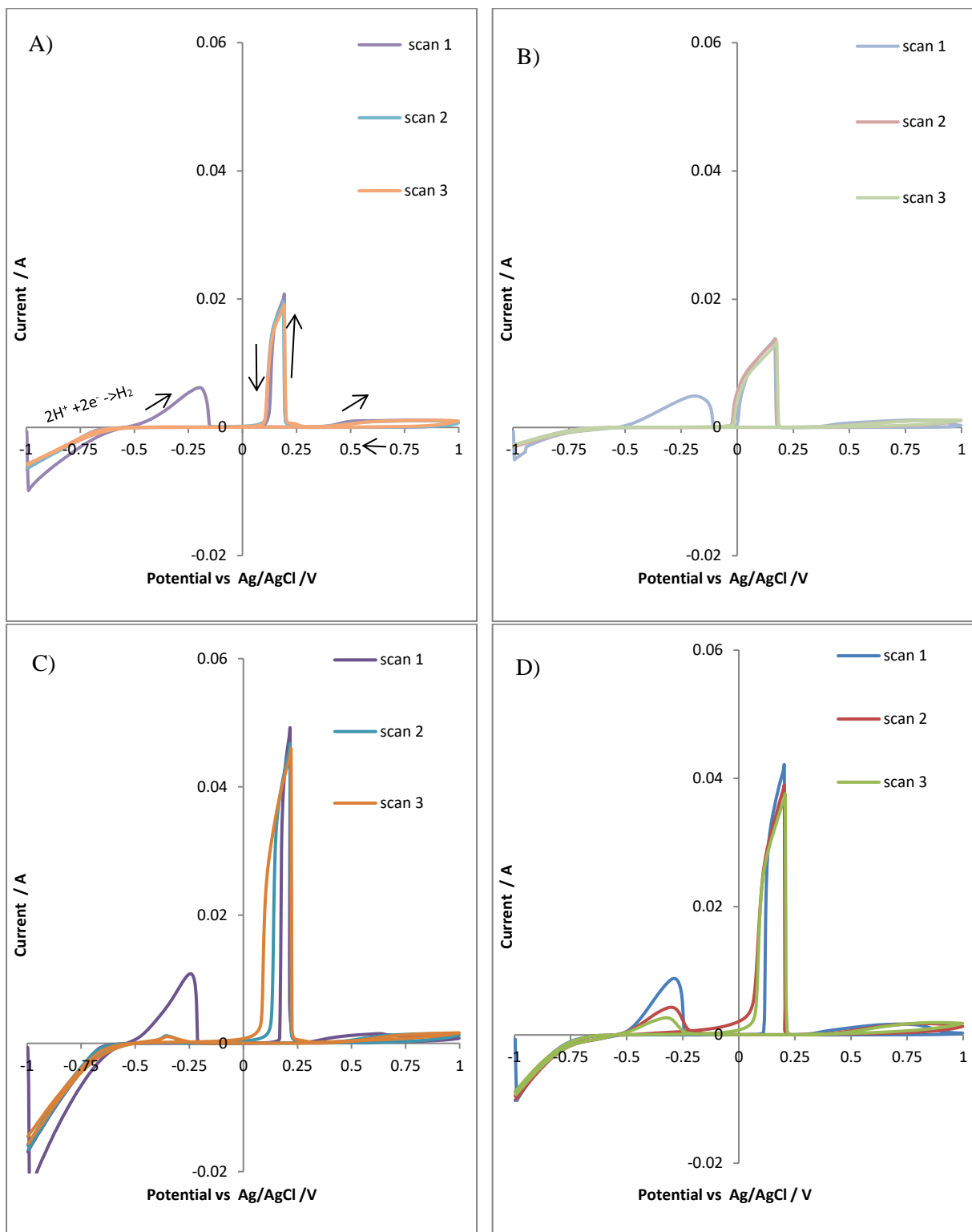


**Figure 3.1.1.:** Comparing cyclic voltammograms of mild carbon steel, (A) and (C), and iron electrodes, (B) and (D), in 1wt % oxalic acid, pH=1.3 (A) and (B) and 8wt% oxalic acid, pH=0.85 (C) and (D). Scan rate = 0.01V/s.

- Hydrogen evolution can be seen in the range -1V to -0.5V.
- During the forward going sweep, two oxidation peaks are observed with onsets of -0.5 V and +0.35 V, the former exhibiting an abrupt current decrease at  $\sim -0.1$  V in 1wt% oxalic acid and  $\sim -0.2$  V in 8wt% oxalic.
- During the reverse going sweep, one sharp oxidation peak is observed with a reverse going onset / peak potential of +0.2 V, dropping away to zero current by 0 V.

These features can be interpreted with the assistance of the simplified  $E_h$ -pH diagrams for the Fe-oxalate- $H_2O$  and Fe- $H_2O$  systems shown in Figure 3.1.2.A and 3.1.2B and adapted from the work of Pourbaix [81] and Saltykov *et al.* [82] respectively, as well as the cyclic voltammetric behaviour of iron in an oxalate free 1wt%  $KNO_3$  solution shown in Figure 3.1.3 recorded in this laboratory.

Let us consider the oxalate - free baseline behaviour shown in Figure 3.1.3 first. During the forward going sweep of Figure 3.1.3, a peak current is observed with onset of  $\sim -0.35$ V dropping away to negligible current. This feature can be interpreted with the assistance of Figure 3.1.2B. The pH of 1wt%  $KNO_3$  is about 3.3 indicating that the peak current during the forward sweep is due to oxidation of iron to  $Fe_2O_3$ . In the presence of  $Fe_2O_3$  the electrode surface passivates and the current is negligible. During the reverse sweep, and at about  $\sim -0.35$ V due to reduction of  $Fe_2O_3$  to  $Fe^{2+}$ , the layer on the surface dissolves and a negative current is observed.

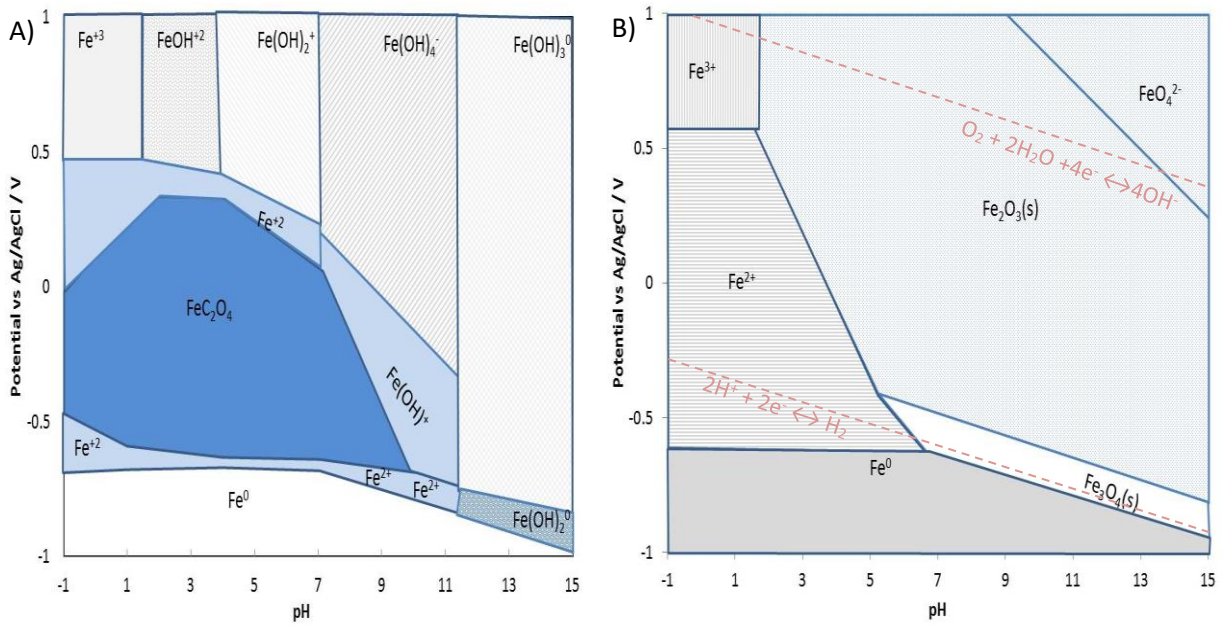


**Figure 3.1.2.:** Simplified  $E_h$ -pH (Pourbaix) diagrams for the (A) Fe-oxalate- $H_2O$  and (B) Fe- $H_2O$  systems, adapted from the work of Saltykov *et al.* [82] and Pourbaix [81].

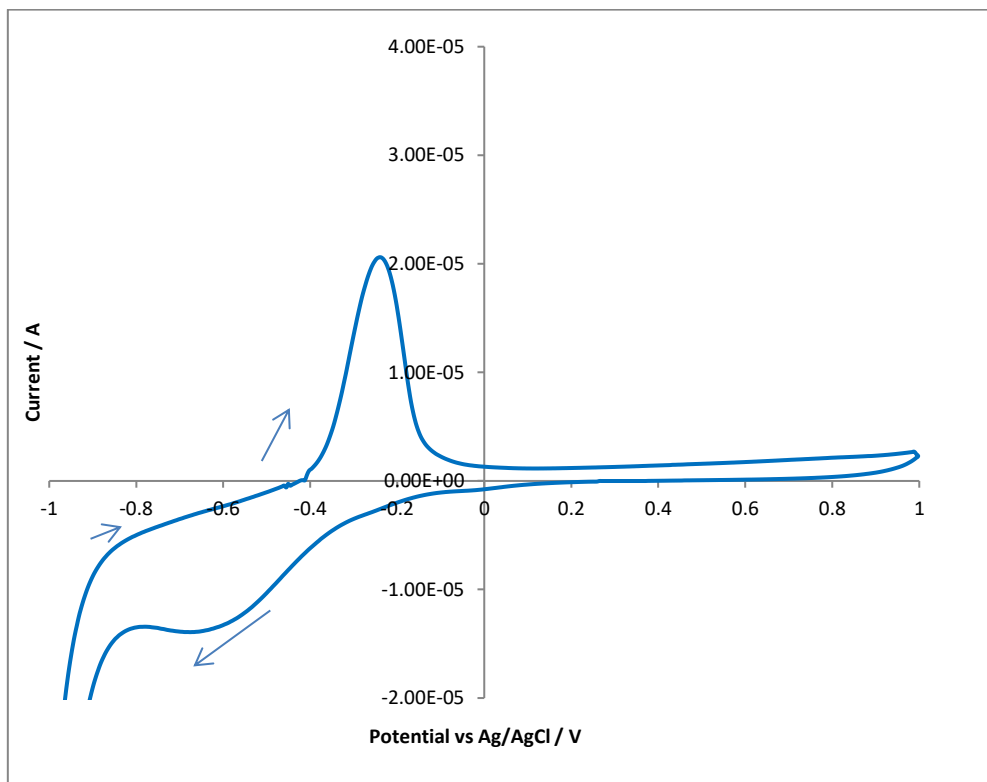


**Figure 3.1.3.:** Cyclic voltammogram of an iron crystal in 1wt%  $KNO_3$ , pH=3.3. Scan rate = 0.01V/s.

Now let us turn to behaviour in the presence of oxalic acid. From Figure 3.1.2A and 3.1.2B, and the fact that the pH of 1wt % and of 8wt % oxalic acid solutions are 1.3 and 0.85 respectively, it can be seen that the onset of the first wave in the forward going sweep of all cyclic voltammograms in Figure 3.1.1 is again due to the oxidation of Fe metal, this time to  $\text{Fe}^{2+}$  ions. In the absence of oxalate, Figure 3.1.2B indicates that this reaction would be expected to continue unimpeded up to  $\sim +0.4$  V vs. Ag/AgCl at which point further oxidation to  $\text{Fe}^{3+}$  occurs with consequent formation of solid phase  $\text{Fe}_2\text{O}_3$ , most likely in the form of  $\gamma\text{-Fe}_2\text{O}_3$ , maghemite (proved by Mengoli and Musiani by recording the photocurrent of the polarized electrode [76]). However, in the presence of oxalate, Figure 3.1.2A indicates that  $\text{Fe}^{2+}$  generated at  $E > -0.5$  V may, as a result of locally exceeding the solubility product, precipitate as ferrous oxalate,  $\text{FeC}_2\text{O}_4$ , at the electrode surface.

An abrupt current decrease can be seen associated with this peak in Figure 3.1.1 at  $E > \sim -0.2$  V suggesting that this ferrous oxalate phase passivates the electrode surface in a manner analogous to the  $\text{Fe}_2\text{O}_3$  derived passivation that occurs in the absence of oxalate – again, see Figure 3.1.3. Passivation occurs in all CVs in Figure 3.1.1 until  $E \sim +0.35$  V at which point an oxidation current begins to flow. From Figure 3.1.2A, this can be seen to be due to the oxidation of  $\text{FeC}_2\text{O}_4$  to potentially form free solution oxalate and  $\text{Fe}^{3+}$ . However, as discussed above, Figure 3.1.2B indicates that at these pHs, the  $\text{Fe}^{3+}$  so released will precipitate as  $\text{Fe}_2\text{O}_3$  at the electrode surface, so inducing a secondary electrode passivation.

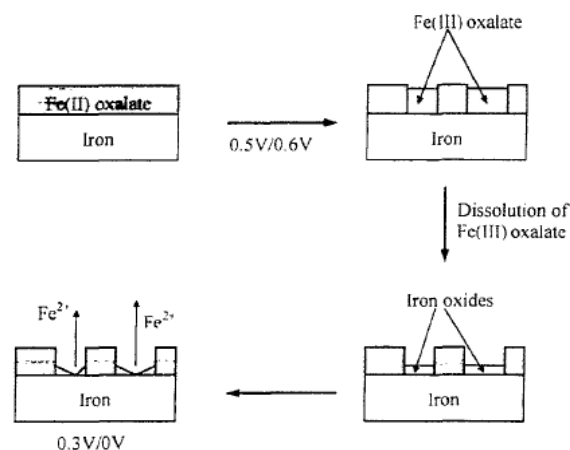


**Figure 3.1.4.:** Modification of the mild carbon steel surface during potentiodynamic polarization in 0.3M (=2.7 wt%) aqueous oxalic acid solution adapted from the work of Camalet et. al [74].

This interpretation is supported by work by Camalet et. al. [74] who used XPS to identify the products formed at the surface of mild carbon steel electrodes when electrochemically cycled in 0.3M (2.7 wt%) oxalic acid. The findings are summarized in Figure 3.1.4 which shows that at  $E < 0.5V$ , the steel surface is covered with a layer of  $FeC_2O_4$  but that at  $E > 0.5V$  that layer partially oxidises (in a process analogue to pitting) to  $Fe(III)$ oxalate a more soluble product. This may then dissolve leaving the mild carbon steel surface partially covered with the pitted layer of  $Fe(II)$ oxalate. The iron surface that has been exposed at the base of each of the pits then oxidises to  $Fe_2O_3$  in accordance with the Pourbaix diagrams of Figure 3.1.2A and B resulting in a composite  $Fe(II)$ oxalate/ $Fe(III)$  oxide layer at the surface- again see Figure 3.1.4.

With this interpretation in mind, let us now return to the results of Figure 3.1.1. During the return sweep, the electrode surface initially comprises a layer of  $Fe_2O_3$  and potentially some remnant  $Fe(III)$  and  $Fe(II)$ oxalate. However, Figure 3.1.2B indicates that at  $E \sim 0.4V$ , the  $Fe_2O_3$  component of the layer is reduced back to solution phase  $Fe^{2+}$ , exposing the Fe metal surface beneath. Almost counter-intuitively, this  $Fe_2O_3$  reduction manifests itself as the sharp oxidation peak seen in all of the reverse scans of Figure 3.1.1. However, this can be understood by realizing that, at the potential of  $Fe_2O_3$  reduction, the exposed Fe metal will be subject to an oxidative dissolution reaction, giving rise to the sharply rising oxidation current observed. The attenuation of that current to zero in all the CVs in Figure 3.1.1 can then be easily understood in the context of Figure 3.1.2A: the  $Fe^{2+}$  released by the reduction of the  $Fe_2O_3$  surface layer and the oxidation of the underlying Fe metal again interacts with solution oxalate to generate a layer wholly comprised of passivating  $FeC_2O_4$  at the electrode surface.

Finally, it appears that, once generated at the electrode surface during the reverse sweep, this layer of passivating  $FeC_2O_4$  is retained into the forward going sweep of the next cycle. This is indicated by the height of the first peak in the forward going sweep decreasing with increasing scan

number – and suggests that  $\text{FeC}_2\text{O}_4$ , once formed, is kinetically resistant to reduction back to Fe metal.

This interpretation is supported by work by Mengoli et al. [76] who records a simultaneous cyclic voltammogram and capacitance-potential curve, seen in Figure 3.1.5, when an iron electrode is electrochemically cycled in 0.11 M (~1 wt%) oxalic acid. This allows us to make the following observations [76]. The first is that the cyclic voltammogram recorded by Mengoli et al is identical in form to these recorded in this laboratory, Figure 3.1.1. The second observation is that during the forward going sweep of the voltammogram of Figure 3.1.5. two oxidation peaks are seen with onsets of -0.5 and +0.35 V as discussed above. Compare this with the capacitance – potential curve of Figure 3.1.5. After the first oxidation peak in the voltammogram, where iron reacts with oxalic acid producing an insoluble iron II oxalate layer, the capacitance in the corresponding capacitance – potential curve decreases to a low levels of ~0.1 $\mu\text{F}$ . This can be explained due to the fact that the aforementioned ferrous oxalate layer is forming, the capacitance then decreasing with increasing layer thickness in qualitative according with the equation 3.1.1 for the capacitance, C, of a parallel plate capacitor;

$$C = \frac{\epsilon \times A}{d} \quad \text{Equation 3.1.1.}$$

where, in this instance,  $\epsilon$  can be considered to be the permittivity of the ferrous oxalate layer, A the area of the electrode and d the ferrous oxalate thickness.

At +0.35V ferrous oxalate transforms to iron (III) species and the capacitance of the electrode increases (~1.5 $\mu\text{F}$  at ~+1V). This is due to the pitting of the layer of Fe(II)oxalate as discussed above and shown in Figure 3.1.4. resulting in an effective decrease in layer thickness and thus increasing surface capacitance in accordance with equation 3.1.1. Finally, in the reverse scan of the voltammogram one sharp oxidation peak is observed (as discussed again above) with an onset of +0.2 V due to ferrous oxalate regeneration at the surface of the reductive stripping of  $\text{Fe}_2\text{O}_3$ . This regeneration and

regrowth of the iron oxalate layer ones again results in the decrease in capacitance in the capacitance – potential curve in accordance with equation 3.1.1, as can be seen in Figure 3.1.5. eliminating the capacitance of the electrode ( $\sim 0.1\mu\text{F}$ ).

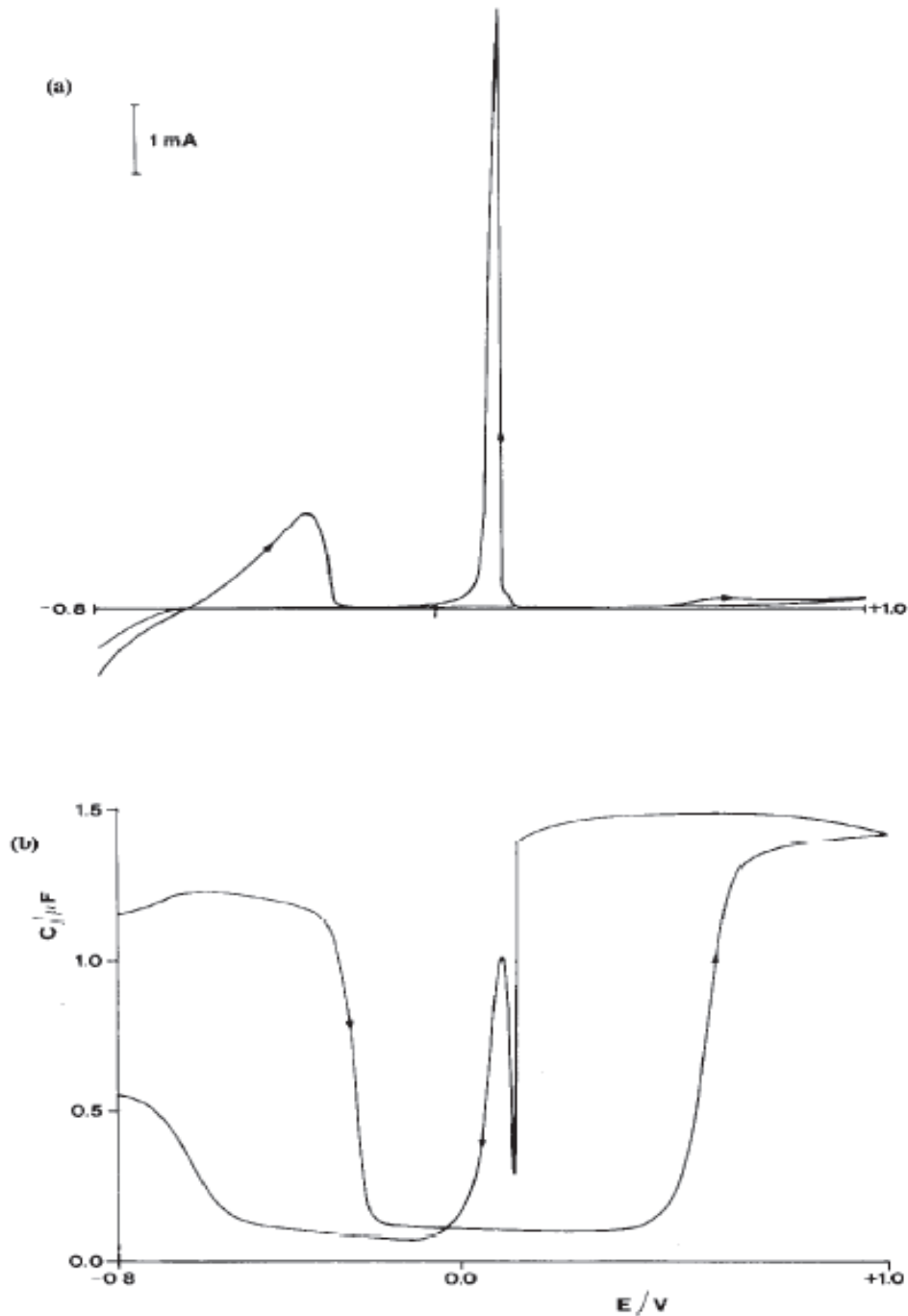


**Figure 3.1.5.:** A) Current – Potential, B) Capacity – Potential curves recorded at an iron electrode immersed in 0.11M oxalic acid solution adapted from the work of Mengoli et al [76]. Scan rate  $20\text{mVs}^{-1}$ .

It is apparent from the results of Figure 3.1.1 that mild carbon steel and pure iron samples behave in a broadly similar fashion with respect to their voltammetric behaviour in the presence of oxalic acid and that the interpretation of the behaviour of mild carbon steel provided by Camalet et al [74], shown in Figure 3.1.4, is broadly appropriate to both materials.

This similarity is further underscored by the Tafel curves shown in Figure 3.1.6 of the forward going sweeps in the first scan cyclic voltammograms of iron piezoelectrodes in 1 and 8wt% oxalic acid respectively and which can be interpreted in accordance with the description of the forward going sweeps of Figure 3.1.1 as described above. From these results, it is again apparent that mild carbon steel and pure iron behave in a broadly similar fashion with respect to their electrochemical behaviour in the presence of oxalic acid – suggesting that pure iron may be used as a low carbon steel surrogate. Finally, the similarity between iron and mild carbon steel is further demonstrated by the results shown in Figure 3.1.7 of  $E_{OC}$  measurements for both electrode materials as a function of oxalic acid concentration in the range 1 to 8 wt%. In the range 0 to 1wt% oxalic acid, the measured  $E_{OC}$  value abruptly decreases to -0.49 V for both iron and mild carbon steel. It is then near-invariant with increasing oxalic acid concentration reaching values of -0.49V and to -0.53V for mild carbon steel and iron respectively.

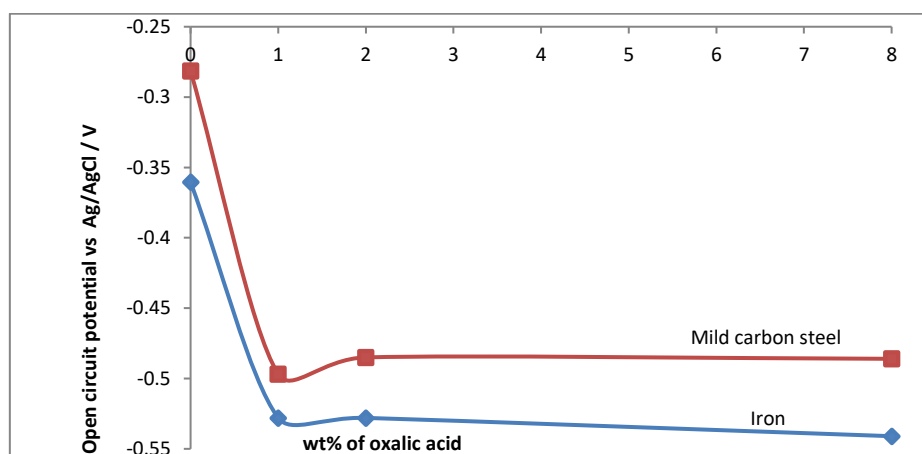


**Figure 3.1.7.:**  $E_{OC}$  measurements for iron and mild carbon steel electrodes as a function of oxalic acid concentration in the range 1 to 8 wt%.

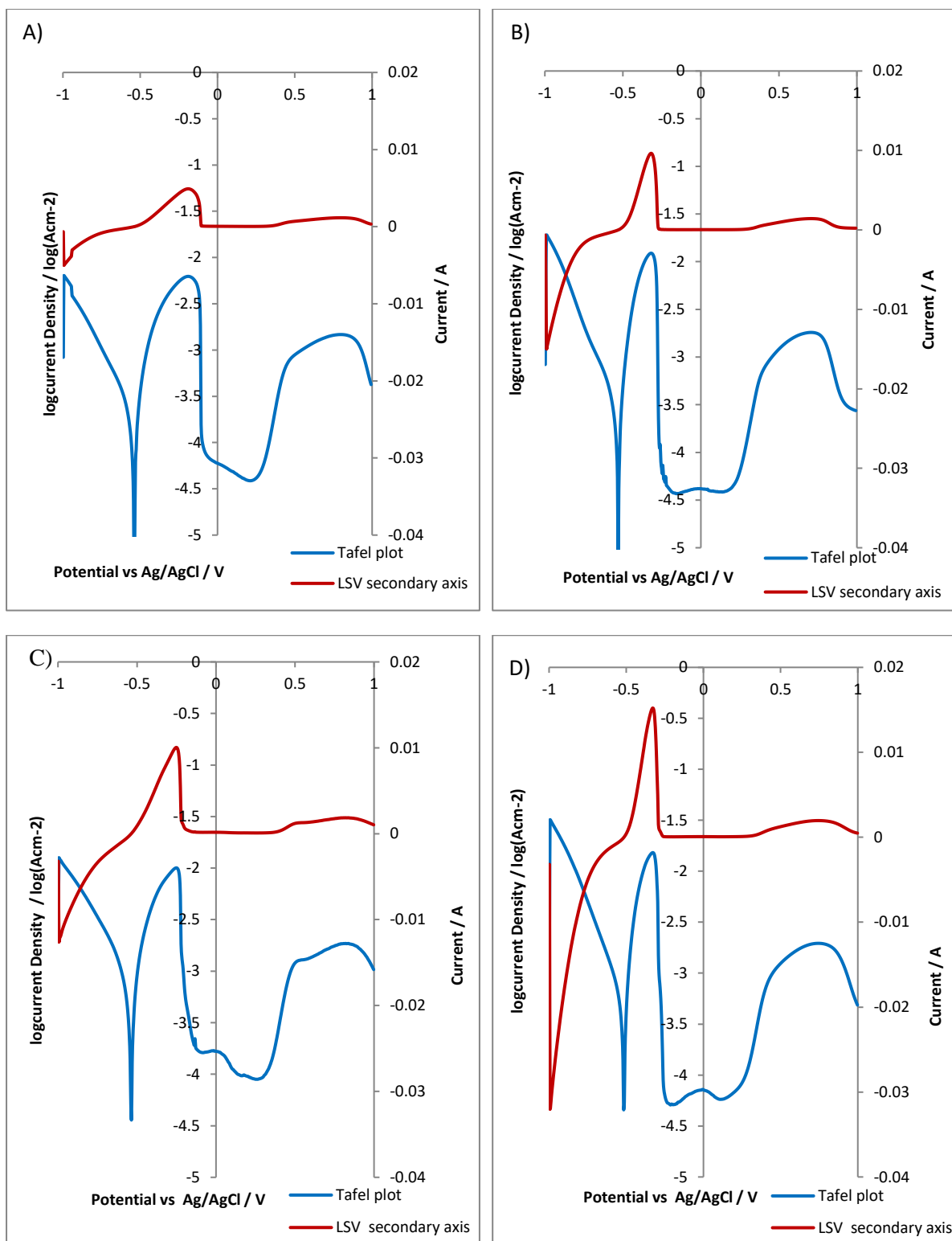


**Figure 3.1.6.:** Forward going sweeps in the first scan cyclic voltammograms, and associated LSVs, of iron rod electrodes in (A) 1 and (B) 8 wt% oxalic acid and of iron piezoelectrodes in (C) 1 and (D) 8 wt% oxalic acid. Scan rate = 0.01V/s.

### 3.2. Behaviour of mild carbon steel and iron electrodes in the presence of oxalic acid and hydrogen peroxide as a simulant for the products of the radiolysis of water

Several reports and papers cite the use of  $H_2O_2$  as an experimental surrogate to simulate irradiated and especially gamma radiated environments. Thus it is appropriate that our comparison of the behaviour of iron and mild carbon steel electrodes should include use of oxalate solutions wherein  $H_2O_2$  has been deliberately added as a radiolysis simulant. For the cyclic voltammogram experiments detailed here, zero to 100 mM  $H_2O_2$  was mixed with low (=1wt%) and high (=8wt%) concentrations of oxalic acid respectively. For the open circuit potential experiments detailed here, 60 mM  $H_2O_2$  was titrated into low (=1wt%) and high (=8wt%) concentrations of oxalic acid. The reasons for the choice of experimental conditions with respect to  $H_2O_2$  concentration are as follows.

As reported in section 1.1.4 the properties of the waste tank walls and the waste liquids in SRS have similar properties and characteristics with those that can be found in Hanford site. As shown in section 1.1.4.1 approximately  $68.2 \times 10^6$  litre with  $447.7 \times 10^{16}$  Bq have been stored in 22 nuclear waste tanks across the SRS with an average activity of approximately  $6.6 \times 10^{10}$  Bq/litre. In more detail, the salt supernate contains  $222 \times 10^{16}$  Bq with volume of  $23.6 \times 10^6$  litre ( $9.4 \times 10^{10}$  Bq/litre), the saltcake contains  $25.9 \times 10^{16}$  Bq with  $40 \times 10^6$  litre volume ( $0.6475 \times 10^{10}$  Bq/litre) and the sludge contains  $199.8 \times 10^{16}$  Bq with  $3.6 \times 10^6$  litre volume ( $55.5 \times 10^{10}$  Bq/litre) as can be seen in Figure 1.1.4.1.2. An average Hanford tank contains  $\sim 1$  Curie/litre or  $3.7 \times 10^{10}$  Becquerel/litre of combined beta and gamma activity (alpha activity is negligible) [83]. The radioactive decay energy deposits almost entirely in the waste to yield radiolytic doses rates up to 7 Gray/h [83].

Shourian et.al. have provided a relationship between gamma dose radiolytically generated hydrogen peroxide as shown in Figure 3.2.1 generated by irradiation detecting the dosimetry, the gamma rays were emitted from two elements ,Thallium -201 (  $^{201}Tl$ ) and Technetium-99m (  $^{99m}Tc$ ) with the hydrogen peroxide concentration determined using a chemiluminescence technique [84].

Shourian et.al. then provide equations 3.2.1.and 3.2.2 relating radiolytically generated hydrogen peroxide concentration to dose:

$$[\text{H}_2\text{O}_2]=9.310X + 74.57 \quad \text{Equation 3.2.1.}$$

$$[\text{H}_2\text{O}_2]=8.446X + 68.49 \quad \text{Equation 3.2.2.}$$

Where  $[\text{H}_2\text{O}_2]$  and X is the hydrogen peroxide concentration in nM and the radiolytic doses rates in  $\mu\text{Gray/h}$  respectively.

Assuming that the radiolytic doses rates at the waste tank wall in SRS and Hanford site during the chemical cleaning process is up to  $7 \times 10^6 \mu\text{Gray/h}$  and assuming, as a worst case scenario, that equations 3.2.1 and 3.2.2 apply up to dose rates of 7 Gy/h, the hydrogen peroxide concentration as a simulant for the products of the radiolysis of water can be found using equation 3.2.1 (for  $^{201}\text{Tl}$ ) and 3.2.2. (for  $^{99\text{m}}\text{Tc}$ ). For radiolytic doses rates equal to  $7 \times 10^6 \mu\text{Gray/h}$  the hydrogen peroxide concentration as a simulant for the products of the radiolysis of water calculated using equation 3.2.1 and 3.2.2 is then approximately 60mM-hence the choice of peroxide concentration in the simulant experiments that follow herein. The above assumption comes in an agreement with work presented by T. Song et. all, see Figure 3.2.1B which reports that the hydrogen peroxide concentration increases linearly against radiation doses until about 80mM [85].

Thus, this section reports on the appropriateness of using iron as a surrogate for mild carbon steel in the study of its electrochemical and corrosion behaviour in the presence of oxalic acid and in a wide range of hydrogen peroxide concentrations as a simulant for the products of the radiolysis of water and especially focusses on the range of 20-100mM  $\text{H}_2\text{O}_2$ . However, before considering the associated electrochemical results in detail, it is informative to first consider the effect of these concentrations of peroxide on the primary product of electrooxidation of iron surfaces, namely the  $\text{Fe}^{2+}$  ion.

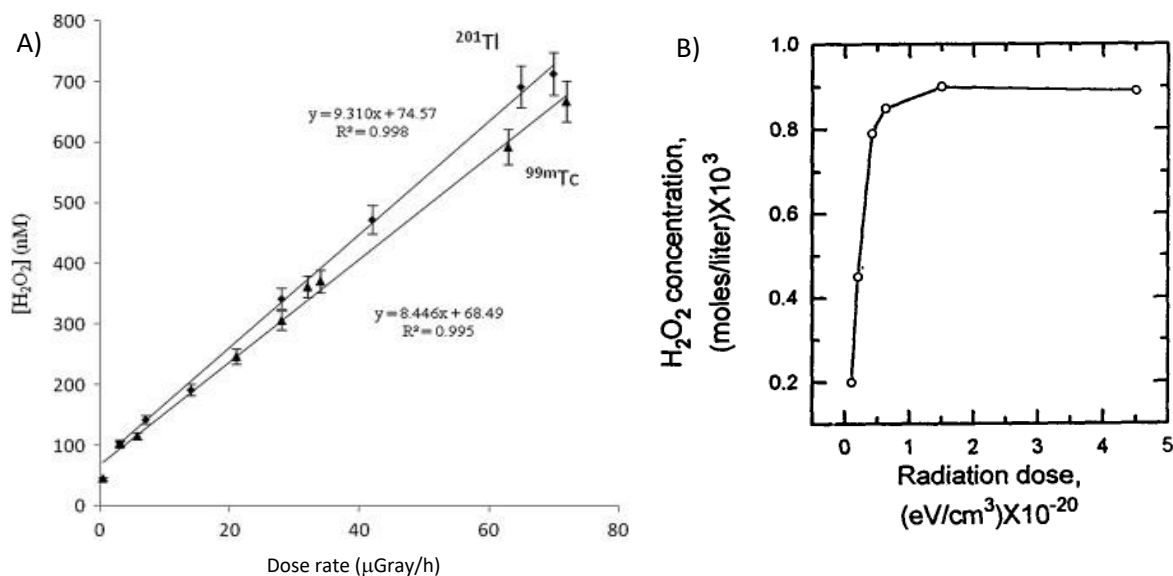
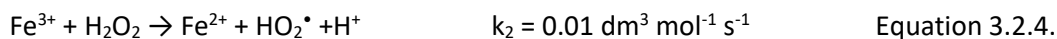
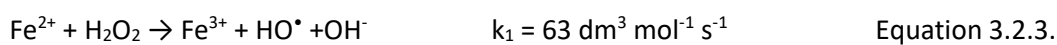


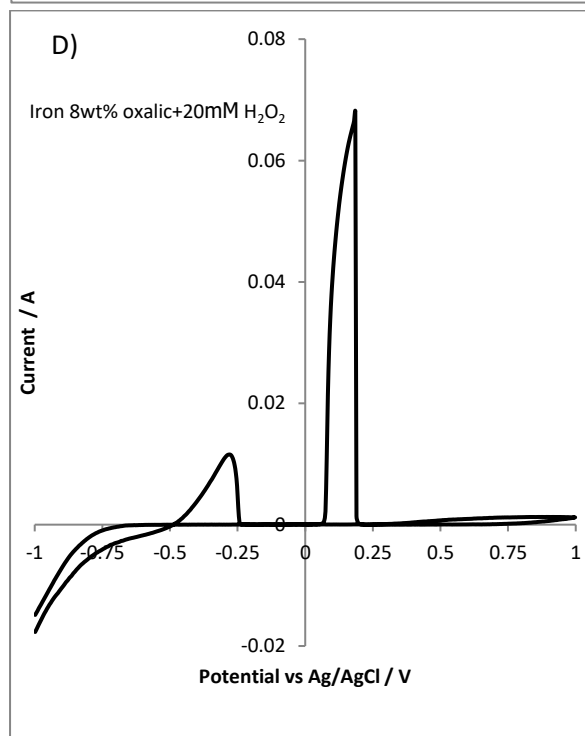
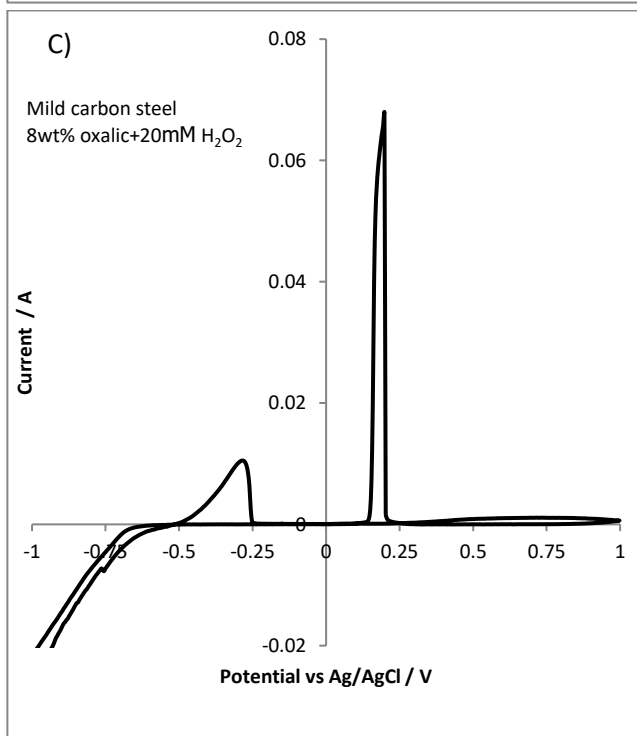
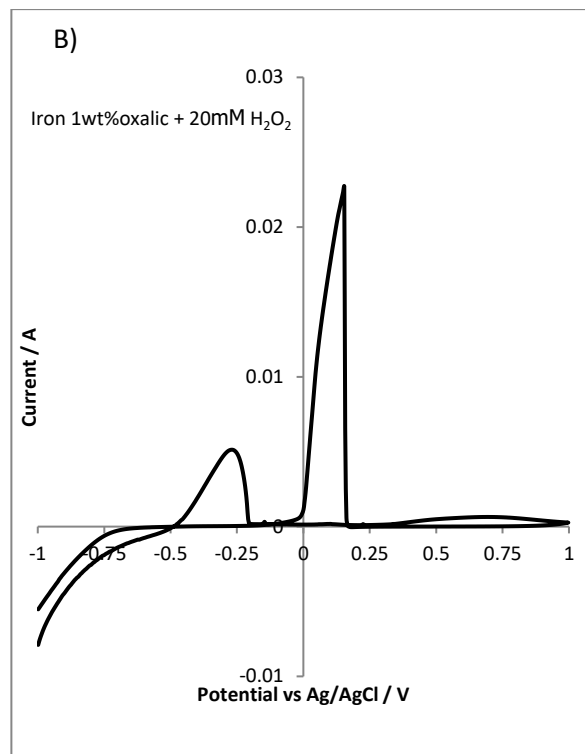
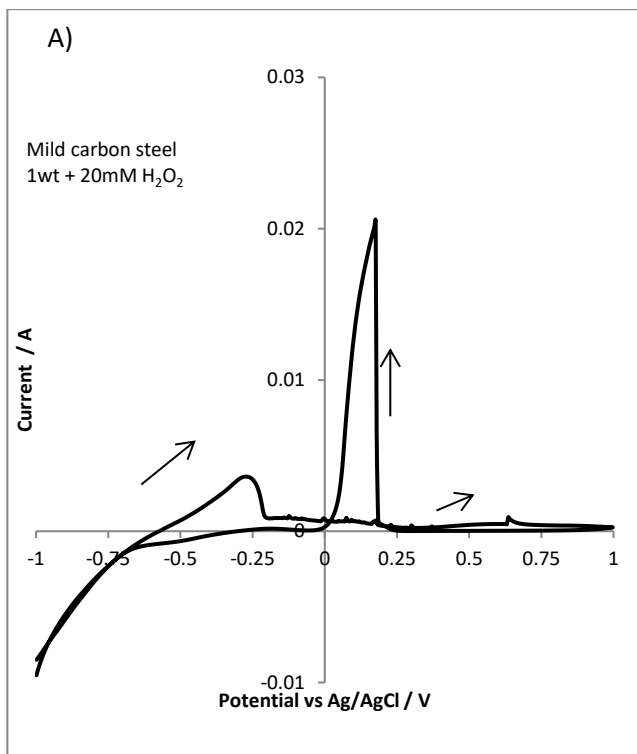
**Figure 3.2.1.:** A) The calibration curve for hydrogen peroxide generated by irradiation. The squares and triangles stand for hydrogen peroxide concentration generated by thallium-201 and technetium-99m respectively adapted from the work of Shourian et.al [84]. B) Accumulation of  $H_2O_2$  during the irradiation of water saturated with oxygen adapted from the work of T. Song et. all [85].

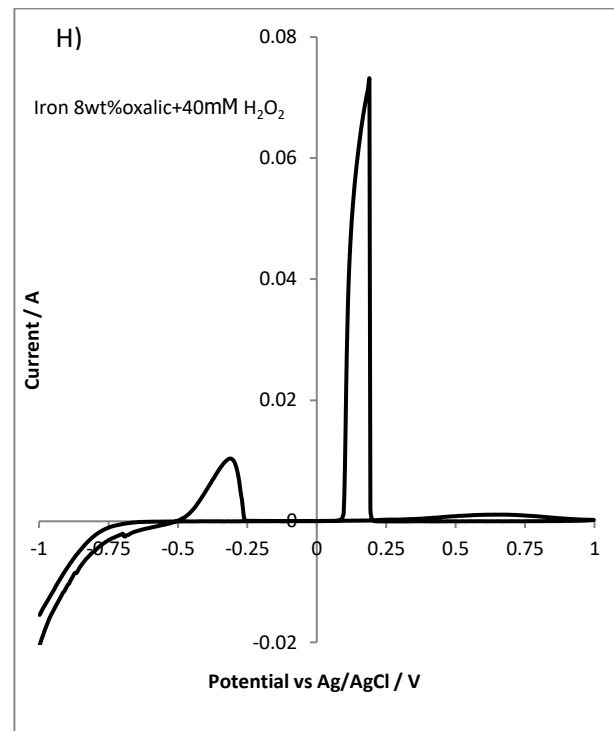
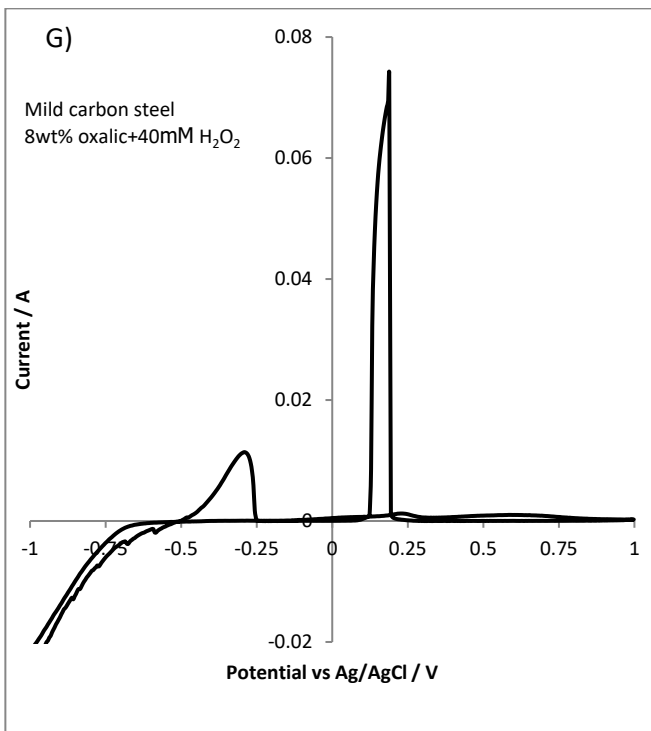
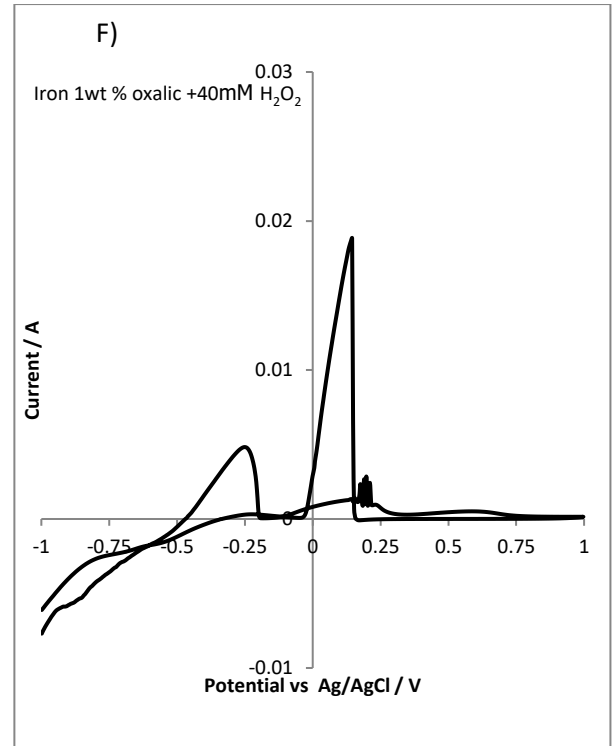
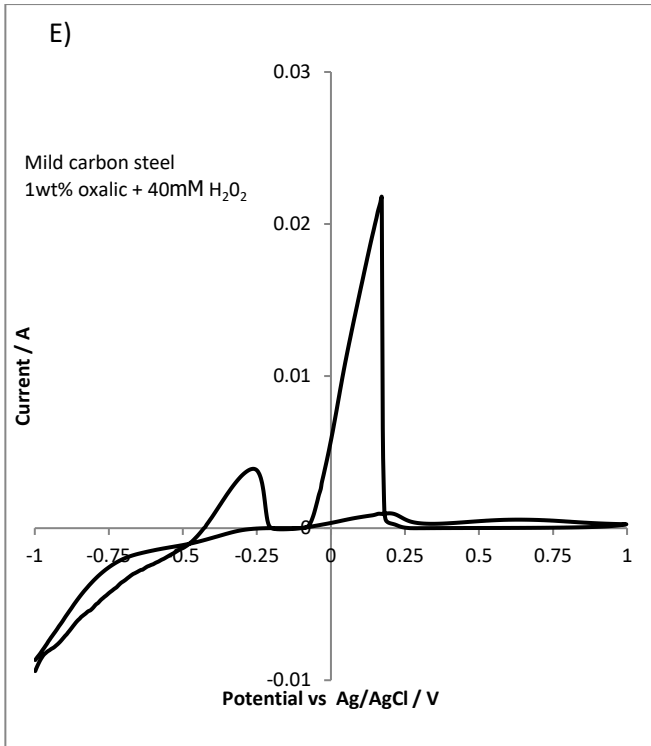
In the presence of  $H_2O_2$ , fast oxidation of  $Fe^{2+}$  to  $Fe^{3+}$  and the converse slow back reaction of  $Fe^{3+}$  to  $Fe^{2+}$  is expected with solution rate constants of  $63 \text{ dm}^3 \text{ mol}^{-1} \text{ s}^{-1}$  and  $0.01 \text{ dm}^3 \text{ mol}^{-1} \text{ s}^{-1}$  respectively, as can be seen in equations 3.2.3 and 3.2.4 [86]. As can be seen in equation 3.2.3,  $Fe^{3+}$  production due to  $Fe^{2+}$  oxidation is four orders of magnitude faster than the  $Fe^{2+}$  production shown in equation 3.2.4 [87]. Therefore in the presence of  $H_2O_2$ , so called Fenton reactions of the type shown in equations 3.2.3 and 3.2.4 will generate  $Fe^{3+}$  species while the  $Fe^{2+}$  concentration will be negligible [88], [89].

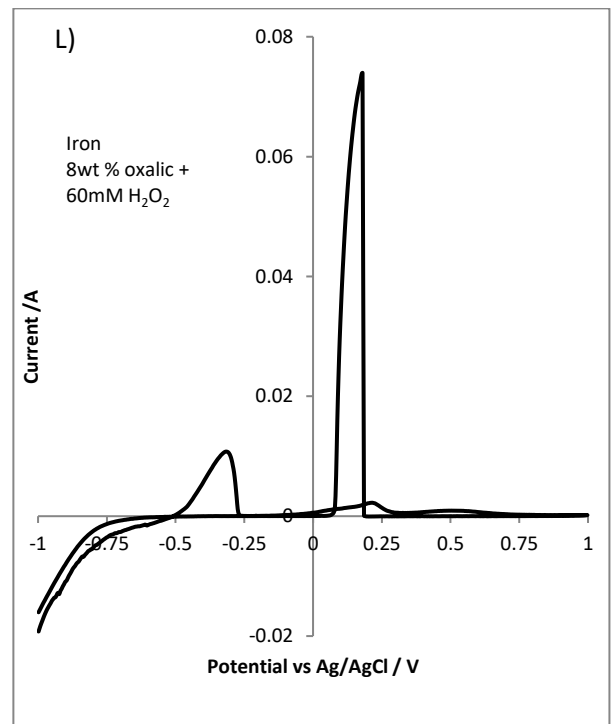
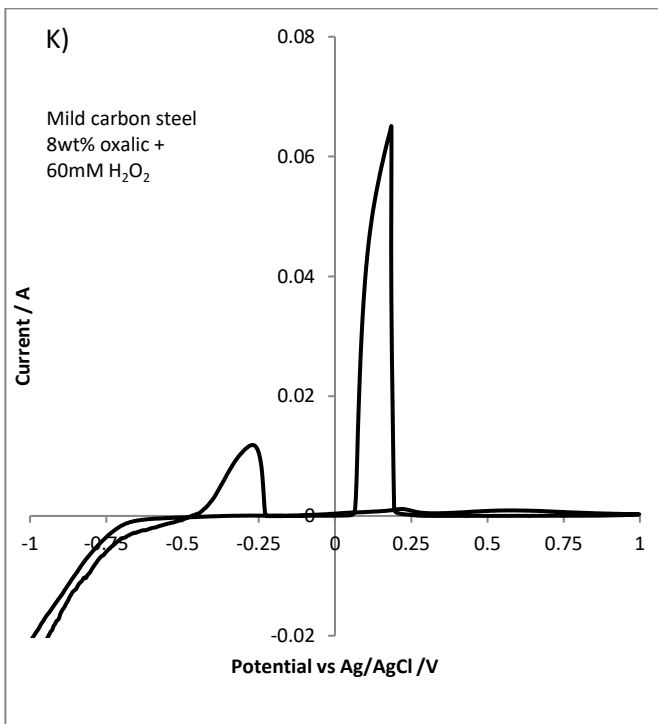
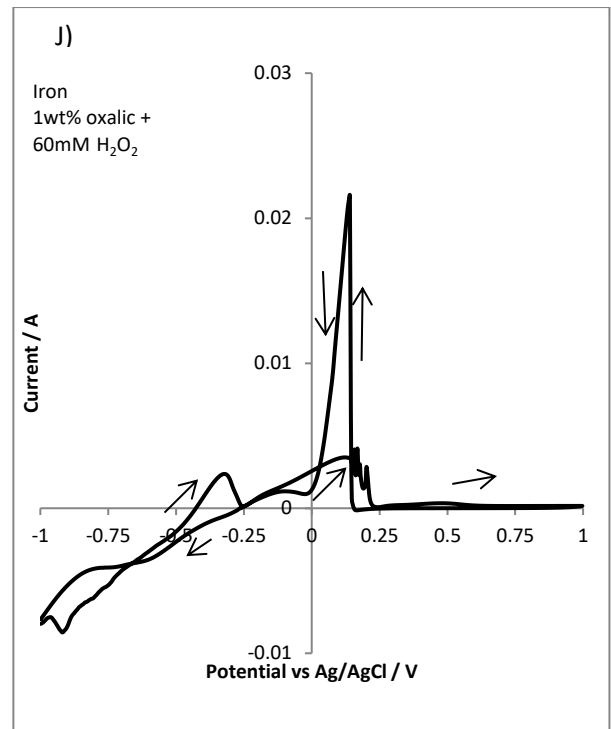
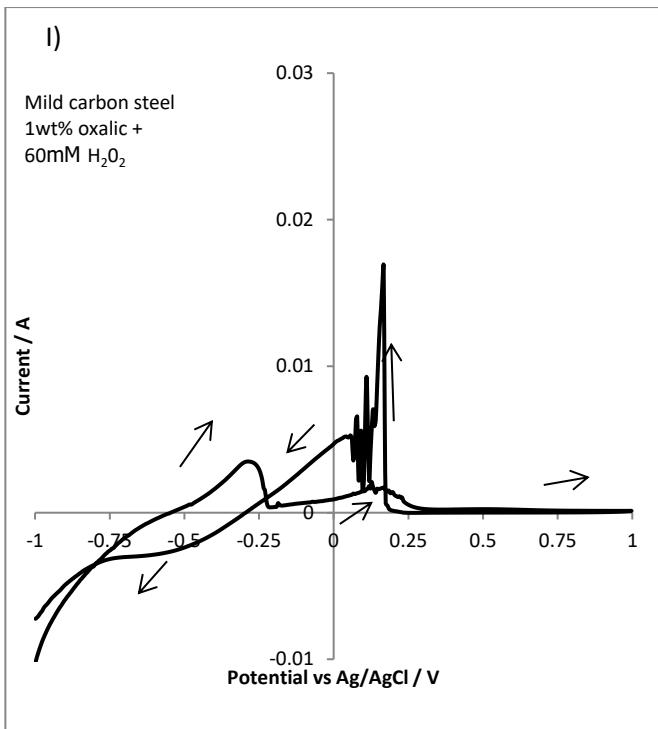


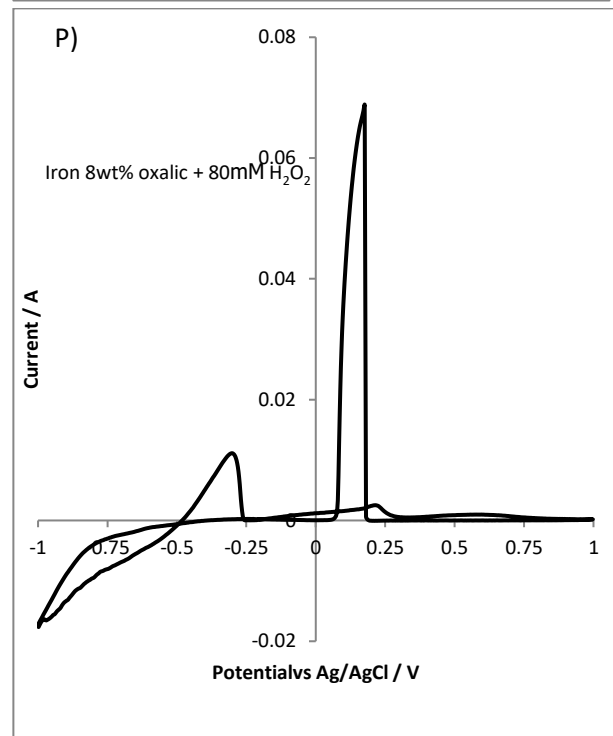
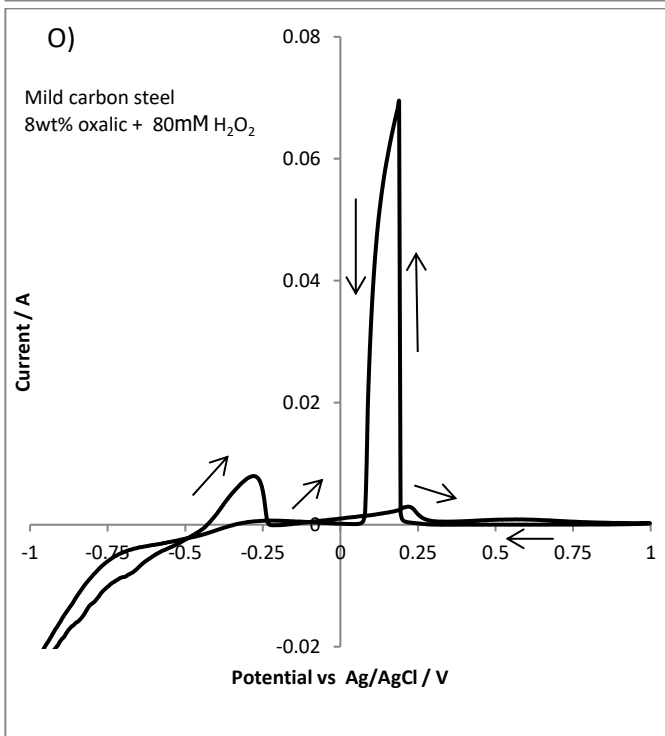
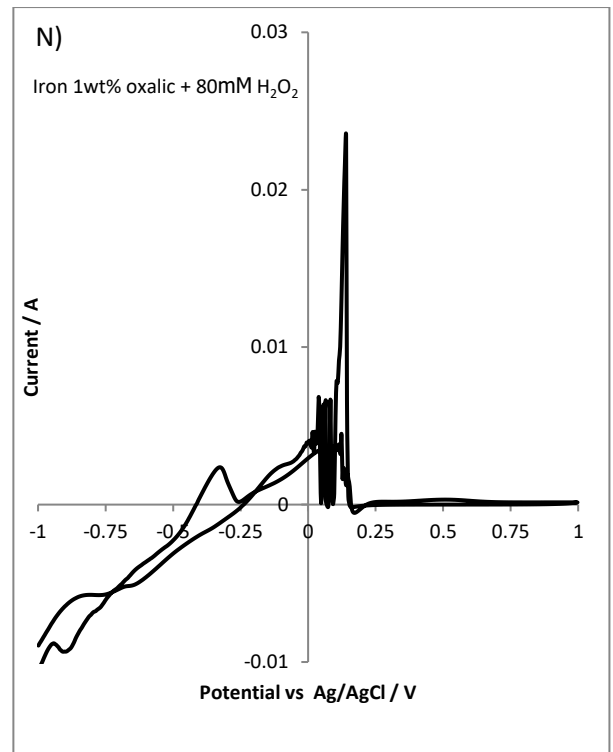
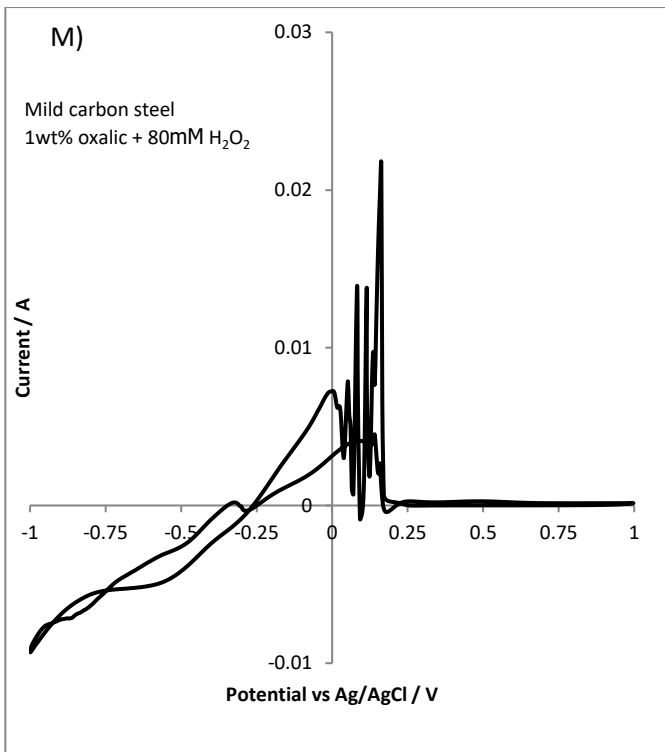
Let us now turn to the electrochemical behaviour of iron and mild carbon steel electrodes in the oxalic acid/hydrogen peroxide system with a view to assessing the utility of iron as a mild carbon steel surrogate in such systems. Solutions comprising 1 or 8 wt% oxalic acid and 20 to 100mM hydrogen peroxide have very low pH values (<0.5). Figure 3.2.2 illustrates the cyclic voltammetric behaviour observed from Fe and mild carbon steel rod electrodes in solutions of 1 and 8 wt% oxalic acid in 20-100mM  $H_2O_2$ . These experiments allow the following observations to be made:

- During the forward going sweep, two oxidation peaks are seen with onsets of -0.5 and -0.25 V.
- During the reverse going sweep, one strong sharp oxidation peak is observed with an onset of +0.2 V and a tail extending to ~-0.25 V.









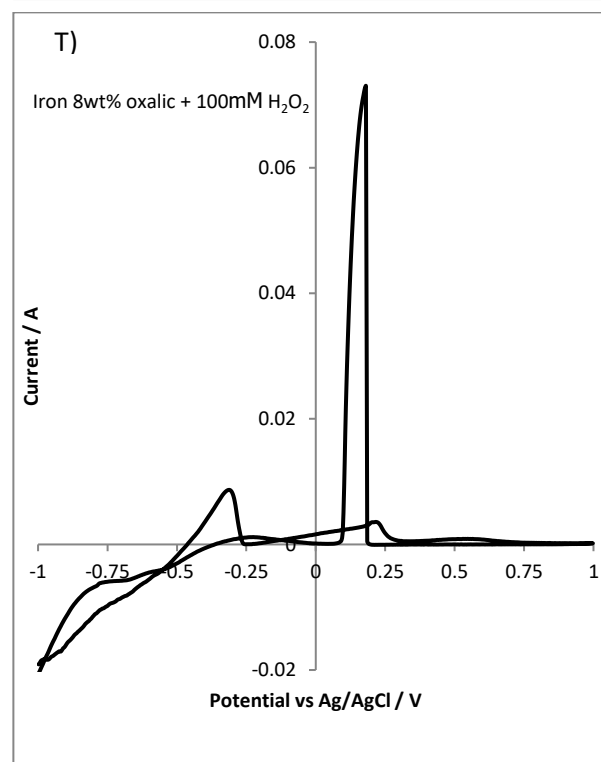
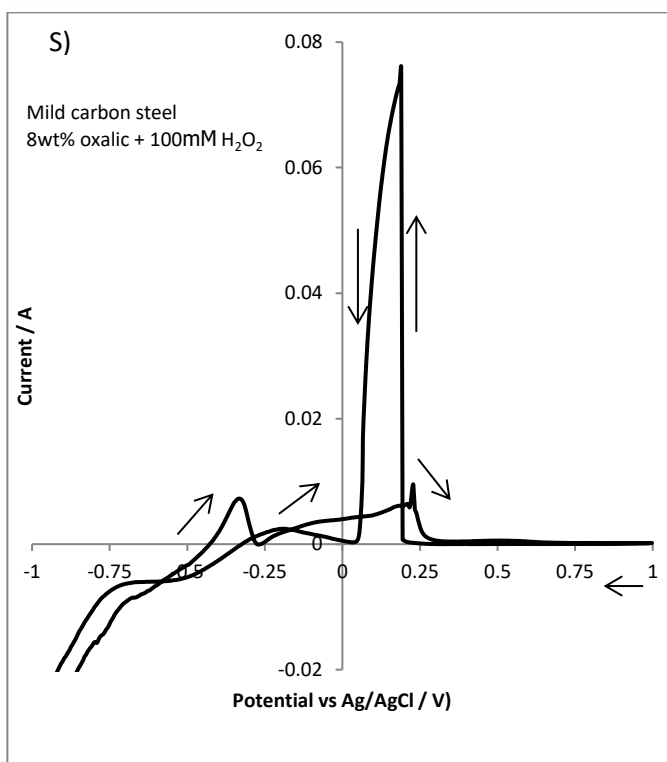
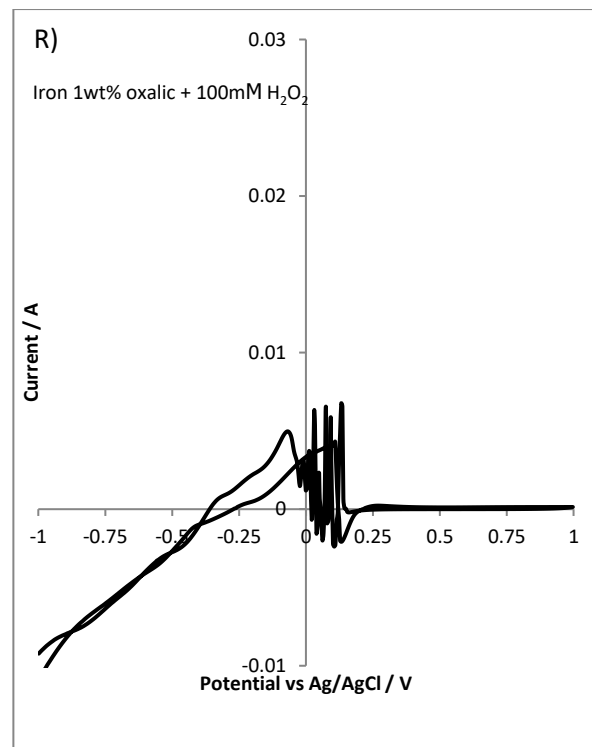
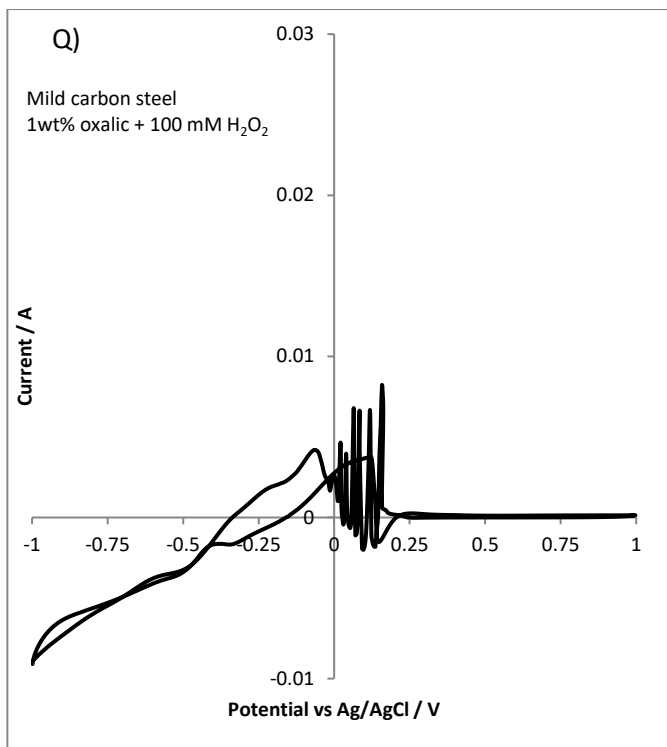


**Figure 3.2.2.:** Comparing cyclic voltammograms of mild carbon steel, (A), (C), (E), (G), (I), (K), (M), (O), (Q), (S) and iron electrodes (B), (D), (F), (H), (J), (L), (N), (P), (R), (T) in 1 and 8 wt % oxalic acid as a function of [H<sub>2</sub>O<sub>2</sub>] from 20 to 100 mM. Scan rate = 0.01V/s.

From Figures 3.2.2 C, D, G, H, K, L, O, P, S and T it can be seen that, for the high oxalic acid concentration of 8 wt%, the cyclic voltammograms recorded in the presence of  $\text{H}_2\text{O}_2$  have much the same form as those recorded in the absence of  $\text{H}_2\text{O}_2$  as shown in Figure 3.1.1. Specifically, two anodic peaks are observed in the forward going sweep with onsets of  $\sim -0.5$  and  $+0.25$  V vs Ag/AgCl, and one sharp anodic peak is observed in the reverse sweep with an onset of  $\sim +0.2$  V. As in Figure 3.1.1, the more positive peak in the forward going sweep is both broader and characterised by substantially smaller currents than either of the other major peaks in the cyclic voltammogram. It is of note that the onset of this peak moves towards more negative potentials with increasing peroxide concentration – specifically from  $+0.25$  V at 20 mM  $\text{H}_2\text{O}_2$  to  $\sim -0.2$  V at 100 mM  $\text{H}_2\text{O}_2$  – indicating that the peroxide is assisting and promoting the process associated with this peak.

The first oxidation peak recorded in the forward going sweep onset =  $-0.5$  V, is similar in form to the first oxidation peak seen in the forward going sweep in the cyclic voltammogram recorded in the absence of hydrogen peroxide shown in Figure 3.1.1, i.e. it is associated with the oxidation of the electrode surface to produce an insoluble passive ferrous oxalate layer. As alluded to above, the second oxidation peak during the forward going sweep, that has an onset of  $-0.25$  V at higher hydrogen peroxide concentrations, is associated with the oxidation of the ferrous oxalate layer due in part to Fenton type reactions as described in reference to equation 3.2.3 and 3.2.4. Due in part to the oxidative boost provided by Fenton type reactions, the ferrous oxalate is oxidised to  $\text{Fe}^{3+}$  at  $\sim -0.2$  V in a manner similar to that which happens at  $+0.25$  V in the absence of hydrogen peroxide, see section 3.1.

During the reverse going sweep the electrochemical behaviour of the electrodes in the presence (Figure 3.2.2) and absence (Figure 3.1.1) of hydrogen peroxide is similar. According to Pourbaix diagram of Figure 3.1.2.B and at a potential of  $\sim 0.2$  V, iron oxides can be reduced to  $\text{Fe}^{2+}$  resulting in the exposure of the underlying electrode material surface to solution resulting a one

strong sharp oxidation peak with an onset of +0.2 V which is associated with the oxidation of iron to ferrous oxalate as described in section 3.1.

To summarize: In 8wt% oxalic acid solution, the main difference between the cyclic voltammetric behaviour of the electrodes in presence and absence of hydrogen peroxide is that in the forward going sweep the second oxidation peak moves towards more negative potentials. This is due to Fenton type reactions, promoting and assisting the transformation of the ferrous oxalate passive layer, produced during the first peak of the forward going sweep, into iron oxide species. Now, let us turn to the behaviour observed in 1 wt% oxalic acid solution.

From a comparison of Figures 3.2.2 A, B, E, F, I, J, M, N, Q and R with Figures 3.2.2 C, D, G, H, K, L, O, P, S and T it can be seen that, for the low oxalic acid concentration of 1 wt%, in presence of  $H_2O_2$  the cyclic voltammograms have much the same forms as those recorded in 8wt%. Specifically, two anodic peaks are observed in the forward going sweep with onsets of  $\sim -0.5$  and  $\sim +0.25$  V vs Ag/AgCl, and one sharp anodic peak is observed in the reverse sweep with an onset of  $\sim +0.2$  V. However, at high hydrogen peroxide concentrations ( $\geq 60$  mM) the sharp anodic peak in the reverse going sweep is followed by a sharply oscillating current feature reminiscent of metastable pit formation on passivated steel surfaces. Whilst this feature is observed for 1wt% oxalic acid it is not seen for 8wt% oxalic acid. The general form of the voltammogram recorded from iron electrodes in 1wt% oxalic acid in the presence of hydrogen peroxide can thus be explained as follows.

For 1wt% oxalic acid in presence of hydrogen peroxide the first oxidation peak with an onset of  $\sim -0.5$  V is associated with the oxidation of the iron metal producing an insoluble ferrous oxalate layer onto the surface. The second oxidation peak with an onset of approximately +0.25 V is associated with the oxidation of the ferrous oxalate layer to iron oxide species. Both of these two oxidation peaks behave in a similar manner as seen for the 8wt% oxalic acid as described above. At the end of the forward going scan it is thus expected that iron oxides and unoxidised ferrous oxalate compounds will be present on the electrode surface. During the reverse scan, and according to the

Pourbaix diagram of Figure 3.1.2B, the iron oxides are reduced back to solution phase  $\text{Fe}^{2+}$  at  $E \lesssim +0.4\text{V}$ , exposing the Fe metal surface beneath which then at  $+0.25\text{V}$  reacts with oxalic acid producing again an insoluble ferrous oxalate layer. However at this point three reactions are taking place;

I. Reaction one: According to the Pourbaix diagram shown in Figure 3.1.2B and as discussed in section 3.1.1 iron oxides at  $E \lesssim +0.4\text{V}$  will be reduced back to solution phase  $\text{Fe}^{2+}$ .

II. Reaction two: Due to the stripping of the iron oxide passivating layer the underlying electrode is exposed to solution, so allowing for iron to be oxidised to  $\text{Fe}^{2+}$  and then, upon encountering solution oxalate, precipitating as Fe(II) oxalate at the electrode surface as described in section 3.1.

III. Reaction three: In the presence of hydrogen peroxide, the precipitation of  $\text{Fe}^{2+}$  as Fe(II)oxalate at the electrode surface is in part interrupted by the oxidation of the  $\text{Fe}^{2+}$  (which has been released via the simultaneous reduction of  $\text{Fe}_2\text{O}_3$  and oxidation of exposed iron as described above) to solution phase  $\text{Fe}^{3+}$ .

For 1wt% oxalic acid solutions, reaction III occurs most readily at high hydrogen peroxide concentrations i.e.  $[\text{H}_2\text{O}_2] \geq 60\text{mM}$ , resulting in the metastable pitting feature seen in Figures 3.2.2 (I), (M) and (Q) for mild carbon steel and Figures 3.2.2 (J), (N) and (R) for iron electrodes. At lower hydrogen peroxide concentrations, the rate of oxidation of solution released  $\text{Fe}^{2+}$  to  $\text{Fe}^{3+}$  is too slow to effectively compete with Fe(II)oxalate precipitation; thus normal passivation of the electrode surface by Fe(II)oxalate is seen at  $E \lesssim 0.2\text{V}$  during the reverse going sweep at  $[\text{H}_2\text{O}_2] \leq 40\text{mM}$ .

However, the question arise as to why this metastable pitting feature, seen at  $[\text{H}_2\text{O}_2] \geq \sim 60\text{mM}$  in 1wt% oxalic acid, is not seen at any of the peroxide concentrations employed in the studies performed in 8wt% oxalic acid solution. The answer is simple: For the high oxalic acid concentration of 8wt% the second reaction is the most pronounced compared to the first and third processes, eliminating the metastable pitting formation (which is observed for 1wt% oxalic acid plus

≥60mM hydrogen peroxide) as can be seen in Figure 3.2.2 (C), (G), (K), (O) and (S) for mild carbon steel and Figures 3.2.2 (D), (H), (L), (P) and (T) for iron electrodes respectively.

The microstructure of the electrode surface plays a key role in the corrosion effect of the surface and generally, according to Jones et.al. pitting preferentially happens at grain boundaries (in the areas between the grains) and discontinuities [90]. Generally, the iron rod surface has a crystalline structure due to the solidification of the metals from the molten phase where crystals grow to form the grains onto the surface. For the QCN resonators, the metal was sputtered onto the quartz crystal resonator resulting in a more homogeneous surface profile. Moreover, QCN resonators (fabricated by sputtering) are flatter and have less discontinuities compared to freshly polished rod electrodes that were used for experiments presented in Figure 3.2.2. Previous paragraphs presented a metastable pitting formation that is more pronounced at low oxalic acid (=1wt%) and high hydrogen peroxide (=100mM) concentrations. If this formation preferentially happens in grain boundaries and discontinuities, then it is expected that the metastable pitting formation will be more pronounced in freshly polished rod electrodes rather than in sputtered iron quartz resonator crystals. Comparing Figure 3.2.2 with Figure 5.2.6 (which is discussed in Chapter 5) shows that the metastable pitting formation can be seen only in freshly polished rod samples and not in iron quartz resonator crystals, indicating that the pitting formations described here happen between the grain boundaries.

As with analogous data recorded in the absence of peroxide, Figure 3.1.1, Figure 3.2.2 shows that mild carbon steel and iron behave in a similar fashion with respect to their electrochemistry in the presence of oxalic acid with hydrogen peroxide - again suggestive of pure iron being a suitable surrogate for low carbon steel under the experimental conditions employed here.

This is further confirmed by the data of Figure 3.2.3 which shows  $E_{oc}$  data from both pure iron and mild carbon steel electrodes, recorded as a function of added peroxide concentration in both 1 and 8wt% oxalic acid. Figure 3.2.3A shows how the  $E_{oc}$  value evolves with time after the addition of each aliquot of peroxide, whilst Figure 3.2.3B shows the equilibrium  $E_{oc}$  obtained after the addition of

successive aliquots of 60 mM, again as a function of  $[H_2O_2]$ . Figure 3.2.3B shows that the  $E_{OC}$  vs  $[H_2O_2]$  plots recorded from the two electrode materials closely track each other at both 1 and 8wt% oxalic acid, again confirming the appropriateness of using Fe as an analogue for mild carbon steels in corrosion studies of this type. As well, as can be seen from Figure 3.2.3.A, both iron and mild carbon steel exhibit unstable  $E_{OC}$  behaviour at  $[H_2O_2] > 180$  mM in 1wt% oxalic acid, behaviour that is typical of metastable pit formation and repassivation [91]. For  $E_{OC}$  readings recorded at these high hydrogen peroxide values, the maximum value of the  $E_{OC}$  recorded in each instance has been used in the compilation of Figure 3.2.3B. The metastable pitting formation can be seen at low oxalic acid concentrations (= 1wt%) titrated with high concentrated hydrogen peroxide (>180mM) and not at high oxalic acid concentrations (8wt%) and that can be explained as follows.

As discussed above, high oxalic acid concentrations (=8wt%) have the ability to insulate the surface producing an insoluble thick ferrous oxalate layer. Moreover, at these high oxalic acid concentration(=8wt%), the oxalate ions can easily re-generate new ferrous oxalate layers after any possible loss of the ferrous oxalate layer due to the oxidation of  $Fe^{2+}$  via equation 3.2.3.

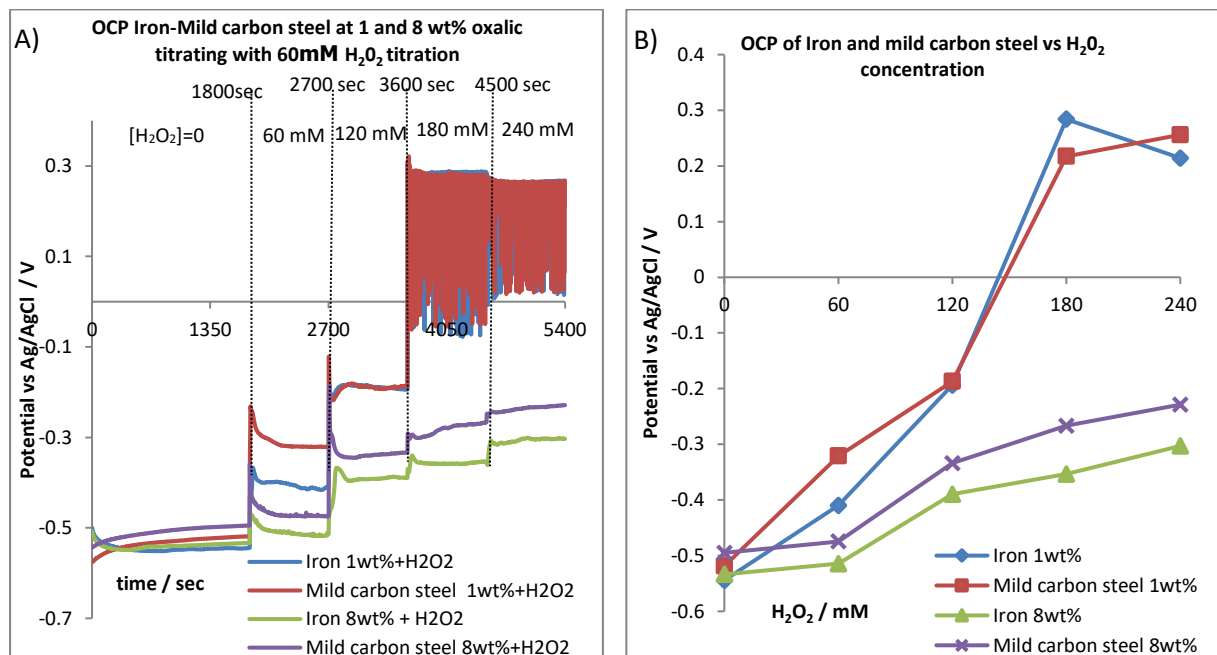


**Figure 3.2.3.:**  $E_{OC}$  measurements for iron and mild carbon steel rod electrodes in 1 and 8 wt% oxalic acid as a function of hydrogen peroxide concentration in the range 0 to 240 mM for titrating 60 mM of hydrogen peroxide periodically after 1800, 2700, 3600 and 4500sec in 1 and 8 wt% oxalic. (A) The relationship between  $E_{OC}$  and the time (B) The relationship between  $E_{OC}$  and  $[H_2O_2]$ .

Low oxalic acid concentrations (=1wt%) mixed with a high hydrogen peroxide concentration (>180mM) will produce an insoluble ferrous oxalate layer but again due to equation 3.2.3, that layer partially oxidises (in a process analogue to pitting) to soluble Fe(III)oxalate leaving the surface partially covered with the pitted layer of Fe(II)oxalate. The released Fe(III) then precipitates as iron oxides within the pits / pores, resulting in a composite Fe(II)oxalate/Fe(III) oxide layer at the surface.

### **3.3. Behaviour of mild carbon steel and iron electrodes in the presence of oxalic acid at high temperature**

This section compares the corrosion behaviour of mild carbon steel and iron electrodes in the presence of oxalic acid at high temperature. This section is focussed on determining whether iron can be used as an analogue for mild carbon steel during the enhanced chemical cleaning process of waste tanks at SRS and at Hanford site at 75°C. The temperature of 75°C was selected for the following two reasons.

The first reason is associated with evidence shown that possibly oxalic acid at temperatures close to 75°C can achieve better cleaning results compared to those at room temperature and the resultant interest in exploring the corrosion behaviour of mild carbon steel samples in the presence of oxalic acid at high temperature [42]. Ketusky et.al report that under specific conditions, including for instance temperature increase and agitation, 1wt% oxalic acid may be more effective compared to 4 or 8 wt% oxalic acid in tank clean out [42]. Moreover, Spires et.al report successful waste tank decontamination campaigns in SRS and Hanford site using oxalic acid as a cleaning agent at 60°C and report that keeping the temperature high and the pH low, the dissolution rates of the solids from the surface of the metal wall of the tank will be increased meeting the waste tank closure requirements as described in section 1.2.4. [43]. Lastly, Wiersma et. al [92] has explored the temperature increase

effect in the carbon steel - oxalic acid system using oxalic acid at 50°C and 75°C, and reports that the ferric ion reduction reaction is dominant at these high temperatures (50°C and 75°C).

The second reason is associated with evidence that suggests that the ambient temperature of the waste tank wall under specific conditions can be 75°C. In more detail, Wiersma reports temperature limits for radioactive waste tanks and presents temperatures of the supernate, salt/sludge and the steel waste tank wall [93]. The temperature of the waste tank wall in a full or empty waste tank can, according to the tank temperature decision tree, vary from 60°C to 122°C [93]. Moreover, the temperature of the waste tank wall in the absence of supernate under specific conditions (nitrate composition of waste to be less than 1M) can be determined to be equal to 75°C [93].

For the above two reasons, we look the opportunity to study the corrosion behaviour of mild carbon steel in high temperature, 75°C, oxalic acid environments and to compare mild carbon steel and pure iron electrochemical behaviour in the presence of oxalic acid at the same temperature. Where appropriate, results at 75°C are compared with results obtained at room temperature as shown in section 3.1.1.

The pH of 1 to 8 wt% oxalic acid at 75°C is approximately 0.5. Figures 3.3.1 A and B show the forward going sweeps of the first scan cyclic voltammograms of iron and mild carbon steel samples in 1 and 8 wt% of oxalic acid at 75°C and comparing these features with those obtained at ambient temperature (Figure 3.1.1), it can be seen that they have several features in common. During the forward going sweep, two oxidation peaks can be observed with onsets of -0.5 V and +0.35 V. These features can be interpreted with the assistance of the simplified  $E_h$ -pH diagrams for iron at  $10^{-6}$  M at 100°C shown in Figures 3.3.2 adapted from the work of Beverskog [94]. Comparing Figure 3.3.2 with Figure 3.1.2 B it can be seen that these simplified  $E_h$ -pH diagrams for iron at room temperature and at 100°C have several features in common, suggesting that much of the interpretation of

voltammogram data developed at room temperature maybe exported to the analogous data recorded at 75°C.

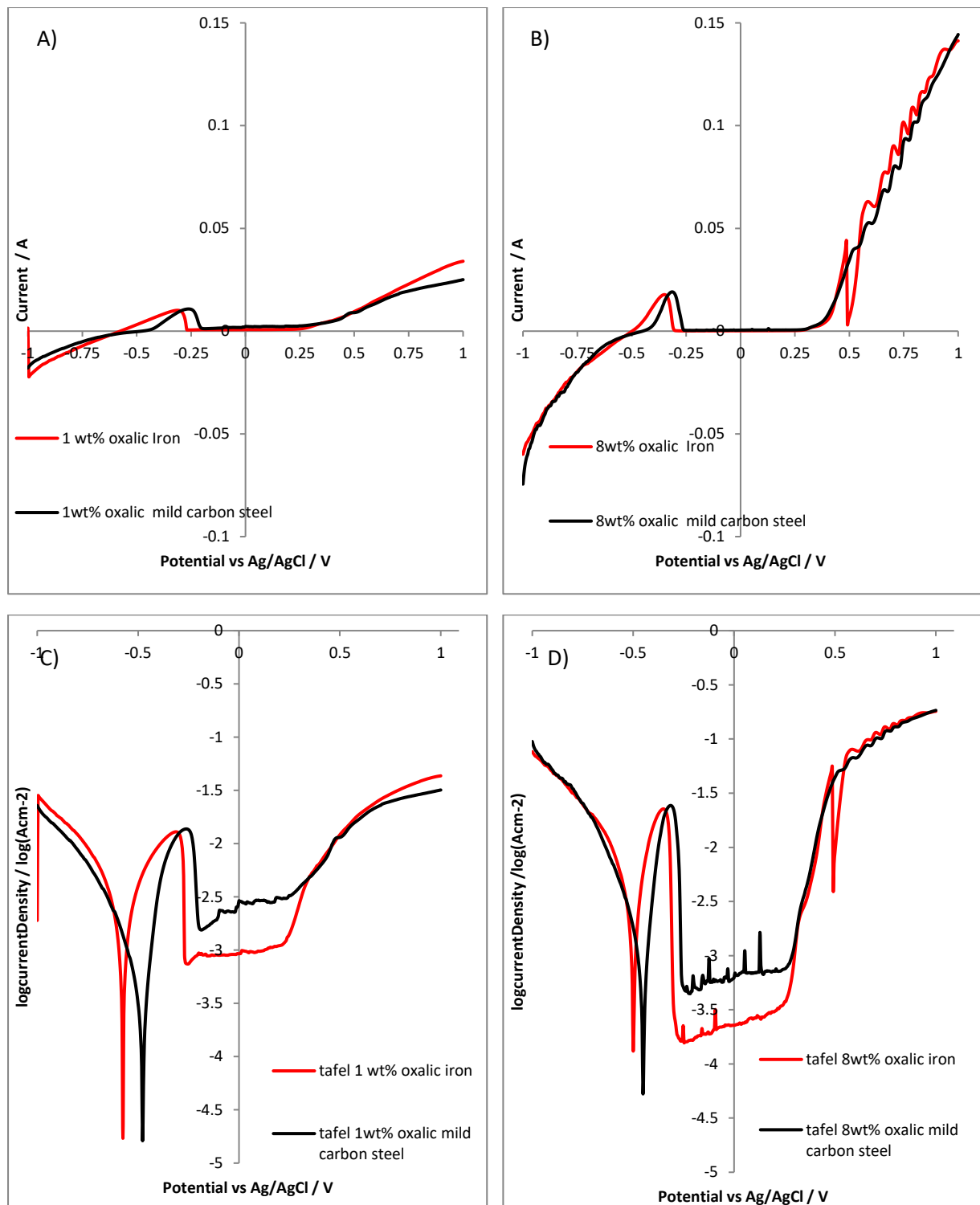


**Figure 3.3.1.:** Forward going sweeps in the first scan cyclic voltammograms, of iron and mild carbon steel rod electrodes at 75°C in (A) 1 and (B) 8 wt% oxalic acid and associated LSVs in (C) 1 and (D) 8 wt% oxalic acid. Scan rate = 0.01V/s.

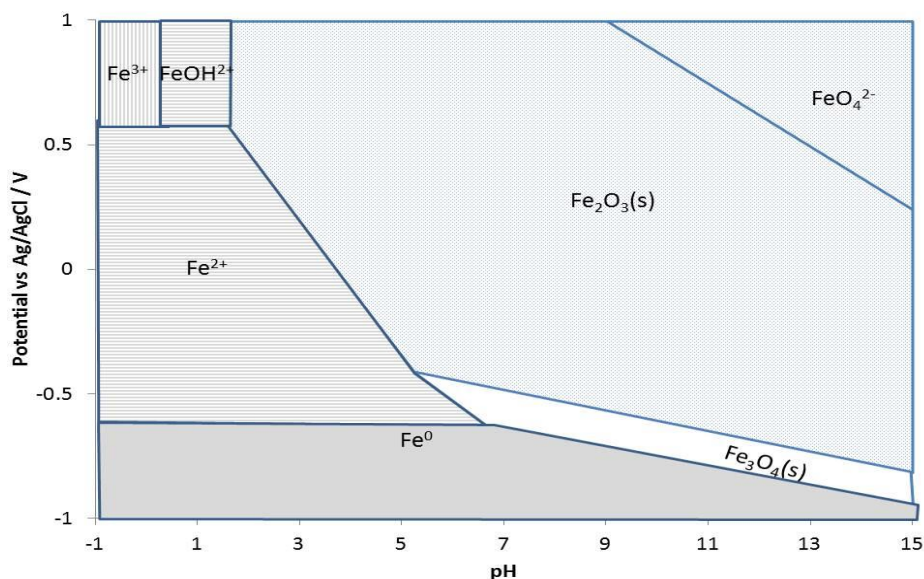


**Figure 3.3.2.:** Simplified  $E_h$ -pH (Pourbaix) diagrams for iron at  $10^{-6}$  M at  $100^{\circ}\text{C}$  adapted from the work of Beverskog [94].

It is commonly known that in many reactions, increasing the temperature will increase the reaction rate. From Figures 3.3.1 and 3.1.1 it can be seen that increasing the temperature increases the peak current as well. Figures 3.3.1A and B show that, as at low temperature, ferrous oxalate produced from the first oxidation peak, onset  $-0.5\text{V}$ , transforms to ferric oxide in a wave with onset of  $+0.35\text{V}$ . The currents associated with the second wave are substantial, rising to  $0.05$  and  $0.15\text{A}$  at  $1\text{V}$  in  $1\text{wt}\%$  and  $8\text{wt}\%$  oxalic acid respectively. These findings can be compared with the room temperature data shown in Figure 3.1.1 where the currents associated with the oxidation of  $\text{Fe}(\text{II})$  to  $\text{Fe}(\text{III})$  are negligible rising to no more than approximately  $0.001\text{A}$  as shown in Figure 3.1.1.A, B, C and D.

Figure 3.3.3 shows a comparison of the open circuit potentials of iron and mild carbon steel samples at different oxalic acid concentrations at  $75^{\circ}\text{C}$ . Comparing the corrosion behaviour of the samples shown in Figures 3.3.1 and 3.3.3 it can be observed that iron samples have broadly similar corrosion behaviour to mild carbon steel samples in oxalic acid environments at high temperature. This would thus allow the use of the less expensive iron-based QCN crystals (compared to high unit

price steel crystals) for the monitoring of corrosion during the application of oxalic acid at these high temperatures. As these crystals will be used destructively, this is an economically significant finding. Consequently, the QCN-based corrosion monitoring studies described in the next chapters focus on iron coated piezoelectrodes as mild steel surrogates.

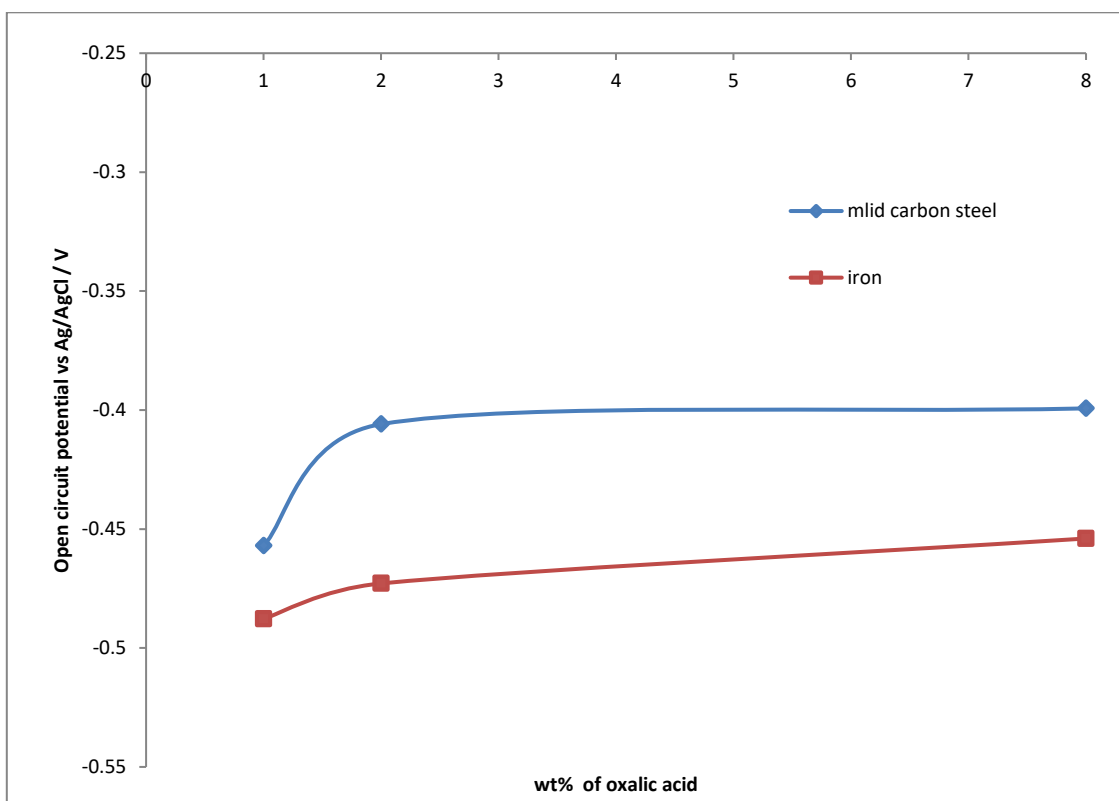


**Figure 3.3.3.:**  $E_{OC}$  measurements for iron and mild carbon steel electrodes as a function of oxalic acid concentration in the range 1 to 8 wt% at 75°C.

### 3.4. Exploration of the electrochemical activity of oxalic acid and oxalic acid / hydrogen peroxide mixtures at high temperatures

This section explores the electrochemical activity of solutions of oxalic acid and oxalic acid / hydrogen peroxide mixtures at 90°C with the intent of characterizing any baseline electrochemical activity of oxalic acid in the solvent system that may interfere with the electrochemistry of the mild carbon steel / iron itself at these temperatures. Low and high concentrations of oxalic acid (=1wt% and =8wt% respectively) were used in presence and absence of extremely high hydrogen peroxide

concentrations (=100mM) as a simulant (as has been discussed in section 2) for the products of the radiolysis of water at very high temperatures. A temperature of 90°C was used so as to maximize the chance of seeing any intrinsic electrochemistry of the oxalic acid solvent system.

It is commonly known that carbon electrode materials react neither with oxalic acid nor with hydrogen peroxide in any chemical sense, and so for this group of experiments carbon has been chosen as an inert working electrode to check if solutions of oxalic acid and oxalic acid / hydrogen peroxide mixtures at 90°C are electrochemically active. The pH of oxalic acid, oxalic acid / hydrogen peroxide mixtures at 90°C is in the range of 0.2 to 1.5. Figures 3.4.1A and B show cyclic voltammograms for a carbon electrode in 1 and 8wt% oxalic acid at 90°C respectively. Results are presented both in the presence and absence of deliberately added hydrogen peroxide.

Figure 3.4.1 illustrates that for 1wt% and 8wt% oxalic acid solutions, the measured current within the solvent window of water, ie from  $\sim -0.2V$  to  $\sim +0.8V$ , is negligible. Hydrogen and oxygen evolution can be seen in the range of  $-1V$  to  $\sim -0.5V$  and  $+0.8V$  to  $+1V$  respectively, consistent with the Pourbaix diagram of water shown in Figure 3.1.2.B. Broadly similar results are seen in the presence of hydrogen peroxide the sole major difference being a reduction wave with a negatively going onset potential of  $\sim -0.2V$ . This is most likely due to the reduction of hydrogen peroxide to water but, due to the small currents associated with this feature,  $\sim 10^{-4} A$ , compared to the  $Fe \rightarrow Fe^{2+}$  oxidate process that occurs in the same potential range on iron,  $\sim 10^{-2} A$ , would not be expected to interfere with the electrochemistry of the Fe system.

Thus, to all intents and purposes, results illustrate that solutions of oxalic acid and oxalic acid / hydrogen peroxide mixtures at 90°C are electrochemically silent compared to the intrinsic electrochemistry of iron, thus the current peaks shown in the cyclic voltammograms under oxalic acid solutions presented in section 3.1 and under oxalic acid / hydrogen peroxide mixtures presented in section 3.2 in the presence of iron or mild carbon steel working electrode are associated with electron transaction of the solution phase with iron species produced from the iron

or mild carbon steel surface (used as working electrode) as presented in section 3.1 and 3.2 respectively.

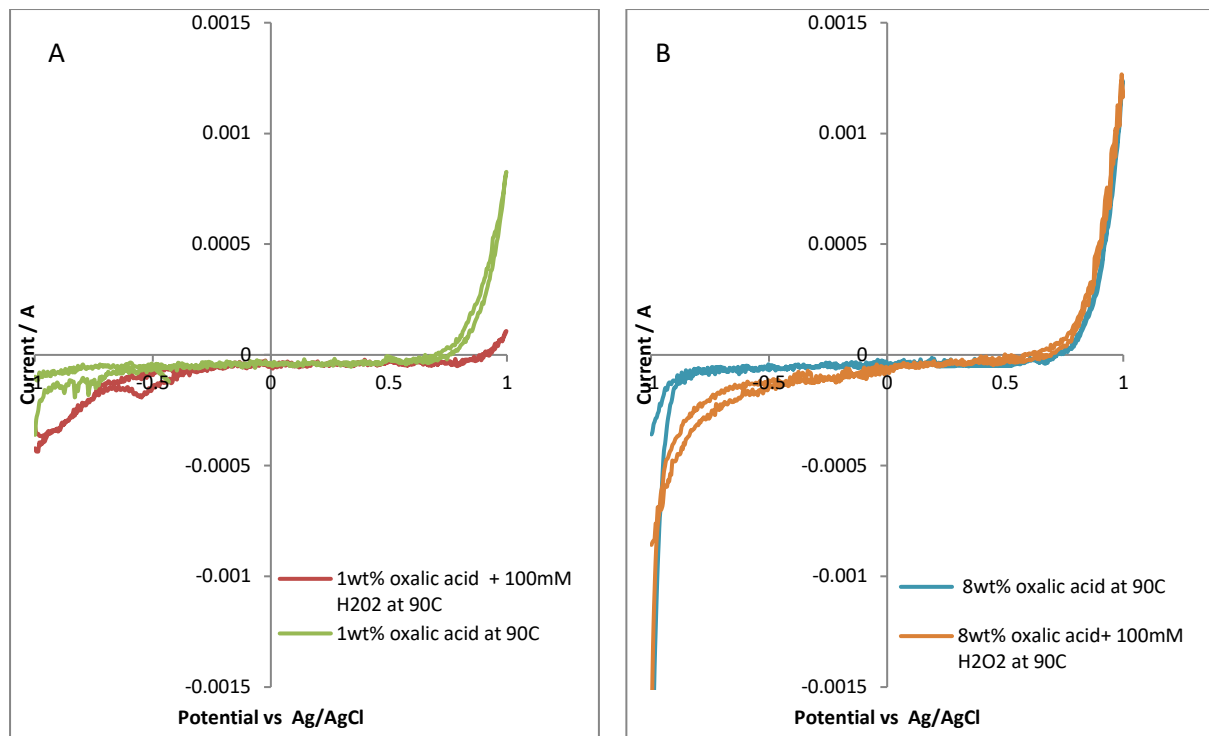


**Figure 3.4.1:** Cyclic voltammograms of carbon electrode in (A) 1wt % oxalic acid, pH=1.3 and (B) in 8wt% oxalic acid, pH=0.85. Scan rate = 0.01V/s.

### 3.5 Summary

In this chapter the electrochemical behaviour of iron and mild steel samples have been studied and compared for different non-radioactive and simulated radioactive environments at room and at high temperatures. This work reveals that iron samples can be used as a surrogate to mild steel samples. The open circuit potential was measured and found to be approximately -0.5 V, at which point iron species react with oxalic acid producing an insoluble ferrous oxalate layer. In simulated radioactive environments, insoluble ferrous oxalate can be oxidized to soluble ferric oxalate by the radiolysis simulant H<sub>2</sub>O<sub>2</sub>. Again, this behaviour is seen on both iron and mild carbon steel electrodes, again supporting use of iron as a mild carbon steel surrogate. The oxidation of the

protective iron oxalate layer to  $\text{Fe}^{3+}$  can result in the observation of pitting current features at 1wt% oxalic acid. However, these are lost at high 8wt% oxalic acid concentration where the higher oxalate concentration regenerates the passivating ferrous oxalate layer faster than the hydrogen peroxide can attack it. Again, this behaviour is seen on both iron and mild carbon steel electrodes.

The above experiments were all conducted at room temperature. Thus, the behaviour of iron and mild carbon steel electrodes was also compared at the high temperatures expected to arise in high level waste storage tanks due for instance to liquor self-heating.

Again, similar electrochemical behaviour can be seen at high temperatures for mild carbon steel and iron samples.

Lastly, solutions of oxalic acid and oxalic acid / hydrogen peroxide mixtures at high temperatures are electrochemically silent and possibly can be assumed that oxalic acid and oxalic acid / hydrogen peroxide mixtures are electrochemically silent and at room temperatures.

## Chapter 4

## 4. Optical Microscope (OM) imaging and Raman studies

Last chapter we compared the cyclic voltammetric behaviour of iron and mild carbon steel samples in oxalic acid environments and established that the former is a suitable surrogate for the latter in the context of the electrochemical corrosion studies to be reported in this thesis. Also, based on literature reports, we formulated postulates as to the species formed on the metal surfaces at key stages throughout the voltammogram. This chapter will be presenting Optical Microscope (OM) and Raman spectroscopy data in order seeking to confirm the applicability of the surface reaction scheme developed by Camalet et al. and invoked last chapter (Figure 3.1.4) to the systems under study here and to verify the species formed.

Prior moving on to the results and discussions section of this chapter, it is essential to introduce Figure 4.1 and 4.2 which are associated with the Raman spectra of iron oxalate and iron particles, which are based only in literature and will be referred in this chapter. [95], [96], [97], [98].

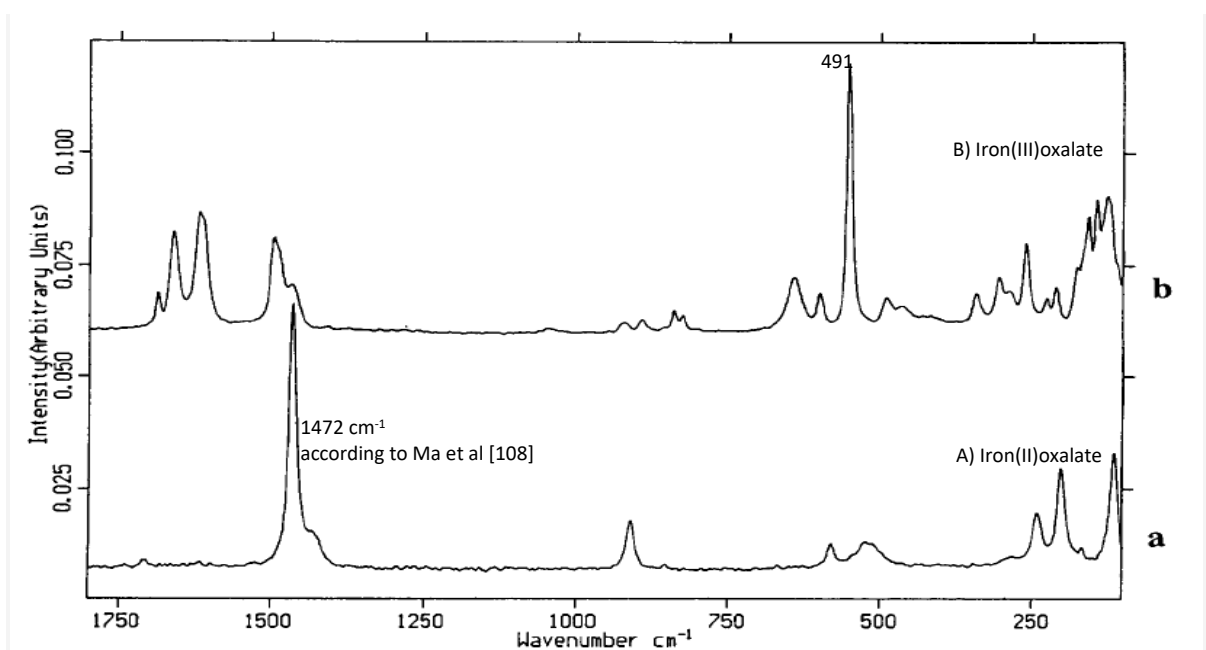
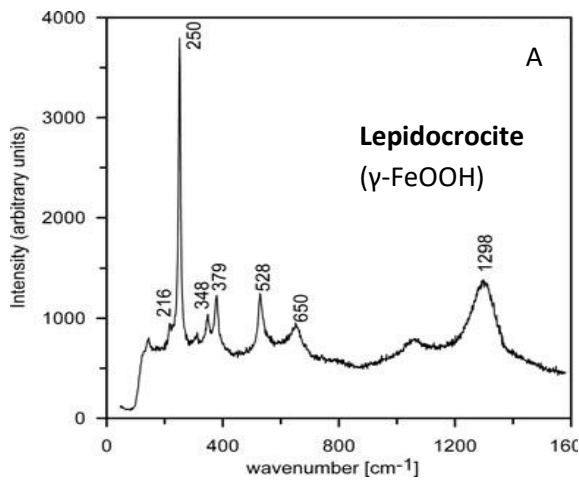
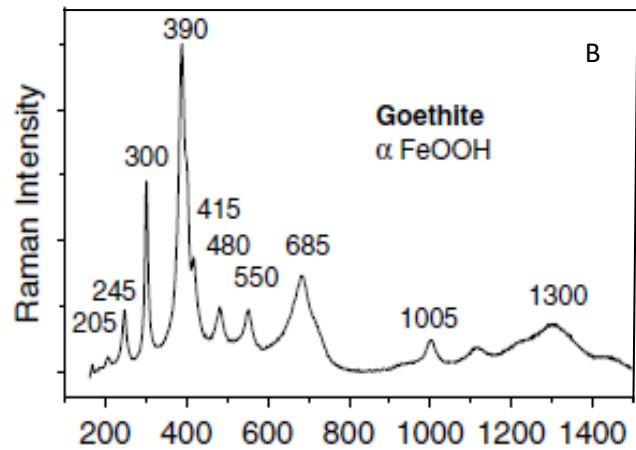


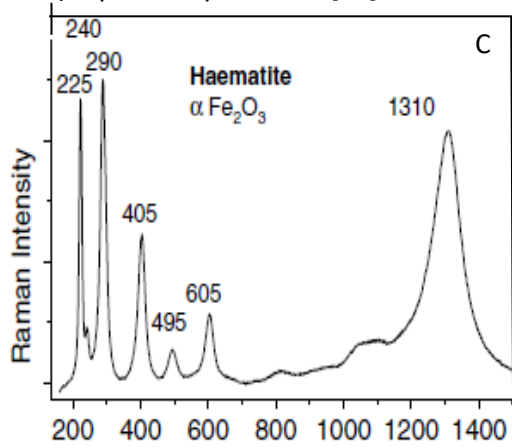
**Figure 4.1.:** Raman spectra of A) iron(II)oxalate and B) iron(III) oxalate adapted from the work of Edwards et al.[95].



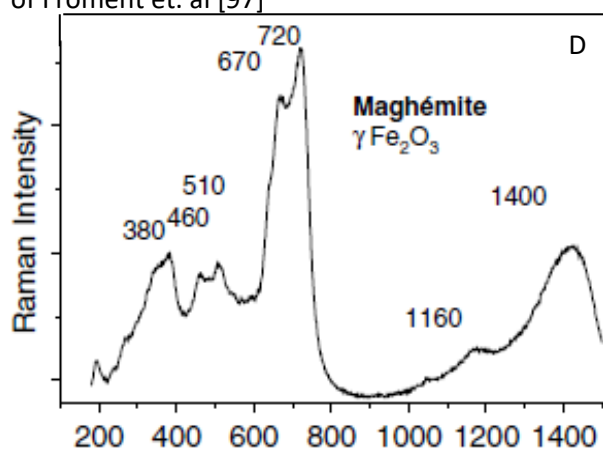
Raman spectra of synthetic lepidocrocite ( $\gamma$ -FeOOH) reported by Hanesch [96]



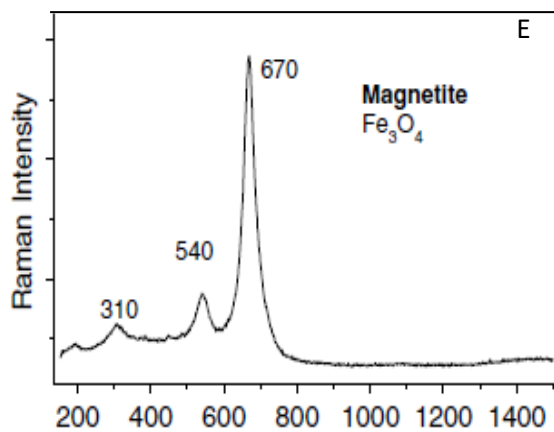
Raman spectra of  $\alpha$ -FeOOH adapted from the work of Froment et. al [97]



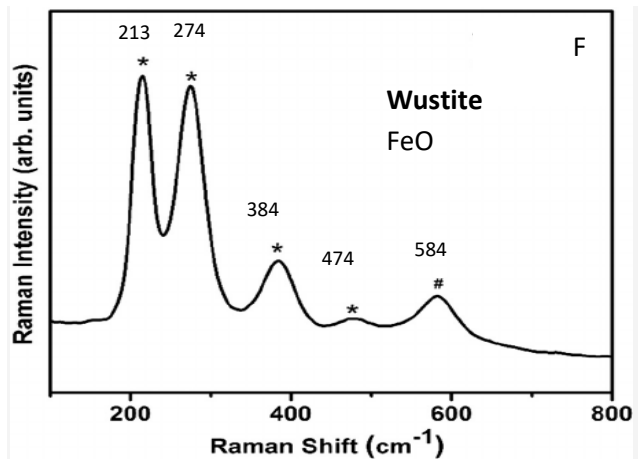
Raman spectra of a  $\text{Fe}_2\text{O}_3$  adapted from the work of Froment et. al [97]



Raman spectra of  $\gamma\text{Fe}_2\text{O}_3$  adapted from the work of Froment et. al [97]



Raman spectra of  $\text{Fe}_3\text{O}_4$  adapted from the work of Froment et. al [97]



Raman spectra of iron oxide ( $\text{FeO}$ ) adapted from the work of Mitchell et.al. [98]

**Figure 4.2.:** Raman spectra of iron particles.

## 4.1. Optical Microscope (OM) imaging and Raman studies of the iron rod surface immersed in 8wt% oxalic acid

As discussed in the previous chapter, it is expected that during the first oxidation peak of the forward scan of Figure 3.1.1 iron reacts with oxalic acid and the surface passivates due to the formation of ferrous oxalate layer; at higher potentials the layer breaks down and mainly ferric oxides can be found onto the surface.

In the first instance, we shall discuss the OM data and it is helpful to do that in the context of voltammetry of the type presented in Figure 3.1.1. As well it is especially helpful to discuss it in the context of a simultaneously recorded cyclic voltammogram that allows for the recording of the electrode mass changes during the observed electrochemistry of the voltammogram. Figure 4.1.1 shows such a combined voltammogram / voltammogram for an iron piezoelectrode being cycled in an 8 wt% oxalic acid solution. This is interpreted in detail later in the next chapter; however, for the convenience of the reader its key features are reported here and may be summarised as follows.

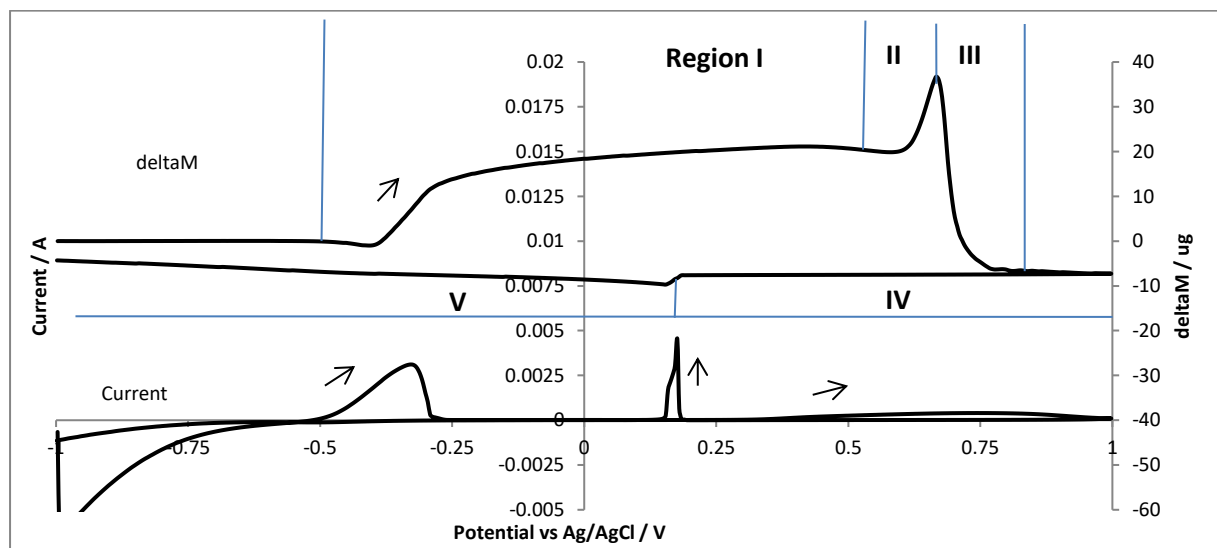


**Figure 4.1.1.:** Voltammogram / voltammogram for an iron piezoelectrode in 8 wt% oxalic acid cycled from -1 to 1V.

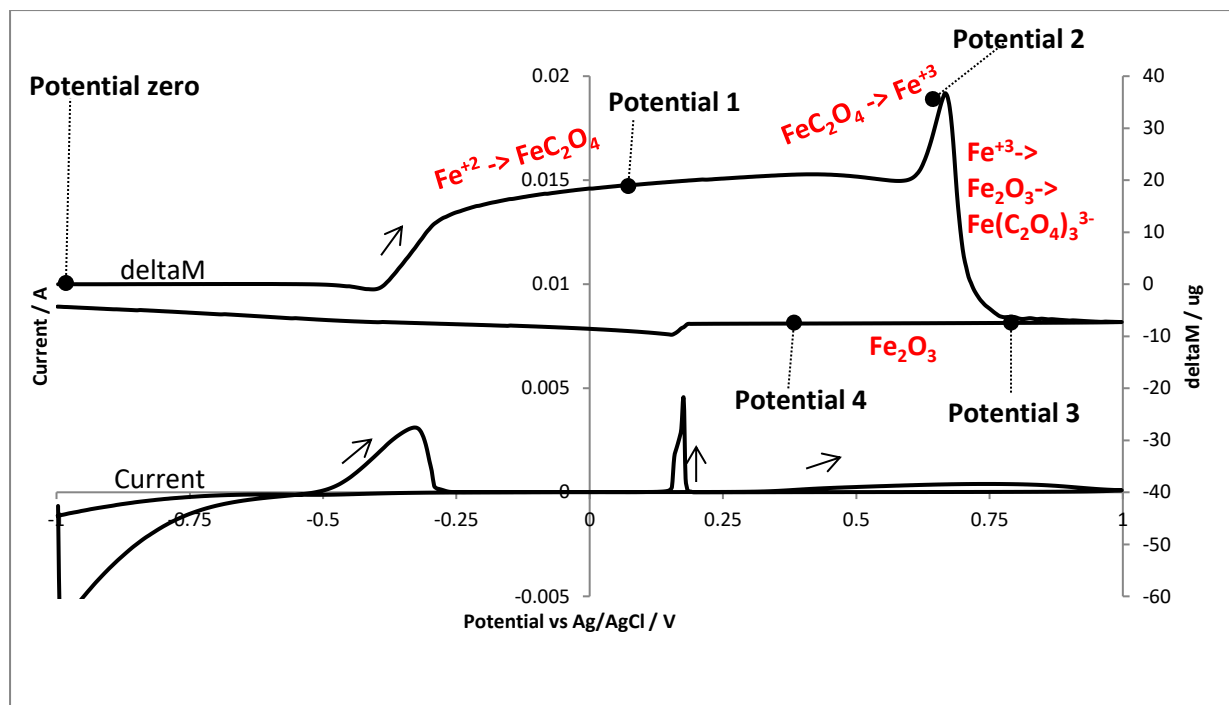
In summary: as the applied potential is increased over the range -1 to +1V, iron(II) generated at the electrode surface at  $\sim -0.5$  V reacts with solution oxalate to form an insoluble passivating Fe(II)oxalate layer and a mass gain associated with the formation of the Fe(II)oxalate layer is observed in the region of the voltammogram denoted as region I in Figure 4.1.1. This persists until about +0.5 V whereupon Fe (II) oxalate is, according to Camalet et. al [74], oxidized to Fe(III)oxalate, a process that continues until  $\sim +0.65$  V, region II. Fe(III)oxalate is known to be more soluble than Fe(II)oxalate and passes into solution as the  $\text{Fe}(\text{C}_2\text{O}_4)_3^{3-}$  complex. The voltammogram of Figure 4.1.1 indicates that this oxidation of ferrous oxalate to ferric oxalate is accompanied by a mass increase suggesting that, within region II at least, some Fe(III)oxalate is retained at the iron surface, most likely under a layer of un oxidized Fe(II)oxalate. However, it can be expected that, once growth of the Fe(III)oxalate within/under the Fe(II)oxalate layer reaches the Fe(II)oxalate layer/electrolyte interface, the soluble Fe(III)oxalate may then dissolve into solution in a process analogous to pitting, resulting in a mass loss. This expectation is confirmed by the mass loss that is subsequently observed in the potential range  $\sim +0.65\text{V}$  to  $\sim +0.75\text{V}$ , region III of Figure 4.1.1. Consistent with our earlier interpretation of these results, the iron surfaces exposed at the base of the pits formed by Fe(II)oxalate dissolution then oxidize to form  $\text{Fe}_2\text{O}_3$ . That the forward-going voltammogram trace at +1V returns to an overall electrode mass very similar to that recorded at the start of the forward going scan at -1V suggests that most, if not all, of the iron oxalate has dissolved into solution, leaving a surface that is predominantly composed of iron oxides/oxyhydroxides. Camalet et. al [74] suggest that the surface has significant iron oxalate character; however, these voltammogram results suggest otherwise. We shall return to that point below in our discussion on the OM/Raman data.

During the reverse scan, this (potentially composite ferrous oxalate/)iron oxide surface then maintains unchanged with near zero accompanied mass change until +0.3V, region IV. At +0.3V, region V, a small mass loss can be observed, consistent with an earlier suggestion that the anode current seen in its reverse scan at this potential is due to the reductive stripping of Iron (III) oxides,

forming  $\text{Fe}^{2+}$  in solution and exposing the Fe underneath. The released Fe(II) then rapidly reacts with the 8wt% oxalic acid solution in generating a thin layer of passivating ferrous oxalate at the electrode surface. The data of Figure 4.1.1 was recorded on an iron piezoelectrode.

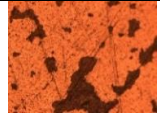
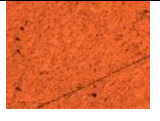
Now, let us turn to optical microscopy images recorded using an InVia Raman Microscope and taken at a series of key potentials throughout cyclic voltammogram and performed on the iron rod. Five potentials, including a starting point (freshly polished iron rod) were selected as can be seen in Figure 4.1.2. The optical microscopy images taken at series key potentials with 20 times magnification can be seen in Table 4.1.1.

Comparison of the potentials where microscope images were taken on the cyclic voltammogram of the iron rod shown in Figure 4.1.2 and Table 4.1.1 with the corresponding potentials on the iron piezoelectrode of Figure 4.1.1 allows for the following correlations to be determined.



**Figure 4.1.2.:** Cyclic Voltammograms of iron crystal in 8 wt% oxalic acid scanned from -1 to 1V.

**Table 4.1.1.:** Optical microscopy (OM) images taken at a series of key potentials throughout cyclic voltammogram of iron rod in 8wt% oxalic acid.

OM images 20 times magnification						
Surface scanned from	-	-1V to ~+0.1V	-1V to ~+0.67V	Sample 1 -1V to ~+0.85V	Sample 2	-1V to +1V and from +1V to ~ +0.3V
Potential	Zero clean iron	1	2	3		4

From -1 to +1V the first image from the iron rod was taken at potential zero, corresponding to unperturbed, unoxidised iron. The next image was recorded at potential during the passivation of the surface by ferrous oxalate (potential 1); the third image of the rod was recorded where there is a peak associated with a mass gain of the iron crystal in the corresponding voltammogram, postulated to be due to Fe(III)oxalate formation (potential 2); the fourth image of the rod was taken during the dramatic mass loss of the crystal at ~+0.85V postulated to be due to iron oxalate dissolution to solution (potential 3). A final OM image of the rod was recorded during the reverse scan before the peak current at about ~+0.4V (potential 4) immediately before the mass loss due to iron oxide stripping at +0.3V seen in the voltammogram.

The optical microscopy image presented in Table 4.1.1 at potential zero reveals that the homogeneous surface is composed of a single compound. As discussed above with respect to the voltammogram of Figure 4.1.1 for the potential zero the iron rod was polished before performing imaging and it is therefore expected that the surface is simply comprised predominantly of unperturbed iron or iron that has been part oxidised to iron oxides/oxyhydroxides by air.

At potential 1, as described in section 3.1, the iron rod surface is oxidised and reacts with oxalic acid producing an insoluble ferrous oxalate layer onto the electrode surface. The microscopy image presented in Table 4.1.1 at potential 1 reveals that the homogeneous surface is composed of a single compound - again most likely iron(II)oxalate based on the above.

At potentials 2 and 3 the optical microscopy images reveal a heterogeneous surface suggesting that it is now comprised of at least two components. These observations are consistent with the work of Camalet et. al [74] who suggests that at  $E > 0.5V$  (potential 2) the layer partially oxidises (in a process analogous to pitting) to soluble Fe(III)oxalate that eventually leaves the surface. The surface as imaged at potentials 2 and 3 is thus most likely partially covered with the pitted layer of remaining Fe(II)oxalate. The released Fe(III) then (potential 3) precipitates as  $Fe_2O_3$  within the pits / pores, resulting in a composite Fe(II)oxalate/Fe(III) oxide layer at the surface- again see Figure 3.1.4.

At potential 4 optical microscopy images indicate that at 8wt% oxalic acid solution the surface is homogeneous and is composed of a single compound. Again, this is consistent with the above explanation developed from the work of Camalet et. al [74] and our voltammogram data of Figure 4.1.1 i.e. that the surface is now predominantly iron oxide/oxyhydroxide in nature with any remaining iron oxalate forming only a minority component.

Prior moving on to present the Raman spectroscopy experiments performed using an InVia Raman Microscope with a 785 nm laser (Renishaw PLC, Wotton-Under-Edge, Gloucestershire, UK) on the iron electrode, it is helpful to discuss concerns about the settings used on the laser power of the Raman.

For Raman spectroscopy experiments, it is possible, even at very low laser power, to induce iron phase transformations and to convert iron (oxy)hydroxides (FeOOH species such as goethite ( $\alpha$ -FeOOH), lepidocrocite ( $\gamma$ -FeOOH) etc) to haematite ( $\alpha$ - $Fe_2O_3$ ) [96]. However, the use of extremely low laser power presents signal-to-noise challenges in the identification of compounds on the surface. These issues could lead to erroneous voltammetric peak assignments in the coupled electrochemical-Raman studies. Thus, a series of experiments were conducted to understand the extent of these transformations in the Raman spectrometer used here. Magnetite powders ( $Fe_3O_4$ , 98% pure, Sigma-Aldrich Ltd) were used because it is especially vulnerable to laser power induced

transformation to other Fe/O phases. The laser of the Raman instrument was then played over these powders so as to identify spectrometer settings where  $\text{Fe}_3\text{O}_4$  can be identified and where the laser power does not change the nature of the surface. Raman spectrum of magnetite can be seen in Figure 4.2E reported by Froment et. al [97]. The dominant band at  $670\text{cm}^{-1}$  identifies the magnetite [97].

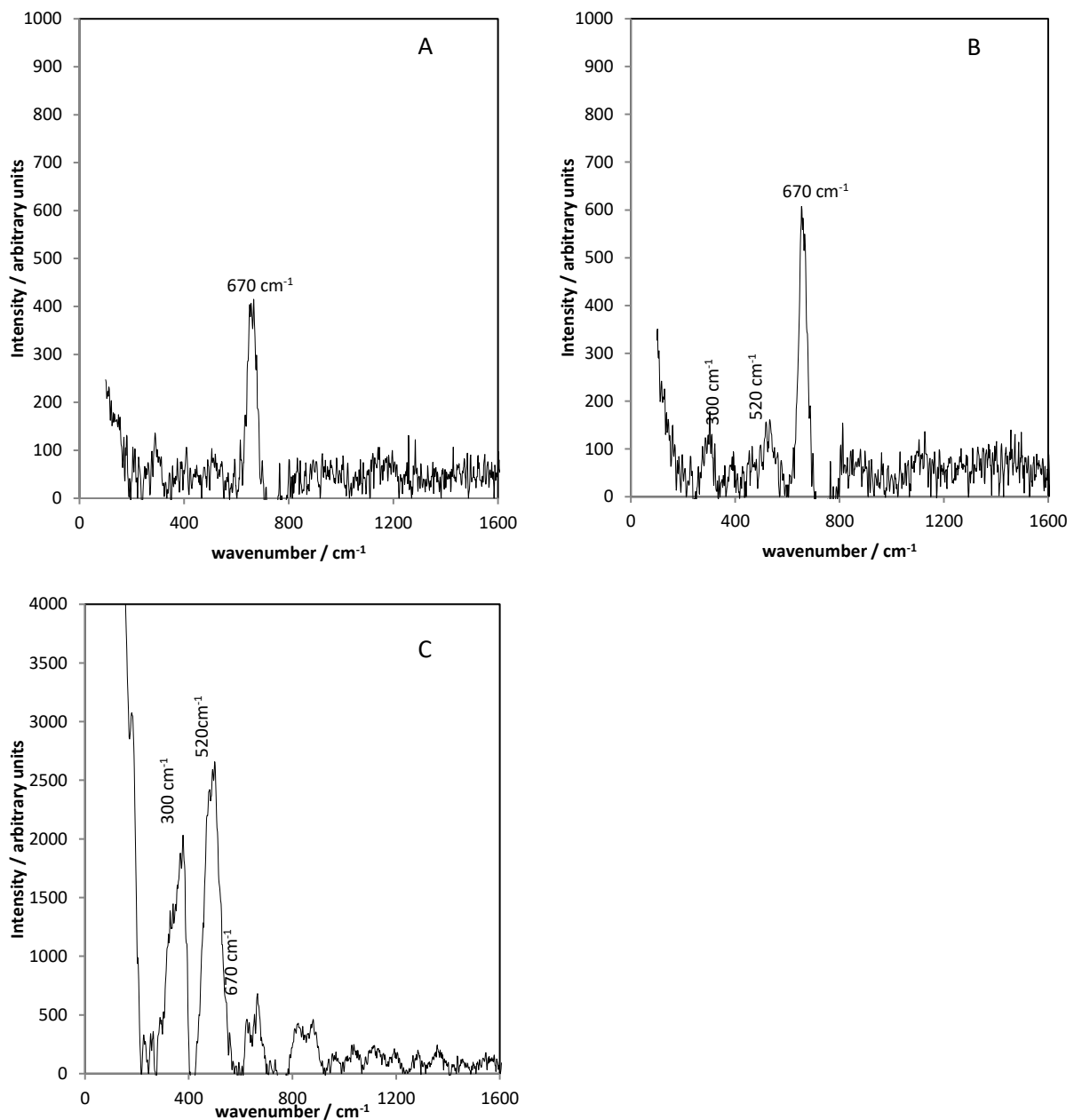
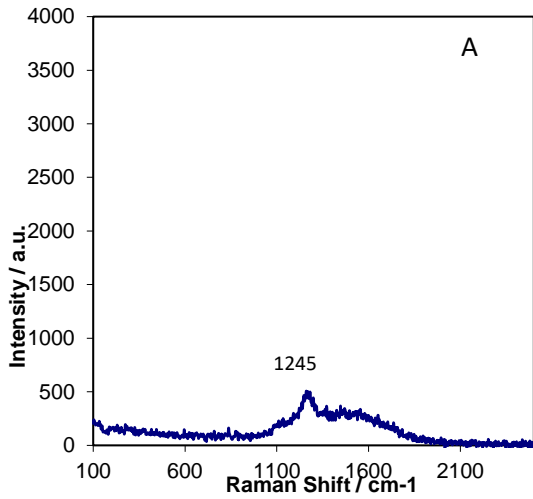


**Figure 4.1.3.:** Comparison of the Raman spectra of iron species at different laser powers: A) Raman spectrum of  $\text{Fe}_3\text{O}_4$  powder duration time 400sec, 30% of the full laser power of 30mW B) Raman spectrum of  $\text{Fe}_3\text{O}_4$  powder duration time 600sec, 30% of the laser power of 30mW, C) Raman spectrum of  $\text{Fe}_3\text{O}_4$  powder duration time 600sec, 100% of the laser power of 30mW

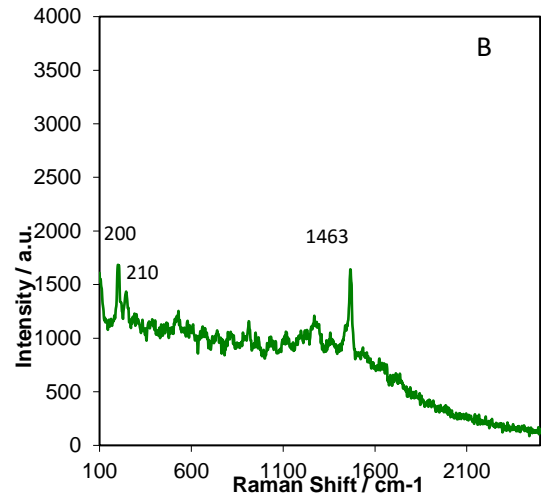
In the first instance, a sample time of 400 seconds was used with laser power at 30% of its maximum power of 30mW and the filters set at 90% as can be seen in Figure 4.1.3.A. The resultant spectrum show one peak at  $\sim 670\text{ cm}^{-1}$  commonly associated with  $\text{Fe}_3\text{O}_4$ . If the sample time is increased to 600 seconds, minor peaks at  $\sim 300$  and  $520\text{ cm}^{-1}$  as can be observed to grow in, Figure 4.1.3.B, indicating the onset of surface transformation. These changes become more pronounced as can be seen in Figure 4.1.3.C when a sample time of 600 seconds is used at full laser power. It can be seen that in Figure 4.1.3C the dominant peak at  $667\text{cm}^{-1}$  cannot be observed indicating full transformation of  $\text{Fe}_3\text{O}_4$  to other Fe/O phases.

Thus, Raman experiments on the iron rod electrode of section 3.1 were performed using the same settings as employed for Figures 4.1.3A and B in order to minimize surface transformation. As in the optical microscopy experiments of Figure 4.1.2, for each Raman experiment, linear sweep voltammetry was run on the rod electrode from -1V up to and including the end of each current peak studied and ex situ Raman spectra recorded. The same key potentials were used for measurement of the Raman spectra as these used for the optical microscopy experiments of Figure 4.1.2. The spectra recorded at these potentials, again designated potentials 0 to 4, are shown in Figure 4.1.4. Where the surface appears homogeneous from the optical microscopy, only one spectrum has been recorded. Where the surface appears multi composition and heterogeneous from the microscopy, efforts have been made to record a spectrum from each component. This is especially the case at potentials 2 and 3.

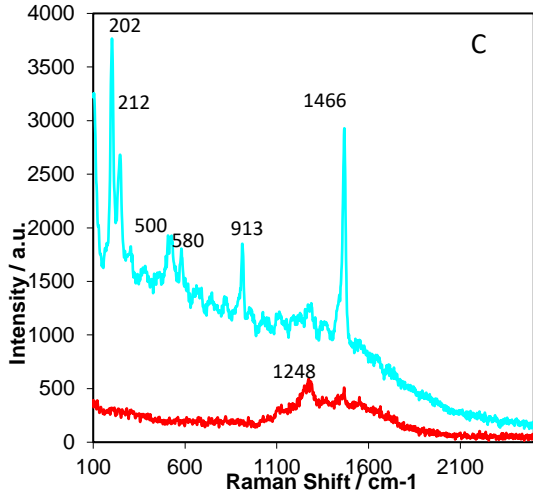
For ease of interpretation of the spectra of Figure 4.1.4, Figure 4.1 and 4.2 presented, based in literature, the Raman spectra of the most commonly encountered iron oxides ( $\alpha\text{-Fe}_2\text{O}_3$ ,  $\gamma\text{-Fe}_2\text{O}_3$ ,  $\text{FeO}$ ,  $\text{Fe}_3\text{O}_4$ ), oxyhydroxides ( $\gamma\text{-FeOOH}$ ,  $\alpha\text{-FeOOH}$ ) and the oxalates of Iron (II) and Iron (III) respectively. With these in mind, the data of Figure 4.1.4 may now be interpreted as follows.



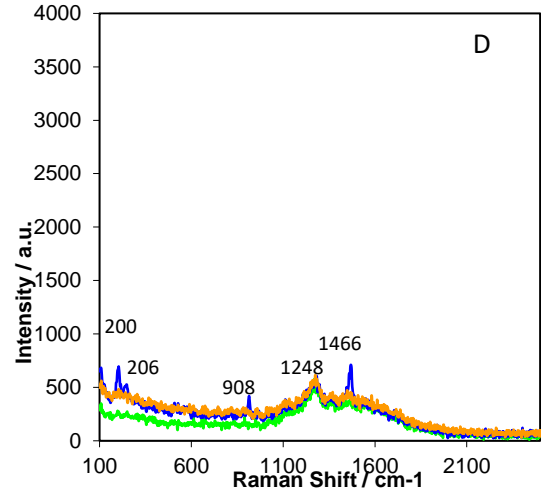
Potential zero  
(Clean electrode)



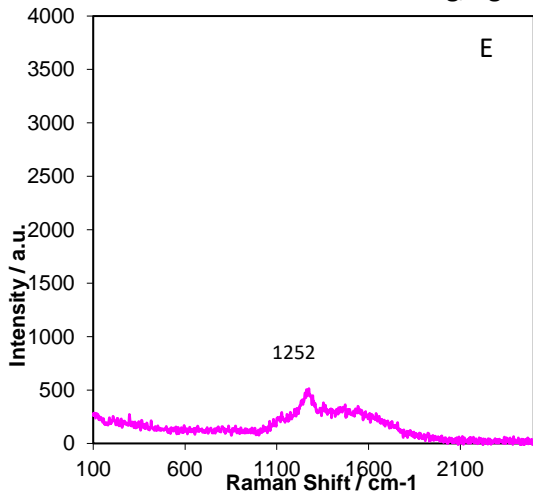
Potential 1  
Surface scanned from -1 to +0.1V vs Ag/AgCl



Potential 2  
Raman spectra at two different points  
Surface scanned from -1 to +0.7 V vs Ag/AgCl



Potential 3  
Raman spectra at three different points  
Surface scanned from -1 to +0.83V vs Ag/AgCl



Potential 4  
Surface scanned from -1 to +1V and  
from -1 to +0.38V vs Ag/AgCl

**Figure 4.1.4.:** FT-Raman spectra of iron samples at 4 points during a cyclic voltammogram of an iron rod in 8wt% oxalic acid.

At potential 0, a strong peak is observed at  $1245\text{ cm}^{-1}$ , superimposed over a less intense broad peak centred at approximately  $1550\text{cm}^{-1}$ . Comparison with the spectra of Figure 4.2 suggests that the major constituent of the surface is either  $\alpha\text{-Fe}_2\text{O}_3$ ,  $\gamma\text{-Fe}_2\text{O}_3$ ,  $\alpha\text{-FeOOH}$  or  $\gamma\text{-FeOOH}$  or a combination thereof. These most likely arise due to adventitious aerial oxidation of the polished iron electrode surface.

At potential 1 a strong and two less intense peaks can be observed at 1463, 200 and  $210\text{ cm}^{-1}$  respectively. Comparison with the spectra of Figure 4.1 suggests that the surface consists primarily of ferrous oxalate. This is due to iron surface oxidation leading to ferrous oxalate formation as has been discussed in section 3.1.

At potential 2, two spectra have been recorded one from each of the two major surface components observed from the optical microscopy of Figure 4.1.2. One of them, coloured light blue in Figure 4.1.4, shows two strong and four less intense peaks at 1466, 202, 212, 500, 580 and  $913\text{ cm}^{-1}$  respectively. Comparison with the spectra of Figure 4.1 suggests that the surface consists of ferrous oxalate and/or ferric oxalate compounds. As described in the previous paragraphs, ferrous oxalate is (possibly partially) oxidised to soluble ferric oxalate at potential two. These findings are again in an agreement with Camalet's et. al. work [74]. The second spectrum, coloured red in Figure 4.1.4., shows a strong peak at  $1248\text{ cm}^{-1}$  superimposed over a less intense broad peak centred at approximately  $1550\text{cm}^{-1}$ . Comparison with the spectra of Figure 4.2 suggests that similar to potential zero, the major constituent of the surface is either  $\alpha\text{-Fe}_2\text{O}_3$ ,  $\gamma\text{-Fe}_2\text{O}_3$ ,  $\alpha\text{-FeOOH}$  or  $\gamma\text{-FeOOH}$  or a combination thereof. Thus, according to these two spectra, the two major components of this heterogeneous surface appear to be ferrous oxalate and/or ferric oxalate and oxide species such as  $\alpha\text{-Fe}_2\text{O}_3$ ,  $\gamma\text{-Fe}_2\text{O}_3$ ,  $\alpha\text{-FeOOH}$  and / or  $\gamma\text{-FeOOH}$ .

At potential 3, a similar heterogeneous surface to that seen at potential two is observed and thus three spectra have been recorded. One of them, coloured blue in Figure 4.1.4, has similar properties with the first spectrum discussed with respect to potential two in the previous paragraph

with peaks at 200, 206, 908, 1248, and 1466  $\text{cm}^{-1}$  giving evidence of the presence of oxalate species (ferrous and/or ferric oxalate). The other two spectra (coloured green and yellow in Figure 4.1.4), show similar properties with the second spectrum recorded at potential 2, showing a strong peak at 1248  $\text{cm}^{-1}$  indicating the presence of oxide species (a combination or one of  $\alpha\text{-Fe}_2\text{O}_3$ ,  $\gamma\text{-Fe}_2\text{O}_3$ ,  $\alpha\text{-FeOOH}$  and  $\gamma\text{-FeOOH}$  species). Spectra recorded at potential 3 indicate the presence of oxide and oxalate species with the oxide/oxyhydroxide component now more dominant than at potential two. This is strongly suggestive of iron oxalate stripping / dissolution having occurred-again in agreement with Camalet et. al [74].

At potential 4 a strong peak is observed at 1252  $\text{cm}^{-1}$ . Comparison with the spectra of Figure 4.2 suggests that the major constituent of the surface is either  $\alpha\text{-Fe}_2\text{O}_3$ ,  $\gamma\text{-Fe}_2\text{O}_3$ ,  $\alpha\text{-FeOOH}$  or  $\gamma\text{-FeOOH}$  or a combination thereof. Moreover, oxalate compounds cannot be found onto the surface and that can be explained due to the dissolution of ferric oxalate as has been alluded to immediately above and discussed in the previous paragraphs.

## 4.2. Summary

This section presents optical images and ex-situ Raman experimental results at a series of key potentials throughout the cyclic voltammogram performed on the iron rod in order to identify the metal compounds that can be found onto an iron electrode.

Results reveal that at  $E < 0.5\text{V}$ , the steel surface is covered with a ferrous oxalate layer. At  $E > 0.5\text{V}$  the surface consists of iron oxalate and / or ferric oxalate and oxide species. At approximately 0.7V the surface appears to be ferrous oxalate and/or ferric oxalate with the oxide species now to be more dominant, whilst at the reverse scan and at about 0.4V the surface appears to be covered only with oxide species.

This work investigates the chemical change of the surface for iron systems and comes in an agreement with the chemical analysis of Camalet et. al [74]. However, this optical microscope imaging and Raman studies doesn't provide any information about the pit formation as described by Camalet et. al [74] for iron systems.

These findings will now inform the detailed interpretation of the cyclic voltammetric and voltammogram data to be presented in the next chapter.

## Chapter 5

## 5. Nanogravimetric and electrochemical analysis of iron crystals in oxalic acid environments

This chapter presents the use of the QCN technology for measuring the mass changes that occur during electrochemical experiments on the iron / oxalic acid system, and discusses new insights into the corrosion behavior of the system that may be obtained.

The first part of this chapter presents cyclic voltammograms of iron-on-quartz crystals in oxalic acid environments. The second part presents again cyclic voltammograms of iron-on-quartz crystals but in oxalic acid/hydrogen peroxide mixtures. Hydrogen peroxide is used here as an experimental surrogate to simulate radiated environments as has been discussed in chapter 3.2.

### 5.1 Non-radioactive environments

A QCN mounted iron-on-quartz piezoelectrode was connected to a potentiostat as described in Chapter 2 and its potential scanned from -1V to +1V in solutions containing oxalic acid, simultaneously measuring the mass change and the current.

Cyclic voltammetric studies of mild carbon steel and iron electrodes in oxalic acid solutions were discussed in detail in chapter 3, wherein it was established that they behave similarly to each other in both 1 and 8 wt% oxalic acid (Figure 3.1.1), thus allowing the use of iron-based QCN crystals, instead of expensive steel crystals, as a low carbon steel surrogate for corrosion monitoring during oxalic acid-driven decontamination.

The main observations that may be made from the forward going sweep of the voltammetry presented in Chapter 3 and represented in Figure 5.1.1 (Figure 5.1.1A for 1 and Figure 5.1.1B for 8wt% oxalic acid) were as follows: as the applied potential is increased over the range -1 to +1 V,

iron(II) generated at the electrode surface at  $\sim -0.5$  V reacts with solution oxalate to form an insoluble passivating Fe(II) oxalate layer. This persists until  $+0.4$  V whereupon Fe(II) oxalate is partially oxidized to soluble Fe(III) oxalate, a process that continues until repassivation at  $\sim 0.75$  V.

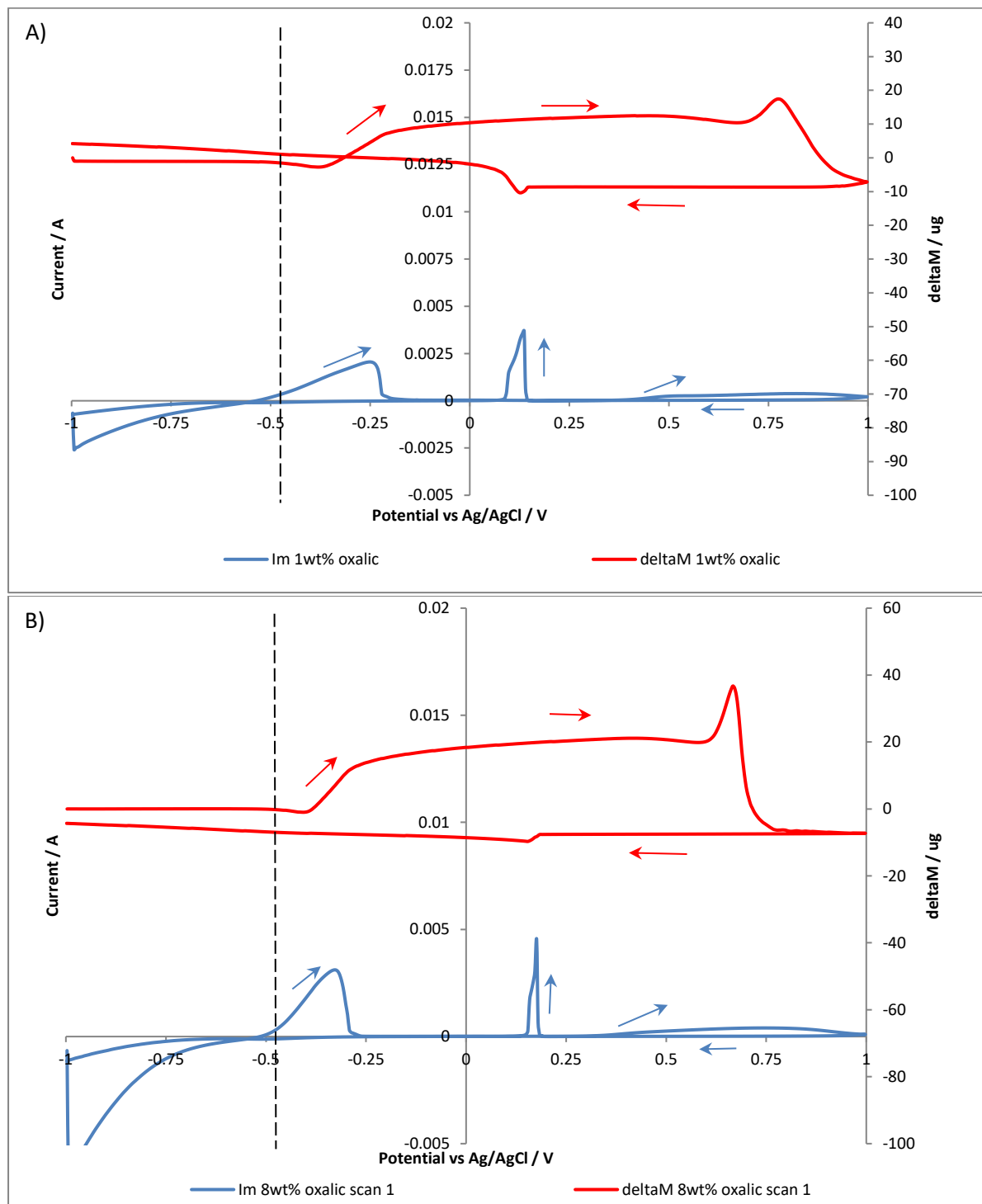


**Figure 5.1.1.:** Cyclic voltammogram of an iron crystal in A) 1 and B) 8 wt% oxalic acid solution respectively (scan rate = 0.01V/sec).

As alluded to in Chapter 4, studies conducted using the QCN with Fe electrodes support this interpretation as do the Raman and optical microscopy studies in the same chapter. During the forward scan of the cyclic voltammogram shown in Figure 5.1.1 a mass increase associated with the formation of the Fe(II) oxalate layer is observed at -0.4V whilst a mass loss, associated with partial oxidation of the Fe(II) oxalate layer to soluble Fe(III) oxalate, is seen at +0.5V.

This partial oxidation occurs via a process analogous to pitting, resulting in a pitted layer of Fe(II)oxalate at the iron surface. At the same time as the formation of the soluble Fe(III)oxalate via this pitting process, Camalet et. al [74] suggest that a minority of the released Fe(III) precipitates as a thin layer of Fe<sub>2</sub>O<sub>3</sub> although the data of Figure 5.1.1 indicates that the predominant mass change in the associated potential range is a mass loss, indicating that this layer of Fe<sub>2</sub>O<sub>3</sub> is thin at best.

In the reverse scan then, the electrode surface is initially comprised of a layer of Fe<sub>2</sub>O<sub>3</sub> and some remnant Fe(II)oxalate. The voltammetry of Chapter 3 and the Raman and optical microscope studies of Chapter 4 indicate that, at ~0.2V, the Fe<sub>2</sub>O<sub>3</sub> of this composite layer is reduced to soluble Fe<sup>2+</sup>, exposing the iron beneath; this iron surface is in turn oxidized, releasing further Fe<sup>2+</sup> that then participates as Fe(II)oxalate - the whole process manifesting itself as a current spike at ~+0.2V, see Figure 5.1.1. The voltammogram of Figure 5.1.1 again confirms this analysis as the reverse scan passes through 0.2V, we first see a mass loss (dissolution of Fe<sub>2</sub>O<sub>3</sub>) followed by a mass gain (precipitation of Fe(II)oxalate).

The voltammogram traces of Figure 5.1.2 show that the ferrous oxalate layer produced from the first oxidation peak during the forward going sweep, E=~-0.5V to~-0.2V, are heavier, and thus thicker, at higher oxalic acid concentrations. However, increasing the oxalic acid concentration from 1 wt% to 8 wt% does not result in a factor of 8 increase in the ferrous oxalate layer mass. At the end of the first scan ferric oxide and ferrous oxalate species, at both oxalic acid concentrations, insulate part of the iron crystal surface.

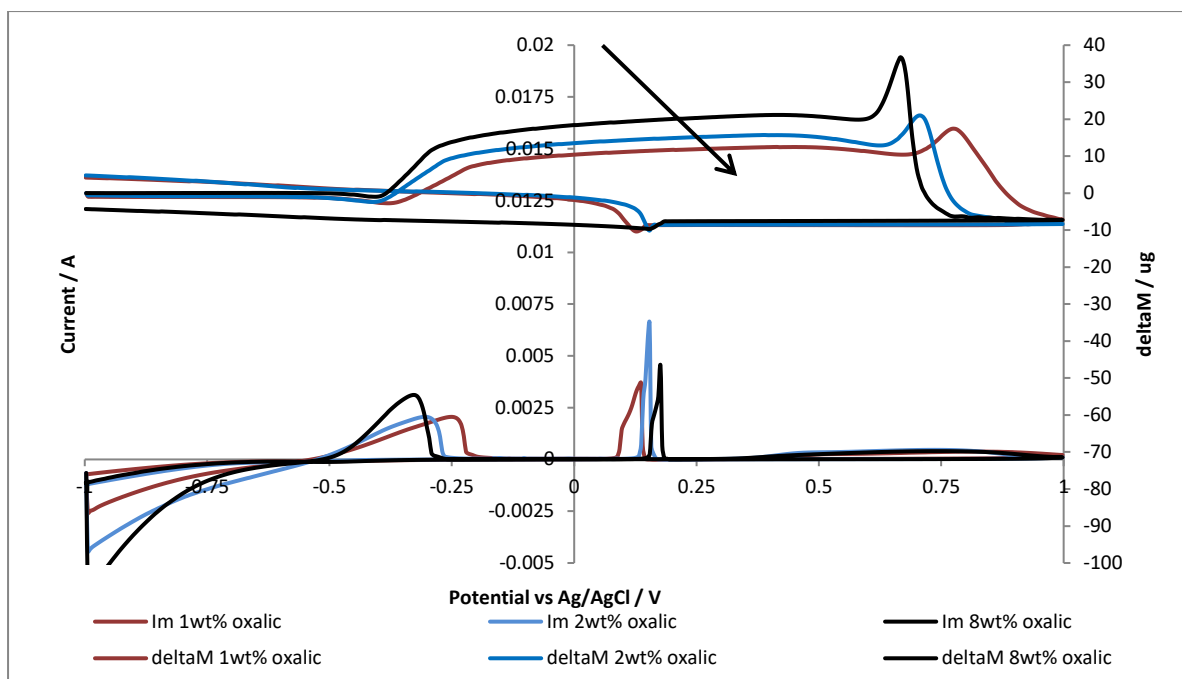


**Figure 5.1.2.:** Cyclic voltammograms of iron crystals in 1, 2 and 8wt% of oxalic acid (scan rate = 0.01V/sec).

Figure 5.1.3 shows the effect of running more than one scan. Due to the iron oxide and iron oxalate formations from the first scan maintaining into subsequent scans, the peak current seen at -0.4 V and +0.2 V in the first scan decreases during the second and third scan as can be observed in Figure 5.1.3. The associated mass change in the voltammassogram also decrease with increasing scan number.

QCN offers a method of calculating the molar mass of any insoluble layer that is electrodeposited onto the electrode overlaying the quartz crystal surface. Specifically, the molar mass of the ferrous oxalate layer that is electrodeposited during the forward going sweep can be calculated from the cyclic voltammogram and voltammassogram data recorded over the voltage range -0.45V to +0.25V, in Figure 5.1.1A and B for 1 and 8wt% oxalic acid respectively. Such a calculation will provide further information as to the identity of the main compound of the layer, hopefully supporting the conclusions drawn from the Raman and optical microscopy studies earlier. The method for calculating the molar mass is given in Chapter 2 by use of equation 2.4.2 and 2.4.6. It can be implemented as follows.

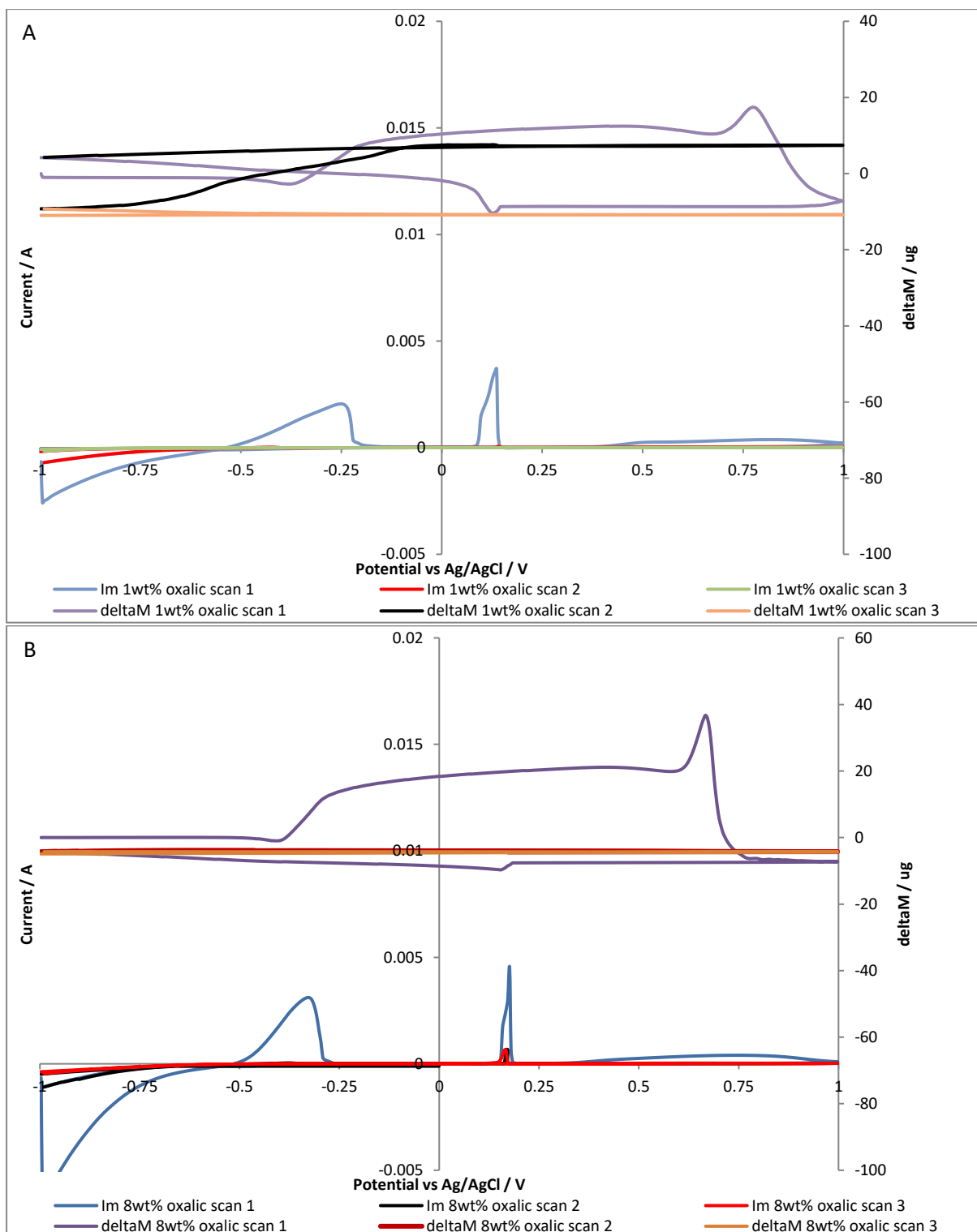


**Figure 5.1.3.:** Comparing 3 scan cyclic voltammograms of iron crystals, in 1wt % oxalic acid (A) and in 8wt% oxalic acid (B).

The molar mass of the deposited layer can be found by first calculating the charge passed through the electrode, by integrating the measured current in accordance with Equation 2.4.2 of Chapter 2. This may be done by use of the trapezium rule in an Excel® spreadsheet, using Equation 2.4.3 of Chapter 2, given here as equation 5.1.1 for the convenience of the reader.

$$\Delta Q = \sum_j \left( \frac{i_j + i_{j+1}}{2} \right) \cdot \frac{\Delta E}{v} \quad \text{Equation 5.1.1.}$$

Where  $\Delta Q$  is the charge passed over a potential window  $\Delta E$ ,  $i_j$  is the current for data point  $j$  and  $v$  is the scan rate of the experiment which in these experiments is  $0.01 \text{ V s}^{-1}$ .

Assuming a 100% current efficiency for the electrodeposition process, this charge passed may now be converted to a number of moles of material deposited,  $n$ , by use of Faraday's Law of electrolysis.

$$n = \frac{\Delta Q}{z \cdot F} = \frac{\sum_j \left( \frac{i_j + i_{j+1}}{2} \right) \frac{\Delta E}{v}}{z \cdot F} \quad \text{Equation 5.1.2.}$$

Where  $z$  is the electron number for the electrodeposited reaction (assumed to be 2 here due to the oxidation of Fe to  $\text{Fe}^{2+}$ ) and  $F$  is the Faraday constant.

The mass of material deposited,  $\Delta m$ , can then be obtained from the change in the resonant frequency of the piezoelectrode over the same voltage range over which  $\Delta Q$  was obtained i.e.  $-0.45\text{V}$  to  $+0.25\text{V}$ . The molar mass,  $M$ , then be obtained by simply dividing  $\Delta m$  by  $n$  i.e.

$$M = \frac{\Delta m}{n} = \frac{z \cdot F \cdot \Delta m}{\Delta Q} = \frac{z \cdot F \cdot \Delta m}{\sum_j \left( \frac{i_j + i_{j+1}}{2} \right) \frac{\Delta E}{v}} \quad \text{Equation 5.1.3.}$$

Integrating equation 5.1.3 in an Excel® spreadsheet for 1 and 8 wt% oxalic acid the observed molar mass,  $M$ , of the material deposited can be found as a function of the limits of potential windows,  $E_L$  (lower potential limit) and  $E_u$  (upper potential limit) where  $\Delta E = E_u - E_L$ . Figure 5.1.4 show the molar mass of the deposited material calculated as a function of  $E_u$  up to  $E_u = +0.25\text{V}$  when  $E_L$  is held constant at  $-0.45\text{V}$ .

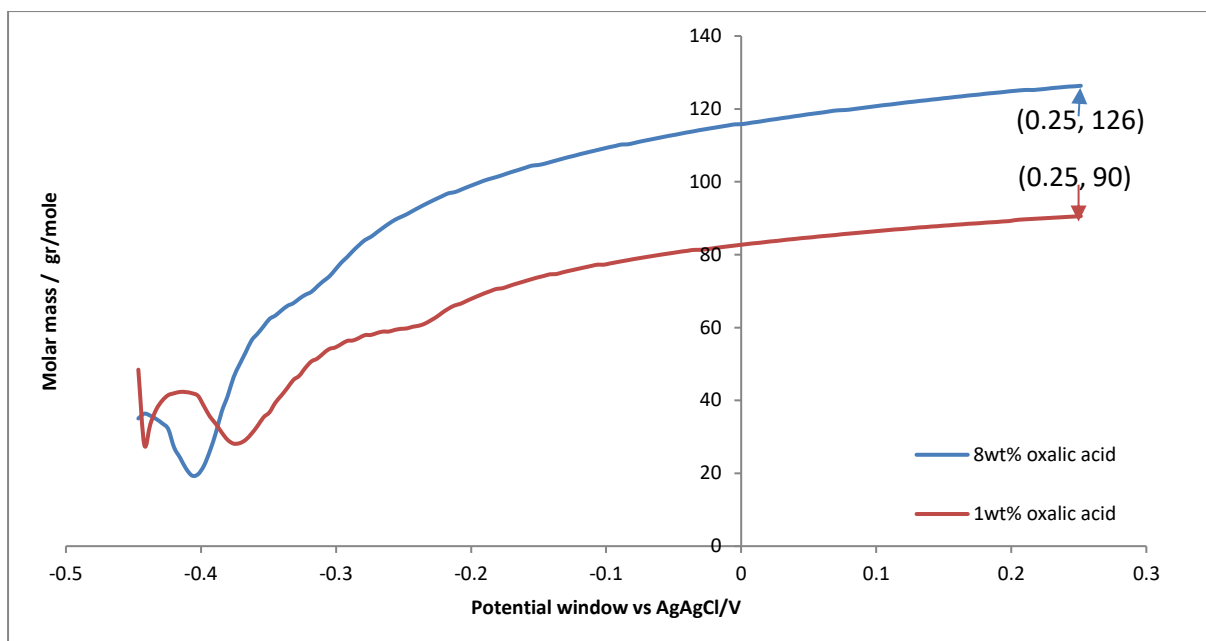


**Figure 5.1.4.:** The molar mass of the deposited material layer in function of the potential window with starting point of -0.45V when iron quartz crystals immersed in oxalic acid solution.

Figure 5.1.4 shows that as  $E_u$  is increased, the observed molar mass of the deposited material increases. Of relevance to this observation is that it can be seen from Figure 5.1.1 that, at  $E >$  the onset of the deposition wave at -0.45V, the mass gain associated with deposited material formation lags behind the observed increase in current. This is commonly observed in QCN experiments and can be understood by considering that the current increase is associated with fast electrochemical step of oxidation of the Fe electrode surface to form  $Fe^{2+}$ , while the mass gain is due to a slower, chemical deposition step associated with the reaction of the electrogenerated  $Fe^{2+}$  with species in solution, the resultant reaction product exceeding its local solubility product at the electrode surface and the consequent deposition of that product onto the surface. This results in the observed delay of the mass change with respect to current change as can be seen at -0.45V in Figure 5.1.1. Due this lag, the molar obtained by integrating current immediately after the onset of the current wave does not reflect the true mass; it is there for necessary to integrate over a wider potential window to ensure that both the entire current passage and mass change associated with a deposition are captured by the data analysis. Thus, the wider the potential window, the closer the calculated value of  $M$  is to its true value. This can be seen in Figure 5.1.4 wherein the higher the

value of  $E_u$  used, the larger the value of  $M$  obtained. Ideally, the widest window should be used, employing an  $E_u$  value up to the point in the cyclic voltammogram just before the onset of any following electrochemical process.

Using this approach and as can be seen from Figure 5.1.4. the molar mass derived from experiments using 1 and 8 wt% oxalic acid can be found to be equal to 90 g/mole and 126 g/mole respectively, which are in a good agreement with the molar mass of the anhydrous oxalate anion (=88g/mole) and dihydrate oxalate anion (=124g/mole) respectively. This suggests that for every mole of Fe oxidized to  $Fe^{2+}$ , 1 mole of oxalate is incorporated into the surface layer a finding in agreement with the conclusions drawn in Chapters 3 and 4 regarding layer composition. It also suggests that the iron oxalate layer formed from 1wt% oxalic acid is more compact than that formed from 8wt%. We shall return to that point below.

## 5.2 Simulated radioactive environments

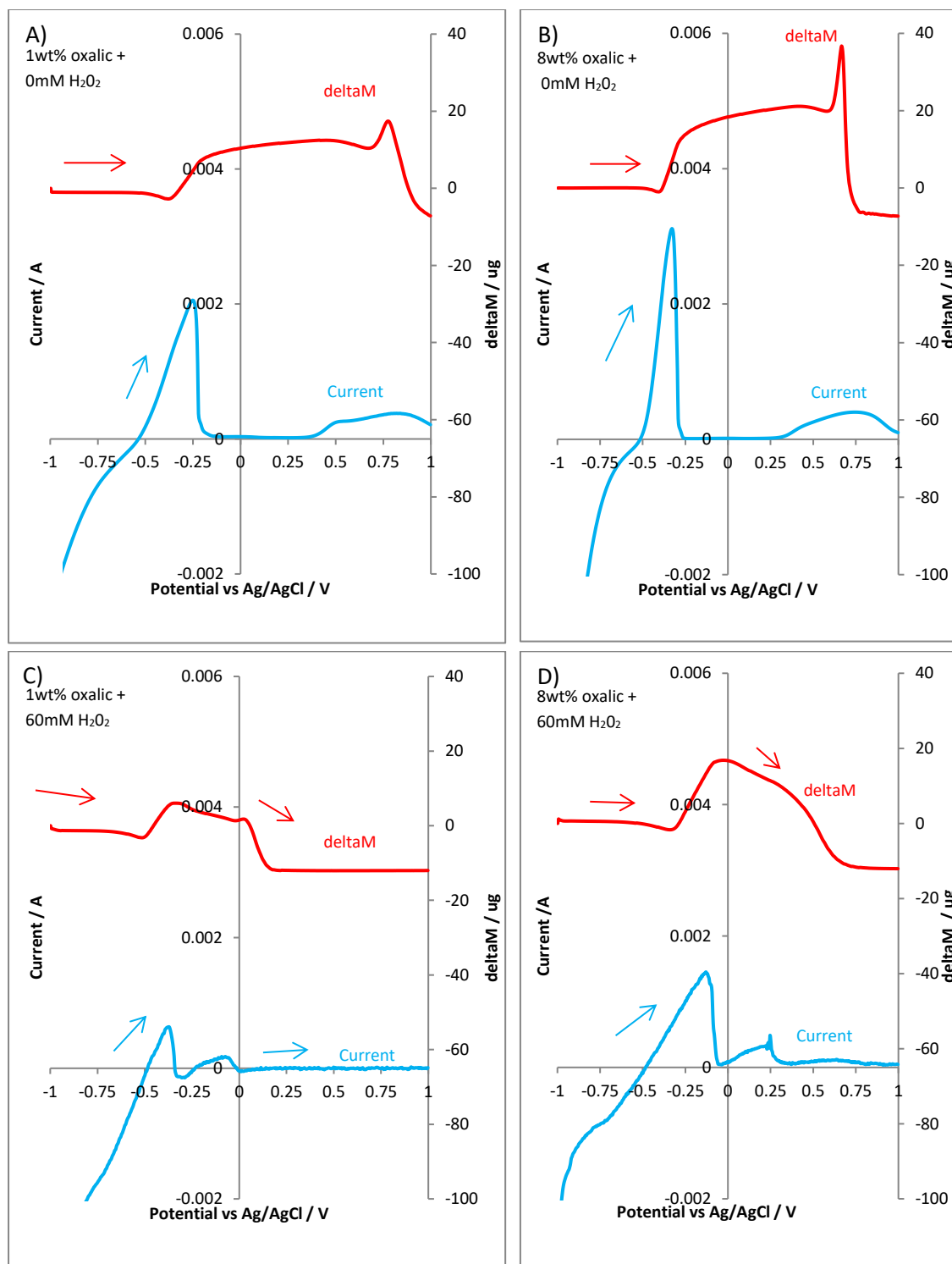
$H_2O_2$  is widely used as an experimental surrogate to simulate the effect of radiation, especially  $\gamma$  radiation, in aqueous environments (discussed in chapter 3.2). We have conducted QCN-based corrosion rate measurement experiments with the Fe/oxalic acid system in the presence of  $H_2O_2$ , so simulating the effect of the radiolysis of water on Fe/oxalate corrosion processes. Measurements indicate the involvement of Fenton chemistry in the observed Fe/oxalate formation and dissolution processes, indicating that QCN technology offers unique advantages for real time and potentially *in-situ* corrosion measurements in a complex environment where more than one reaction is observed. This section presents the nanogravimetric and the electrochemical behavior of iron coated quartz crystals in mixtures of oxalic acid and hydrogen peroxide. Studies are presented where the electrode is scanned from -1 to +1V with the forward and reverse scans interpreted separately. An overview of the iron coated quartz crystal behavior when the surface is scanned for

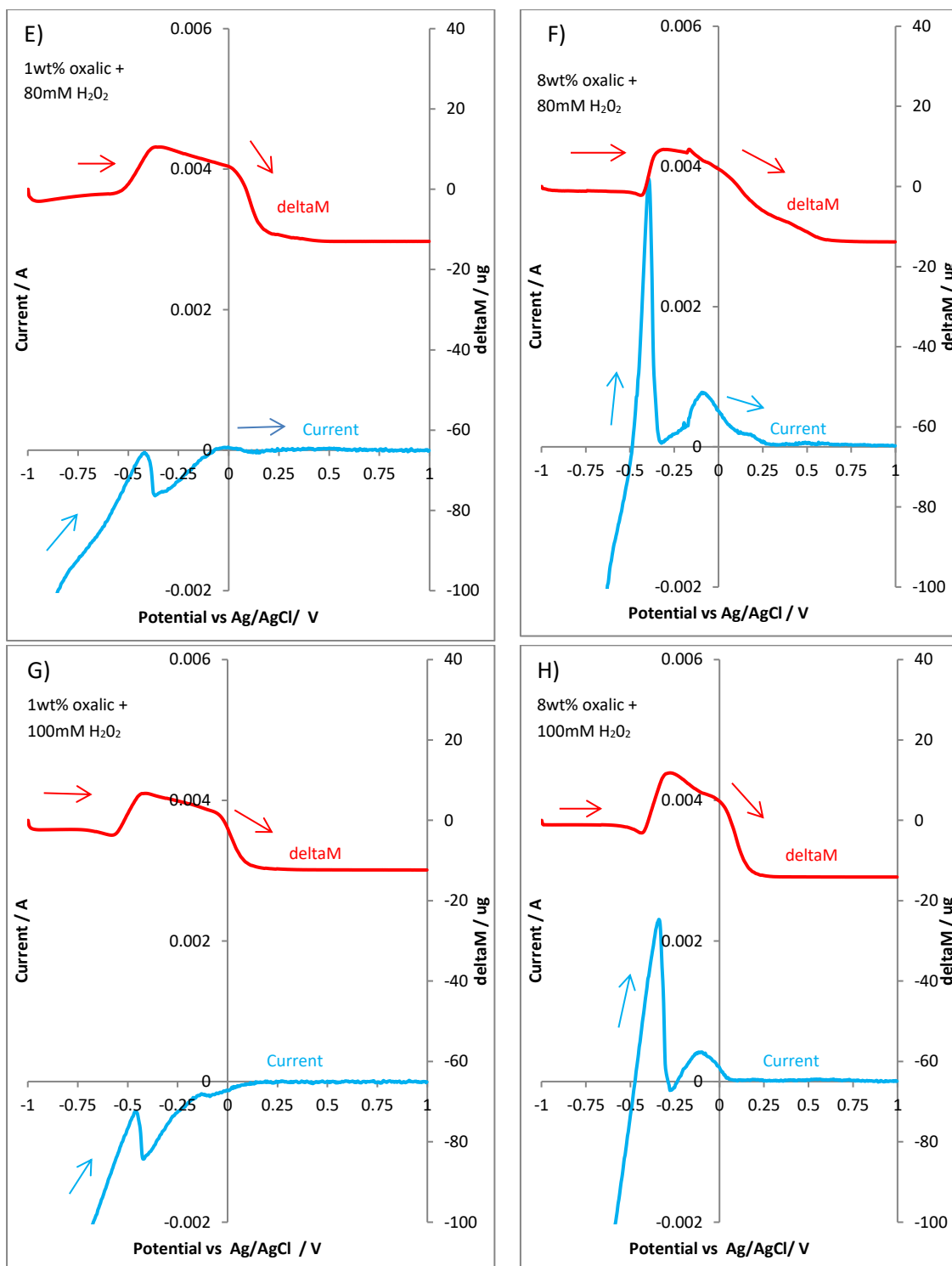
more than one cycle is also described. Lastly, the molar mass of deposited layer on the iron coated crystal is investigated in a similar manner with that described in section 5.1. This work is the subject of the section below a key insight gained being that, for the enhanced chemical cleaning process of the type used at Savannah River Site (see above), at low oxalic acid concentrations and at high simulated radioactive environments, it is possible that oxalic acid may not be acting as a corrosion inhibitor.

Figure 5.2.1 shows a QCN experiment where an iron piezoelectrode crystal, immersed in various mixtures of 1 and 8 wt% oxalic acid and  $H_2O_2$  in the concentration range 0-100mM, is scanned from -1V to +1V. At  $\sim -0.5V$  a mass gain associated with the formation of Fe (II) oxalate is observed at all peroxide concentrations studied. This is similar to that seen in the absence of hydrogen peroxide e.g. Figure 5.1.1 represented here as Figure 5.2.1A and B for reader convenience. This mass gain is then followed by a slow mass loss in the potential range of  $\sim -0.25V$  to 0V which we attribute the effect of hydrogen peroxide on the oxalate surface - a process that potentially involves some oxalate mineralization by hydroxyl radicals generated via equation 3.2.3 and 3.2.4 as discussed above. Finally, at  $\sim +0.1V$  there is a faster mass loss related to the electrochemical oxidation of Fe(II)oxalate to soluble Fe(III)oxalate accompanied by the simultaneous precipitation at the surface of some  $Fe_2O_3$ .

As alluded to in Chapter 4, Raman and optical microscopy studies indicate that in the absence of hydrogen peroxide and during the forward scan of the cyclic voltammassogram shown in Figure 5.1.1 a mass increase associated with the formation of the Fe(II) oxalate layer is observed at -0.4V whilst a mass loss, associated with part oxidation of the Fe(II) oxalate layer to soluble Fe(III) oxalate, is seen at +0.5V. At the same time as the formation of the soluble Fe(III)oxalate, Camalet et. al [74] suggest that a minority of the released Fe(III) precipitates as a thin layer of  $Fe_2O_3$ , which is in an agreement with the Raman and optical microscopy studies presented in Chapter 4. However, in

the presence of an oxidising agent, such as  $\text{H}_2\text{O}_2$ , this transformation appears to be promoted to occur at lower potentials ( $\sim 0\text{V}$  instead of  $\sim +0.5\text{V}$ ).





**Figure 5.2.1.:** Comparing the voltammetry and mass changes observed on an iron piezoelectrode when the electrode is scanned from -1V to +1V in 1 and 8wt% oxalic acid as a function of  $[\text{H}_2\text{O}_2]$ .

Returning to Figure 5.2.1, the form of the forward going current-voltage curves can be understood upon consideration of Figures 5.2.2 A and B which shows the CV and nanogravimetric behaviour of an iron piezoelectrode in a solution of 60 mM  $\text{H}_2\text{O}_2$  in 1wt%  $\text{KNO}_3$  solution and the corresponding Tafel curve. Comparing Figure 5.2.2A with the iron rod cyclic voltammogram shown in Figure 3.1.3, it can be seen that the presence of peroxide eliminates the oxidation peak seen at  $\sim -0.3$  V in Figure 3.1.3. This peak was originally assigned to Fe oxidation to solution  $\text{Fe}^{2+}$  by electrochemical oxidation of the latter to Fe(III) with subsequent ferric (hydr)oxide formation at the electrode surface and resultant passivation. The absence of this peak in Figure 5.2.2A is most likely as a result of any  $\text{Fe}^{2+}$  generated at an applied potential of  $\sim -0.3$  V being quickly oxidised to  $\text{Fe}^{3+}$  (Equation 3.2.3), so immediately passivating the electrode surface and thereby preventing further Fe dissolution. Peroxide is thus having a demonstrable effect on Fe electrochemistry.

There are two other features of note in Figure 5.2.2: the large reduction wave seen at negative potentials and the oxidation peak seen at +0.5 V. Absent in Figure 3.1.3, these may be attributed to  $\text{H}_2\text{O}_2$  reduction and oxidation processes respectively [99]. The former in particular will have ramifications for the measurement of iron / mild carbon steel corrosion rates in peroxide bearing solutions by the  $i_{\text{CORR}}$  method and this is discussed below.

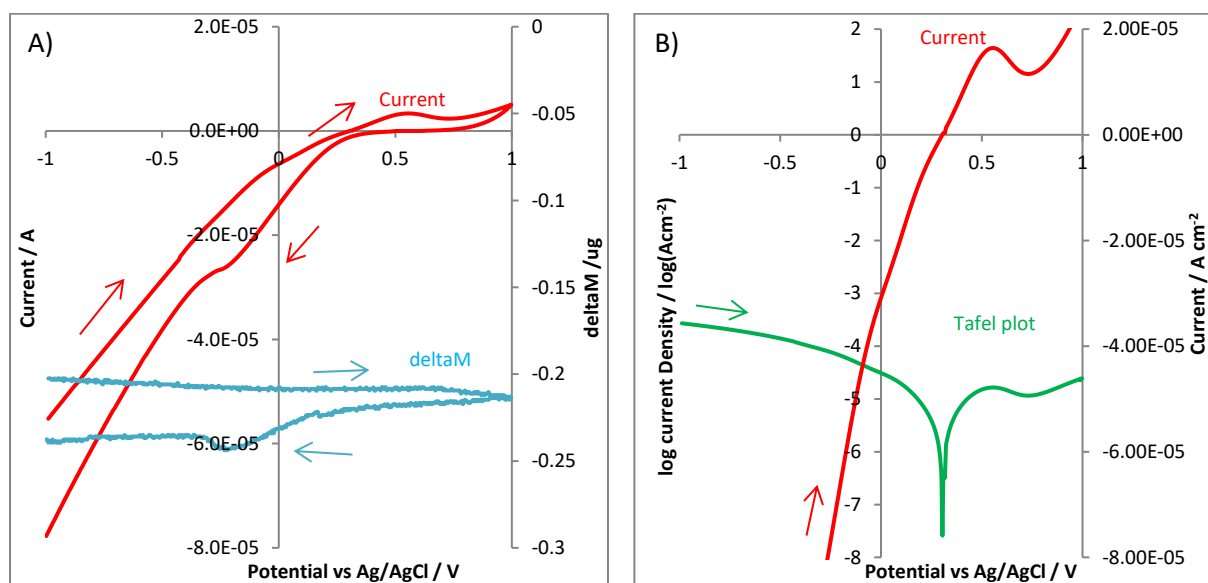


**Figure 5.2.2.:** Cyclic voltammogram of an iron crystal in 60mM  $\text{H}_2\text{O}_2$  A) and the corresponding Tafel plot per surface area B).

However, there is a need to understand the nature of the two peaks observed in the presence of peroxide in the forward going voltage sweeps seen first in Figure 3.2.2. Figure 5.2.1 represents these scans from -1V to +1V as well as their associated nanogravimetric data. Figure 5.2.1 also shows the analogous data for Figure 3.1.1 i.e. the forward going scans observed from iron piezoelectrodes in 1 and 8wt % oxalic acid in the absence of peroxide, and their associated nanogravimetric traces. The nanogravimetric data of Figures 5.2.1A and 5.2.1B accords with the interpretation of Figure 3.1.1 given above i.e. the peak with an onset of  $\sim -0.5$  V accords with the oxidation of Fe to  $\text{Fe}^{2+}$  with subsequent formation of a passive layer of ferrous oxalate and an associated electrode mass increase. The second oxidation peak, with an onset of  $\sim +0.4$  V, corresponds to the oxidation of the ferrous oxalate to free ferric (with an associated small mass loss) prior to prompt precipitation at the electrode surface as ferric (hydr)oxide, with an accompanying mass gain. This mass gain is then reversed as the ferric oxide / hydroxide layer is part reduced to  $\text{Fe}^{2+}$  leaving a thin layer of  $\text{Fe}_2\text{O}_3$  at the piezoelectrode surface.

Inspection of Figures 5.2.1C, D, E, F G and H indicate that the same processes as those in Figure 5.2.1 A and B obtain, save that the oxidation of the ferrous oxalate layer to ferric oxalate that occurs at +0.5 to +0.75 V in the absence of peroxide occurs at -0.25 to +0.25 V in the presence of peroxide. The reason for this is the action of peroxide on the ferrous oxalate formed at the electrode surface by the oxidation reaction at -0.5 to -0.25 V. This is slowly dissolved (and potentially mineralised) by peroxide to produce free  $\text{Fe}^{2+}$  (and possibly  $\text{CO}_2$ ), as suggested by the net mass losses observed for instance in the potential ranges of -0.4 to 0 V and 0 to +0.4 V in Figures 5.2.1C and 5.2.1D respectively. The released  $\text{Fe}^{2+}$  is then oxidised in accordance with equation 3.2.3 to ultimately produce ferric oxalate and a thin residual layer of passivating ferric oxide at the Fe piezoelectrode surface.

The negative shift in the onset potentials of the more anodic of the two oxidation peaks seen in the traces in Figures 5.2.1A and 5.2.1B relative to the position that they occupy in Figures 5.2.1C, D, E, F, G and H can therefore be easily explained – as can the fact that, in contrast, the onset potential of the more cathodic oxidation peak is unaffected by the presence of peroxide, occurring at  $\sim -0.5$  V in all

of Figures 5.2.1A to 5.2.1D. Invariance in the position of this peak with peroxide concentration is almost certainly due to peroxide undergoing electrochemical reduction in the potential range  $E < 0$  V as seen in Figure 5.2.2, with the result that its local concentration at the electrode surface at  $E < 0$  V is reduced to near zero so eliminating its effect on Fe/Fe(II)/ferrous oxalate electrochemistry in this range.

By comparing Figures 5.2.1C with 5.2.1D, Figures 5.2.1E with 5.2.1F and Figures 5.2.1G with 5.2.1H it can be seen that the increased electrode mass associated with ferrous oxalate film formation occurs over a wider potential range at 8wt% oxalic acid than at 1wt%, suggesting that the film formed in the presence of 8wt% oxalic acid is thicker than that formed in the presence of 1wt%. This would also explain the  $E_{OC}$  vs  $[H_2O_2]$  data of Figure 3.2.3 wherein a stronger dependence of  $E_{OC}$  on  $[H_2O_2]$  is observed from solutions containing 1wt% oxalic acid than 8wt%; the thinner passivating ferrous oxalate film formed in the presence of 1wt% oxalic acid allows the Fe and mild carbon steel electrodes studied to be more responsive to solution phase-derived oxidative stresses than the thicker films formed in the presence of 8wt% oxalic acid. Comparison of the results shown in Figure 3.2.3 with those shown in Figures 5.2.1C with 5.2.1D indicates that the  $E_{OC}$  potentials measured from solutions containing 8wt% oxalic acid increase from  $\sim -0.5$  to  $\sim -0.3$  V over the  $[H_2O_2]$  range of 0 to 240 mM, remaining wholly within the range of ferrous oxalate stability of  $\sim -0.5$  to  $\sim -0.1$  V shown in Figure 5.2.1D. In contrast, values of  $E_{OC}$  recorded over the same  $[H_2O_2]$  range in 1wt% oxalic acid increase from  $\sim -0.5$  V, where Figure 5.2.1C indicates that ferrous oxalate is stable, to  $+0.25$  V at 180 mM peroxide where Figure 5.2.1C indicates that ferrous oxalate breakdown will be occurring. The instability in  $E_{OC}$  data seen in this  $[H_2O_2]$  range in Figure 3.2.3A for experiments recorded in 1wt% oxalate can thus be explained. Under these conditions, the ferrous oxalate film can be compromised by peroxide driven oxidative attack whilst fresh ferrous oxalate formation happens simultaneously. In other words, the observed instability in  $E_{OC}$  is due to metastable pit formation and closure / repassivation. We have previously discussed electrochemically driven pit formation in Fe(II)oxalate

layers in peroxide free systems in chapter 3 – specifically in reference to Figure 3.1.1 and 3.1.4. Pitting phenomena would therefore seem to be ubiquitous in the redox chemistry of Fe(II)oxalate layers.

The metastable pit formation and closure discussed above is further illuminated by the data of Figure 5.2.3, which shows  $E_{OC}$  and mass data measured as a function of time from an iron piezoelectrode immersed in a solution of 60 mM peroxide in 1wt%  $KNO_3$ . The latter data are characterized by a short period of mass loss followed a period of no net mass loss, punctuated by periodic spikes of mass loss / gain. The  $E_{OC}$  data indicate that the open circuit potential moves from +0.3 to +0.5 V over the timescale of the experiment, a range that is wholly located within the area of  $Fe_2O_3$  stability in the  $E_h$ -pH diagram of Figure 3.1.2B. Figure 5.2.3 thus indicates that, after an initial short period of peroxide driven oxidative dissolution of the Fe surface, forming  $Fe^{2+}$  and ultimately  $Fe^{3+}$ , represented in Equation 3.2.3, with an associated mass loss, a passivating layer of  $Fe_2O_3$  forms at the surface, so arresting the rate of mass loss. However, this layer is not fully coherent and is subject to pit formation and repassivation processes.

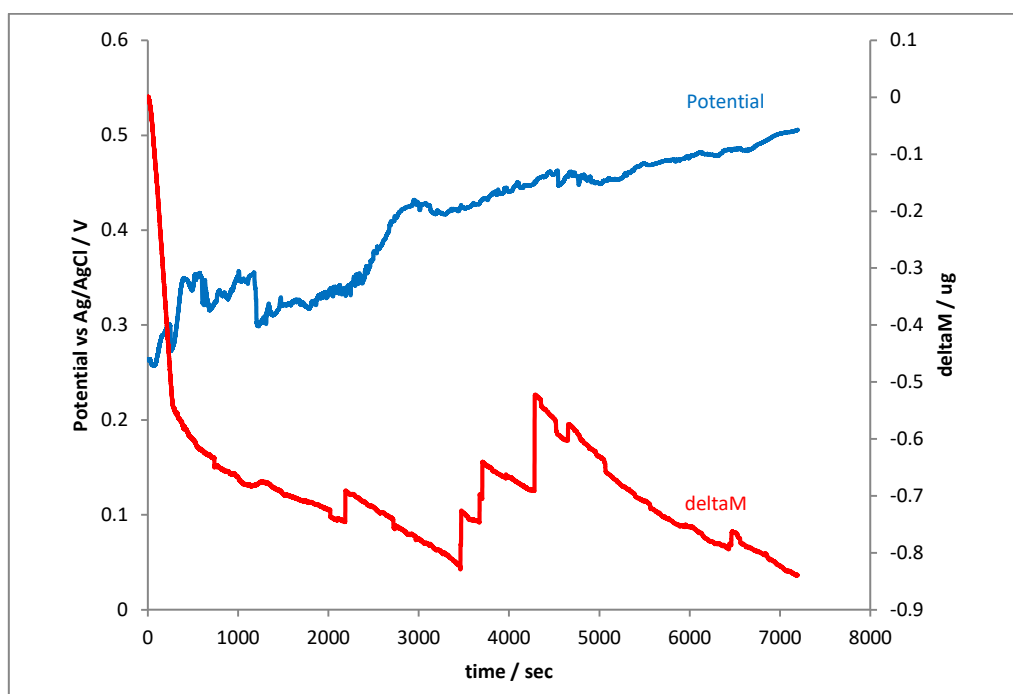


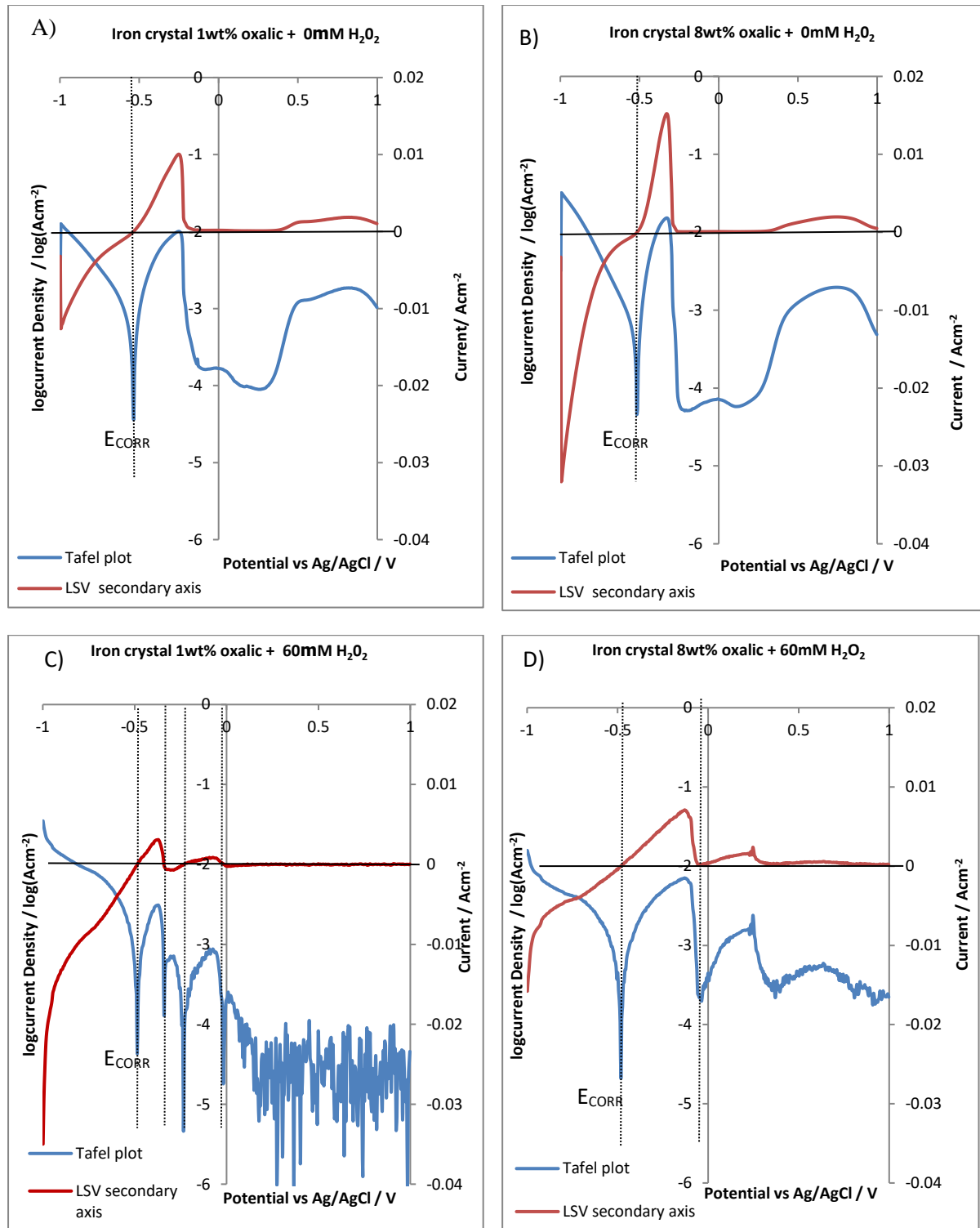
**Figure 5.2.3.:**  $E_{OC}$  and nanogravimetric data as a function of time, recorded from Fe piezoelectrodes using the QCN in 60mM  $H_2O_2$ .

Increasing the concentration of the reactant in a chemical process commonly increases the reaction rate. It is therefore to be expected that increasing the hydrogen peroxide concentration will result in an increase in the rates of oxidation of  $\text{Fe}^{2+}$  to  $\text{Fe}^{3+}$  as per equation 3.2.3. Thus, Figure 5.2.1 also shows the effect on the cyclic voltammogrammetric behaviour of iron crystals in oxalic/hydrogen peroxide mixtures upon increasing hydrogen peroxide concentration. Increasing the hydrogen peroxide concentration increases the rate of equation 3.2.3 and so decreases the potential range over which the presence of Fe(II)oxalate at the electrode surface can be inferred from the mass-voltage trace. For example in Figure 5.2.1D, recorded at 60mM  $\text{H}_2\text{O}_2$  and 8wt% oxalic acid, a mass increase associated with Fe(II)oxalate formation is seen at  $E \sim -0.3\text{V}$ , whilst the mass loss associated with its oxidative dissolution is seen at  $E \sim +0.6\text{V}$ . The corresponding data recorded at 100mM  $\text{H}_2\text{O}_2$ , Figure 5.2.1H exhibits analogous mass gain and losses at  $-0.4\text{V}$  and  $+0.2\text{V}$  - a potential range that is shorter by 300mV compared to that seen in Figure 5.2.1D.

Comparing Figures 5.2.1 B, D, F and H and Figures 5.2.1 A, C, E and G, it can be seen that at higher oxalic acid concentrations the mass gain due to ferrous oxalate production can be found over a wider potential range than at low oxalic acid concentrations. This can be explained by the production of a thicker oxalate layer in the presence of 8 wt% oxalic acid compared to that formed in the presence of 1wt% oxalic acid. Due to this being a complex system where more than one reaction takes place within the same potential range, it is difficult to make similar conclusions from the peak current.

Figure 5.2.4 represents the forward going sweeps in the first scan cyclic voltammograms of iron piezoelectrodes in oxalic/hydrogen peroxide mixture. Figure 5.2.4 also shows the Tafel plots calculated from these scans. Figure 5.2.4A and B showing data recorded using solutions of 1 and 8 wt% oxalic acid, but in the absence of hydrogen peroxide, were originally presented in Figures 3.1.6C and 3.1.6D, and discussed in section 3.1. These suggest the existence of one  $E_{\text{CORR}}$  value for both the 1 and 8wt% systems at  $\sim -0.5\text{V}$ , which is associated with the oxidation of Fe to  $\text{Fe}^{2+}$  with subsequent

formation of a passive ferrous oxalate layer as has been discussed in chapters 3 and 4 and in section 5.1.



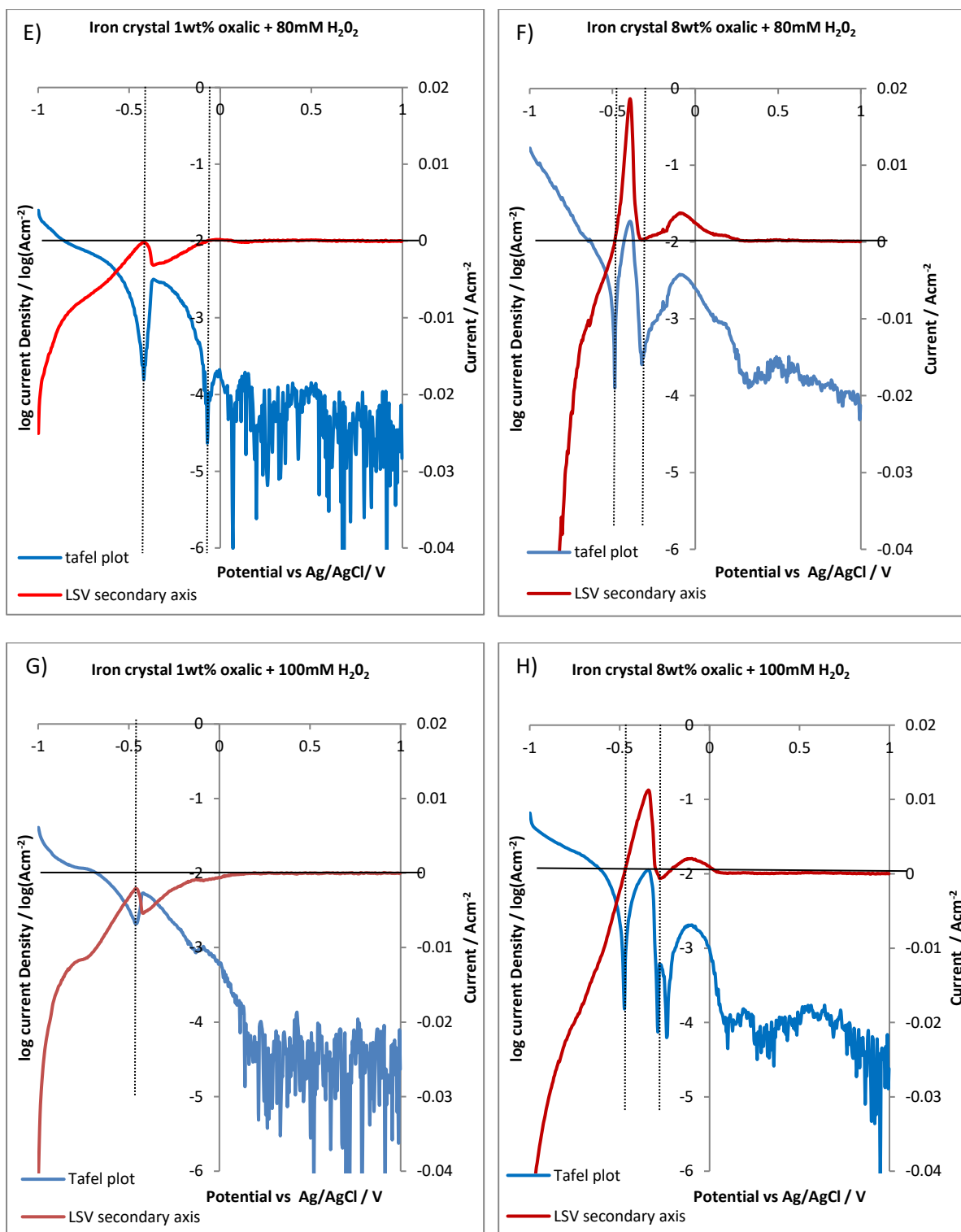


**Figure. 5.2.4.:** Forward going sweeps per surface area in the first scan cyclic voltammograms, and associated LSVs, of iron piezoelectrodes in a mixture of 1 and 8 wt% oxalic acid and a variety of H<sub>2</sub>O<sub>2</sub> concentrations.

For a mixture of 8wt% oxalic acid and 60mM hydrogen peroxide, the Tafel data of Figures 5.2.4 D suggests the existence of two  $E_{CORR}$  values, one of  $\sim -0.5$  V and another at  $\sim 0$  V. The data recorded from the mixture of 1wt% oxalic acid and 60mM hydrogen peroxide, see Figure 5.2.4C, suggests the existence of at least four  $E_{CORR}$  values at  $\sim -0.5$ ,  $\sim -0.35$ ,  $\sim -0.25$  and  $\sim 0$  V. This observation can be explained simply by consideration of Figure 5.2.4A and B with Figure 5.2.2B. The latter shows the reductive behaviour of hydrogen peroxide on iron electrodes in the absence of oxalic acid whilst the former shows the oxidative electrochemistry of iron electrodes in the presence of oxalic acid but absence of hydrogen peroxide. Simplistically, Figure 5.2.4C and D can be regarded as the additive convolutions of Figure 5.2.2B and 5.2.4A, and 5.2.2B and 5.2.4B respectively i.e. the oxidative electrochemistry of the iron/oxalate system superimposed over the reduction of hydrogen peroxide. This superimposition then results in a current trace that crossed the zero current axis at least three times, giving rise to at least three apparent  $E_{CORR}$  values in the corresponding Tafel curves. However, as can be seen from comparison of Figure 5.2.4C and D with Figure 5.2.4A and B only the most cathodic of these  $E_{CORR}$  values is "real". The above observation also applies to the data for 80 and 100mM hydrogen peroxide solutions presented in Figure 5.2.4 E, F, G and H, where the hydrogen peroxide reduction is more pronounced.

However, at these higher hydrogen peroxide concentrations, the reduction currents of hydrogen peroxide are greater and dominate the electrochemistry observed at  $E < 0$  V in Figure 5.2.4E-H. Thus, for these systems, even the most negative of the observed " $E_{CORR}$ " values is affected by hydrogen peroxide reduction and so cannot be considered as such. Thus, we shall restrict any further discussion of  $E_{CORR} / i_{CORR}$  values in the presence of peroxide to systems where  $[H_2O_2] < 60$  mM. We shall return to this point in chapter 6.

All of the above concerned the forward going sweeps of cyclic voltammograms obtained when an iron coated piezoelectrode crystal is immersed in oxalic acid / hydrogen peroxide mixture. Let us now consider the forms of the reverse scans of these cyclic voltammograms. Figure 5.2.5

thus shows a full cyclic voltammogram of an iron coated piezoelectrode crystal, immersed in a mixture of 1wt% oxalic acid and 60mM H<sub>2</sub>O<sub>2</sub>.

The reverse scan, shown in Figure 5.2.5, is characterized by the presence of a single sharp oxidation peak at  $\sim+0.1V$ . This feature is also seen in the reverse scan of analogous studies on iron and mild carbon steel rods in 1wt% oxalic acid and 60mM hydrogen peroxide, see Figure 3.2.2 I and Figure 3.2.2. J. However, the reverse scan in these latter two Figures also exhibits a second oxidation feature in the region  $+0.1V$  to  $\sim-0.25V$ , said second oxidation feature being characterized by sharply oscillating current spikes. This feature is absent in the cyclic voltammogram of Figure 5.2.5. The origin of both of these reverse scan oxidation features, as well as the reason for the absence of the second feature in the cyclic voltammogram of Figure 5.2.5. are discussed in the next paragraph.

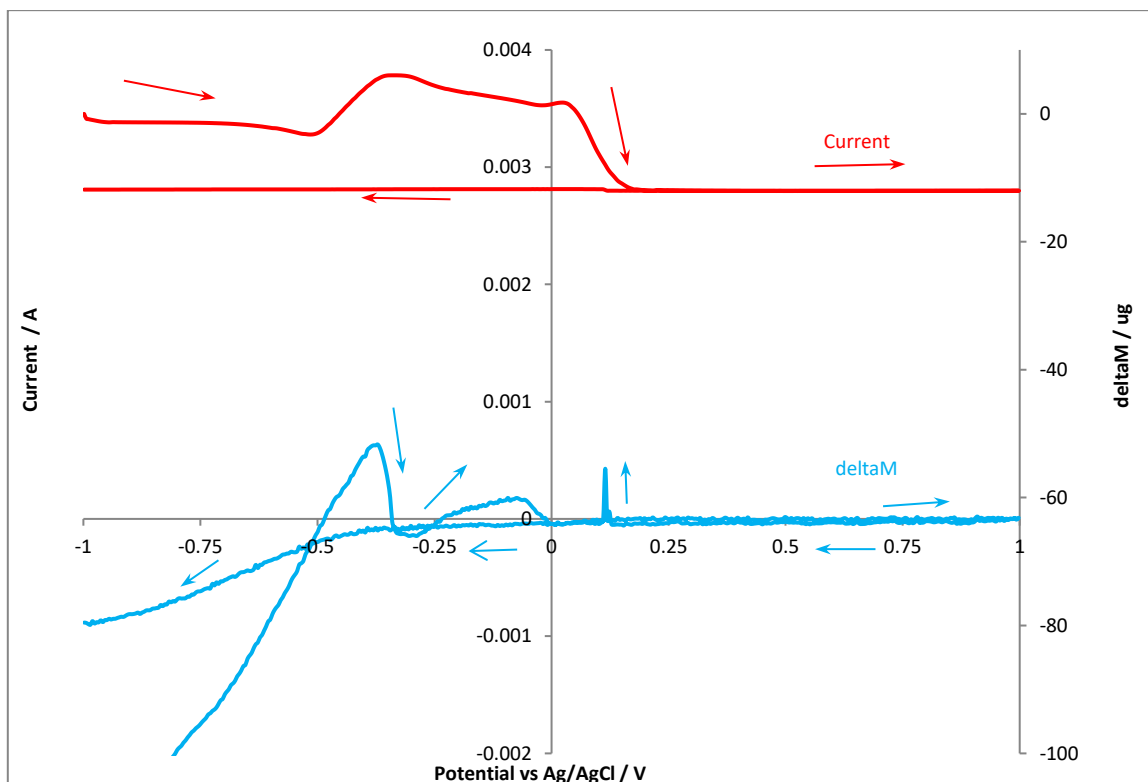


**Figure 5.2.5.:** Cyclic voltammogram of an iron crystal in a mixture of 1wt% oxalic acid and 60 mM H<sub>2</sub>O<sub>2</sub>.

As discussed in section 5.1, in the absence of hydrogen peroxide and during the reverse scan, the electrode surface is initially comprised of a layer of  $\text{Fe}_2\text{O}_3$  and some remnant  $\text{Fe(II)oxalate}$ . The voltammetry of Chapter 3 and the Raman and optical microscope studies of Chapter 4 indicate that, at  $\sim+0.2\text{V}$ , the  $\text{Fe}_2\text{O}_3$  of this composite layer is reduced to soluble  $\text{Fe}^{2+}$ , exposing the iron beneath; the exposed Fe is then oxidized, also generating  $\text{Fe}^{2+}$ , the two  $\text{Fe}^{2+}$  fluxes then reacting with the oxalic acid producing  $\text{Fe(II)oxalate}$  manifesting itself as a sharp peak current and the associated mass gain due to precipitation of  $\text{Fe(II)oxalate}$  at  $\sim0.2\text{V}$ .

However, in the presence of hydrogen peroxide, and as discussed in section 3.2 for iron and mild carbon steel rod electrode samples, this transformation is complicated by the reactions of equations 3.2.3 and 3.2.4. It therefore depends upon the initial iron oxide reduction (which, for brevity, we will subsequently identify as reaction 1), the following oxidation of the so-exposed iron to ferrous ions and subsequent precipitation as the oxalate (similarly identified as reaction 2) and the peroxide-driven oxidation of the so-formed ferrous oxalate to solution phase  $\text{Fe}^{3+}$  (identified as reaction 3). Reaction 3 interrupts the passivation of the iron / mild carbon steel surface by  $\text{Fe(II)oxalate}$ , resulting in the second sharply oscillating current feature seen in the reverse scans of Figure 3.2.2 I and 3.2.2 J above- a feature similar to that seen in metastable pit formation processes. Having explained the origin of this second feature in Figure 3.2.2 I and J, its absence in Figure 5.2.5 can now be explained as follows.

Again as reported in section 3.2 the microstructure of the electrode surface plays a key role in the corrosion effect of the surface and generally pitting preferentially happens at grain boundaries and discontinuities. The rod electrode surface has a crystalline structure due to the solidification of the metals from the molten phase where crystals grow to form the grains onto the surface. For the QCN resonators, the metal was sputtered onto the quartz crystal resonator resulting in a more homogeneous surface profile. Moreover, QCN resonators are flatter with fewer discontinuities compared to freshly polished rod electrodes. The metastable pitting formation is more pronounced

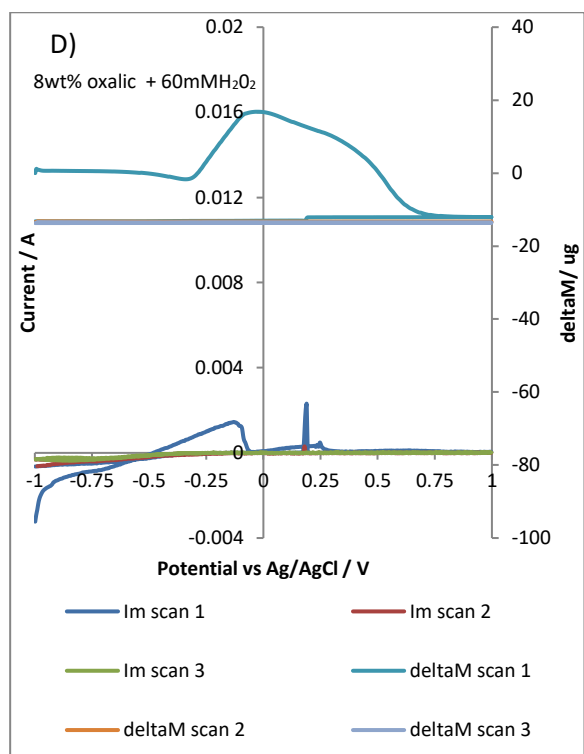
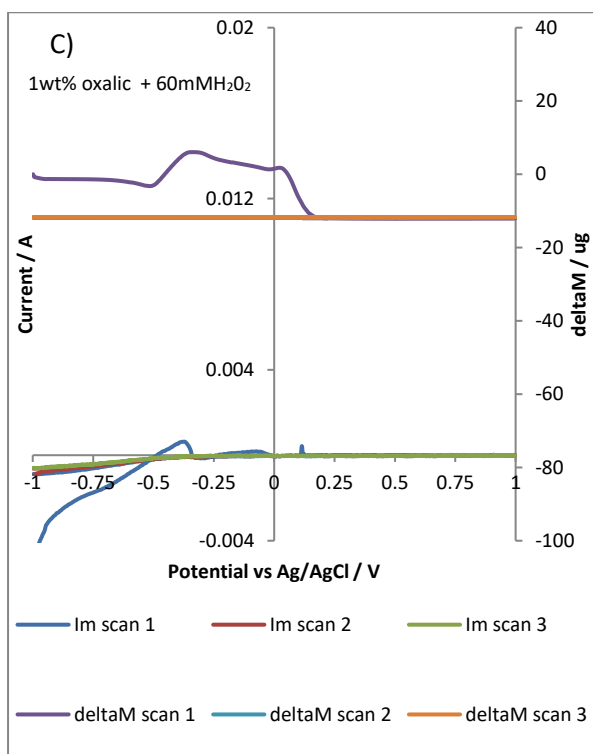
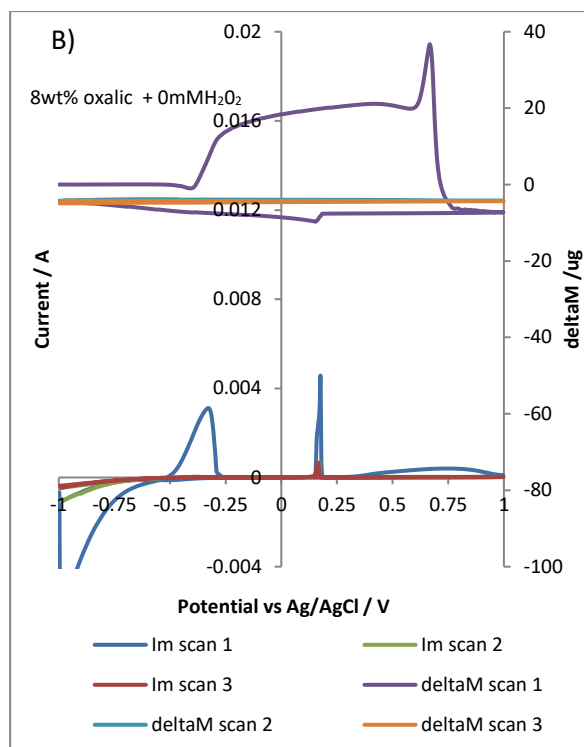
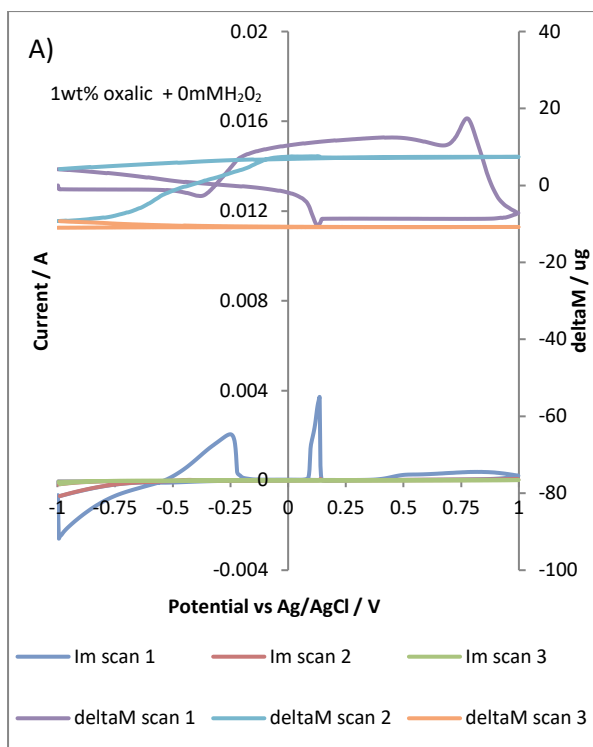
in freshly polished rod electrodes rather than in sputtered iron quartz resonator crystals resulting in a negligible metastable peak current on the resonators compared to these seen on the iron and mild carbon steel rods.

The above described in detail the main features seen in the forward and reverse scans of the initial cyclic voltammograms and voltamassograms of iron piezoelectrodes in oxalic/hydrogen peroxide mixtures. Let us now compare these initial scans with the two subsequent cyclic voltammograms and voltamassograms of these iron piezoelectrodes, again recorded in oxalic acid/hydrogen peroxide mixtures. These are shown in Figure 5.2.6.

These show that the currents and mass changes recorded in scan 2 and 3 are, generally, significantly suppressed compared to these seen in scan 1. This is most likely due to the presence of a passivating layer of Fe(II)oxalate/Fe<sub>2</sub>O<sub>3</sub> at the electrode surface at the beginning of the second scan, this layer being generated during and retained from scan 1 (see above). This observation illustrates how important the history of these samples is in determining their corrosion behaviour.

Finally, let us consider the feasibility of using initial scan data to calculate the molar mass of the electrodeposited oxalate layer in the presence of hydrogen peroxide. Such calculations were presented in section 5.1 for data recorded in the absence of hydrogen peroxide and an exactly analogous approach will be adopted here.

In the absence of hydrogen peroxide, a potential window of -0.45V up to +0.25V was used to generate the mass change and total charge passed values used to calculate the molar mass of the electrogenerated oxalate via equation 5.1.3. This window was identified by inspection of Figure 5.1.1, the lower potential limit being the point at which the observed current crosses the zero current axis to give a net positive value, and the upper limit being the potential at which oxidation of Fe(II)oxalate to Fe(III)oxalate species begins.



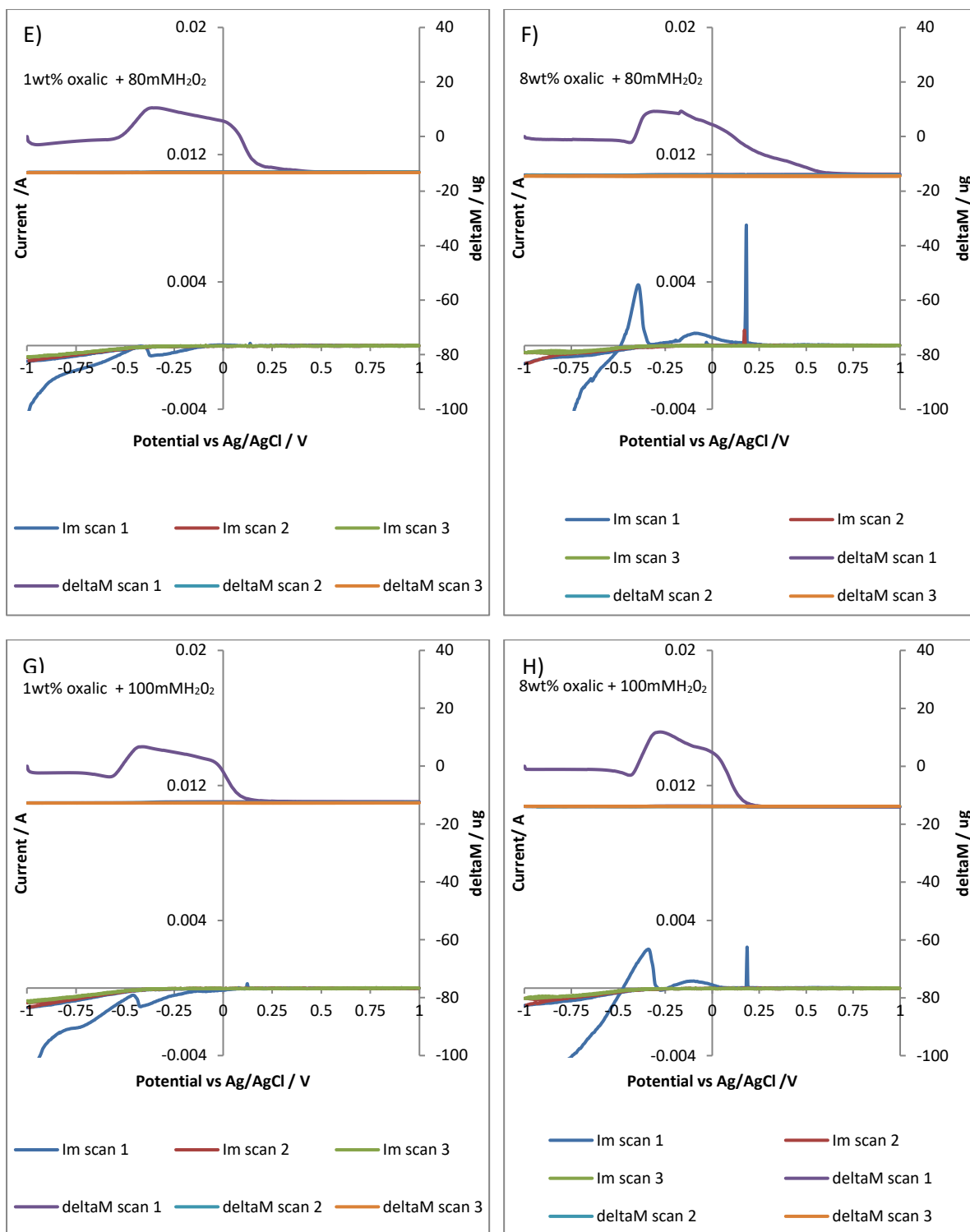


**Figure 5.2.6.:** Comparing the mass change of an iron crystal when the surface is scanned from -1V to +1V in 1 and 8wt% oxalic acid as a function of H<sub>2</sub>O<sub>2</sub> concentration.

In the presence of hydrogen peroxide, similar limits can be identified by inspection of Figure 5.2.1. If we consider the data recorded in the presence of 60mM H<sub>2</sub>O<sub>2</sub> first, inspection of Figures 5.2.1 C and D indicates that different windows should be used for the data recorded from 1 and 8wt% oxalic acid solutions. For 1wt% oxalic acid, the window should be -0.45V to -0.25V; however, for 8wt% oxalic acid the window should be -0.45V to 0V.

Thus, Figures 5.2.7A and B show plots analogous to these shown in Figure 5.1.4 for solutions containing 60mM hydrogen peroxide and 1 and 8wt% oxalic acid respectively. That is, both Figures show the molar mass of the deposited oxalate layer as a function of the upper limit of the potential window – the molar masses in each Figure being calculated using equation 5.1.3 and the data of Figures 5.2.1C and D respectively.

For 1wt% oxalic acid data, Figure 5.2.7A shows that in presence of 60mM hydrogen peroxide the molar mass calculated over the potential range -0.45 to -0.25V is 384 g/mole; the analogous molar mass obtained in the absence of hydrogen peroxide, calculated over the potential range -0.45V to +0.25V, is 90 g/mole. For 8wt% oxalic acid data, Figure 5.2.7B shows that the molar mass calculated in presence of 60mM hydrogen peroxide over the potential range -0.45 to 0V is 116 g/mole; this is approximately equal to the analogous molar mass calculated in the absence of hydrogen peroxide over the potential range -0.45V to +0.25V. The reasons for these differences in the molar masses can be obtained as follows.

As described above, the molar mass is calculated in these experiments by use of equation 5.1.3, given bellow.

$$M = \frac{z \cdot F \cdot \Delta m}{\Delta Q} \quad \text{Equation 5.1.3.}$$

Where  $\Delta Q$  is obtained from the integrated oxidation current passed over the potential window of interest and  $\Delta m$  is the mass change at the iron piezoelectrode surface obtained via the Sauerbrey equation.

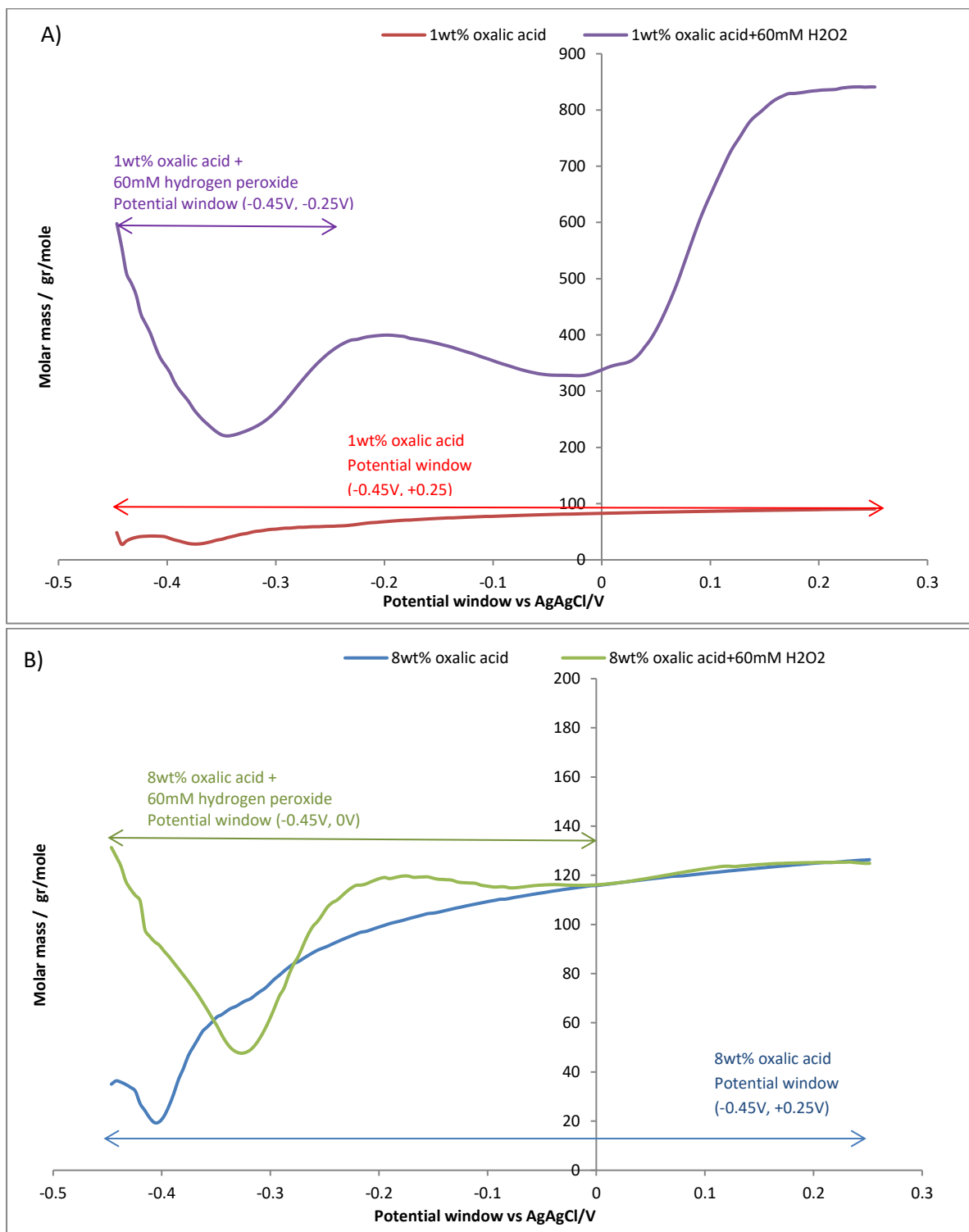


**Figure 5.2.7.:** The molar mass of the deposited material layer in function of the potential window with starting point of -0.45V when iron quartz crystals immersed in, 1wt% oxalic acid / hydrogen peroxide mixtures A) and in 8wt% oxalic acid / hydrogen peroxide mixtures B)

The presence of hydrogen peroxide can thus seem to affect the molar mass calculated of equation 5.1.3 in two ways:

- i. The electrochemical reduction of hydrogen peroxide observed in Figure 5.2.2 will artificially suppress the net oxidation current passed during Fe(II)oxalate formation, so leading to a smaller  $\Delta Q$  value that might be expected. This will result in an artificial increase in the calculated value of M.
- ii. As described above, hydrogen peroxide will, through the hydroxyl radicals generated via equations 3.2.3 and 3.2.4, partly mineralize the Fe(II) oxalate generated at the piezoelectrode surface. This will result in a decrease in the value of  $\Delta m$  obtained and so a similar decrease in the value of M via equation 5.1.3.

The increase in the value of M calculated from data 1wt% oxalic acid solutions in the presence of hydrogen peroxide compared to that calculated in the absence of hydrogen peroxide can thus be readily understood in light of these two effects. It appears that effect (i) dominates, leading to an artificial increase in the value of M.

That no such discrepancy in the value of M calculated from 8wt% oxalic acid solutions in the presence and absence of hydrogen peroxide is then initially counter - intuitive – but can be understood in light of the fact that, again as discussed above, the Fe(II)oxalate layer formed in 8wt% oxalic acid is thicker than that formed in 1wt%. This thicker layer seems to have the effect of blocking the hydrogen peroxide reduction reaction, so attenuating its impact of effect (i); it also seems that the larger mass of Fe(II)oxalate deposited swamps any mass loss due to effect (ii), similarly attenuating the impact of effect (ii) on M. The values of M obtained in the presence and absence of hydrogen peroxide are thus similar.

### 5.3 Summary

A potentiostat and a QCN were connected in tandem in order to measure the mass change of an iron quartz crystal during electrochemical experiments in simulated radioactive and non-radioactive environments.

In non-radioactive environments, results reveal that at the potential window of -0.45V to +0.4V the QCN has the ability to measure the mass gain while insoluble ferrous oxalate insulates the surface of the crystal. It is also shown that increasing the oxalic acid concentration the thickness of the oxalate layer increases as well. At higher potentials the mass loss due to ferrous oxalate being oxidized to ferric oxide species can be measured.

In simulated radioactive environments, results reveal that at the potential window of -0.5V to +0.25V the QCN has the ability to measure the mass gain or loss during two chemical processes such as the ferrous oxalate production and the Fenton reactions. This ability makes the QCN an interesting technique for measuring corrosion rates of nuclear plant, such as high active waste tanks.

Finally, this chapter illustrates the ability of the QCN to measure the molar mass of any electrodeposited layer when the surface is scanned at a certain potential window, highlighting key points for accurate results.

## Chapter 6

## 6. Monitoring corrosion rates using corrosion current ( $i_{\text{CORR}}$ ) measurements

Chapter 5 described how the QCN can be used to provide additional insights into the mechanisms and products of the corrosion reactions of iron (as a mild carbon steel surrogate) in the presence of oxalic acid. One aspect of these corrosion processes that was not discussed was its quantification of the rate of corrosion itself. Thus, these next two chapters discuss these corrosion rates in detail. In this chapter, we report how the corrosion rate may be determined from  $i_{\text{CORR}}$  values obtained from linear sweep voltammetry data using a method described by the ASTM [52]. The next chapter then describes a new and novel method of determining corrosion rates from QCN data and compares those values with these obtained from the  $i_{\text{CORR}}$ . Thus, this chapter details how the  $i_{\text{CORR}}$  values to be used for calculating the mass change of an iron crystal in non-radioactive and in simulated radioactive environments can be measured. In this work 60mM hydrogen peroxide was used as a simulant for the effects of radiation on water i.e. the product of gamma radiolysis, in the waste tanks at the Hanford and Savannah River Sites (SRS) in the US as has been described in section 3.2.

### 6.1 Non-radioactive and simulated radioactive environments

Advantageously in terms of quantifying the corrosion behaviour of iron piezoelectrodes immersed in oxalic acid/hydrogen peroxide mixture, the data of Figure 5.2.4 given here as Figure 6.1.1 for the convenience of the reader, can be used to obtain both the corrosion potential (as described in chapter 5) and corrosion rate, expressed as a mass change rate, for these mixtures.  $E_{\text{CORR}}$  can be obtained from the plots of  $\log|\text{current}|$  vs potential also shown in Figure 6.1.1 from which  $E_{\text{CORR}}$  values for these systems may be seen to be  $\sim -0.5\text{V}$  (again, see chapter 5 for more detail).

The corrosion rate for each system may be obtained by use of the  $i_{CORR}$  and a standard data treatment method as defined by the ASTM [52].

As described in chapter 5, one  $E_{CORR}$  value is obtained from linear sweep voltammetry experiments conducted in the presence of 1 and 8 wt% oxalic acid but in the absence of  $H_2O_2$ . However, the situation is more complicated for experiments conducted in the presence of  $H_2O_2$ , with up to four possible values of  $E_{CORR}$  being manifest, see e.g. Figure 6.1.1.C. However, again as described in chapter 5, the three higher ' $E_{CORR}$ ' values are as a result of a hydrogen peroxide reduction current being super-imposed over iron passivating reactions in the presence of oxalate, and so can be ignored. The lowest of these  $E_{CORR}$  values can, however, be considered a genuine corrosion potential arising from coupling of iron oxidation processes to the peroxide reduction process. We shall therefore use the  $i_{CORR}$  value associated with this  $E_{CORR}$  in the usual way.

Excerpted from the data of Figures 6.1.1 A, B, C and D, Figure 6.1.2 show the detail of the Tafel plots and Tafel relationships for the anodic and cathodic current branches either side the  $E_{CORR}$  for Fe piezoelectrodes immersed in 1 and 8 wt% oxalic acid in absence and presence of 60mM  $H_2O_2$ . Extrapolated  $E_{CORR}$  and  $i_{CORR}$  values, obtained by equating the anodic and cathodic current branch Tafel relationships at each solution, are given in Table 6.1.1.

In each case, the  $i_{CORR}$  value can be converted to a mass change rate by use of Equation 6.1.1 [52]:

$$\text{Mass change rate} = K_2 i_{CORR} EW \quad \text{Equation 6.1.1}$$

Where  $K_2$  ( $K_2=8.954 \cdot 10^{-3} \text{ gcm}^2/\mu\text{Am}^2\text{d}$ ) is a constant and EW is the so – called equivalent weight, based on the assumption that key anodic process is  $\text{Fe} \Rightarrow \text{Fe}^{2+} + 2e^-$ ; EW here is equal to  $55.84/2=27.42$ . Mass change rates calculated using Equation 6.1.1 are also given in Table 6.1.1.

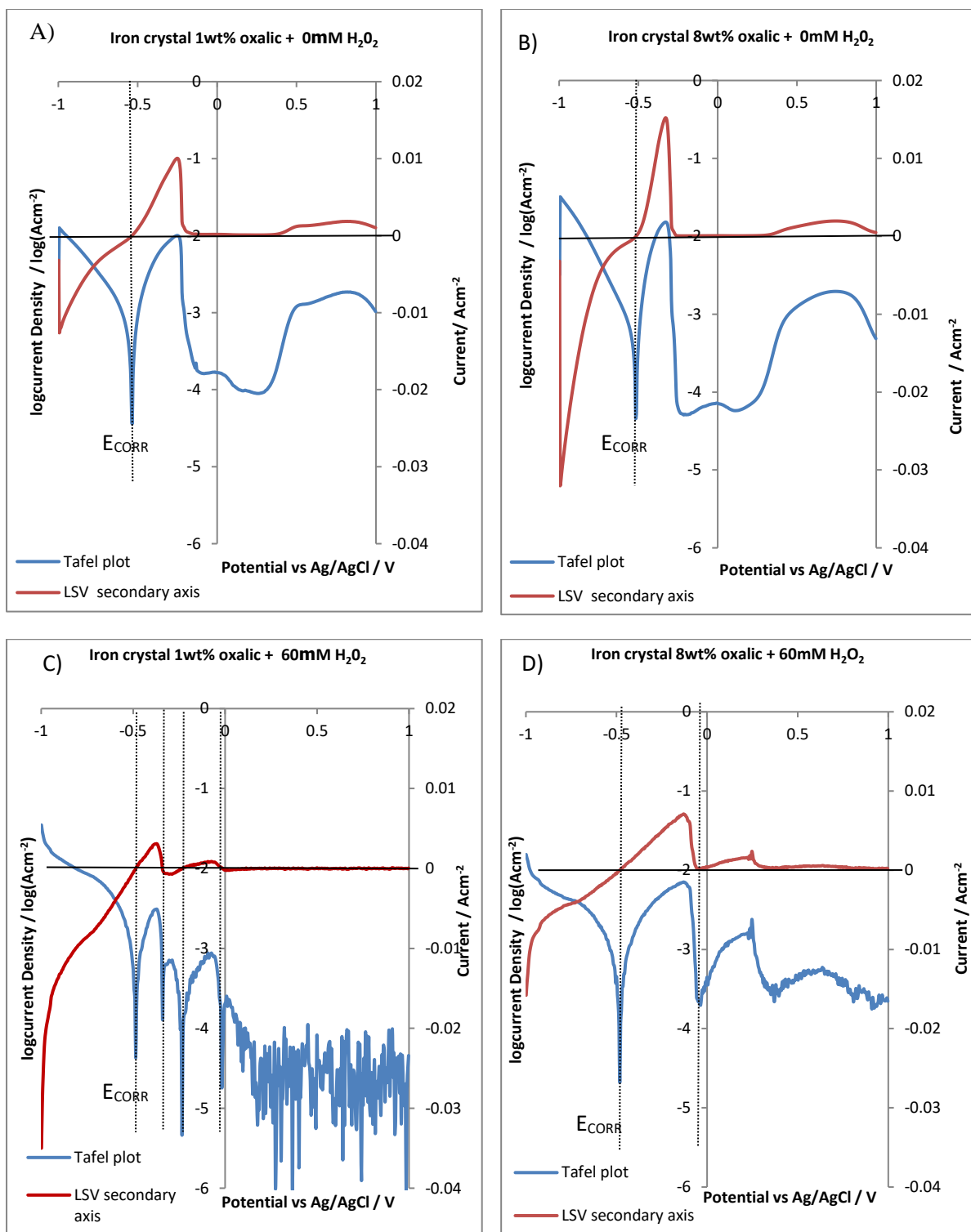


**Figure. 6.1.1.:** Forward going sweeps per surface area in the first scan cyclic voltammograms, and associated LSVs, of iron piezoelectrodes in a mixture of 1 and 8 wt% oxalic acid in presence and absence of H<sub>2</sub>O<sub>2</sub> concentrations.

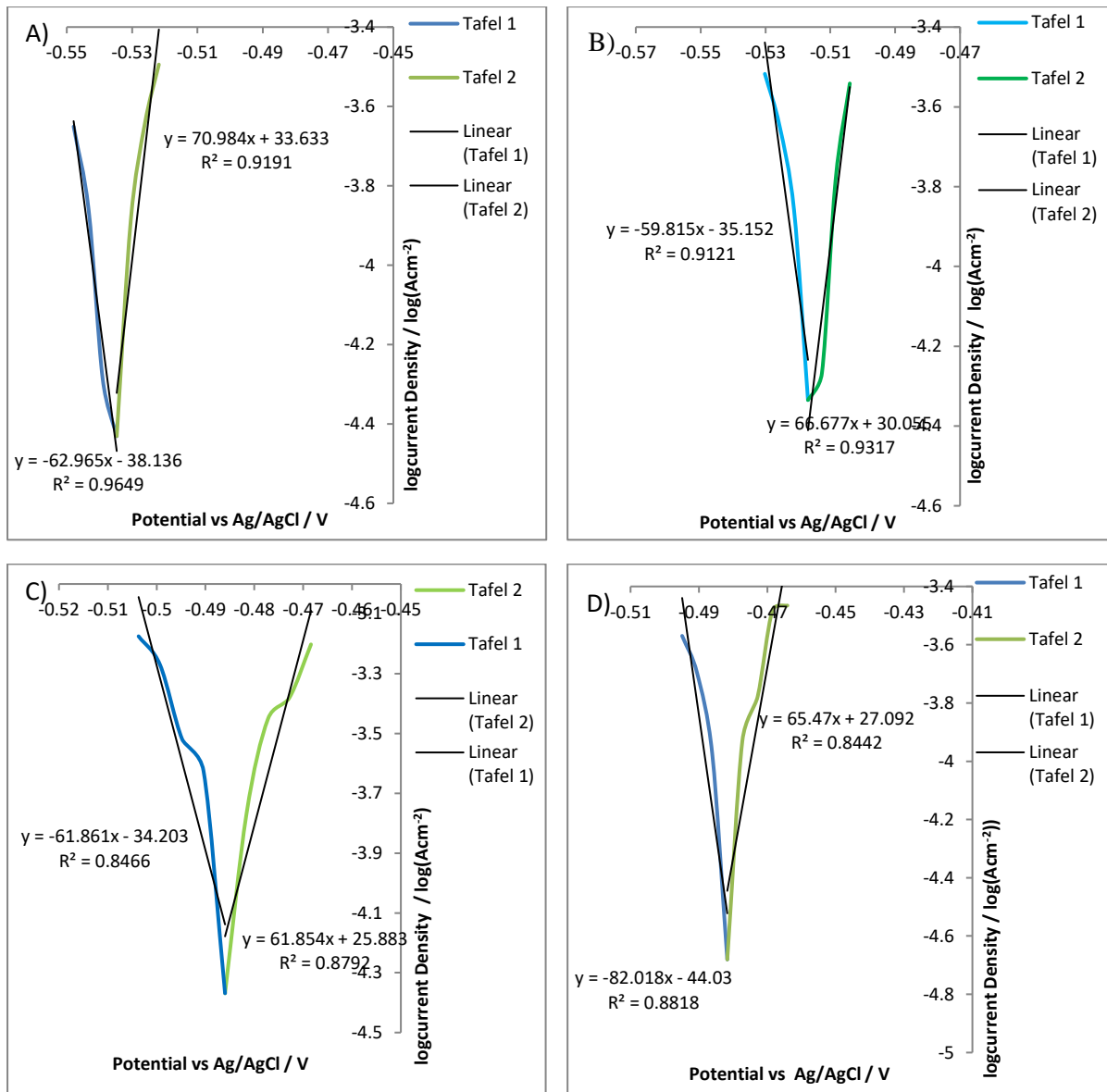


**Figure 6.1.2.:** Tafel plots for data in the vicinity of the  $E_{CORR}$ , extracted from Figures 6.1.1.A, B, C and D respectively. Extrapolated  $E_{CORR}$  and  $i_{CORR}$  values are given in Table 6.1.1.

**Table 6.1.1.:** Calculating the mass change using  $i_{CORR}$  values obtained from the data of Figure 6.1.1 via the extrapolation of the Tafel relationships shown in Figure 6.1.2.

Parameters	1wt% oxalic acid	8wt% oxalic acid	1wt% oxalic acid + 60mM H <sub>2</sub> O <sub>2</sub>	8wt% oxalic acid + 60mM H <sub>2</sub> O <sub>2</sub>
$E_{CORR}$ (V)	-0.536	-0.515	-0.486	-0.482
$i_{CORR}$ ( $\mu A/cm^2$ )	38.5	48.2	69.4	32.3
$K_2$ ( $gcm^2/\mu Am^2d$ )	$8.954 \times 10^{-3}$	$8.954 \times 10^{-3}$	$8.954 \times 10^{-3}$	$8.954 \times 10^{-3}$
$W$	55.845	55.845	55.845	55.845
$n$	2	2	2	2
$EW = W/n$	27.92	27.92	27.92	27.92
Mass change rate $= K_2 i_{CORR} EW \left( \frac{g}{cm^2 d} \right)$	$\pm 0.96 \times 10^{-3}$	$\pm 1.2 \times 10^{-3}$	$\pm 1.7 \times 10^{-3}$	$\pm 0.8 \times 10^{-3}$

A key issue here is that  $i_{\text{CORR}}$  measurements give no insight into whether the  $\text{Fe} \Rightarrow \text{Fe}^{2+}$  oxidation leads to a dissolution derived mass loss from the electrode or a precipitation derived mass increase associated with for instance the formation of Fe(II) oxalate. QCN based corrosion measurements avoid this ambiguity as will be seen below.

This limitation aside, it is worth comparing all the corrosion rates reported in Table 6.1.1 from which it can be seen that they all have similar values. This suggests that:

1. Increasing the oxalate concentration does not affect the corrosion rate. This can be understood from comparing the  $E_{\text{CORR}}$  values reported from the experiments conducted in 1 and 8 wt% oxalic acid but in the absence of hydrogen peroxide. Both return a  $E_{\text{CORR}}$  value of  $\sim -0.5\text{V}$  from solutions with pH of  $\sim 1$ . Inspection of the Pourbaix diagram for the Fe-oxalate- $\text{H}_2\text{O}$  system in Figure 3.1.2 indicates that this places the system in the region where  $\text{Fe}^{2+}$  is stable. i.e. the processes coupling at this  $E_{\text{CORR}}$  are simply  $\text{H}^+$  reduction and Fe oxidation to form  $\text{Fe}^{2+}$  - hence the independence of the  $i_{\text{CORR}}$  (and  $E_{\text{CORR}}$ ) on oxalate concentration.
2. Introduction of  $\text{H}_2\text{O}_2$  into these oxalate systems has little effect on both  $i_{\text{CORR}}$  and  $E_{\text{CORR}}$ ; thus the kinetics of  $\text{H}_2\text{O}_2$  reduction under these conditions of these experiments must be similar to those of  $\text{H}^+$  reduction. From comparison of Figure 5.2.2 and Figure 3.1.3 this can be seen to be the case.

## 6.2 Summary

The main objective of the work described in this chapter was to measure mass change using basic electrochemical experiments and to explore the possibility of using these techniques in complex environments where more than one reaction can be observed near to  $E_{\text{CORR}}$  potentials.

Results reveal that the mass change can be calculated using the  $i_{\text{CORR}}$  measurements. Next chapter measures the mass change in real time using the QCN technology and compares them with those presented in this chapter.

## Chapter 7

## 7 Real time nanogravimetric monitoring of corrosion using QCN

Monitoring and understanding of corrosion on nuclear sites plays a key role in safe asset management and supporting informed choice of decontamination methods for steels due for decommissioning. Recent advances in Quartz Crystal Nanobalance (QCN) technology offer a means to monitor corrosion in-situ in radiologically harsh environments, in real time and with high sensitivity. In this experimental work the open circuit potential and the mass change of iron crystals mounted within a commercially available QCN probe have been measured in real time in simulated radioactive and non-radioactive environments. This chapter shows how the mass change and open circuit potential observed when an iron crystal is immersed in simulated ECC environments can be used for QCN-based real time corrosion monitoring.

### 7.1. Non-radioactive environments

This section details the comparison of the open circuit potential and the mass change recorded from an iron coated quartz crystal mounded with a commercially available QCN probe (see chapter 2) immersed in 1 and 8wt% oxalic acid.

Figures 7.1.1A and B show  $E_{OC}$  and nanogravimetric data recorded as a function of time, from Fe piezoelectrodes using the QCN in 1 and 8 wt% oxalic acid. Time  $t = 0$  corresponds to the point at which the QCN mounted Fe piezoelectrode is first immersed in the oxalic acid solution. The  $E_{OC}$  and nanogravimetric traces at 1 and 8 wt% oxalic acid both exhibit 4 distinct sequential regions:

- **Region 1:** Little to no change in mass with an initial  $E_{OC}$  of +0.3 V in 1 wt% oxalic acid and +0.5V in 8 wt%.

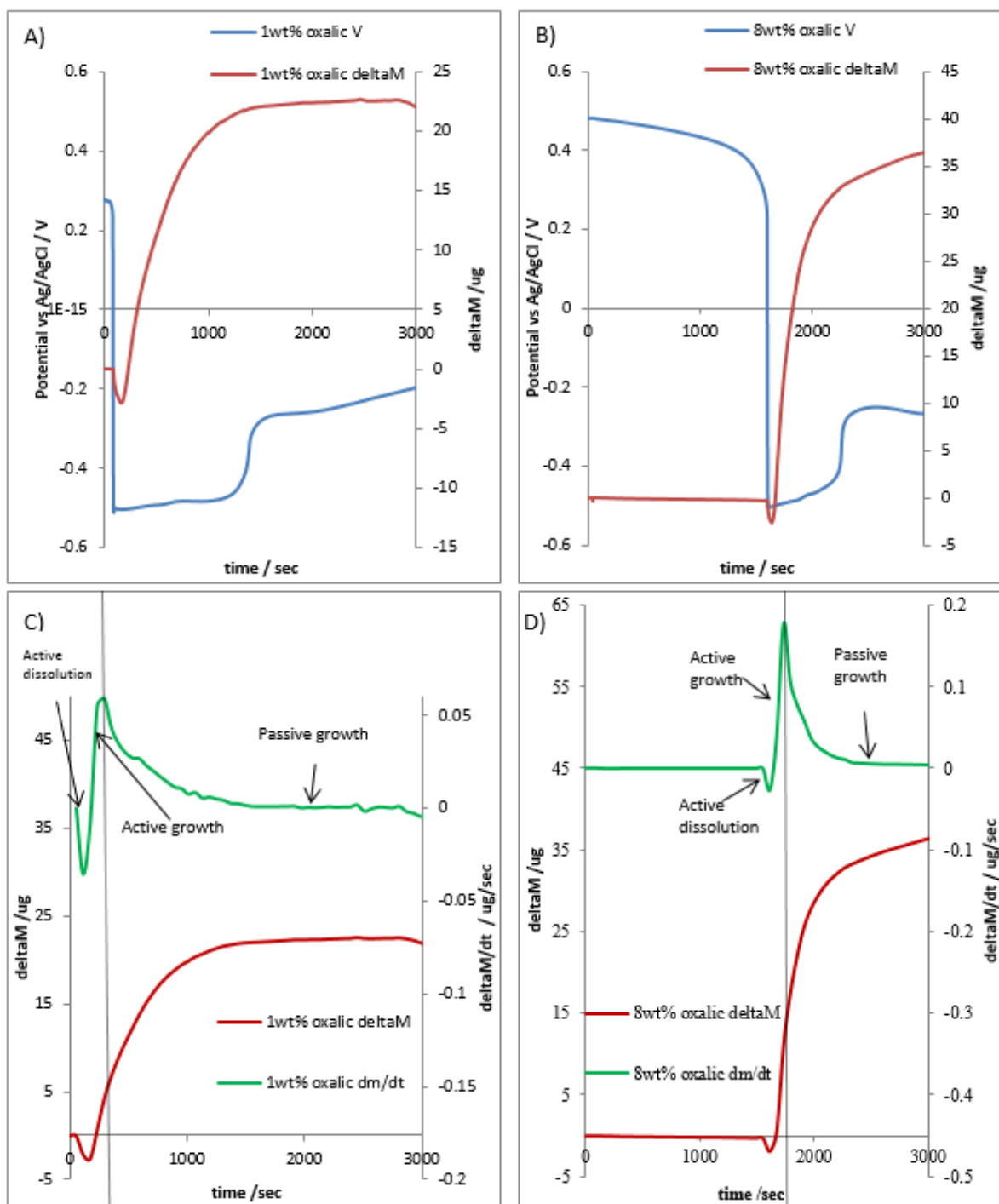


**Figure 7.1.1.:** (A) & (B):  $E_{oc}$  and nanogravimetric data as a function of time, recorded from Fe piezoelectrodes using the QCN in 1 and 8 wt% oxalic acid respectively. Time  $t = 0$  corresponds to the point at which the QCN mounted Fe piezoelectrode is first immersed in the relevant oxalic acid solution. (C) & (D): Derivatives with respect to time of the nanogravimetric data of Figures 7.1.1A & 7.1.1B respectively. For convenience, source nanogravimetric data are also reproduced from Figures 7.1.1A and 7.1.1B.

- **Region 2:** A rapid decrease in the  $E_{OC}$  to  $\sim -0.5$  V for both oxalic acid concentrations accompanied by a small decrease in piezoelectrode mass.
- **Region 3:** A rapid increase in mass accompanied by a gradual increase in  $E_{OC}$  from  $-0.5$  V to  $\sim -0.4$  V. The end of Region 3 is marked by an abrupt increase in  $E_{OC}$  to  $\sim -0.25$  V and by an almost abrupt slowing of the rate of mass increase.
- **Region 4:** A near constant  $E_{OC}$  of  $-0.25$  V for both oxalic acid concentrations, accompanied by an increase in piezoelectrode mass, albeit at a much slower rate than in Region 3.

The  $E_{OC}$  behaviour in Regions 1 and 2 is similar to that seen by Cartledge when stainless steel 347 electrodes are immersed in pH 1.46 sulfuric acid [100], the Region 1 behaviour being attributed to the slow acid dissolution of a layer of  $Fe_2O_3$  generated at the electrode surface by aerial oxidation prior to electrode immersion [100], [101].

Once this  $Fe_2O_3$  layer has thinned to the point that the underlying Fe is exposed, reduction of the remaining  $Fe_2O_3$  to  $Fe^{2+}$  galvanically couples with the oxidation of Fe metal to  $Fe^{2+}$ , resulting in an abrupt decrease in  $E_{OC}$  and an instantaneous mass loss at the electrode surface [100],[101], Region 2. As seen in Figure 7.1.1, this efflux of  $Fe^{2+}$  into solution then interacts with solution oxalate to generate a layer of passivating  $FeC_2O_4$  at the electrode surface with a corresponding rapid increase in electrode mass and an arrest in the negative trajectory of the  $E_{OC}$ , Region 3.

Finally, both Fe metal oxidation and consequent ferrous oxalate formation is self-limited by the presence of the  $FeC_2O_4$  layer at the electrode surface and the  $E_{OC}$  comes to rest at a potential that, as can be seen from Figures 3.1.2A, 5.2.4A and 5.2.4B, corresponds to a region of  $FeC_2O_4$  derived electrode passivity i.e. the  $FeC_2O_4$  corrosion product layer has entered a region of passive growth. Having explained the forms of the  $E_{OC}$  and mass vs. time traces of Figures 7.1.1A and 7.1.1B, it is informative to consider the first differentials of the mass vs. time traces in order to obtain corrosion

rates, in the form of mass change rates, as a function of time. The resultant (dm/dt) vs. time plots are shown in Figures 7.1.1C and 7.1.1D.

Of particular interest in Figures 7.1.1A and 7.1.1B is the behaviour of the (dm/dt) vs. time plots in the regions where substantive mass changes are occurring i.e. Regions 3 and 4. Here it can be seen that the (dm/dt) vs. t traces rise to a maximum corrosion rate in Region 3 before relaxing back to a smaller, constant corrosion rate in Region 4.

**Table 7.1.1.:** Comparing the mass change rates obtained using  $i_{\text{CORR}}$  and Quartz Crystal Nanobalance measurements as a function of oxalic acid concentration.

oxalic acid concentration / wt%	corrosion rate obtained from $i_{\text{CORR}}$ / $\text{g day}^{-1} \text{cm}^{-2}$	maximum corrosion rate obtained from QCN / $\text{g day}^{-1} \text{cm}^{-2}$	passive corrosion rate obtained from QCN / $\text{g day}^{-1} \text{cm}^{-2}$
1	$\pm 0.96 \times 10^{-3}$	$+24.9 \times 10^{-3}$	$+1.19 \times 10^{-3}$
8	$\pm 1.2 \times 10^{-3}$	$+75.2 \times 10^{-3}$	$+1.71 \times 10^{-3}$

Table 7.1.1 reports both the QCN determined maximum observed corrosion rate of region 3 as well as the lower, constant corrosion rate of region 4 for both investigated concentrations of oxalic acid. It also compares these with the corrosion rates determined from the  $i_{\text{CORR}}$  measurements and calculations of Figures 6.1.2 and Table 6.1.1. Tables 6.1.1 & 7.1.1 and Figure 7.1.1 allow for a number of observations to be made.

1. There is very good agreement between the respective corrosion rates calculated from  $i_{\text{CORR}}$  values and those calculated from QCN data recorded in the passive growth region (Table 7.1.1), indicating that  $i_{\text{CORR}}$  derived rates reflect passive growth rates as well.
2. The QCN allows for time dependence of corrosion rates to be measured in situ and in real time (Figure 7.1.1);  $i_{\text{CORR}}$  based measurements allow for neither.
3. Corrosion rates calculated using QCN data explicitly describe whether the mass changes correspond to mass increases or mass losses (Figure 7.1.1); no such information is available from corrosion rates calculated using  $i_{\text{CORR}}$  values.

4. In contrast to  $i_{\text{CORR}}$  based measurements, corrosion rates calculated using QCN data require no assumptions be made regarding the galvanically coupling half-reactions; indeed the coupling of nanogravimetric data with  $E_{\text{OC}}$  measurements afforded by the QCN can allow for the explicit identification of the reactions giving rise to the measured corrosion derived mass change. For example Figures 7.1.1, by comparison with Figures 3.1.1 and 3.1.2 of chapter 3, reveal that the mass increases measured in each case are due to the oxidation of Fe to  $\text{Fe}^{2+}$  followed by the deposition of a  $\text{FeC}_2\text{O}_4$  product at the electrode surface rather than the  $\text{Fe}/\text{Fe}^{2+}$  oxidation alone, as assumed in the  $i_{\text{CORR}}$  based corrosion rate calculation.

These observations underline the benefits that may be derived from using the QCN as a simple dipstick style corrosion monitor. We now go on to consider the advantages that it may afford in measurement of corrosion rates in peroxide rich environments such as those that may obtain in HLW storage tanks, *vide supra*.

## 7.2. Simulated radioactive environments

The corrosion behaviour of mild carbon steel and iron samples in a variety of oxalic acid solutions in non-radioactive and in simulated radioactive environments has been measured previously and is described in detail in chapter 3. In that work hydrogen peroxide was used as a simulant for the effects of radiation on water i.e. the product of gamma radiolysis. This section extends the work on the advantages of using QCN as a corrosion monitoring technique to  $\text{H}_2\text{O}_2$  - simulated radioactive environments, and demonstrates the ability of QCN technology to measure the effect of the Enhanced Chemical Cleaning (ECC) process at ambient temperature.

As above, the  $E_{\text{OC}}$  and the mass change were measured using a QCN in tandem with a potentiostat. The open circuit potential of an iron QCN coated crystal in 60 mM  $\text{H}_2\text{O}_2$  solution was measured for one hour and then for another hour following the introduction of oxalic acid.

In the concentration of 1wt% oxalic acid addition of oxalate was achieved by titrating in a solution of concentrated oxalic acid that would result in the final oxalate concentration be 1wt%. Such an approach proved to be infeasible for 8wt% and thus experiments at that concentration were not regarded to be reliable and so are not presented here.

Figure 7.2.1 shows the time depending of the mass and the  $E_{OC}$  changes observed from an iron crystal in 60 mM  $H_2O_2$  with 1 wt% oxalic acid. During the first hour and in presence only of 60 mM  $H_2O_2$ , there is no mass change with an initial  $E_{OC}$  of  $\sim +0.3$  V, a value consistent with the electrode being passivated by a layer of  $Fe_2O_3$  at this pH [91]. These results are very similar to these presented in Figure 5.2.3 for an identical experiment (i.e. iron piezoelectrode immersed in 60mM  $H_2O_2$ ) where the fluctuating potential observed is explained in terms of metastable pit formation and repassivation in the  $Fe_2O_3$  layer. After 1 hour and the addition of 1 wt% oxalic acid, 3 distinct sequential regions for the mass and  $E_{OC}$  change can be seen discussed as follow.

- **Region 1:** There is little to no mass change with an  $E_{OC}$  increase to  $\sim +0.4$  V. The end of the region is marked with a sharp mass loss associated with oxalic-driven dissolution of the passivating  $Fe_2O_3$  layer (c.f. region 1 in Figure 7.1.1).
- **Region 2:** There is a rapid mass gain due to iron oxalate formation accompanied by a sharp  $E_{OC}$  decrease to  $-0.5$  V a potential at which oxalic reacts with oxidatively generated  $Fe^{2+}$  to produce  $FeC_2O_4$  [102] (again, c.f. region 2, Figure 7.1.1). This is followed by a sharp mass loss due to oxalate mineralization within the  $FeC_2O_4$  deposit by  $HO\bullet$  produced by the coupling of some of the previously electrogenerated  $Fe^{2+}$  ions with  $H_2O_2$  – the Fenton type reactions of equations 3.2.3 and 3.2.4. This is accompanied by a potential increase to levels close to those seen in the presence of  $H_2O_2$  only (pre-region 1, Figure 7.2.1) and the surface repassivates due to  $Fe_2O_3$  formation.

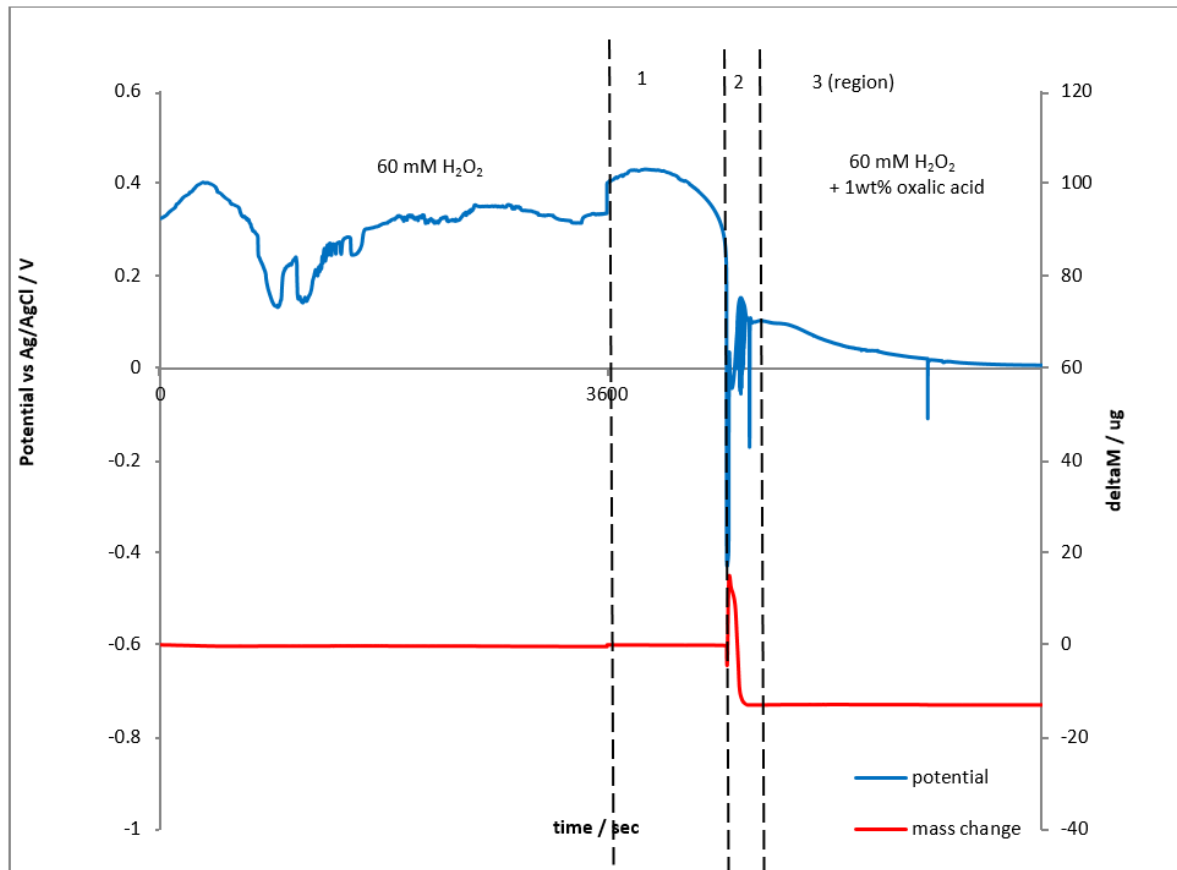


**Figure 7.2.1.:**  $E_{OC}$  and nanogravimetric data as a function of time, recorded from Fe piezoelectrodes in 60 mM  $H_2O_2$  and a mixture of 1wt% oxalic acid and 60 mM  $H_2O_2$ .

- Region 3:** This layer of  $Fe_2O_3$  might then be expected to be redissolved by oxalic acid. However, the mass trace indicates that the  $Fe_2O_3$  layer persists throughout region 3, probably due oxalic acid undergoing local mineralization by  $HO\bullet$  produced by the coupling of  $Fe^{2+}$  (generated in region 2) with  $H_2O_2$  due to equations 3.2.3 and 3.2.4.

Having explained the forms of the  $E_{OC}$  and mass vs. time traces of Figures 7.2.1, it is informative to consider the first differentials of the mass vs. time traces in order to obtain corrosion rates, in the form of mass change rates, as a function of time. Such calculations were presented in section 7.1 for data recorded in the absence of hydrogen peroxide and an exactly analogous approach is adopted here. Of particular interest in Figures 7.2.1 is the behaviour of the m vs. time plots in the time range  $t=4400$  to  $4800$  where the system transitions from region 1 to region 3 and where substantive mass changes are occurring. The resultant  $(dm/dt)$  vs. time plots are shown in Figures 7.2.2 as is the detail

of the  $m$  vs  $t$  plot in the same time range. From Figure 7.2.2, it can be seen that the  $(dm/dt)$  vs.  $t$  traces initially decrease to negative  $(dm/dt)$  values on transitioning from region 1 to region 2 due to active dissolution. The  $(dm/dt)$  values then swings a positive value on entering region 2, exhibiting a maximum corrosion rate due to ferrous oxalate formation at the iron surface. This period of increasing positive  $dm/dt$  is then followed by a period where  $dm/dt$  decreases back to zero i.e. the mass of the electrode decreases. The reason for this can be understood by comparing the form of the mass plot of Figure 7.2.2 with the  $m$  vs.  $E$  plot of Figure 5.2.1.C. They are of similar form, reflecting their similar origins i.e. the period of mass decrease seen in the region  $t=4580$  to  $4700$ sec is due to the action of peroxide on the ferrous oxalate layer formed in the range  $t=4560$  to  $4580$ s. This forms soluble ferric oxalate, leaving a thin residual layer of passivating  $Fe_2O_3$  at the iron piezoelectrode surface. As can be seen from Figure 7.2.2, the whole cycle of iron to  $Fe^{2+}$ , subsequent formation of ferrous oxalate and oxidative dissolution as ferric oxalate results in a net mass loss from the piezo electrode surface.

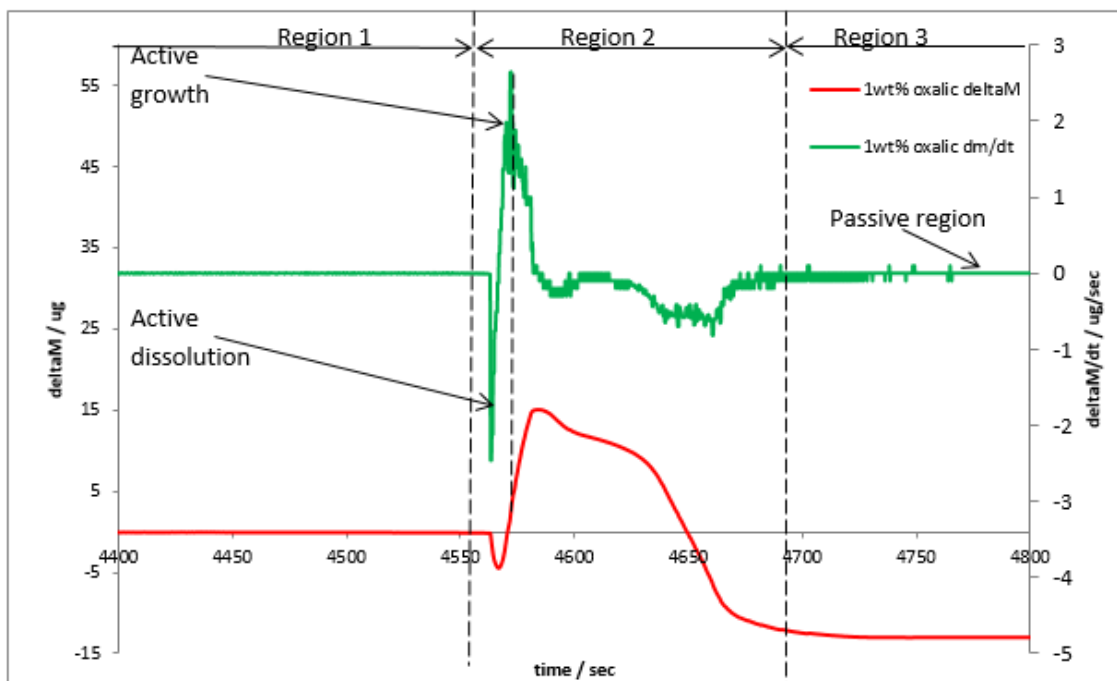


**Figure 7.2.2.:** Derivative with respect to time of the nanogravimetric data of Figures 7.2.1. For convenience, source nanogravimetric data is also reproduced from Figures 7.2.1. Data extracted from  $t=4400$  to  $4800$  in Figure 7.2.1.

**Table 7.2.1.:** Comparing the mass change rates obtained using  $i_{\text{CORR}}$  and Quartz Crystal Nanobalance measurements in presence and absence of 60mM  $\text{H}_2\text{O}_2$ .

concentration	corrosion rate obtained from $i_{\text{CORR}}$ / $\text{g day}^{-1} \text{cm}^{-2}$	maximum corrosion rate obtained from QCN / $\text{g day}^{-1} \text{cm}^{-2}$	passive corrosion rate obtained from QCN / $\text{g day}^{-1} \text{cm}^{-2}$
1wt% oxalic acid	$\pm 0.96 \times 10^{-3}$	$+24.9 \times 10^{-3}$	$+1.19 \times 10^{-3}$
1wt% oxalic acid + 60mM $\text{H}_2\text{O}_2$	$\pm 1.7 \pm \times 10^{-3}$	1.16	$\approx 0$

Let us now compare the quantitative corrosion rates obtained from the QCN data of Figure 7.2.2 with those obtained from the  $i_{\text{CORR}}$  values reported for the same system in chapter 6. This is done in Table 7.2.1.

Thus Table 7.2.1 reports, for experiments conducted in 1wt% oxalic acid in the presence and absence of 60mM  $\text{H}_2\text{O}_2$ , both the QCN - determined maximum observed corrosion rate as well as the lower, constant corrosion rate and compares these with the corrosion rates determined from the  $i_{\text{CORR}}$  measurements and calculations of Figures 6.1.2 and Table 6.1.1. Table 7.2.1 and Figure 7.2.1 allow for a number of observations to be made.

- In the presence of hydrogen peroxide the maximum corrosion rates obtained using real-time QCN measurements is  $1.16 \text{ g day}^{-1} \text{cm}^{-2}$ . It is notable that the associated mass gain of this peak happens in approximately 20 sec (see Figure 7.2.1). The above observation indicate the ability of the hydrogen peroxide to act as a very good oxidation agent with the added characteristic to act as a catalytic element on the iron – oxalate- hydrogen peroxide system, resulting in a very high mass change in a short period of time.
- In the presence of hydrogen peroxide the passive corrosion rates obtained using the QCN technology drops close to zero levels which corresponds to a passive region where the reactions of the iron – oxalate- hydrogen peroxide system have occurred fully resulting in system passivation (via the formation of the thin residual layer of  $\text{Fe}_2\text{O}_3$  alluded to above).

- Corrosion rates calculated from  $i_{CORR}$  values correspond to an average corrosion rate over the period of reading of the associated LSV. QCN measurements have the advantage of measuring the changes in corrosion rate as a function of time. This observation is pronounced in the iron – oxalate - hydrogen peroxide system where the maximum and thus total corrosion rate depends on reactions that happen only in region 2 of Figure 7.2.1. The later finding is beneficial information for corrosion protection monitoring in nuclear applications. For instance, and during a decontamination campaign in Savannah River Site Savannah River Site, the mass body of the waste tank wall is expected to change in a short time period (corresponding to region 2 of Figure 7.2.1 and 7.2.2) whilst the mass change of the waste tank wall in long time period is expected to be negligible (corresponding to region 3 of Figure 7.2.1). According to this information it is expected that very long time breaks between several oxalic acid strikes will not affect the waste tank decontamination process.

These findings indicate that QCN technology can measure active (pre-passive) and the passive corrosion rates as discussed above, instead of the average corrosion rates calculated from  $i_{CORR}$  measurements underlining the advantages of the QCN as a simple dipstick style corrosion monitor to measure the corrosion rates in real time in situ in simulated radioactive environments.

### 7.3 Summary

The electrochemical quartz crystal nanobalance has been used as a corrosion monitor for steel analogues for the first time under conditions relevant to nuclear decommissioning in simulated radioactive environments. Results reveal that QCN can be a useful technological tool for measuring the corrosion rates in situ in real time when two chemical reactions are taking place such as the ferrous oxalate layer production and Fenton like reactions.

This chapter reports the ability of QCN to measure the mass change of a quartz crystal in simulated ECC environments at room temperature. Measuring the mass change and the open circuit potential at the same time gives the advantages of:

- i. instantaneous and real time measurement;
- ii. potentially in situ and higher sensitivity measurement;
- iii. insight into the mechanism of the action of oxalic acid on Fe-rich steels;
- iv. introduce the active (pre-passive) and the passive corrosion rates

## Chapter 8

## 8 The use of QCN technology for the electrochemical / nanogravimetric analysis of steel, and real time monitoring of corrosion, for nuclear clean-out applications.

Chapters 5-7 describe the development of the QCN as a corrosion monitor during mild carbon steel tank decontamination using well developed oxalic acid based techniques currently employed at Savannah River Site. Chapters 5-7 also describe the insights that the QCN can provide relating to the underpinning chemistry of this decontamination technique. However, several decontamination methods are currently under development at Savannah River Site and Hanford Site such as the use of nitric/oxalic mixtures, alkaline permanganate and acidic permanganate washes. The interest of Savannah River Site and Hanford Site in these decontamination agents arises for the following reasons, pointing out preferred concentrations of these mixtures for our experiments;

- For nitric/oxalic mixtures, King *et.al.* report that a 1/1 mixture of oxalic acid / nitric acid can achieve better tank cleaning results than oxalic acid alone for iron rich highly active liquid waste sludge heels, thus minimizing the oxalate concentration in secondary wastes [103]. Typically 4-8 wt% of oxalic acid is used for single component ECC. However, as discussed above process engineering and secondary waste management issues have arisen due to low Na oxalate salt solubility ( $37 \text{ g kg}^{-1}$  or  $0.28 \text{ mol kg}^{-1}$  at  $303.15 \text{ }^{\circ}\text{K}$  in water [72]). In order to these decrease downstream issues, research has been focusing on 1 wt% solutions of oxalic acid and it has been proposed that under specific conditions 1 wt% can be more effective than higher oxalic acid concentrations [42]. For the above reasons and only for the needs of this chapter a mixture of 1wt% oxalic acid with 0.18M  $\text{HNO}_3$  (~1wt%) is under development at Savannah River Site and Hanford Site and so will be studied in this chapter.

- It has been reported that both alkaline and acidic permanganate solutions can be used for removal of Strontium (Sr) and actinides from the waste tanks at Savannah River Site and Hanford Site; after permanganate treatment, the sludge can be disposed of as low-activity waste [104], [105]. Little is known about the mechanisms by which the permanganate treatment process removes Sr

and actinides and so these decontamination agents are also under development at Savannah River Site and Hanford Site [105]. During this programme, it has been reported that 0.05M permanganate can achieve good decontamination results [106]; thus, this chapter will also present studies of the corrosion of mild carbon steel analogous at these permanganate concentrations specifically experiments with mixtures of 0.05M  $\text{KMnO}_4$  with 3, 5 and 10M sodium hydroxide will be presented. For the acidic permanganate 0.18M  $\text{HNO}_3$  mixtures with 0.05M  $\text{KMnO}_4$ , pH to 1, will be presented.

As in chapters 5-7 experimental work performed in this chapter uses mild carbon steel samples and iron-on-quartz QCN piezoelectrodes (as a surrogate to mild carbon steel) to represent the waste tank wall. Solutions of nitric/oxalic mixture, alkaline permanganate and acidic permanganate are used as described above, in order to simulate the decontamination campaigns.

Thus, the two objectives of this chapter are to study the effects of cleaning mild steel samples immersed in several decontamination agents under development by Savannah River Site and Hanford Site and identify corrosion behaviour in such solutions using electrochemical techniques. Moreover, this chapter tests the feasibility of using the QCN technology as a corrosion monitor technique for nuclear decontamination applications.

In this chapter, only the corrosion behaviour of mild steel samples immersed in decontamination agents currently being studied at Savannah River Site such as alkaline permanganate, acidic permanganate, oxalic acid and nitric/oxalic mixture is discussed. However, this work may have wider utility as iron rich steel alloys such as mild carbon steel are ubiquitous on nuclear sites and the aforementioned cleaning agents are widely used in decontamination campaigns; thus this work can be applicable to other nuclear decontamination applications such as water cooling circuits and evaporators for volumetric reduction of nuclear liquid waste.

## 8.1 Nanogravimetric and electrochemical analysis of iron and mild steel samples in H<sub>2</sub>C<sub>2</sub>O<sub>4</sub> + HNO<sub>3</sub> at ambient temperature and at 50°C

As described above, metals such as stainless steel and mild steel are ubiquitous on nuclear sites. These metals can form corrosion products, such as ferrous oxide, which can act to insulate the surface of the metal. In some areas of application, highly radioactive isotopes can become entrained in this oxide layer and it is thus essential that corrosion products be removed in order to minimise radiation hazards to operators and, ultimately, closure engineers. There are several methods that can be used to do this. However, one of the most well-known techniques is to treat the oxide layer with a strong acid cleaning agent such as HNO<sub>3</sub> or oxalic acid. An example for the under-primary chemistry is given in equation 8.1.1. [29].



H<sup>+</sup> Produced from acid    Fe<sup>+2</sup> and Fe<sup>+3</sup> Can be found in solution

Equation 8.1.1.

Equation 8.1.1 shows an exemplar reaction that takes place during decontamination of iron rich steel alloys such as mild carbon steel. Organic acid or mineral acids such as oxalic and nitric acid respectively can be used for the H<sup>+</sup> production [29]. King *et.al.* report that 1/1 mixture of oxalic acid / nitric acid can achieve better cleaning results than oxalic acid alone for iron rich highly active liquid waste sludge heels, thus minimizing the oxalate concentration in secondary wastes [103]. In this section, the electrochemical behaviour of a mild steel sample in nitric, oxalic and nitric/oxalic mixture solutions is discussed. The mass change in real time using iron-based (in lieu of more expensive steel based) QCN crystals for corrosion monitoring is reported.

Figures 8.1.1A, B, C and D show the cyclic voltammetric behaviour of a mild carbon steel disc electrode scanned between -1V and +1V in 1wt% oxalic acid and 0.18M HNO<sub>3</sub> single component systems and in 0.18M HNO<sub>3</sub> /1wt% (~0.11M) oxalic mixture (at room temperature and at 50°C) solutions respectively. For all figures, hydrogen evolution can be seen in the range -1V to -0.5V. The

results obtained from the 1wt% oxalic acid solution, Figure 8.1.1.A, are as described in Chapters 5-7 i.e. during the forward going sweep, two oxidation peaks with onsets of -0.5 V and +0.35 V are observed, the former exhibiting an abrupt current decrease at  $\sim -0.1$  V, due to surface passivation arising from the formation of an insoluble protective iron oxalate phase (vide supra). In contrast, in the presence of  $\text{HNO}_3$ , Figure 8.1.1B, only one oxidation peak can be observed at -0.5V to  $\sim +0.9$ V (Figure 8.1.1B). Similarly in nitric/oxalic mixtures only one oxidation peak is again observed but over a shorter voltage range of -0.5V to  $\sim +0.5$ V (Figures 8.1.1 C and D).

During the reverse going sweep, one sharp oxidation peak is observed in 1wt% oxalic acid, with a reverse going onset / peak of +0.2 V, dropping away to zero current by 0 V, Figure 8.1.1A. Again, the formation of this peak has been described in detail in chapters 5-7. A similar feature is seen in the voltammetry of 0.18M nitric acid, Figure 8.1.1.B, with an onset of  $\sim +0.25$ V, dropping to zero current by -0.5V and this feature is also seen in the voltammogram recorded from nitric acid / oxalic acid mixtures, Figure 8.1.1.C and 8.1.1.D.

These features can be interpreted with the assistance of the simplified  $E_h$ -pH diagrams for the Fe-oxalate- $\text{H}_2\text{O}$  and Fe- $\text{H}_2\text{O}$  systems shown in Figures 3.1.2A and B adapted from the work of Pourbaix [81] and Saltykov *et al.* [82] respectively.

From both Figures 3.1.2 A and B, and the fact that the pH of 0.18M  $\text{HNO}_3$ , 1wt% oxalic acid and mixtures of 0.18M  $\text{HNO}_3$  /1wt% oxalic acid (at room temperature and at 50°C) solutions are all approximately 1, it can be seen that the onset of the first wave in the forward going sweep of all CVs in Figure 8.1.1 is due to the oxidation of Fe metal to  $\text{Fe}^{2+}$  ions. In the absence of oxalic acid, Figure 8.1.1B indicates that this reaction can be expected to continue unimpeded up to  $\sim +0.9$  V vs. Ag/AgCl at which point an iron oxide, most likely a ferric oxide phase, can be found on the surface. However, in the presence of oxalic acid, Figure 8.1.1A indicates that  $\text{FeC}_2\text{O}_4$  generated at  $E > -0.2$  V in the single component system can ultimately insulate the electrode surface. In the case of the nitric acid / oxalic

acid mixtures, this passivation point is displaced to  $\sim +0.4$  and  $+0.25V$  at room temperature and  $50^{\circ}C$  respectively.

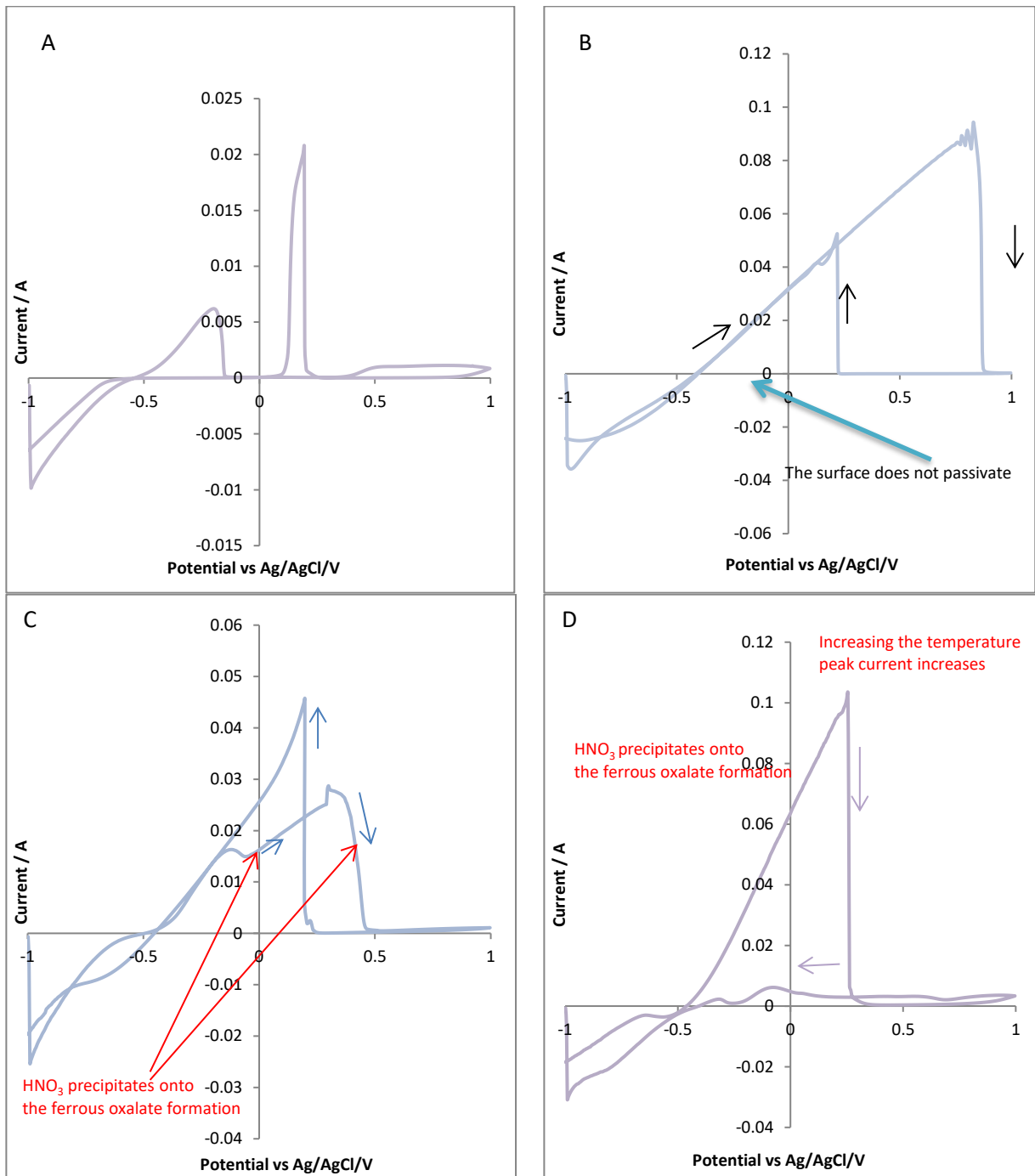


**Figure 8.1.1.:** Comparing cyclic voltammograms of mild carbon steel in: A) 1wt% oxalic acid pH=1, B) 0.18M nitric acid pH=1, C) 0.18M nitric acid / 1wt% oxalic acid mixture at room temperature pH=1 and D) 0.18M nitric acid / 1wt% oxalic acid mixture at  $50^{\circ}C$  pH=1.

The interpretation of these features can be assisted by Figures 8.1.2A, 8.1.2B, 8.1.2C and 8.1.2D which show the corresponding Tafel plots of the forward going sweeps in the first scan cyclic voltammograms of the mild steel electrode in 1wt% oxalic acid, 0.18M nitric acid and in a 0.18M nitric acid / 1wt% oxalic mixture at room temperature and at 50°C respectively.

Figures 8.1.2A, 8.1.2B, 8.1.2C and 8.1.2D show that the principal  $E_{CORR}$  value for all systems is  $\sim -0.45V$ . From Figure 8.1.2B it can be seen that for 0.18M  $HNO_3$  solution iron transforms to  $Fe^{+2}$  and at about +0.9V it is possible that the surface passivates as a result illustrated by the dramatic decrease in the log |current| value at this potential. Figure 8.1.2A shows that in oxalic acid environments iron transforms to ferrous oxalate in the region of  $E_{CORR}$  values ( $\sim +0.5V$ ) and a primary passivation takes place (from -0.12V to +0.35V) followed by a transpassive region (from +0.35V to +0.5V) followed by a secondary passive region (from +0.5V to +1V)- again, as discussed in detail in chapters 5-7.

Figures 8.1.3 A, B, C show the  $E_{OC}$  measurements of a mild steel electrode immersed in  $HNO_3$ , oxalic acid and in  $HNO_3$ / oxalic acid mixture at room temperature and at 50°C respectively. It can be seen that the open circuit potential of the mild steel sample in  $HNO_3$  remains constant at approximately -0.45V. In 1wt% oxalic acid it is approximately -0.5V. The open circuit potentials of the mixture of oxalic acid and nitric acid at room temperature and at 50°C are in between the  $E_{OC}$  of nitric acid and the  $E_{OC}$  of oxalic acid as can be seen in Figure 8.1.3. C. According to Figures 8.1.1 and 3.1.2, within the potential window near to -0.45V, iron transforms to  $Fe^{+2}$ . Interpreting Figure 8.1.2 with Figure 8.1.3 it can be observed that the  $E_{CORR}$  values agree with the open circuit potential.

Figure 8.1.4 shows the  $E_{OC}$  and nanogravimetric values as a function of time, recorded from Fe piezoelectrodes using QCN in A) oxalic acid, B) nitric acid, C) nitric acid / oxalic acid mixture at room temperature and D) nitric acid / oxalic acid mixture at 50°C respectively. Time  $t = 0$  corresponds to the point at which the QCN mounted Fe piezoelectrode is first immersed in the relevant solution.

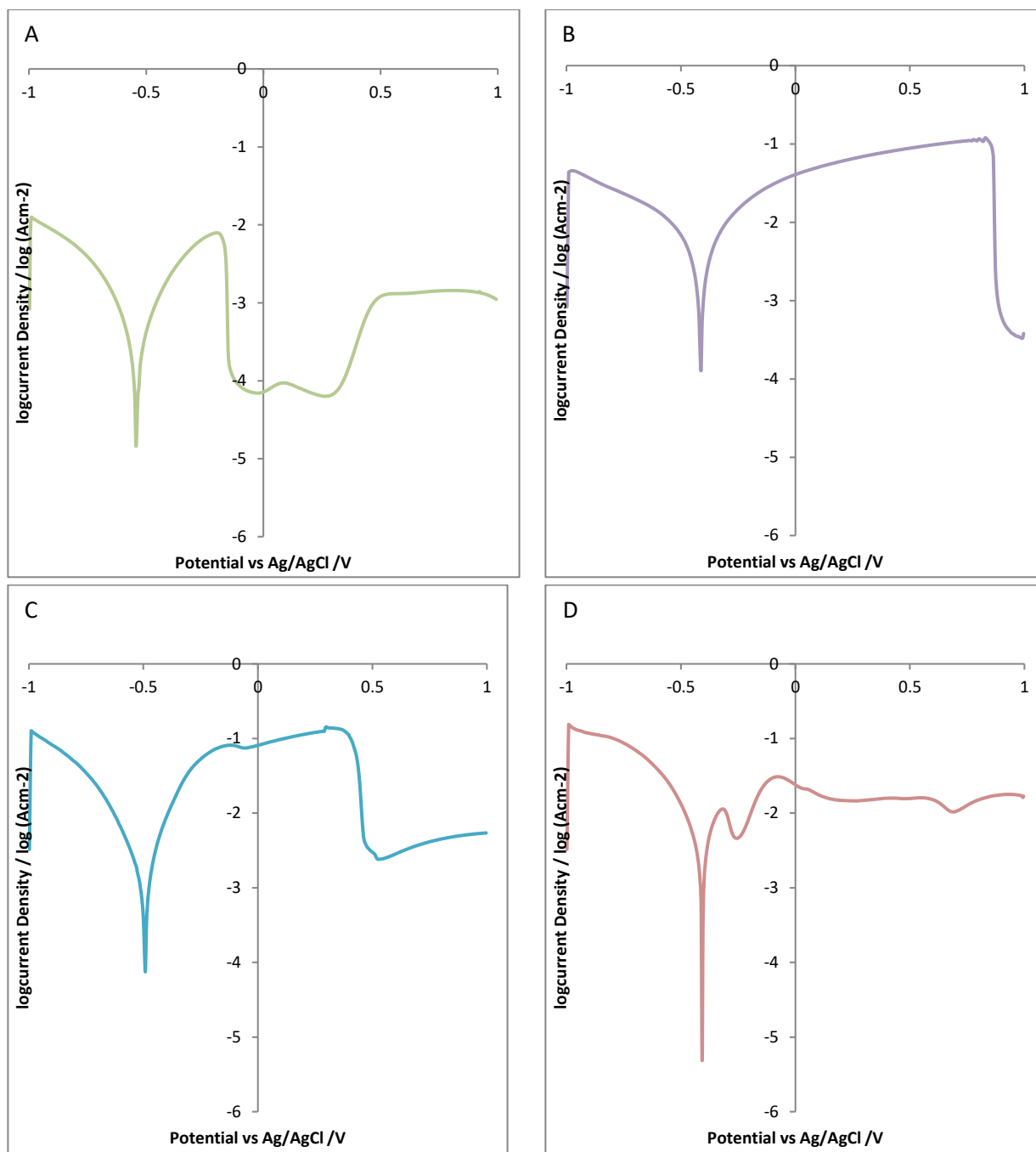


**Figure 8.1.2.:** Tafel curves of mild steel disc electrodes in: A) 1wt% oxalic acid, B) 0.18M nitric acid C) 0.18M nitric acid / 1wt% oxalic acid mixture at room temperature and D) 0.18M nitric acid / 1wt% oxalic mixture at 50°C.

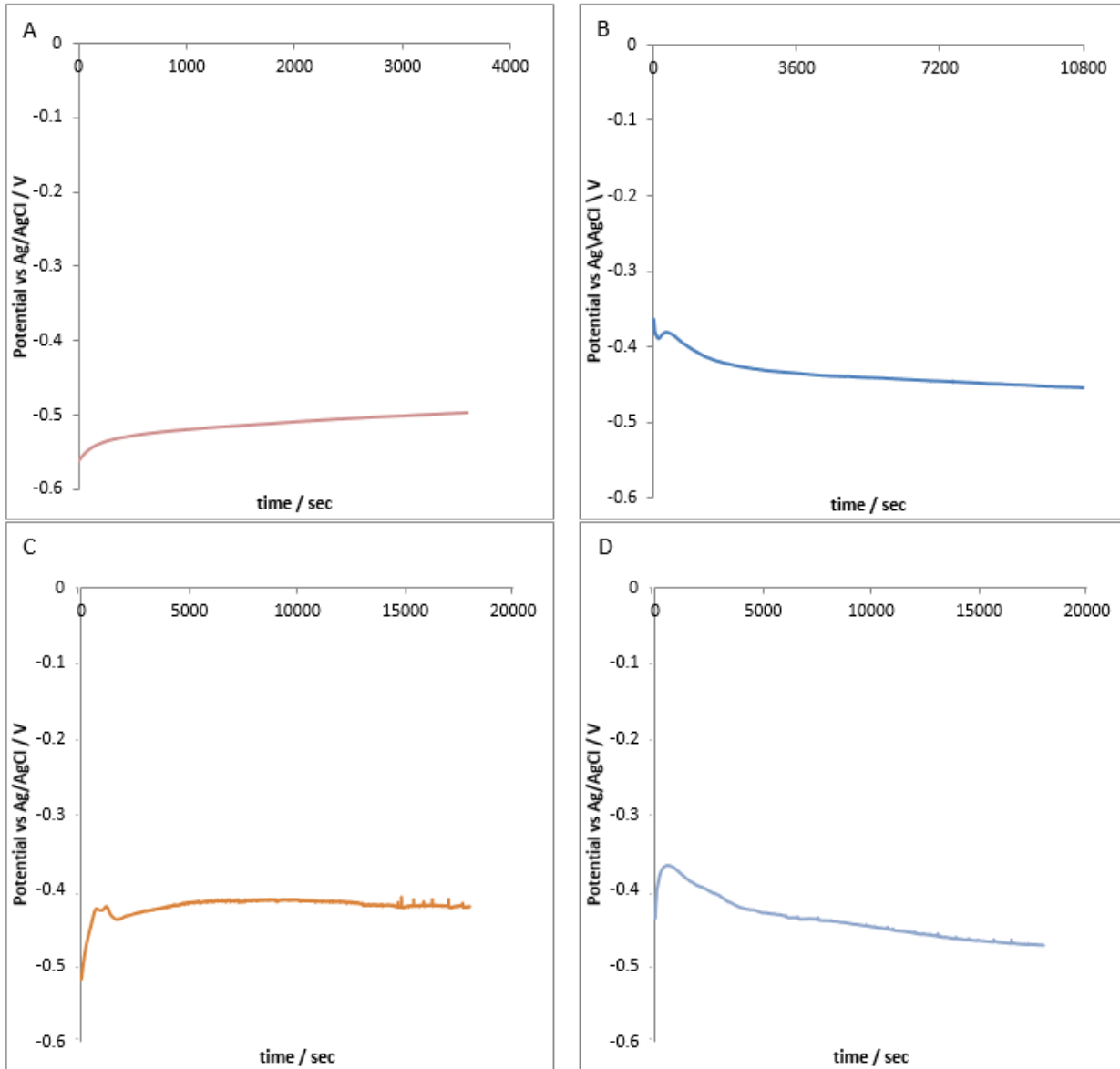


**Figure 8.1.3.:**  $E_{oc}$  measurements for a mild steel electrode immersed in: A) 1wt% oxalic acid, B) 0.18M nitric acid C) 0.18M nitric acid / 1wt% oxalic acid mixture at room temperature D) 0.18M nitric acid / 1wt% oxalic acid mixture at 50°C.

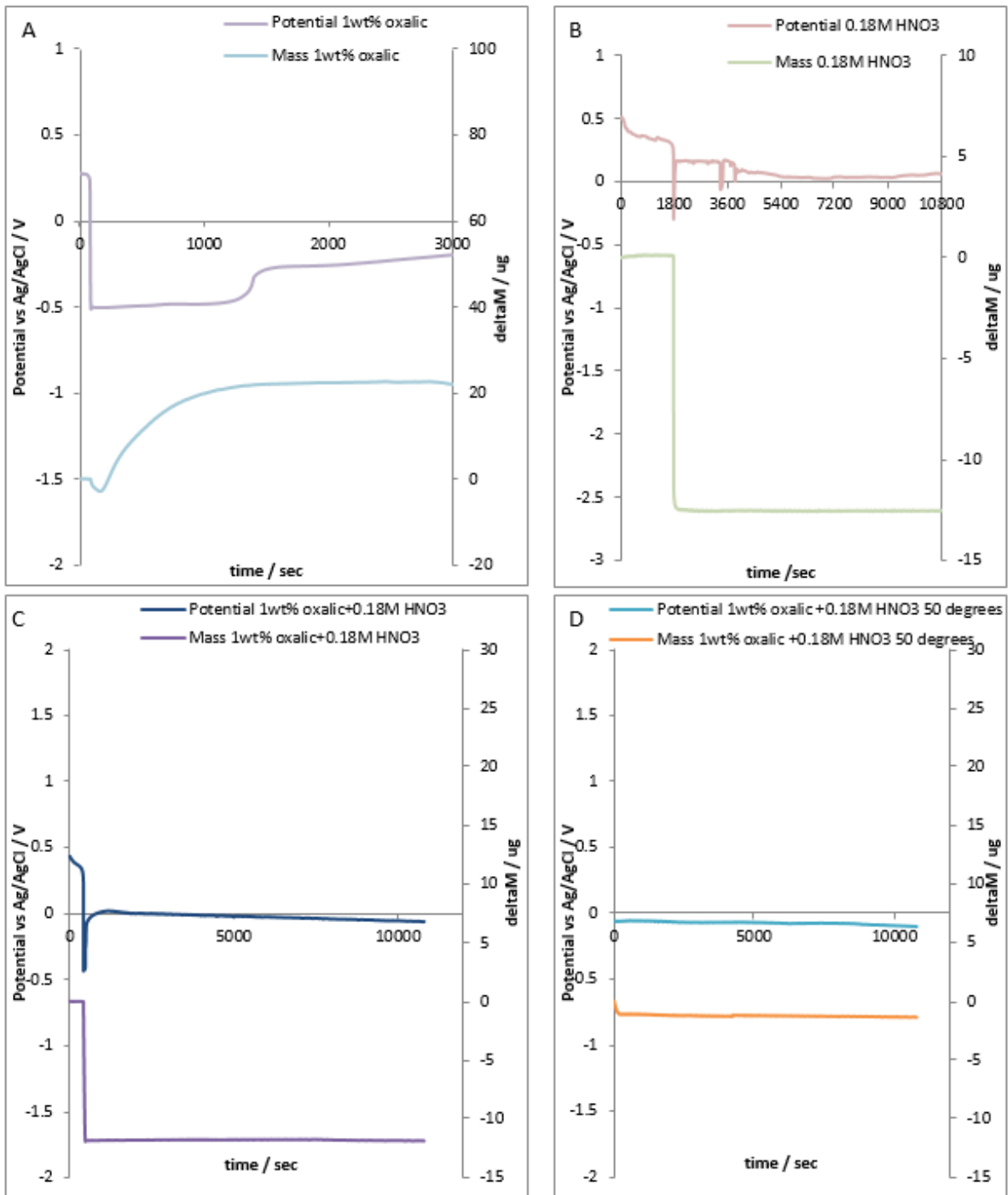


**Figure 8.1.4.:**  $E_{oc}$  and nanogravimetric data as a function of time, recorded from Fe piezoelectrodes in A) 1wt% oxalic acid, B) 0.18M nitric acid C) 0.18M nitric acid / 1wt% oxalic acid mixture at room temperature and D) 0.18M nitric acid / 1wt% oxalic acid mixture at 50°C.

As described in Chapter 7 the  $E_{OC}$  and nanogravimetric traces at 1wt% oxalic acid exhibit 4 distinct sequential regions.

- **Region 1:** Little to no change in mass with an initial  $E_{OC}$  of +0.3 V in 1 wt% oxalic acid.
- **Region 2:** A rapid decrease in the  $E_{OC}$  to  $\sim -0.5$  V accompanied by a small decrease in piezoelectrode mass.
- **Region 3:** A rapid increase in mass accompanied by a gradual increase in  $E_{OC}$  from -0.5 V to  $\sim -0.4$  V. The end of Region 3 is marked by an abrupt increase in  $E_{OC}$  to  $\sim -0.25$  V and by an almost abrupt slowing of the rate of mass increase.
- **Region 4:** A near constant  $E_{OC}$  of -0.25 V accompanied by an increase in piezoelectrode mass, albeit at a much slower rate than in Region 3.

The  $E_{OC}$  behaviour in Regions 1 and 2 is similar to that seen by Cartledge when stainless steel 347 electrodes are immersed in pH 1.46 sulfuric acid [100], the Region 1 behaviour being attributed to the slow acid dissolution of a layer of  $Fe_2O_3$  generated at the electrode surface by aerial oxidation prior to electrode immersion [100], [101].

Once this  $Fe_2O_3$  layer has thinned to the point that the underlying Fe is exposed, reduction of the remaining  $Fe_2O_3$  to  $Fe^{2+}$  galvanically couples with the oxidation of Fe metal to  $Fe^{2+}$ , resulting in an abrupt decrease in  $E_{OC}$  and an instantaneous mass loss at the electrode surface [100],[101], Region 2. As seen in Figure 7.1.1, this efflux of  $Fe^{2+}$  into solution then interacts with solution oxalate to generate a layer of passivating  $FeC_2O_4$  at the electrode surface with a corresponding rapid increase in electrode mass and an arrest in the negative trajectory of the  $E_{OC}$ , Region 3.

Finally, both Fe metal oxidation and consequent ferrous oxalate formation is self-limited by the presence of the  $FeC_2O_4$  layer at the electrode surface and the  $E_{OC}$  comes to rest at a potential

that, as can be seen from Figures 3.1.2A, 5.2.4A and 5.2.4B, corresponds to a region of  $\text{FeC}_2\text{O}_4$  derived electrode passivity i.e. the  $\text{FeC}_2\text{O}_4$  corrosion product layer has entered a region of passive growth.

The  $E_{oc}$  and nanogravimetric traces for 0.18M nitric acid are substantially different, exhibiting 3 regions.

- **Region 1:** Analogous to region 1 in 1wt% oxalic acid.
- **Region 2:** A rapid mass loss of about  $14\mu\text{g}$  with a corresponding fluctuating E vs t signal which eventually settles at  $\sim 0\text{V}$  vs Ag/AgCl.
- **Region 3:** No further variation in mass.

These observations can be explained as follows. Region 1 again corresponds to the removal by  $\text{HNO}_3$  of the thin layer of  $\text{Fe}_2\text{O}_3$  formed at the electrode surface by aerial oxidation routes. Upon removal of this protective layer of iron oxide, new iron is exposed and dissolved by the nitric acid in solution. This dissolution continuous until the piezoelectrode is completely or near completely denuded of its iron coating (these piezoelectrodes are coated with a  $16\mu\text{g}$  layer of iron).

Figure 8.1.4.C presents behaviour that is a combination of Figures 8.1.4A and 8.1.4.B in that a region 1 associated with aerial oxidation – generated iron oxide removal is again observed. This is followed by a rapid mass loss as the so-exposed iron surface is attacked by nitric acid with accompanying potential excursion similar to these seen in Figure 8.1.4A and B. However, in contrast to Figure 8.1.4.B, this mass loss is then arrested by the formation of an oxalate layer above to that formed in region 3 of Figure 8.1.4A.

The data of Figure 8.1.4.D is similar to that of Figure 8.1.4.C; however, the oxalate-passivated final state of the electrode is reached faster in Figure 8.1.4.D than in Figure 8.1.4C due to the high temperature and thus faster kinetics.

Thus, in summary, it can be seen from Figure 8.1.4.B that nitric acid does indeed drive iron surface dissolution and thus surface decontamination and sludge heel removal but in an uncontrolled and unconstrained way as the iron piezoelectrodes are completely dissolved. Use of such system in sludge heel removal would also lead to the compromising of the tank fabric.

Figure 8.1.4.C indicates that the introduction of oxalic acid introduces some control to the process as the oxalate arrests the nitric acid – driven dissolution before complete dissolution of the iron piezoelectrode has occurred. Nonetheless, some of the iron surface is dissolved, again suggesting that this mixed acid solution will be of use in sludge heel removal and decontamination applications. Similar results are obtained at 50°C as at room temperature for these mixed acid systems. Advantageously though, the oxalate does provide some protection to the iron of the tank wall and thus tank integrity will be maintained.

Having explained the oxalic acid / nitric acid system and gained some insights into the roles played by each acid, let us now move on to the final decontamination and heel removal system under study at Savannah River Site – the permanganate system.

## **8.2 Nanogravimetric and electrochemical analysis of iron and mild steel samples in $\text{KMnO}_4$ + NaOH environments**

The electrochemical and nanogravimetric behaviour of mild steel and iron samples immersed in nitric, oxalic and nitric/oxalic mixture solutions has been reported in the previous section. In order to achieve fast heel dissolution and surface cleaning it is essential to use highly concentrated acid [29]; however this will increase the secondary waste treatment costs. With the objectives of reducing costs and minimizing secondary waste generation, alkaline potassium permanganate, currently under development at Savannah River Site, can be used as a decontamination agent. The fact that the mechanism is not well understood and knowledge gaps

still remain makes it an ideal opportunity to extend this work and to test the feasibility of using QCN technology as a corrosion monitoring technique in alkaline environments. [29]

In order to understand the corrosion behavior of mild steel samples when immersed in alkaline potassium permanganate solution, it is essential to perform experiments in  $\text{KMnO}_4$  and  $\text{NaOH}$  separately. So as to determine the role of the pH in this system, experiments have been conducted in three sodium hydroxide concentrations of 3, 5 and 10M.

Thus, Figures 8.2.1. A, B, C show the  $E_{\text{OC}}$  measurements of a mild steel electrode immersed in 0.05M  $\text{KMnO}_4$ , 10M  $\text{NaOH}$  and  $\text{NaOH} / \text{KMnO}_4$  mixture respectively. It can be seen that the open circuit potential of the mild steel sample in 0.05M  $\text{KMnO}_4$  reaches an anodic equilibrium value at approximately +0.7V. In contrast, in 10M  $\text{NaOH}$ , the equilibrium value is cathodic at approximately -0.8V. The open circuit potentials of the  $\text{NaOH} / \text{KMnO}_4$  mixture are between the  $E_{\text{OC}}$  of 0.05M  $\text{KMnO}_4$  and the  $E_{\text{OC}}$  of the 10M  $\text{NaOH}$ , i.e. from +0.3V to +0.5V as can be seen in Figure 8.2.1. C. Similar results can be seen in Figure 8.2.2 where iron coated QCN piezoelectrode crystals have been used as an analogue to mild steel quartz crystals.

These features can be interpreted with the assistance of the simplified  $E_{\text{h}}$ -pH diagrams for the Mn- $\text{H}_2\text{O}$  and Fe- $\text{H}_2\text{O}$  systems shown in Figures 8.2.3 and adapted from the work of Pourbaix [81]. Please note the slightly different scales on the potential axis. The pH of 0.05M  $\text{KMnO}_4$  and 10M  $\text{NaOH}$  is approximately 9 and 15 respectively. For the  $\text{NaOH} / \text{KMnO}_4$  mixtures the pH for 3, 5 and 10M  $\text{NaOH}$  is 14.4, 14.7 and 15 respectively.

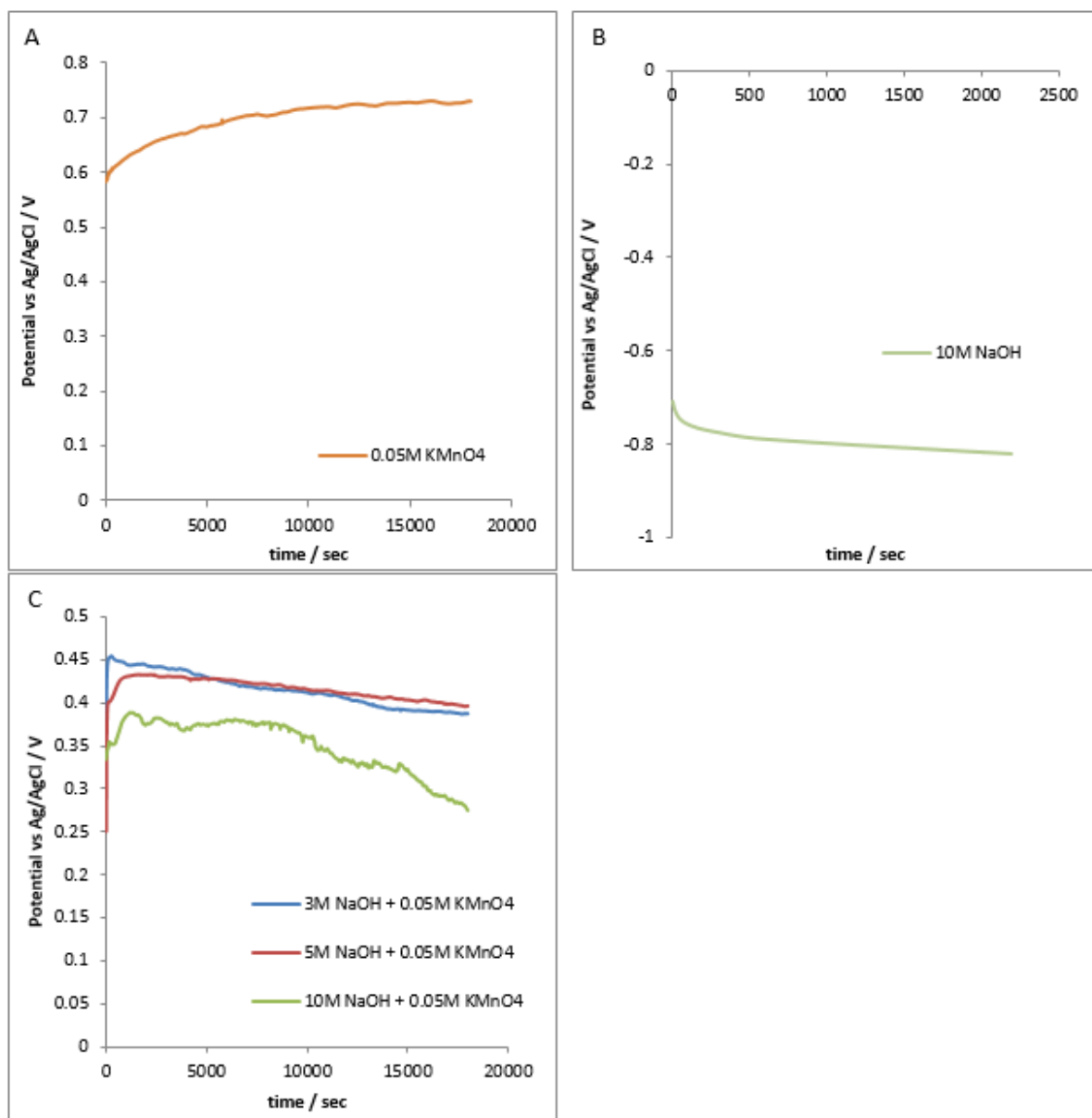


**Figure 8.2.1.:** E<sub>oc</sub> measurements of mild steel electrode immersed in: A) 0.05M KMnO<sub>4</sub>, pH=9 B) 10M NaOH, pH=15 C) 3M NaOH / 0.05M KMnO<sub>4</sub> , 5M NaOH / 0.05M KMnO<sub>4</sub>, 10M NaOH / 0.05M KMnO<sub>4</sub> mixtures, pH=14.4, 14.7 and 15 respectively.

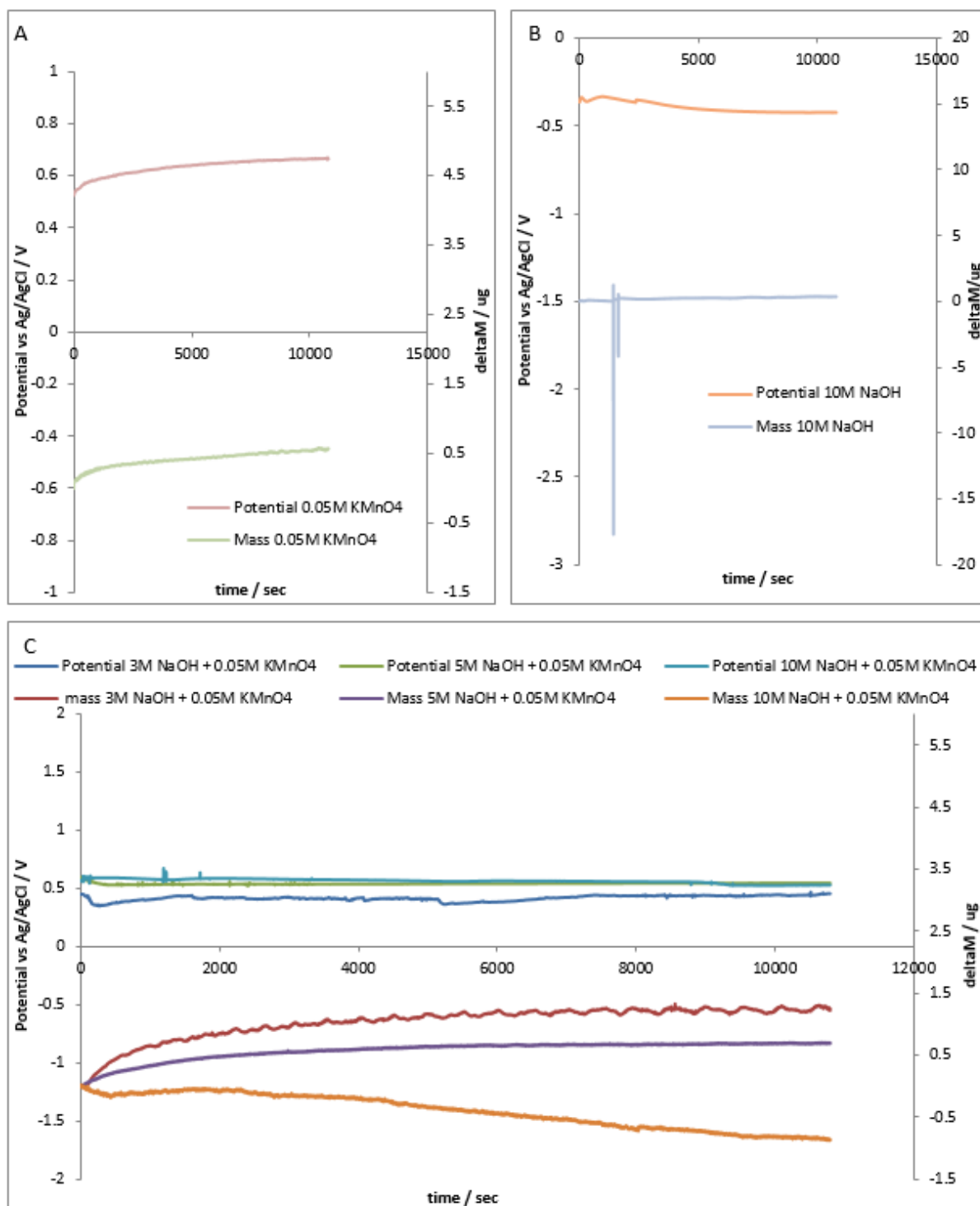


**Figure 8.2.2.:**  $E_{oc}$  and nanogravimetric data as a function of time, recorded from Fe piezoelectrodes in: A) 0.05M  $\text{KMnO}_4$ , pH=9 B) 10M NaOH, pH=15 C) 3M NaOH / 0.05M  $\text{KMnO}_4$ , 5M NaOH / 0.05M  $\text{KMnO}_4$ , 10M NaOH / 0.05M  $\text{KMnO}_4$  mixtures, pH=14.4, 14.7 and 15 respectively.

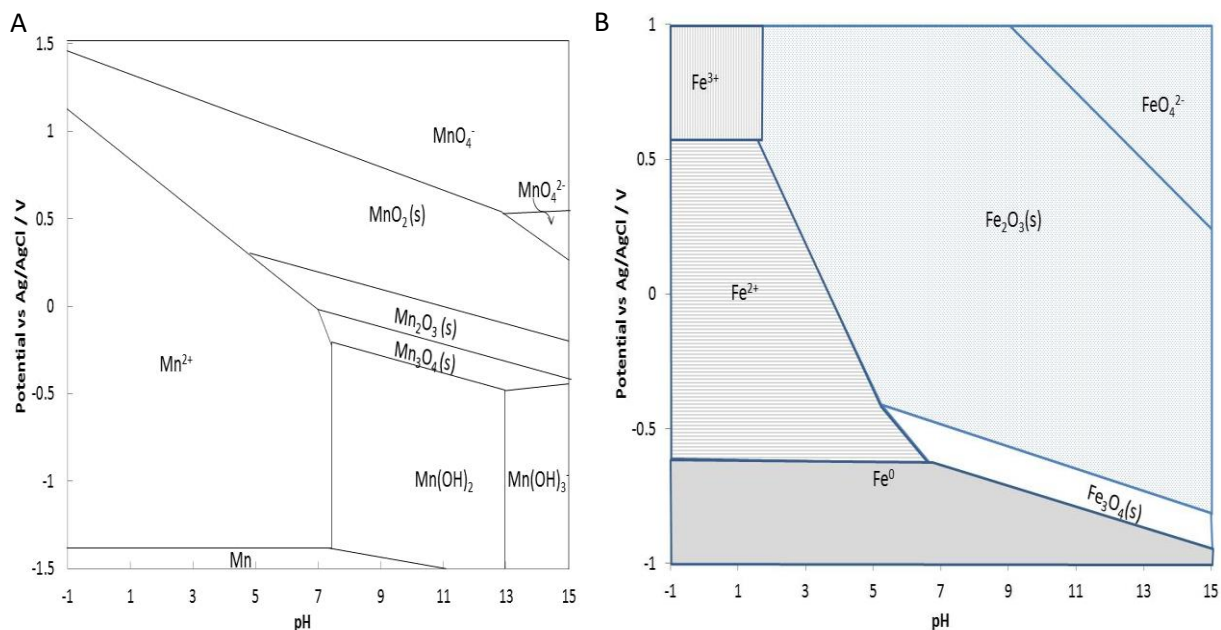


**Figure 8.2.3.:** Simplified Eh-pH (Pourbaix) diagrams for A) Mn-H<sub>2</sub>O system, B) Fe-H<sub>2</sub>O system, both adapted from the work of Pourbaix [81]. Please note the slightly different scales on the potential axis.

According to Figure 8.2.3B and in very alkaline environments (pH>14) for potentials close to +0.5V the dominant iron specie that participates on all of the three NaOH/KMnO<sub>4</sub> systems is the soluble FeO<sub>4</sub><sup>2-</sup>. Usually iron exists in the +2 or +3 oxidation stage. However at high pHs and potentials iron can be found as a stable Ferrate (VI) (FeO<sub>4</sub><sup>2-</sup>) existing in the +6 state.

The question therefore arises as to whether the permanganate solutions used here have a high enough oxidising power to drive Fe<sub>2</sub>O<sub>3</sub> into the Fe(IV) state. If this were to be the case, then alkaline permanganate solutions would be of use in sludge heel dissolution- provided the kinetics of dissolution are fast enough. This can be studied using the QCN technique as before. Accordingly, during the E<sub>oc</sub> vs time experiments of Figure 8.2.2 we also recorded the mass vs time signal obtained from these piezoelectrodes. With the assistance of the Pourbaix diagram of Figure 8.2.3 these data can be interpreted as follows.

- **3M NaOH / 0.05M KMnO<sub>4</sub>:** According to Figure 8.2.2., the open circuit potential is approximately +0.44V; the pH of this mixture is the lowest out of the three mixtures investigated at 14.4. According to Figure 8.2.3A, the dominant manganese specie under these conditions is the MnO<sub>4</sub><sup>2-</sup>

whilst the dominant iron species is  $\text{Fe}_2\text{O}_3$  – suggesting that, if anything, the permanganate will induce a growth in  $\text{Fe}_2\text{O}_3$  at the piezoelectrode surface. The concurrently recorded mass vs time trace exhibits an increase in piezoelectrode mass with time- suggesting that  $\text{Fe}_2\text{O}_3$  growth is indeed what occurs in this system.

- **5M NaOH / 0.05M  $\text{KMnO}_4$ :** Increasing the NaOH concentration in the mixture to 5M, increases the pH to 14.7. This increase notwithstanding, similar  $E_{\text{OC}}$  vs time and mass vs time plots as these obtained for 3M NaOH / 0.05M  $\text{KMnO}_4$ , are seen suggesting that the system is exhibiting similar chemistry. Indeed the open circuit potential is approximately +0.5V, the concentration of the dominant manganese species again being  $\text{MnO}_4^{2-}$ . Similarly, at this  $E_{\text{OC}}$  and pH, the dominant iron species is  $\text{Fe}_2\text{O}_3$  – again suggesting that the permanganate is inducing  $\text{Fe}_2\text{O}_3$  growth at the piezoelectrode surface. As above, the mass vs time plot supports this conclusion.
- **10M NaOH / 0.05M  $\text{KMnO}_4$ :** Increasing the NaOH concentration in the mixture to 10M increases the pH to 15.1. From Figure 8.2.2., it can be seen that the equilibrium open circuit potential is approximately +0.5V. At this pH and  $E_{\text{OC}}$ , the dominant Mn species is again  $\text{MnO}_4^{2-}$ ; however, the dominant iron species is now  $\text{FeO}_4^{2-}$  - suggesting that, at this elevated pH, permanganate is dissolving the  $\text{Fe}_2\text{O}_3$  surface in accordance with  $\text{Fe}_2\text{O}_3 + 6\text{MnO}_4^- + 10\text{OH}^- \rightarrow 2\text{FeO}_4^{2-} + 6\text{MnO}_4^{2-} + 5\text{H}_2\text{O}$ . The associated mass vs time plot shows a slow mass loss over the period of this experiment, supporting this conclusion.

Thus, in summary it can be seen that potassium permanganate does not drive iron surface dissolution at  $\text{pH} < 15$ ; however, at  $\text{pH} > 15$  it can oxidise iron or  $\text{Fe}_2\text{O}_3$  to soluble ferrate (VI) acting as a rust remover and thus a surface decontamination and sludge heel removal agent. In contrast to the oxalate system, use of such a system in sludge heel removal will not provide any protection to the iron of the tank wall thus care will have to be exercised in deployment if the tank integrity is to be maintained.

### 8.3 Nanogravimetric and electrochemical analysis of iron and mild steel samples in $\text{KMnO}_4 + \text{HNO}_3$

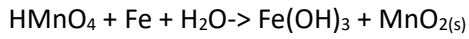
The electrochemical behaviour and the mass changes occurring in a simulated decontaminant using alkaline potassium permanganate have been reported in the previous section. However, oxides of iron and nickel can be easily dissolved in acidic environments and a document issued by the IAEA report that acidic permanganate may therefore be more effective on heel removal with fewer secondary waste arisings than alkaline permanganate [29].

It is well known that carbon steel is very vulnerable to attack in acidic environments. However, the corrosion behaviour of carbon steel in acid permanganate solution is complicated and further study is essential in order to identify the corrosion behaviour of a mild steel surface in permanganic acid solution. In this section, the electrochemical behaviour of mild steel samples and the mass change of an iron coated crystal when an electrode is immersed in acidic permanganate solution are reported.

Rajesh *et. al.* have studies the effect of acid permanganate solutions on mild steel. Measuring the weight loss by using mild steel coupons and measuring the decomposition of permanganic acid using a spectrophotometer, they reported that the weight loss of mild steel samples immersed in high concentrations of permanganic acid solution is below the detection limit of the coupon technique. [28]

This is, therefore, an ideal opportunity to test the feasibility of using QCN technology for measuring the mass gain or loss from of iron piezoelectrodes (as a mild steel surrogate) in highly concentrated permanganic acid solutions.

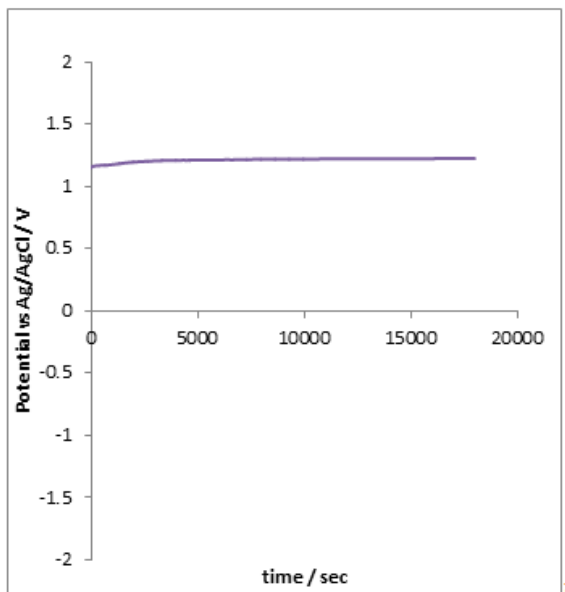
At low pH, iron reacts with permanganic acid, according to Equation 8.3.1., with the permanganate decomposing to manganese oxide. [28]



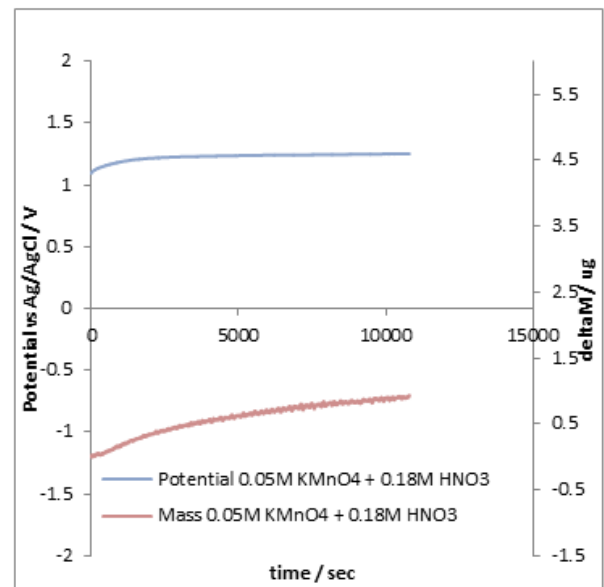
Equation 8.3.1

Figure 8.3.1 shows the  $E_{OC}$  measurements of a mild steel electrode immersed in 0.18M  $\text{HNO}_3$  / 0.05M  $\text{KMnO}_4$  mixture. It can be seen that the open circuit potential of a mild steel sample in 0.18M  $\text{HNO}_3$  / 0.05M  $\text{KMnO}_4$  mixture is approximately constant at +1.2V, which is in very good agreement with work reported by Rajesh *et. al.* [28]. From Figures 8.1.3B and 8.2.1A, the open circuit potentials of a mild steel sample in 0.18M  $\text{HNO}_3$  and in 0.05M  $\text{KMnO}_4$  are approximately -0.45V and +0.7V respectively indicating that the open circuit potential of the 0.18M  $\text{HNO}_3$  / 0.05M  $\text{KMnO}_4$  mixture is not between the  $E_{OC}$  of the 0.18M  $\text{HNO}_3$  and the  $E_{OC}$  of the 0.05M  $\text{KMnO}_4$  due to the two reagents acting in concert to increase the oxidative power of the reaction  $\text{MnO}_4^- + 3e^- + 4\text{H}^+ \rightarrow \text{MnO}_2 + 2\text{H}_2\text{O}$  in accordance with the Nernst equation  $E = E^o + \frac{RT}{3F} \ln \frac{[\text{MnO}_4^-][\text{H}^+]^4}{[\text{MnO}_2]}$ . On the bases of these observations, we would expect acid permanganate to readily dissolve iron oxide based sludge heels. In fact the opposite is observed as follows.

Figure 8.3.2 shows the  $E_{OC}$  and the mass change of an iron coated QCN crystal in 0.18M  $\text{HNO}_3$  / 0.05M  $\text{KMnO}_4$  mixture. The  $E_{OC}$  in Figure 8.3.1, using a mild steel rod as a working electrode, agrees with the  $E_{OC}$  in Figure 8.3.2, using an iron crystal as an analog to a mild steel quartz crystal.



**Figure 8.3.1.:**  $E_{OC}$  measurements of mild steel electrode immersed in  $\text{KMnO}_4$ /  $\text{HNO}_3$  mixture. pH=1.



**Figure 8.3.2.:**  $E_{OC}$  and nanogravimetric data as a function of time, recorded from Fe piezoelectrodes in  $\text{KMnO}_4$  /  $\text{HNO}_3$  mixture. pH=1.

With the assistance of the simplified  $E_h$ -pH diagrams, shown in Figure 8.2.3, at pH equal to 1 and at potentials near to +1.2V, we might expect all iron species to be converted to soluble  $Fe^{3+}$ . However, the mass vs time plot indicates that the mass of the piezoelectrode is increasing with immersion time. This can be explained by inspection of the Mn-H<sub>2</sub>O Pourbaix diagram in Figure 8.2.3A which shows that, at this  $E_{OC}$  and pH,  $MnO_2$  is expected to be formed at the piezoelectrode surface with a both consequent increase in electrode mass and, possibly, a passivity effect on the electrode surface. Such a passivity effect in  $HMnO_4$  / steel system has been previously reported by Rajesh *et. al.* [28]. At low permanganic acid concentrations, though, according to work reported by Rajesh *et. al.*, the open circuit potential will lie within a negative potential window. This can be explained by the inability of permanganic acid at low concentrations to insulate the surface of the metal. [28]

Figure 8.3.3A and B shows the cyclic voltammetric behaviour and the corresponding forward Tafel curve of a mild carbon steel disc electrode scanned between -1.5V and +1.5V in 0.18M  $HNO_3$  / 0.05M  $KMnO_4$  mixture respectively. During the forward sweep three  $E_{CORR}$  values which correspond to three different electrochemical reactions with onsets of -0.4V, +0.6V and +1.1V can be seen in Figure 8.3.3B. The first is due to dissolution of iron, the second is due to  $Fe^{2+}$  oxidation to ferric oxide and the third is due to permanganate decomposition according to Equation 8.3.1. These assignments are made with the assistance of Figure 8.2.3A and B.

In conclusion, according to Figures 8.3.1 and 8.3.2, the open circuit potential is approximately constant at +1.2 V and agrees with the  $E_{CORR}$  that corresponds to permanganate decomposition (according to Figure 8.3.3.B). Within this potential window any ferrous oxides would be expected to be oxidised to ferric compounds such as ferric nitrate, which is soluble to water. However, the permanganate driven electrode passivation due to  $MnO_2$  formation onto the surface of the electrode (according to Figures 8.3.2 and 8.2.3) acts to inhibit corrosion.

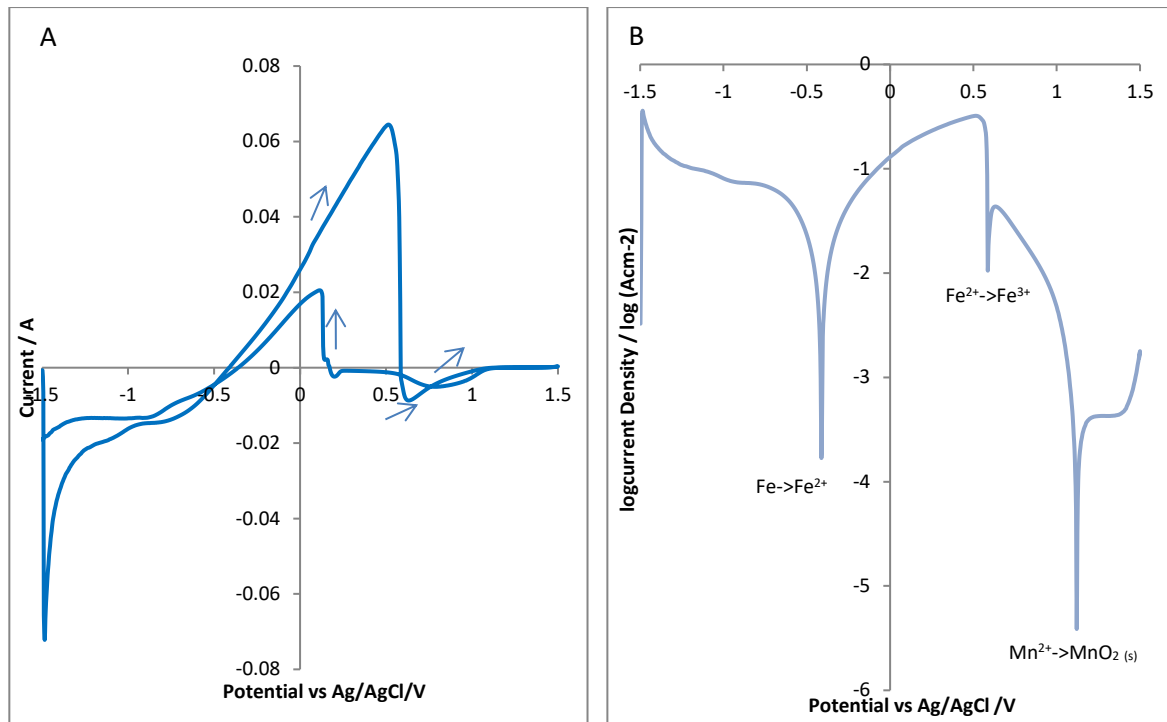


**Figure 8.3.3.:** A) Cyclic voltammogram and the corresponding forward B) Tafel curve of mild carbon steel in 0.05M KMnO<sub>4</sub>/0.18M HNO<sub>3</sub> mixture respectively.

The above observation indicates the ability of the acidic permanganate to act as a corrosion inhibitor rather than a rust remover and heel dissolution agent. Thus acidic permanganate is not suitable as a cleaning agent for surface decontamination and sludge heel removal applications, although the MnO<sub>2</sub> does provide some protection to the tank wall surface and thus tank integrity will be maintained.

## 8.4 Summary

The main objective of this chapter was to use the QCN as a real time corrosion monitoring technique and to measure the corrosion rates in real time for several novel nuclear decontamination cleaning agents currently under development by Savannah River National Laboratory.

This provided in turn an ideal opportunity to perform experiments in the laboratory in terms of testing the feasibility of using the QCN technology for measuring the corrosion rates in real time in different acidic or alkaline environments (i.e.  $\text{KMnO}_4$ ,  $\text{NaOH}$ ,  $\text{HNO}_3$ ) at room temperature and at  $50^\circ\text{C}$ .

Results indicate that QCN is a very promising technique for the study of the efficacy of these new decontamination agent formulations. The sensor provides useful mechanistic information derived from the mass change regarding the modus operandi of the decontaminating agent. Measurements were taken in real time when a quartz crystal was immersed in acidic or alkaline solutions at ambient or high temperature.

## Chapter 9

## 9. Conclusions and summary

This chapter lists the key points of each chapter of this thesis and presents new findings for the development of the QCN sensor.

### 9.1 Conclusions

As discussed in section 1.3, there are four main commonly used methods of monitoring corrosion rates, all with practical limitations. These are:

- i. linear polarisation resistance (suitable only for uniform corrosion phenomenon [51])
- ii. the coupon weight loss testing technique (unsuitable for real time monitoring [50])
- iii. electrical resistance monitoring (suitable only for uniform corrosion measurements [51])
- iv. the galvanic monitoring technique (measures the mass change indirectly [51]).

Recent advances in Quartz Crystal Nanobalance technology [65] offer a means of avoiding the above disadvantages and of measuring the corrosion rates in real time and potentially *in-situ*. Using the Sauerbrey equation, the frequency change observed during corrosion testing can be converted to an instantaneous mass change (gain or loss, depending upon the direction of frequency change) and thus the corrosion rate can be measured with nanogram sensitivity. The recent availability of a wide range of metal coated crystal resonators (steel, Al, Fe, Ti etc) makes the QCN ideal for real time, instantaneous corrosion monitoring of steels. Its sensitivity makes it ideal for the measurement of low corrosion rates (i.e. passive corrosion) whilst its capacity for remote deployment allows for use in high radiation environments with reduced operator exposure times, a key safety consideration for radiation workers (see section 1.3.2).

As discussed in section 1.2 there are many applications where QCN technology can be a very useful tool in terms of understanding the corrosion behaviour and measuring the corrosion rates in the nuclear industry:

- i. Reactor water cooling circuits exposed to oxidising coolant (see section 1.2.1).
- ii. The metal components found in reprocessing plants (see section 1.2.2.)
- iii. The metal walls of the evaporators used for the volumetric reduction of waste (see section 1.2.3).
- iv. The decontamination of waste tanks on the Savannah River Site and Hanford Site (see section 1.2.4 and 1.2.5).

This work examines the feasibility of using QCN as a corrosion monitoring sensor for measuring the corrosion rates in an exemplar system, such as the ECC process used for cleaning the walls of the waste tanks on the Savannah River and Hanford Sites. Results of this work can be seen in Chapters 3, 4, 5, 6, 7 and 8.

Work presented in Chapter 3 reveals that:

- i. Mild carbon steel and pure iron behave in a broadly similar fashion, with respect to their electrochemistry, in the presence of oxalic acid. Iron samples (as tank wall surrogates) can be used in place of mild steel samples.
- ii. The open circuit potential is found to be approximately -0.5 V, at which point iron species react with oxalic acid producing an insoluble ferrous oxalate layer.
- iii. In simulated radioactive environments, ferrous oxalate can be oxidized to ferric oxalate due to Fenton reactions. The latter are dependent upon oxalic acid concentrations and radiation levels.
- iv. Samples of mild carbon steel and iron show similar electrochemical behaviour at high temperatures.

v. Near to the open circuit potential, the thermally induced decomposition of oxalic acid is not observed in either non-radioactive or simulated radioactive environments.

Work presented in Chapter 4 reveals that:

i. Throughout the cyclic voltammogram performed on the iron rod at  $E < 0.5V$ , the steel surface is covered with a ferrous oxalate layer. At  $E > 0.5V$  the surface is covered with iron oxalate and / or ferric oxalate and oxide species. At approximately  $0.7V$  the surface is composed from ferrous oxalate and/or ferric oxalate with the oxide species now to be more dominant, whilst at the reverse scan and at about  $0.4V$  the surface appears to be covered only with oxide species. This work doesn't provide any information associated with the pits as described by Camalet et. al [74]. However, it provides the chemical change of the surface, which is in a good agreement with Camalet et. al [74].

Work presented in Chapter 5 reveals that:

i. In non-radioactive environments and near to the open circuit potential, QCN has the capability of measuring mass gain while insoluble ferrous oxalate insulates the surface of the crystal and at high over potentials of measuring mass loss while ferrous oxalate is oxidized to ferric oxide species. Moreover, QCN has the capability of measuring the molar mass of the insoluble ferrous oxalate layer.

ii. In non-radioactive environments, increasing the oxalic acid concentration results in an increase in the growth of the oxalate layer.

iii. In simulated radioactive environments and at near to the open circuit potential, QCN has the capability of measuring mass gain or loss during two chemical processes, such as ferrous oxalate production and Fenton reactions. Moreover, QCN has the capability of measuring the molar mass of any insoluble layer.

iv. In simulated radioactive environments it is possible that oxalic acid may not act as a corrosion inhibitor.

Chapters 6 and 7 reveal that the corrosion rates measured using QCN are found to agree with those obtained using corrosion current ( $i_{\text{CORR}}$ ) measurements, with the added advantages of:

- i. Instantaneous and real time measurement;
- ii. Potentially in situ and higher sensitivity measurement;
- iii. Reduced uncertainty in the conversion of the QCN measured frequency change to a mass change-based corrosion rate compared to the conversion of the LSV-determined  $i_{\text{corr}}$  to similar;
- iv. the provision of insight into the mechanism of the action of oxalic acid on Fe-rich steels.

Work presented in Chapter 8 reveals that:

- i. QCN is a very promising technique for studying the efficacy of new decontamination agent formulations with the sensor providing useful information concerning reaction mechanisms.
- ii. This work can be extended using stainless steel quartz resonator crystals at different cleaning agent concentrations and at different temperatures.

To conclude, the real time nanogravimetric monitoring of corrosion in radioactive environments which is the heart of this project using the Enhanced Chemical Cleaning process of the waste tanks at Savannah River Site as a model system has been measured and compared as can be seen in Chapter 7 and summarized in Table 7.2.1, whilst new insights into the corrosion mechanism of decontamination systems has been provided.

## 9.2 Summary

The corrosion rates of steels measured using QCN technology has been compared to  $i_{\text{CORR}}$  measurements. Whilst overall corrosion rates are in agreement,  $i_{\text{CORR}}$  measurements suffer from being perturbative, the potential is swept separately from cathodic and anodic extremes in recording

i-V curves to a previously identified  $E_{\text{CORR}}$  prior to calculation of the  $I_{\text{CORR}}$ , necessarily changing the nature of the surface under study and being conducted in non-real time. QCN based corrosion monitoring is non-perturbative, it simply involves sample immersion, provides direct access to two important corrosion parameters, mass change with the aforementioned nanogram sensitivity and  $E_{\text{CORR}}$ , and can be conducted in real time. The latter two features allow for the study of changes in corrosion rate on the sub-second timescale and thus the elucidation of the mechanism of the corrosion process under study [102]. Work has centred on determining corrosion rates in acids and complexants used in chemical decontamination processes, particularly methods involving the commonly used cleaning agents nitric acid and oxalic acid (e.g. the CORD-UV process). Oxalic acid is currently being studied as an Enhanced Chemical Cleaning (ECC) decontamination agent in the decommissioning of high level waste (HLW) storage tanks at the Hanford and Savannah River Sites (SRS). Oxalic acid has the twin ability to act as a rust remover and as a corrosion inhibitor [39], [40]. Therefore, it is preferred over bulk nitric acid [20]. The waste tanks are made of low carbon steel. For this reason, any decontamination process must be carefully monitored to avoid over-aggressive decontamination that may result in a loss of asset structural integrity. To this end, the oxalic acid concentration being used has been reduced to 1 wt% from the 4-8 wt% range typically used during decontamination campaigns hitherto [42]. Using QCN, the rates of corrosion of mild carbon steel surrogates have been measured in the presence of these oxalic acid-based decontamination solutions and both the removal of iron oxide corrosion product and the formation of a protective layer of ferrous oxalate at the metal surface have been observed [91], [107]. Studies have been extended to newer decontamination solution formulations including alkaline and acid permanganate solutions and oxalic acid / nitric acid blends. In the case of the former, preliminary results indicate that, counter-intuitively; base concentrations of  $> 10 \text{ mol dm}^{-3}$  will lead to a loss of HLW storage tank structural integrity. In the case of the latter, it is possible that oxalic / nitric mixtures may be more effective as a cleaning agent compared to commonly used oxalic acid. Results reveal that QCN is a very promising technique for measuring the corrosion rates in real time in situ for nuclear

applications with the sensor providing information regarding the corrosion behaviour and the mass change of the metal surface in simulated decontamination environments.

## References

- [1] ISO 8044:2015, "Corrosion of metals and alloys — Basic terms and definitions," 2015. [Online]. Available: <https://www.iso.org/obp/ui/#iso:std:iso:8044:ed-4:v1:en>. [Accessed: 13-Apr-2018].
- [2] U.S.NRC, "Stages of the nuclear fuel cycle," 2017. [Online]. Available: <https://www.nrc.gov/materials/fuel-cycle-fac/stages-fuel-cycle.html>. [Accessed: 25-May-2017].
- [3] CLPgroup, "Pressurised Water Reactor vs Boiling Water Reactor," 2013. [Online]. Available: [https://www.clpgroup.com/nuclearenergy/Eng/power/power4\\_1\\_2.aspx](https://www.clpgroup.com/nuclearenergy/Eng/power/power4_1_2.aspx). [Accessed: 25-May-2017].
- [4] E. Nonbol, "Description of the Advanced Gas Cooled Type of Gas Cooled Reactor (AGR)," *Riso Natl. Lab. Denmark NKS/RAK2(96)TR-C2*, 1996.
- [5] IEE, "Nuclear Reactor Types. An Environment & Energy FactFile provided by the IEE," *lee*, 2005.
- [6] M. F. Ashby and M. Smidman, "Materials for Nuclear Power Systems," *Granta Mater. Inspir. MFA*, 2010.
- [7] G. D. Jarvinen, "Nuclear Fuel Cycle," *Plutonium Futures - Sci. 2010*, pp. 1–20, 2010.
- [8] R. Taylor and F. Livens, "Advanced Reprocessing Research and Development Needs," no. National Nuclear Laboratory Position Paper.
- [9] K. Sreenavasa Rao, R. Shyamlal, C. V. Narayan, U. Jambunathan, and A. Ramanujam, "Uranous nitrate production for Purex process applications using PtO<sub>2</sub> catalyst and hydrazine nitrate as reductant," 2003.
- [10] Japan Atomic Energy Agency, "Reprocessing Technology Development." [Online]. Available: <https://www.jaea.go.jp/english/04/tokai-cycle/02.htm>. [Accessed: 25-May-2017].
- [11] Z. Lovasic, "Spent Fuel Reprocessing Options," *IAEA-TECDOC-1587 Spent*, no. August, 2008.
- [12] J. A. Wilusz and N. Greenberg, "Engineering and design aspects of high level radioactive waste evaporator."
- [13] United States Department of Energy, "Basis for Section 3116 Determination for Closure of F-Tank Farm at the Savannah River Site," *DOE/SRS-WD-2012-001 Revis. 0*, no. March, 2012.
- [14] Savannah River Site, "SRS Building 235-F," *factsheet 235 F*, 2011. [Online]. Available: [http://www.srs.gov/general/news/factsheets/235\\_f.pdf](http://www.srs.gov/general/news/factsheets/235_f.pdf). [Accessed: 21-Jun-2017].
- [15] G. R. Caskey, R. L. Sindelar, and J. K. Thomas, "Potential for Radiation Damage to Carbon Steel Storage Tanks for High Level Radioactive Waste (U)," *U.S. DOE*, vol. WSRCMS9300, 1993.
- [16] R. P. Anantatmula and J. R. Divine, "Corrosion of Low-Carbon Steel Under Environmental Conditions at Hanford : Two-Year Soil Corrosion Test Results," *U.S. DOE*, no. WHC-EP-0891, 1995.
- [17] K. H. Subramanian, P. E. Zapp, and B. J. Wiersma, "Review of Corrosion Inhibition in High

- Level Radioactive Waste Tanks in the DOE Complex," *WSRC-MS-2003-00882*.
- [18] J. P. Pavletich, "Liquid Waste Tank Residuals Sampling and Analysis Program Plan," *SRR-CWDA-2011-00050 Revis.*, no. October, 2015.
- [19] V. M. Abbasov, H. M. Abd El-Lateef, L. I. Aliyeva, E. E. Qasimov, I. T. Ismayilov, and M. M. Khalaf, "A study of the corrosion inhibition of mild steel C1018 in CO<sub>2</sub>-saturated brine using some novel surfactants based on corn oil," *Egypt. J. Pet.*, vol. 22, no. 4, pp. 451–470, 2013.
- [20] N. Davis, E. Ketusky, R. Spires, R. Beatty, S. Jones, J. Remark, and P. Wotjaszek, "Enhanced Chemical Cleaning: A New Process for Chemically Cleaning Savannah River Waste Tanks-9100," *WM2009, March 1-5*, 2009.
- [21] S. Hommel, M. Layton, and R. Jolly, "Critical Assumptions in the F-Tank Farm Operational Closure Documentation Regarding Waste Tank Internal Configurations," *DOE/US SRR-CWDA-2012-00051 Revis. 0*, 2012.
- [22] S. Savannah River Remediation, "General Information Input Package for the Section 3116 Determination for Closure of F-Tank Farm at the Savannah River Site," *FTF-WDIP-001 Revis. 0*, 2010.
- [23] S. Savannah River Remediation, "Industrial Wastewater Closure Module for the Liquid Waste Tanks 16H H-Area Tank Farm , Savannah River Site," *SRR-CWDA-2013-00091 Revis. 0*, 2015.
- [24] R. K. Mahidhara, T. S. Elleman, and K. L. Murty, "Corrosion and Failure Processes in High-Level Waste Tanks," *LA-SUB-94-183*, 1992.
- [25] K. I. Johnson, J. E. Deibler, N. K. Karri, S. E. Sanborn, F. G. Abatt, K. L. Stoops, L. J. Julyk, and B. M. Larsen, "A Summary of the Hanford Single-Shell Tank Structural Analysis of Record a - 15526," *WM2015*.
- [26] R. W. Hanf, L. F. Morasch, T. M. Poston, and R. L. Dirkes, "Hanford Site Environmental Report for Calendar Year 2003," *PNNL-14687-SUM Summ.*, 2004.
- [27] A. J. Dobson and C. Phillips, "High Level Waste Processing in the U.K.—Hard Won Experience that can Benefit U.S. Nuclear Cleanup Work," *WM'06 Conf. Febr. 26-March 2, 2006, Tucson, AZ*, 2006.
- [28] P. Rajesh, P. S. Kumar, S. Suresh, S. Chandran, H. Subramanian, S. Velmurugan, and S. Narasimhan, "Corrosion Compatibility Studies on Carbon Steel and Type 304 Stainless Steel in Acid Permanganate and Organic Acid Mixtures," *Corros. Eng. Sci. Technol.*, vol. 42, no. 2, pp. 174–182, 2007.
- [29] International Atomic Energy Agency, "New methods and techniques for decontamination in maintenance or decommissioning operations," *IAEA-TECDOC-1022*, 1998.
- [30] R. C. Woodhouse, C. Boxall, and R. J. Wilbraham, "Nitric acid reduction on 316L stainless steel under conditions representative of reprocessing," *ECS Trans.*, vol. 53, no. 21, pp. 33–44, 2013.
- [31] "Materials used in a nuclear fuel reprocessing plant," 2001. [Online]. Available: [http://www.azom.com/article.aspx?ArticleID=627#\\_Austenitic\\_Stainless\\_Steels](http://www.azom.com/article.aspx?ArticleID=627#_Austenitic_Stainless_Steels). [Accessed: 21-Jun-2017].
- [32] NEA Nuclear Energy Agency, "Spent nuclear fuel reprocessing flowsheet," *Nucl. Sci. NEA/NSC/WPFC/DOC(2012)15*, 2012.

- [33] B. . Paige, "Distribution of this document is," in *NACE International Corrosion/75 conference, Toronto, Canada, 1975*, no. April.
- [34] B. Raj and U. K. Mudali, "Materials development and corrosion problems in nuclear fuel reprocessing plants," *Prog. Nucl. Energy*, vol. 48, no. 4, pp. 283–313, 2006.
- [35] H. W. Godbee, "Use of the evaporation for the treatment of liquids in the nuclear industry," *ORNL-4790*, 1973.
- [36] T. B. Calloway, C. J. Martino, C. M. Jantzen, W. R. Wilmarth, M. E. Stone, R. A. Pierce, J. E. Josephs, C. D. Barnes, W. E. Daniel, R. E. Eibling, A. S. Choi, T. L. White, D. A. Crowley, M. A. Baich, J. D. Johnson, K. Vijayaraghavan, A. Nikolov, and D. T. Wasan, "Radioactive waste evaporation: Current Methodologies employed for the development, design and operation of waste evaporators at the Savannah river site and Hanford waste treatment plant," in *ICEM '03 WSRC-MS-2003-00050, Rev.0*, 2003, no. 865.
- [37] E. Ketusky and K. Subramanian, "Advanced Oxidation Oxalate Decomposition Testing with Ozone - 12534," *WM2012 Phoenix, AZ, SRR-LWE-2012-00006-2*, 2012.
- [38] K. A. Wusu, M. J. Barnes, N. E. Bibler, J. R. Cantrell, F. F. Fondeur, B. A. Hamm, C. C. Herman, D. T. Hobbs, E. T. Ketusky, M. Singleton, M. E. Stallings, W. E. Stevens, and B. J. Wiersma, "Waste tank heel chemical cleaning summary," *WSRC-TR-2003-00401*, 2003.
- [39] S. Rahfield and B. Newman, "Composition for rust removal and method of use thereof," *Pat. US4828743 A*, 1989.
- [40] M. A. Streicher, "Corrosion – inhibition of oxalic acid," *Pat. US 2793190 A*, 1957.
- [41] B. Menczel, A. Apelblat, and E. Korin, "The molar enthalpies of solution and solubilities of ammonium, sodium and potassium oxalates in water," *J. Chem. Thermodyn.*, vol. 36, no. 1, pp. 41–44, 2004.
- [42] E. Ketusky, K. Subramanian, and B. Wiersma, "Savannah River Site Tank Cleaning : Corrosion Rate for One Versus Eight percent Oxalic acid Solution - 11413," *WM2011, Phoenix, AZ*, 2011.
- [43] R. Spires, E. Ketusky, B. Barton, and D. Jones, "Comparison of Oxalic Acid Cleaning Results at SRS and Hanford and the Impact on Enhanced Chemical Cleaning Deployment," in *WM2010 Conference, March 7-11, 2010, Phoenix, AZ*, 2010.
- [44] C. J. Martino and W. D. King, "Testing of Enhanced Chemical Cleaning of SRS Actual Waste Tank 5F and Tank 12H Sludges," *SRNL-STI-2011-00360 Revis. 0*, no. August, 2011.
- [45] A. A. A. El-Raady and T. Nakajima, "Effect of UV radiation on the removal of carboxylic acids from water by H<sub>2</sub>O<sub>2</sub> and O<sub>3</sub> in the presence of metallic ions," *Ozone-Science Eng.*, vol. 28, no. 1, pp. 53–58, 2006.
- [46] R. G. Zepp, B. C. Faust, and J. Holgne, "Hydroxyl Radical Formation in Aqueous Reactions (pH 3-8) of Iron(II) with Hydrogen Peroxide: The Photo-Fenton Reaction," *Environ. Sci. Technol.*, vol. 26, no. 2, pp. 313–319, 1992.
- [47] C. J. Martino, W. D. King, and E. T. Ketusky, "Actual-Waste Tests of Enhanced Chemical Cleaning for Retrieval of SRS HLW Sludge Tank Heels and Decomposition of Oxalic Acid - 12256," *WM2012 SRNL-STI-2011-00496*, 2012.
- [48] K. L. Murty and T. S. Elleman, "A Study of Hydrogen Effects on Fracture Behavior of

- Radioactive Waste Storage Tanks," *DOE/ER/75784--77*, 1998.
- [49] J. Davis, *Corrosion: Understanding the Basics*. ASM International, 2000.
- [50] L. L. Shreir, R. A. Jarman, and G. T. Burstein, *Corrosion: Volume 2 Corrosion Control*, 3rd ed. 1994.
- [51] P. R. Roberge, *Handbook of Corrosion Engineering*. McGraw-Hill, 2000.
- [52] ASTM-Standards, "Standard practice for calculation of corrosion rates and related information from electrochemical measurements," *ASTM G 102-89*, no. Reapproved, pp. 1–7, 1999.
- [53] NACE International, "Techniques for Monitoring Corrosion and Related Parameters in Field Applications," *NACE Int. Publ. 3T199*, no. 24203, 1999.
- [54] P. Marcus and F. Mansfeld, *Analytical Methods in Corrosion Science and Engineering*. Taylor & Francis Group, 2006.
- [55] Gamry, "Basics of a Quartz Crystal Microbalance." [Online]. Available: <http://www.gamry.com/application-notes/physechem/basics-of-a-quartz-crystal-microbalance/>. [Accessed: 24-Oct-2016].
- [56] A. P. M. Glassford and D. A. Wallace, "Comparison of mass sensitivities of 10- and 15- MHz Quartz Crystal Microbalances," *J. Thermophys. Heat Transf.*, vol. 10, no. 3, pp. 532–534, 1996.
- [57] C.-O. A. Olsson, D. Hamm, and D. Landolt, "Electrochemical Quartz Crystal Microbalance Studies of the Passive Behavior of Cr in a Sulfuric Acid Solution," vol. 147, no. 7, pp. 2563–2571, 2000.
- [58] A. J. Bard, R. Parsons, and J. Jordan, "Standard potentials in aqueous solution," *CRC Press*, 1985.
- [59] D. A. Buttry, "Applications of the quartz crystal microbalance to electrochemistry," *Electroanal. Chem.*, vol. 17, 1991.
- [60] D. A. Buttry, *Electrochemical Interfaces: Modern techniques for in-situ interface characterisation*. VHC Publishers Inc., 1991.
- [61] M. R. Deakin and D. A. Buttry, "Electrochemical Applications of the Quartz Crystal Microbalance," *Anal. Chem.*, vol. 61, no. 20, p. 1147A–1154A, 1989.
- [62] P. Schmutz and D. Landolt, "In-situ microgravimetric studies of passive alloys: Potential sweep and potential step experiments with Fe-25Cr and Fe-17Cr-33Mo in acid and alkaline solution," *Corros. Sci.*, vol. 41, no. 11, pp. 2143–2163, 1999.
- [63] B. Seifried and F. Temelli, "Use and limitations of a quartz crystal microbalance to measure viscosity of carbon dioxide-expanded fish oil fatty acid ethyl esters," *J. Supercrit. Fluids*, vol. 101, pp. 104–109, 2015.
- [64] K. Park, M. Koh, C. Yoon, H. Kim, and H. Kim, "The behavior of quartz crystal microbalance in high pressure CO<sub>2</sub>," *J. Supercrit. Fluids*, vol. 29, pp. 203–212, 2004.
- [65] P. S. Foran and C. Boxall, "Photo-induced changes in the Langmuir adsorption constants of metal oxide layers in self- cleaning cation sensors.," *Mater. Res. Soc. Symp.*, vol. 1406, 2012.

- [66] G. Instruments, "Gamry Instruments 'Universal Dummy Cell 4 Operator's Manual'," 2011.
- [67] P. Foran, "Photo-induced changes in metal oxides and their applications as self-cleaning piezoelectric based caesium sensors," Phd thesis, Lancaster University, 2013.
- [68] F. P. L. Andrieux, "The micro-optical ring electrode: Development of a novel thin ring based device for spectrophotoelectrochemistry and its application to the study of rose bengal," Phd thesis, University of Central Lancashire, 2004.
- [69] R. J. Wilbraham, C. Boxall, and R. J. Taylor, "Photocatalytically driven dissolution of macroscopic metal surfaces. Part 1: Silver," *J. Photochem. Photobiol. A Chem.*, vol. 249, pp. 21–28, 2012.
- [70] R. M. Sellers and W. J. Williams, "High-temperature Dissolution of Nickel Chromium Ferrites by Oxalic Acid and Nitrioltriactic Acid," *Faraday Discuss. Chem. Soc.*, vol. 77, pp. 265–274, 1984.
- [71] J. A. Ayres, *Decontamination of Nuclear Reactors and Equipment*. New York: Ronald Press, 1970.
- [72] P. Rahim Shima, R. Abdul Abdul Aziz, and D. Wan Mohd Ashri Wan, "Review on the application of modified iron oxides as heterogeneous catalysts in Fenton reactions," *J. Clean. Prod.*, vol. 64, no. 2014, pp. 24–35, 2014.
- [73] M. Abdallah and H. E. Megahed, "Cyclic voltammograms of iron and C-steels in oxalic acid solutions and investigation of the effect of phenyl phthalimide as corrosion inhibitors," *Monatshefte fur Chemie*, vol. 126, no. 5, pp. 519–527, 1995.
- [74] J. L. Camalet, J. C. Lacroix, S. Aeiyaeh, K. Chane-Ching, and P. C. Lacaze, "Electrosynthesis of adherent polyaniline films on iron and mild steel in aqueous oxalic acid medium," *Synth. Met.*, vol. 93, no. 2, pp. 133–142, 1998.
- [75] M. G. Wankhede, P. M. Koinkar, M. a More, P. P. Patil, and S. a Gangal, "Poly(O-anisidine) coatings on low carbon steel," *Mater. Sci. Eng. A*, vol. 332, pp. 161–166, 2002.
- [76] G. Mengoli and M. M. Musiani, "Protective coatings on iron by anodic oxidation of phenols in oxalic acid medium," *Electrochim. Acta*, vol. 31, no. 2, pp. 201–210, 1986.
- [77] J. L. Camalet, J. C. Lacroix, S. Aeiyaeh, K. Chane-Ching, and P. C. Lacaze, "Electrodeposition of protective polyaniline films on mild steel," *J. Electroanal. Chem.*, vol. 416, no. 1–2, pp. 179–182, 1996.
- [78] N. M. Martyak, "Chronoamperometric studies during the polymerization of aniline from an oxalic acid solution," vol. 81, pp. 143–151, 2003.
- [79] N. M. Martyak, P. McAndrew, J. E. McCaskie, and J. Dijon, "Electrochemical polymerization of aniline from an oxalic acid medium," vol. 45, pp. 23–32, 2002.
- [80] M. R. Mahmoudian, Y. Alias, and W. J. Basirun, "Electrodeposition of (pyrrole-co-phenol) on steel surfaces in mixed electrolytes of oxalic acid and DBSA," *Mater. Chem. Phys.*, vol. 124, no. 2–3, pp. 1022–1028, 2010.
- [81] Pourbaix M., *Atlas of Electrochemical Equilibria in Aqueous Solutions Version 2*, 2nd Editio. Houston, Texas, USA: NACE, 1974.
- [82] S. N. Saltykov, G. V. Makarov, E. L. Toroptseva, and Y. B. Filatova, "Anodic behavior of white

- iron phases in oxalic media," *Prot. Met.*, vol. 40, no. 1, pp. 56–61, 2004.
- [83] D. Reed, S. Clark, and L. Rao, *Actinide speciation in high ionic strength media*. Springer, 1999.
- [84] M. Shourian, H. Tavakoli, H. Ghourchian, and H. A. R. Pour, "Detection and dosimetry of gamma ray emitted from thallium-201 and technetium-99m based on chemiluminescence technique," *Radiat. Meas.*, vol. 45, no. 8, pp. 906–910, 2010.
- [85] T. Song, I. Kim, and S. Rho, "Effect of H<sub>2</sub>O<sub>2</sub> on the corrosion behavior of 304L stainless steel," *J. Korean Nucl. Soc.*, vol. 27, no. 4, pp. 453–462, 1995.
- [86] S. Pouran, A. Raman, and W. Daud, "Review on the application of modified iron oxides as heterogeneous catalysts in Fenton reactions," *J. Clean. Prod.*, vol. 64, pp. 24–35, 2014.
- [87] P. Salgado, V. Melin, D. Contreras, Y. Moreno, and H. D. Mansilla, "Fenton reaction driven by iron ligands," *J. Chil. Chem. Soc.*, vol. 58, no. 4, pp. 2096–2101, 2013.
- [88] C. Wang, H. Liu, and Z. Sun, "Heterogeneous photo-Fenton reaction catalyzed by nanosized iron oxides for water treatment," *Int. J. Photoenergy*, vol. 2012, no. 1, 2012.
- [89] P. Bautista, A. F. Mohedano, J. A. Casas, J. A. Zazo, and J. J. Rodriguez, "Review An overview of the application of Fenton oxidation to industrial wastewaters treatment," *J. Chem. Technol. Biotechnol.*, vol. 83, pp. 1323–1338, 2008.
- [90] K. Jones and D. W. Hoepfner, "The interaction between pitting corrosion, grain boundaries, and constituent particles during corrosion fatigue of 7075-T6 aluminum alloy," *Int. J. Fatigue*, vol. 31, no. 4, pp. 686–692, 2009.
- [91] I. Tzagkaroulakis, C. Boxall, and D. Trivedi, "Real time nanogravimetric monitoring of corrosion for nuclear decommissioning in simulated radioactive environments – 16170," in *WM2016, March 6 – 10*, 2016.
- [92] B. Wiersma and J. Mickalonis, "Electrochemical Studies on the Corrosion of Carbon Steel in Oxalic Acid Cleaning Solutions," in *NACE International*, 2008, no. NACE-08593.
- [93] B. J. Wiersma, "Determination of Temperature Limits for Radioactive Waste Tanks," *WSRC-TR-98-001 31, Rev. 1*, 1999.
- [94] B. Beverskog and I. Puigdomenech, "Revised Pourbaix diagrams for iron at 25-300 C," *Corros. Sci.*, vol. 38, no. 12, pp. 2121–2135, 1996.
- [95] H. G. M. Edwards and N. C. Russell, "Vibrational spectroscopic study of iron (II) and iron (III) oxalates," *J. Mol. Struct.*, vol. 443, pp. 223–231, 1998.
- [96] M. Hanesch, "Raman spectroscopy of iron oxides and (oxy)hydroxides at low laser power and possible applications in environmental magnetic studies," *Geophys. J. Int.*, vol. 177, no. 3, pp. 941–948, 2009.
- [97] F. Froment, A. Tournie, and P. Colombari, "Raman identification of natural red to yellow pigments: ochre and iron-containing ores," *J. Raman Spectrosc.*, vol. 39, no. June, pp. 560–568, 2008.
- [98] E. Mitchell, F. D. Souza, R. K. Gupta, P. K. Kahol, D. Kuma, L. Dong, and B. K. Gupta, "Probing on the hydrothermally synthesized iron oxide nanoparticles for ultra-capacitor applications," *Power Technol.*, vol. 272, pp. 295–299, 2015.

- [99] M. Chanon, M. Julliard, J. Santamaria, and F. Chanon, "Role of single electron transfer in dioxygen activation. Swing activation in photochemistry, electrochemistry, thermal chemistry," *New j. Chem*, vol. 16, pp. 171–201, 1992.
- [100] G. H. Cartledge, "The activation and passivation of stainless steel in aerated sulfuric acid," *J. Electrochem. Soc.*, vol. 104, pp. 420–426, 1957.
- [101] Z. Qin, B. Demko, J. Noel, D. Shoesmith, F. King, R. Worthingham, and K. Keith, "Localized dissolution of millscale-covered pipeline steel surfaces," *Corros. 2004*, vol. 60, no. 10, pp. 906–914, 2004.
- [102] I. Tzagkaroulakis and C. Boxall, "Real time nanogravimetric monitoring of corrosion for nuclear decommissioning," *ECS Trans.*, vol. 66, no. 17, pp. 73–83, 2015.
- [103] W. King, M. Hay, B. Wiersma, and F. Pennebaker, "EM-31 Alternative and Enhanced Chemical Cleaning Program for Sludge Heel Removal-11220," *WM2011 SRNL-STI-2010-00736*, 2011.
- [104] A. M. Gauger and R. T. Hallen, "Individual reactions of permanganate and various reductants," *Student Rep. to DOE ERULF Progr. Work Conduct. May to July 2000 PNNL-21728*, vol. U.S. Depar, no. July 2000, 2012.
- [105] M. C. Duff, D. B. Hunter, D. T. Hobbs, and S. D. Fink, "Characterization of neptunium and plutonium in manganese oxide solids formed from permanganate reduction during simulant radioactive waste treatment," *WSRC-MS-2002-00891*, 2002.
- [106] R. T. Hallen, S. A. Bryan, and F. V. Hoopes, "Development of an alternative treatment scheme for Sr/TRU removal: Permanganate treatment of AN-107 waste," *PNWD-3047*, vol. BNFL-RPT-0, 2000.
- [107] I. Tzagkaroulakis, C. Boxall, and D. Trivedi, "Real-Time Nanogravimetric Monitoring of Corrosion in Radioactive Decontamination Systems," in *MRS2016, November27-December 2*, 2016.
- [108] Q. Ma, H. He, and C. Liu, "Hygroscopic properties of oxalic acid and atmospherically relevant oxalates," *Atmos. Environ.*, vol. 69, pp. 281–288, 2013.

## PUBLICATIONS – PRESENTATIONS - INDUSTRY LINKS - TRAINING EVENTS / RESEARCH SEMINARS – GRANTS DURING PHD STUDIES

### Publications

---

- I. Tzagkaroulakis, C. Boxall, and D. Trivedi, “Real-Time Nanogravimetric Monitoring of Corrosion in Radioactive Decontamination Systems”, *MRS Advances*, vol. 2, 10, pp.577-582, 2016
- I. Tzagkaroulakis, C. Boxall, and D. Trivedi, “Real time nanogravimetric monitoring of corrosion for nuclear decommissioning in simulated radioactive environments-16170”, *WM2016*, Vol 1, pp.5500-5516, 2016
- I. Tzagkaroulakis and C. Boxall, “Real time nanogravimetric monitoring of corrosion for nuclear decommissioning” *ECS Transactions.*, vol. 66, 17, pp. 73–83, 2015

### Presentations

---

- 27/11-2/12/2016: *MRS2016*, Boston,U.S. (oral presentation)
- 21/7/2015: ElectrochemNW 2015, Manchester Metropolitan University, U.K. (oral presentation)
- 30/6/2015-1/7/2015: Lancaster Engineering Dept PG Review Conference 2015 (oral presentation)
- 24-28/5/2015: In the Corrosion Session of the 227th ECS Meeting, Chicago, U.S. (oral presentation)
- 16/12/2014: Lancaster University Faculty of Science & Technology Christmas Conference (poster presentation)
- 1-2/7/2014: Lancaster Engineering Dept PG Review Conference 2014 (oral presentation, PhD registration confirmed)
- 23/6/2014: ElectrochemNW 2014, Liverpool University, U.K. (poster presentation)
- 13-16/4/2014: Universities Nuclear Technology Forum Oxford University, U.K. (oral presentation)
- 2-3/7/2013 Lancaster Engineering Dept PG Review Conference 2013 (oral presentation)

## Industry Links:

---

- 18/1/2017: 5th PhD Research Seminar for NDA Sponsored PhD Projects, 2017 Manchester Conference Centre (oral presentation)
- 20/1/2016: 4th PhD Research Seminar for NDA Sponsored PhD Projects, 2016 Manchester Conference Centre (oral/poster presentation)
- 5/3/2015: Overview of Decommissioning Challenges – NDA sponsored PhD Students visit to Sellafield, UK
- 14/1/2015: 3rd PhD Research Seminar for NDA Sponsored PhD Projects, 2015 Manchester Conference Centre (oral presentation)
- 12/11/2014: Attendance at Radioactive Frontiers in Decommissioning and Radioactive Waste Management Conference, Lancaster University
- 7-8/4/2014: Training Workshop through SACCESS on "Working with Uranium" National Nuclear Laboratory, visit to Springfields, Preston, UK
- 29/1/2014: 2nd PhD Research Seminar for NDA Sponsored PhD Projects, 2014 Manchester Conference Centre (oral/poster presentation)

## Training Events / Research Seminars

---

- 13-17/1/2014: University of Bath Electrochemistry Winter School 2014
- 31/10/2013: Training course "Ionising Radiation: Basic Awareness" Lancaster University
- 13/5/2013: Training course 'Working with substances hazardous to health basic COSHH awareness' Lancaster University

## Grants

---

- 2016 - 2017: Science and Technology Graduate School Travel Grant for international travel
  - 2015 - 2016: Science and Technology Graduate School Travel Grant for international travel
  - 2014 - 2015: Science and Technology Graduate School Travel Grant for international travel
-

